

AEDC-TR-79-56

AFAPL-TR-79-2099



**An Investigation of F-16
Nozzle-Afterbody Forces at
Transonic Mach Numbers with
Emphasis on Support
System Interference**

Earl A. Price, Jr.
ARO, Inc.

December 1979

Final Report for Period January – July 1978

Approved for public release; distribution unlimited.

**ARNOLD ENGINEERING DEVELOPMENT CENTER
ARNOLD AIR FORCE STATION, TENNESSEE
AIR FORCE SYSTEMS COMMAND
UNITED STATES AIR FORCE**

NOTICES

When U. S. Government drawings, specifications, or other data are used for any purpose other than a definitely related Government procurement operation, the Government thereby incurs no responsibility nor any obligation whatsoever, and the fact that the Government may have formulated, furnished, or in any way supplied the said drawings, specifications, or other data, is not to be regarded by implication or otherwise, or in any manner licensing the holder or any other person or corporation, or conveying any rights or permission to manufacture, use, or sell any patented invention that may in any way be related thereto.

Qualified users may obtain copies of this report from the Defense Documentation Center.

References to named commercial products in this report are not to be considered in any sense as an indorsement of the product by the United States Air Force or the Government.

This report has been reviewed by the Information Office (OI) and is releasable to the National Technical Information Service (NTIS). At NTIS, it will be available to the general public, including foreign nations.

APPROVAL STATEMENT

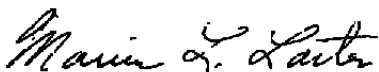
This report has been reviewed and approved.



ELTON R. THOMPSON
Project Manager
Directorate of Technology

Approved for publication:

FOR THE COMMANDER



MARION L. LASTER
Director of Technology
Deputy for Operations

UNCLASSIFIED

20. ABSTRACT (Concluded)

of nozzle-afterbody axial and normal forces obtained from integrating pressure data. The results include parametric studies of the effects of various components of the wingtip support system (i.e., the support blade axial position, wingtip boom diameter, boom spacing, and boom-tip axial location). High-pressure air at ambient temperature was utilized for exhaust plume simulation. The results indicate that a sting support passing through the nozzle with the jet effects simulated by an annular jet appears to offer a minimum interference support system for the type of nozzle-afterbody test described in this report. The basic wingtip support system, as designed for this model, produced significant interference at the high subsonic Mach numbers. Parametric studies of the effect of the components of the wingtip system indicate that a significant portion of the interference could be eliminated by proper placement of the aft support blade. For those cases in which the sting support may not be utilized, an optimized wingtip support system can provide the next most interference-free conditions.

PREFACE

The work reported herein was conducted by the Arnold Engineering Development Center (AEDC), Air Force Systems Command (AFSC), at the request of the Air Force Aero-Propulsion Laboratory (AFAPL/TBA), Wright-Patterson Air Force Base, Ohio, and the Directorate of Technology (AEDC/DOT). The results were obtained by ARO, Inc., AEDC Division (a Sverdrup Corporation Company), operating contractor for the AEDC, AFSC, Arnold Air Force Station, Tennessee. Testing was conducted under ARO Project Numbers P41T-M2A and P41T-25A; analysis of the data was conducted under Project Numbers P32A-R1A and P32G-23E. The Air Force project manager for this program was Mr. Elton R. Thompson, AEDC/DOT. Data analysis was completed on May 4, 1979, and the manuscript was submitted for publication on June 19, 1979.

CONTENTS

	<u>Page</u>
1.0 INTRODUCTION	9
2.0 APPARATUS	
2.1 Test Facility	10
2.2 Model and Support Systems	10
2.3 Instrumentation	13
3.0 PROCEDURE	
3.1 Test Conditions and Procedure	13
3.2 Data Reduction	14
3.3 Uncertainty of Measurements	15
4.0 RESULTS AND DISCUSSION	16
4.1 Basic Data	17
4.2 Support System Interference	21
5.0 CONCLUDING REMARKS	31
REFERENCES	32

ILLUSTRATIONS

Figure

1. General Arrangement of F-16A Fighter Aircraft	35
2. Model Installation in Tunnel 16T	36
3. Air Supply Arrangement to Model Aft Air Supply Tube	40
4. Air Vehicle Nozzles	41
5. Small Sting Support Installation	43
6. Large Sting Support Installation	44
7. Hardware Utilized on Large Sting Support System for Interference Studies	45
8. Model with Wingtip Booms Installed in Tunnel 16T	46
9. Modified Wing Configurations in Tunnel 16T	49
10. Wingtip Support Installation	51
11. Hardware Utilized on Wingtip Support System for Interference Studies	52
12. Strut Support Installation	53
13. Sting Taper Locations Investigated on the Strut Support System	54

<u>Figure</u>	<u>Page</u>
14. Nozzle and Afterbody Static Pressure Instrumentation	55
15. Estimated Uncertainties in Wind Tunnel Parameters	56
16. Variation of Axial-Force Coefficients with Mach Number for Various Nozzle Configurations, Large Sting Support System, $RN = 3.4 \times 10^6$, $\alpha = 0$	57
17. Variation of Axial-Force Coefficients with Mach Number for Various Nozzle Configurations, Small Sting Support System, $RN = 2.1 \times 10^6$, $\alpha = 0$	59
18. Effect of Nozzle Configuration on the Nozzle and After- body Static Pressure Distribution, Large Sting Support System, $RN = 3.4 \times 10^6$, $\alpha = 0$	61
19. Effect of Nozzle Configuration on the Nozzle and After- body Static Pressure Distribution, Small Sting Support System, $RN = 2.1 \times 10^6$, $\alpha = 0$	79
20. Variation of Nozzle-Afterbody Axial-Force Coefficient with Angle of Attack for Various Nozzle Configurations, Large Sting Support System	89
21. Variation of Nozzle-Afterbody Normal-Force Coefficient with Angle of Attack for Various Nozzle Configurations, Large Sting Support System	92
22. Effect of Angle of Attack on the Nozzle-Afterbody Static Pressure Distribution, Large Sting Support System, Max A/B 6.6 Nozzle, NPR = 4.8	95
23. Effect of Horizontal Tail Deflection on the Nozzle- Afterbody Axial-Force Coefficients for Various Nozzle Configurations, $\alpha = 0$	113
24. Effect of Horizontal Tail Deflection on the Nozzle- Afterbody Normal-Force Coefficient for Various Nozzle Configurations, $\alpha = 0$	115
25. Influence of Horizontal Tail Deflection on the Nozzle- Afterbody Pressure Distributions, Large Sting Support System, Max A/B 7.75 Nozzle, NPR = 6.8, $\alpha = 0$	116
26. Variation of Nozzle-Afterbody Axial-Force Coefficient with NPR for Various Nozzle Configurations, Wingtip Support System, $\alpha = 0$	124
27. Effect of Nozzle Pressure Ratio on the Nozzle-Afterbody Pressure Distributions, Cruise 3.4 Nozzle, Wingtip Support System, $\alpha = 0$	129

<u>Figure</u>	<u>Page</u>
28. Effect of Nozzle Pressure Ratio on the Nozzle-Afterbody Pressure Distributions, Max A/B 6.6 Nozzle, Wingtip Support System, $\alpha = 0$	139
29. Comparison of Afterbody Axial-Force Data from Full and Annular Jet Configurations, Wingtip Support System, $\alpha = 0$	149
30. Summary of Annular Jet Axial-Force Comparison at Design NPR, Wingtip Support System, $\alpha = 0$	154
31. Effect of Angle of Attack on the Annular and Full Jet Comparison of Axial-Force Results, Wingtip Support System, Design NPR	155
32. Effect of Angle of Attack on the Annular and Full Jet Comparison of Normal-Force Results, Wingtip Support System, Design NPR	156
33. Comparison of Annular and Solid Plume Simulation of Full Plume Effects on Nozzle-Afterbody Axial-Force Coefficients, Wingtip Support System, Cruise Nozzle, Design NPR, $\alpha = 0$	157
34. Pressure Distributions Comparing Annular and Full Plume Results, $M_\infty = 0.9$, Wingtip Support System, Cruise Nozzle, $\alpha = 0$	158
35. Pressure Distributions Comparing Annular and Full Plume Results, $M_\infty = 1.2$, Wingtip Support System, Cruise Nozzle, $\alpha = 0$	162
36. Effect of Sting Taper Location on the Nozzle-Afterbody Axial-Force Coefficients, Wingtip Support System, Max A/B 6.6 Nozzle	166
37. Total Wingtip Support System Interference on Nozzle-Afterbody Axial Force, Large Sting Support System	168
38. Total Wingtip Support System Interference on Nozzle-Afterbody Normal Force, Large Sting Support System	170
39. Aft Support Blade Interference on Nozzle-Afterbody Axial Force, Large Sting Support System, Max A/B 6.6 Nozzle, NPR = 4.8	171
40. Aft Support Blade Interference on Nozzle-Afterbody Normal Force, Large Sting Support System, Max A/B 6.6 Nozzle, NPR = 4.8	172
41. Effect of Aft Support Blade Movement on Nozzle-Afterbody Axial Force, Max A/B 6.6 Nozzle, NPR = 4.8	173

<u>Figure</u>	<u>Page</u>
42. Sensitivity of Nozzle-Afterbody Axial Force to Aft Support Blade Position, Max A/B 6.6 Nozzle, NPR = 4.8, $\alpha = 0$	175
43. Wingtip Boom Interference on Nozzle-Afterbody Axial Force, Large Sting Support System, Max A/B 6.6 Nozzle, NPR = 4.8	176
44. Wingtip Boom Interference on Nozzle-Afterbody Normal Force, Large Sting Support System, Max A/B 6.6 Nozzle, NPR = 4.8	177
45. Effect of Boom-Tip Axial Location on Nozzle-Afterbody Axial Force, Wingtip Support System, Cruise 3.4 Nozzle, NPR = 3.3	178
46. Effect of Wingtip Boom Lateral Spacing on Nozzle- Afterbody Axial Force, Large Sting Support System, Max A/B 6.6 Nozzle, NPR = 4.8	179
47. Illustration of Boom-Tip Shock Wave Interaction with Model	181
48. Illustration of Boom-Tip Expansion Fan Interaction with Model	182
49. Effect of Wingtip Boom Lateral Spacing on Nozzle- Afterbody Normal Force, Large Sting Support System, Max A/B 6.6 Nozzle, NPR = 4.8	183
50. Effect of Wingtip Boom Diameter on Nozzle-Afterbody Axial Force, Wingtip Support System	184
51. Effect of Wingtip Boom Diameter on Nozzle-Afterbody Normal Force, Wingtip Support System	185
52. Effect of Wing-Planform Modification on Nozzle- Afterbody Axial Force, Large Sting Support System, Max A/B 6.6 Nozzle, NPR = 4.8	186
53. Effect of Wing-Planform Modification on Nozzle- Afterbody Normal Force, Large Sting Support System, Max A/B 6.6 Nozzle, NPR = 4.8	187
54. Comparison of Total Wingtip and Various Wingtip Component Interference Increments on Nozzle-Afterbody Axial Force, Large Sting Support System, Max A/B 6.6 Nozzle, NPR = 4.8	188
55. Comparison of Total Wingtip and Various Wingtip Component Interference Increments on Nozzle-Afterbody Normal Force, Large Sting Support System, Max A/B 6.6 Nozzle, NPR = 4.8	190
56. Strut Interference on Nozzle-Afterbody Axial Force	191
57. Strut Interference on Nozzle-Afterbody Normal Force	193

<u>Figure</u>	<u>Page</u>
58. Comparison of Interference on Nozzle-Afterbody Axial Force from Sting, Wingtip and Strut Support Systems, Cruise 3.4 Nozzle	194
59. Comparison of Interference on Nozzle-Afterbody Normal Force from Sting, Wingtip, and Strut Support Systems, Cruise 3.4 Nozzle, $\alpha = 0$	196
60. Influence of Support Interference on Nozzle Configuration Evaluation	198

TABLES

1. Configuration List	199
2. Configuration Identification	201

NOMENCLATURE	206
--------------------	-----

1.0 INTRODUCTION

The economics of aerodynamic testing as well as of aircraft selection and fabrication require that the best possible flight performance predictions be derived from wind tunnel tests. This requires that reliability of test techniques be continually evaluated in light of current technology and test requirements. The conduct of nozzle-afterbody tests in the wind tunnel presents one of the more difficult challenges for obtaining data for translation into flight predictions. Typical nozzle-afterbody test installations in the past have included support systems which permitted full jet simulation of the exhaust plume while at certain conditions introducing significant interference into the measured data quantities. Use of such support systems is typically justified by using only increments in coefficients between two configurations or test conditions on the same support system and assuming the interference is the same for both sets of data.

The test program reported herein was planned to test a 1/9-scale F-16 nozzle-afterbody model on four different support systems. Support systems chosen for this investigation were a strut attached to the canopy region of the model, a wingtip support system, a 2.75-in.-diam sting, and a 2.4-in.-diam sting. Numerous tests have been conducted previously using strut-supported models, and some (e.g., Ref. 1) have reported the strut interference. Other nozzle-afterbody tests have been conducted which record the interference from wingtip support systems (e.g., Ref. 2). The concept of obtaining nozzle-afterbody data on a sting-supported model utilizing an annular jet has been reported in Refs. 3, 4, and 5. By testing the same model on each type of support system one can evaluate the relative merits of each system.

The purpose of the tests reported herein were (1) to provide data for evaluating support interference from each of the aforementioned-type systems on a single model and (2) to obtain 1/9-scale F-16 nozzle-afterbody data on the most interference-free installation possible for comparison with results from a 0.25-scale model and flight tests.

Afterbody and nozzle surface pressure data were obtained during four wind tunnel entries over the Mach number range from 0.6 to 1.5. The results on the small sting were obtained at a nominal unit Reynolds number of $2.1 \times 10^6/\text{ft}$, and the basic data matrix on the three other support systems was obtained at a unit Reynolds number of $3.4 \times 10^6/\text{ft}$. In addition to recording the total support system interference on each system, the tests included a parametric study of various components of the wingtip support system. This included investigating the effects of support blade axial position, wingtip boom diameter, boom spacing, and boom-tip axial location. High-pressure air at ambient temperature was utilized for exhaust plume simulation. Model angle of attack and horizontal tail deflection angles were varied in the ranges from 0 to 9 deg and 0 to -8 deg, respectively.

2.0 APPARATUS

2.1 TEST FACILITY

The Arnold Engineering Development Center (AEDC) Propulsion Wind Tunnel (16T) is a variable density, continuous flow tunnel capable of operation at Mach numbers from 0.20 to 1.60 and stagnation pressures from 120 to 4,000 psfa. The maximum attainable Mach number can vary slightly depending upon the tunnel pressure ratio requirements with a particular test installation. The maximum stagnation pressure attainable is a function of Mach number and available electrical power. The tunnel stagnation temperature can be varied from about 80 to 160°F depending upon the available cooling water temperature. The test section is 16 ft square by 40 ft long and is enclosed by 60-deg-inclined-hole perforated walls of six-percent porosity. Additional information about the tunnel, its capabilities and operating characteristics is presented in Ref. 6.

2.2 MODEL AND SUPPORT SYSTEMS

The test article was a 1/9-scale model of the F-16 fighter aircraft with overall dimensions as shown in Fig. 1. Since one of the purposes of this test program was to investigate the effects of support system interference on the aft portion of a jet effects model, four tunnel entries on different support systems were required. The four support systems consisted of a 2.4-in.-diam sting (Fig. 2a), a 2.75-in.-diam sting (Fig. 2b), a wingtip support arrangement (Fig. 2c), and a strut support (Fig. 2d).

The aircraft model was designed for jet effects testing by incorporating an aerodynamic fairing over the inlet and internal high-pressure air passages through the support systems to the nozzle exit region of the model. The model aft flow duct arrangement for the different supports is shown in Fig. 3. High-pressure air at ambient temperature was used to simulate the exhaust nozzle flow. The horizontal stabilizers could be remotely driven individually from 1 to -9 deg. Nozzles corresponding to four engine power settings, cruise (3.4), partially augmented (5.1), max augmented-low mode (6.6), and max augmented-high mode (7.75) were used during this test. (The numerals following each nozzle indicate the nozzle full-scale exit area in square feet.) The cross sections of each of the four nozzles are shown in Fig. 4. The four external boattails corresponding to the four nozzles are shown in Fig. 4a for conventional full jet nozzles and in Fig. 4b for the annular jet nozzles. The latter boattails were split longitudinally to facilitate nozzle changes with the sting installation. Internal nozzles for the sting installations (Fig. 4b) were designed to match nozzle divergence angle and exit-to-throat area ratios of the conventional nozzles (Fig. 4a). Inserts were required to adapt the nozzles built for use with the large diameter sting to the proper area ratio for

testing with the small sting. The internal nozzles used with the sting installation were also split longitudinally to facilitate nozzle changes. The size of the cruise nozzle precluded testing it with annular flow on the large sting. Therefore, during tests with the large sting the inner cruise nozzle was removed, and only jet-off data were obtained.

A list of all configurations tested during this series of tests is presented in Table 1. This table provides a complete listing of test configurations even though results from each are not presented in this report. Table 2 includes configuration descriptions and sketches of each configuration included in this report.

2.2.1 Small Sting Support System

The small sting installation consisted of a 2.4-in.-diam sting supporting the model through the exhaust nozzle (Fig. 5). This sting was designed to obtain data with minimum sting interference. The taper was located as far aft as possible while still providing the strength to test at a moderate Reynolds number over the complete Mach number range. Data taken with this sting were obtained at a unit Reynolds number of $2.1 \times 10^6/\text{ft}$ with each of the four air vehicle nozzles installed on the basic aircraft configuration. As was shown in Fig. 3, instrumentation leads were routed through a tube in the center of the sting. High-pressure air was brought on board through the annular passage around the instrumentation tube.

2.2.2 Large Sting Support System

The large sting installation consisted of a 2.75-in.-diam sting supporting the model through the exhaust nozzle (Fig. 6). This support system was utilized to obtain data on the basic aircraft configuration with each of the four nozzles. Annular exhaust flow was used with the three largest nozzles, and jet-off data were obtained on the cruise nozzle. In addition, this support system was utilized for supporting the configurations required to define the wingtip support system interference. Interference from the wingtip support system was evaluated by comparing results from the basic air vehicle configuration (Fig. 6) with a dummy wingtip support as shown in Fig. 7. The dummy wingtip components consisted of a modified wing planform, wingtip booms, and aft-support blade for simulation of the actual wingtip system. A study of wingtip boom spacing was conducted by testing with the booms spaced 6 in. both inboard and outboard of the standard position. These positions are identified by the dashed lines in Fig. 7. Photographs of each of these boom positions are shown in Fig. 8. The influence of the aft-support blade position was also determined by testing with the blade moved aft 6.75 in. as shown by the dashed lines in

Fig. 7. Additional interference increments were assessed by testing with the modified wing (Fig. 9a) and with the modified wing plus the aft-support blade (Fig. 9b).

2.2.3 Wingtip Support System

The wingtip support system (Fig. 10) provided a means of obtaining data from nozzles with full exhaust plume simulation. High-pressure air for the exhaust gas simulation was brought through the center of the booms, through passages in the wings to the internal model high-pressure air passages. To provide sufficient strength and area for high-pressure air and instrumentation leads the aircraft wing planform for this support arrangement was modified to a constant chord outboard of BL 12.0. Aircraft loads were transmitted through the wingtip booms to the horizontal support blade, which was supported by a sting. In addition to obtaining data with full plume jet simulation this support system was also used for parametric studies of interference on the model afterbody associated with changes in size and location of certain components of the wingtip system. Shown in Fig. 11 is the basic wingtip support system with the modified configurations indicated by the dashed lines. These configurations include boom tips extended to the model nose, boom shells to simulate 50-percent larger booms, a support blade location 10.6 in. forward of the standard position, and dummy stings simulating both the 2.4- and 2.75-in. stings. Data from these sting configurations with annular jet flow were obtained to compare with the full plume results. The model photograph in Fig. 2c is with the large dummy sting installed.

2.2.4 Strut Support System

The strut support system was used to obtain data on what may be considered a conventional support system for nozzle-afterbody testing. As illustrated in Fig. 12 the model was inverted and attached to the strut in the canopy region. The model was configured with the aerodynamic wing and wingtip missiles. High-pressure air and instrumentation leads were brought into the model through the strut leading- and trailing-edge fairings. The primary strut-supported configuration included a dummy sting which simulated the large sting support system. This arrangement permitted evaluation of strut interference by comparing the data obtained with that configuration with the sting-supported model data. The influence of sting taper location on the afterbody pressures was also evaluated with this support system as illustrated in Fig. 13.

2.3 INSTRUMENTATION

Model surface pressures, obtained from 207 surface pressure orifices located on the forebody (29), afterbody (112), horizontal tail-shelf (6), and boattail (60) were measured using five 48-port Scanivalves® equipped with ± 15 -psid transducers. The reference and calibrate pressures, measured by precision ± 5 -psid transducers, were used to calculate the transducer sensitivities for each data point. The reference and calibrate pressures of each valve were also measured by the valve transducer at the end of each valve cycle for comparison with the ± 5 -psid transducer measurement as a part of data verification. Only the data obtained on the afterbody and nozzle are presented in this report. The pressure orifice locations, which were located primarily on the right-hand side of the model, are indicated in Fig. 14. Exhaust nozzle flow rate was determined from a critical flow venturi. Pressure transducers of the appropriate ranges were used to measure the pressures in the high-pressure air supply system and model flow duct.

Strain gages were installed on both the large and small stings and on each of the wingtip support booms to monitor model loads and to calculate angular deflections of the support system. A model-mounted angular position indicator was used as the primary angle-of-attack indicator when the dummy wingtip booms were installed on the large sting apparatus; it was also used as a backup system for the other sting and wingtip support configurations. For the strut support system installation, an angular position indicator was mounted on the pitch table at the base of the strut.

The horizontal tail panels were positioned over the range from 1 to -9 deg by electric motors. Horizontal tail deflection for each panel was determined from the output of a potentiometer in each tail panel drive mechanism.

3.0 PROCEDURE

3.1 TEST CONDITIONS AND PROCEDURE

Data were obtained at free-stream Mach numbers from 0.6 to 1.5. The nominal unit Reynolds number for tests on all support systems except the small sting was 3.4×10^6 per foot. Tests on the small sting support system were conducted at a unit Reynolds number of 2.1×10^6 because of structural limitations. Reynolds number excursions were made on certain configurations on the large sting and wingtip support systems. The following listing

presents the matrix of Mach numbers and Reynolds numbers at which data were obtained with each support system.

<u>Support System</u>	<u>Mach Number</u>								
	<u>0.6</u>	<u>0.8</u>	<u>0.9</u>	<u>0.95</u>	<u>1.0</u>	<u>1.05</u>	<u>1.1</u>	<u>1.2</u>	<u>1.5</u>
	<u>Free-Stream Reynolds Number per Foot $\times 10^{-6}$</u>								
Small Sting	2.1	2.1	2.1					2.1	2.1
	3.4								
Large Sting	2.1	2.1	2.1					2.1	2.1
	3.4	3.4	3.4	3.4	3.4	3.4	3.4	3.4	3.4
	4.4	4.4	4.4					4.4	
	5.8	5.8	5.6						
Wingtip	2.1	2.1	2.1					2.1	2.1
	3.4	3.4	3.4	3.4	3.4		3.4	3.4	3.4
	4.4	4.4	4.4					4.4	
	6.0	5.8	5.6						
Strut	3.4	3.4	3.4	3.4	3.4	3.4	3.4	3.4	3.4

The angle-of-attack range varied with each configuration and test condition but was within the limits of 0 to 9 deg. Nozzle pressure ratio was varied from jet-off to 1.5 times the nozzle design pressure ratio. Data were recorded at various horizontal tail deflection angles between 0 and -9 deg.

The test procedure with a given geometric configuration and horizontal tail angle consisted of setting either a constant angle of attack and varying nozzle pressure ratio or a constant nozzle pressure ratio and varying angle of attack. In either mode of data acquisition, nozzle pressure ratio and angle of attack were controlled by the facility computer. Real-time calculation of angle of attack, nozzle pressure ratio, and horizontal tail deflection angles were displayed in the control room to aid in conduct of the test.

3.2 DATA REDUCTION

Pressure coefficients were calculated from the static pressure measured at each orifice. Each pressure was associated with a given projected area in the axial- and normal-force directions so that aft-fuselage and nozzle axial and normal pressure forces could be obtained from a pressure-area integration. The pressure forces determined from pressure measurements on the right-hand side of the model were multiplied by two and

nondimensionalized by free-stream dynamic pressure and model wing reference area. When a pressure orifice was determined to be bad (plugged or leaking), the projected areas associated with that orifice were assigned to the adjacent orifices. Nozzle total pressure was based upon the average of the six total pressures in the aft air supply tube for the conventional full jet configurations and the average of three total pressures for the annular jet configurations. Model angle of attack was calculated from the output of a model-mounted, strain-gaged angular position indicator as well as from the combination of sting pitch angle plus calculated deflections for both sting installation and the wingtip support system. The model-mounted angular position indicator was found to be somewhat unreliable. Although some difficulties were encountered with both systems, the sting pitch angle plus sting deflections method is considered the most reliable and was used as the primary angle measurement for most of the configurations. Since pitch-plane deflections of the strut are negligible, angle of attack for this support system was calculated from a reliable angular position indicator mounted on the base of the strut.

3.3 UNCERTAINTY OF MEASUREMENTS

Uncertainties of the basic tunnel parameters (bands which include 95 percent of the calibration data), shown in Fig. 15, were estimated from repeat calibrations of the instrumentation and uniformity of the test section flow during tunnel calibration. Uncertainties in the instrumentation systems were estimated from repeat calibrations of the systems against secondary standards whose precisions are traceable to the National Bureau of Standards calibration equipment. The instrument uncertainties are combined using the Taylor series method of error propagation described in Ref. 7 to determine the uncertainties of nozzle pressure ratio and pressure coefficient shown below.

UNCERTAINTIES

<u>Parameter</u>	<u>Mach Number</u>			
	<u>0.6</u>	<u>0.9</u>	<u>1.2</u>	<u>1.5</u>
α	± 0.15	± 0.15	± 0.15	± 0.15
NPR	± 0.02	± 0.02	± 0.05	± 0.04
C_p	± 0.0127	± 0.0091	± 0.0066	± 0.0060
C_A	± 0.0008	± 0.0006	± 0.0004	± 0.0004
C_N	± 0.007	± 0.005	± 0.004	± 0.003

The uncertainties in the axial- and normal-force coefficients were calculated by integrating the uncertainty in pressure coefficient over the respective projected areas. The uncertainty in angle of attack is based upon average differences in angle of attack as determined from the redundant systems.

These uncertainties in C_A and C_N represent a worst possible case since any random error in individual pressure measurements is implied to occur in the same direction at the same time for all pressure orifices. Data repeatability is a more useful parameter to consider for the results presented in this report when differences between two configurations are of primary interest. The data presented in the following table illustrate the repeatability in integrated coefficients.

<u>M_∞</u>	REPEATABILITY				Number of Repeat Conditions
	Average <u>ΔC_A</u>	Maximum <u>ΔC_A</u>	Average <u>ΔC_N</u>	Maximum <u>ΔC_N</u>	
0.6	0.00016	0.00045	0.00137	0.00385	12
0.8	0.00008	0.00021	0.00030	0.00181	18
0.9	0.00009	0.00017	0.00097	0.00247	18
1.2	0.00012	0.00038	0.00074	0.00210	18
1.5	0.00002	0.00006	0.00027	0.00115	12

The maximum repeatability values are approximately one-half the calculated uncertainties.

4.0 RESULTS AND DISCUSSION

The results from this investigation are presented in two major subsections. The first subsection (4.1) contains results denoted "basic data," which include nozzle and afterbody pressure-integrated axial- and normal-force coefficients. As supportive evidence of data interpretations, pressure distributions over the nozzle-afterbody region are also presented in certain instances. The second subsection (4.2) contains support system interference results. A portion of these results is presented in terms of integrated axial-force coefficients; however, the majority of the interference data are presented in terms of increments in axial- and normal-force coefficients between two configurations. Except where specific exceptions are noted, results are presented for the horizontal tail at zero deflection angle and at a free-stream Reynolds number per foot of 3.4×10^6 . Portions of the data from this investigation have been presented previously (Refs. 8 and 9).

4.1 BASIC DATA

One of the objectives of this investigation was to obtain nozzle-afterbody data with a minimum interference support system to be used for future comparisons with F-16 0.25-scale and flight test results. It was also desired to determine the sensitivity of the F-16 to some of the model parameters typically encountered in afterbody testing such as nozzle closure, angle of attack, horizontal tail deflection, and nozzle pressure ratio. The effects of variations of the first three of these parameters were measured on the sting support systems. Data showing the effects of the fourth parameter (nozzle pressure ratio) were obtained with the model on the wingtip support system to permit full plume jet simulation.

4.1.1 Effects of Nozzle Closure

Axial-force coefficients as a function of free-stream Mach number are presented in Figs. 16 and 17 for the large and small sting configurations, respectively. The afterbody (F.S. 42.22 to 56.94) and nozzle axial-force coefficients are presented separately in Figs. 16a and 17a, respectively, and the total nacelle axial force is shown in Figs. 16b and 17b. Data with the three larger nozzles and the large sting support system (Fig. 16) were obtained with an annular jet plume operating at the design pressure ratio of each nozzle. The large sting completely filled the cruise nozzle; therefore, only jet-off data were obtained. The data obtained with the cruise nozzle and the large sting are not strictly comparable to the data obtained with the other nozzles, since the effects of jet entrainment are not present in the former. The data obtained with the small sting support system (Fig. 17) were obtained with each of the nozzles flowing at design pressure ratio. For each of the nozzles tested, the nozzle portion of the model experienced a thrust force (negative axial-force coefficient) at subsonic Mach numbers. For Mach numbers of 0.9 and below, the magnitude of this force increased as nozzle closure (axial projected area) increased. At supersonic Mach numbers, however, this trend was reversed with a drag force acting on all nozzles, which increased with increasing closure. The afterbody portion of the model exhibits a decreasing axial force with decreasing nozzle closure for all Mach numbers. The effect of nozzle closure on the afterbody force is significant at the subsonic Mach numbers but is relatively small at the supersonic Mach numbers, decreasing to essentially zero at $M_\infty = 1.5$. When coefficients from these two components are combined (Figs. 16b and 17b), the large effects of nozzle closure on the two components tend to cancel at Mach numbers below 0.95, resulting in a relatively small positive axial force. The component forces are additive at supersonic Mach numbers, resulting in a large, systematic effect of closure with the largest closure having the highest axial force. In general, similar trends are present in the results with both the large and small stings. One difference, which is evident in the total axial-force coefficient, is that

the cruise nozzle data obtained with the large sting are lower, relative to the other nozzles, than those obtained with the small sting. This difference is caused by the absence of jet entrainment with the large sting support system, which typically reduces the nozzle surface pressure, thus increasing drag.

One may visualize more clearly the flow phenomena responsible for the effects of nozzle closure by studying the pressure distributions presented in Figs. 18 and 19 for the large and small sting results, respectively. Data along five rows of pressures on the model upper surface and along four rows of pressures on the lower surface are presented for each given test condition. The vertical dashed line at $X/L = 0.93$ represents the afterbody-nozzle interface.

In general, at subsonic Mach numbers, increasing nozzle closure resulted in increased expansion on the upstream portion of the nozzle and higher compression on the aft portion of the nozzle. The thrust on the nozzle that occurs at subsonic Mach numbers is evident here since most of the nozzle pressure coefficients are positive for all nozzle closures. At supersonic Mach numbers most of the pressure coefficients on the nozzle are negative even though a strong recompression does occur on the nozzle.

The greater expansion over the nozzle, which results when nozzle closure is increased, is also consistently present on a significant portion of the afterbody at subsonic Mach numbers. At $M_\infty = 1.2$, changing nozzle closure had only slight effect on the afterbody, and at $M_\infty = 1.5$ the effects of closure were essentially confined to the nozzle.

These trends observed in the pressure data serve to substantiate the integrated axial-force results presented in Figs. 16 and 17. Changes in pressure on the afterbody may be correlated directly with changes in axial-force coefficient since afterbody areas remain constant. Correlation of the nozzle pressures with nozzle axial force is not as easy, however, since nozzle axial projected area changes by approximately a factor of three from cruise nozzle to the max A/B 7.75 nozzle.

4.1.2 Effects of Angle of Attack

The effects of angle of attack on the nozzle-afterbody axial-force coefficients are presented in Fig. 20 for the model installed on the large sting support system. With the exception of certain Mach numbers near 1.0 there was generally a decrease in axial force with increasing angle of attack. The largest variations of this type were at Mach numbers 0.95 and 1.50. For Mach numbers 1.0, 1.05, and 1.10, there were some significant increases in axial force with increasing angle of attack. The trends with angle of attack are generally

similar for each of the nozzle configurations, the cruise nozzle being slightly more sensitive to angle of attack at the Mach numbers near one.

The effect of angle of attack on the nozzle-afterbody normal-force coefficient is presented in Fig. 21, generally demonstrating a quasi-linear increase in C_N with angle of attack. One notable exception is the data at $M_\infty = 0.9$, where the C_N curves flatten out between $\alpha = 7$ and 9 deg. Similar trends are demonstrated for each nozzle.

Pressure distributions illustrating the effect of angle of attack are presented in Fig. 22 for the max A/B 6.6 nozzle. The effects of angle of attack on the afterbody pressures are generally larger than those on the nozzle. The expansion over the aft end of the afterbody and the subsequent recompression apparently serve to dampen the upstream angle-of-attack effects. At Mach numbers up to 1.0 the effects of α are generally larger on the leeward side of the model than on the windward side, and the magnitude of these effects increases with increasing Mach number. At Mach numbers 1.2 and 1.5, the effects of angle of attack are relatively uniform on both sides of the afterbody, with pressure decreasing on the leeward side and increasing on the windward side. The nozzle pressure distributions indicate a larger effect at angle of attack at these Mach numbers than at lower Mach numbers, particularly on the windward side.

4.1.3 Effects of Horizontal Tail Deflection

The nominal horizontal tail deflection angle for most of the support system interference investigation was zero. However, since one objective of this investigation was to obtain results for comparison with flight test data at various trimmed flight conditions, a study of the sensitivity of the afterbody to tail deflection was conducted.

Data are presented in Figs. 23 and 24 which illustrate the effects of horizontal tail deflection on nozzle-afterbody axial- and normal-force coefficients, respectively. Data are presented for each of the four nozzles at both subsonic and supersonic Mach numbers. At a given Mach number, the variation in both axial- and normal-force coefficients with horizontal tail deflection is similar for each of the four nozzles. There is a general trend of increasing axial force with increasing negative tail deflection. The rate of increase is slightly higher at subsonic than at supersonic Mach numbers. The largest effect on axial force was at $M_\infty = 0.9$, where the 8-deg change in tail angle produced an increase in axial-force coefficient of 11 counts with the max A/B 6.6 nozzle ($C_A = 0.0001$ is one count). The smallest effect was at $M_\infty = 1.2$, where an increase of only 1.5 axial-force counts occurred on the max A/B 7.75 nozzle. Normal force decreased approximately linearly as the horizontal tail was deflected leading-edge down (negative). As with axial force, the normal

force is more sensitive to changes in tail deflection at the subsonic Mach numbers than at the supersonic Mach numbers.

Since the integrated axial- and normal-force data indicate similar effects with each nozzle, pressure distributions are presented in Fig. 25 for only the max A/B 7.75 nozzle as representative of trends on all nozzles. As the horizontal tails were deflected in the negative direction, the compression on the upper tail surface and the expansion on the lower surface have an influence over a significant portion of the afterbody. The expansion on the lower surface generally produced larger changes in the afterbody pressure coefficients than did the compression on the upper surface, accounting for the increase in axial-force coefficient with increasing negative tail deflection. In general, the variation of both the upper and lower surface pressures is in the direction to decrease normal force with increasing negative tail deflection. The noticeable exception to this rule is the row of pressures on the nozzle at AB086 which follow the variation of the lower surface pressures, indicating that rotation of the tail has exposed these orifices to the lower tail surface flow field. At the subsonic Mach numbers the effects of tail deflections are largest on the afterbody and somewhat minor on the nozzles. At supersonic Mach numbers the effects do not extend as far forward on the afterbody as at lower Mach numbers; however, the nozzle region experienced changes in pressure coefficient similar in magnitude to those on the afterbody. Based upon the sensitivity of the afterbody pressures to tail deflection shown in this section, it is concluded that tail deflection must be considered and matched as closely as possible when making comparisons between wind tunnel and flight test results.

4.1.4 Effects of Nozzle Pressure Ratio

The results presented in this section were obtained on the wingtip support system in order to have a full flowing, conventional jet plume simulation. Total nozzle and afterbody axial-force coefficients are presented in Fig. 26 as a function of nozzle pressure ratio for each of the four nozzles. The data obtained at the design pressure ratio for each nozzle are identified by a solid symbol.

The variation of the data with NPR as well as with nozzle closure is typical of other results documented in the literature (e.g., Refs. 2 and 3). Typically, the axial-force variation with NPR consists of a relatively high value jet-off followed by a rapid decrease to a drag "bucket" at low nozzle pressure ratios, then an entrainment-dominated increase to a maximum value near $NPR = 3$, and finally a decrease in axial force with increasing NPR resulting from plume shape dominance. As with the sting-supported model with annular jet simulation at design pressure ratio (Figs. 16 and 17), the nozzle configuration has relatively minor effects on total afterbody drag at subsonic Mach numbers, whereas at supersonic

Mach numbers there are large increases in total afterbody drag as nozzle closure is increased. From the standpoint of aerodynamic drag alone, the data indicate that at supersonic Mach numbers it is distinctly advantageous to have the nozzle as open as possible, regardless of the pressure ratio.

The effects of nozzle pressure ratio on the afterbody pressure distributions may be seen in Figs. 27 and 28, where data for five pressure ratios are presented for the cruise 3.4 and max A/B 6.6 nozzles, respectively. For each nozzle, data are presented for jet-off, $NPR \approx 2.5$, design NPR, 20 percent above design, and 50 percent above design. In general, pressure coefficients on the max A/B 6.6 nozzle (Fig. 28) exhibit considerably more sensitivity to changes in NPR than do those on the cruise 3.4 nozzle. The effects of NPR for both configurations are restricted to the nozzle at the supersonic Mach numbers, whereas at the subsonic Mach numbers the effects of NPR are propagated over significant portions of the afterbody as well. It is of interest to note the different variations in the pressure on the two nozzle configurations at the supersonic Mach numbers. The largest effect of NPR on the max A/B 6.6 nozzle occurs at the nozzle exit, where the pressure increases with increasing NPR. On the cruise nozzle, however, the effects near the nozzle exit are generally small, with larger effects occurring further forward on the nozzle, indicating that a somewhat unstable shock system exists which is apparently influenced by relatively small changes in pressure near the nozzle exit.

4.2 SUPPORT SYSTEM INTERFERENCE

The nature of jet effects testing on wind tunnel models introduces support system problems that typically are not present for other types of aerodynamic testing. The requirements associated with providing exhaust plume simulation on a properly contoured aircraft aft end have typically led to supporting the models by a strut or, more recently, by a wingtip support arrangement. While interference from these systems has been recognized and in some cases reported, the level of interference from each system on the same model has not been experimentally determined. The tests reported herein were planned with the objective of evaluating the interference on a single model from each of the support systems as well as defining the correlation between data obtained with annular and full jet plumes. In addition, a parametric study of interference from various components of the wingtip system was conducted to provide design insight for future tests on models which lend themselves to this system. A discussion of the interference associated with each of the support systems is presented in the following subsections.

4.2.1 Sting Interference

One method of obtaining afterbody aerodynamic data on axisymmetric nozzle

configurations which circumvents interference from support hardware attached to the forward portion of the model is to sting support the model through the nozzle exit. In addition, when the combination of nozzle size and sting diameter permit, an annular nozzle can be installed to provide jet simulation. This technique may be used to determine power effects if correlation of jet effects drag data between annular and conventional jet data can be demonstrated. Results presented in Ref. 3 on an isolated afterbody configuration demonstrated reasonable correlation of annular and conventional jet afterbody drag data for sting-to-nozzle exit diameter ratios (D_S/D_E) as large as 0.866. The purpose of the present investigation was to evaluate the annular/conventional jet correlation on a real aircraft configuration as well as to determine the sensitivity of the annular jet afterbody drag to the sting taper location.

4.2.1.1 Annular Jet Correlation

Presented in Fig. 29 are comparisons of the nozzle-afterbody axial-force coefficients from three conventional full jet and annular jet configurations which have a range of D_S/D_E from 0.656 to 0.865 for the annular jet configurations. These data were obtained on the wingtip support system with a dummy sting having the same external contour as the stings used for the sting-supported phase of testing. Results obtained at the design pressure ratio for each nozzle are denoted by the solid symbols. The annular jet data are presented as a function of both NPR and an effective nozzle pressure ratio, NPREF (dashed fairing). The parameter NPREF corresponds to an NPR of a conventional jet which has the same maximum isentropic plume diameter as the annular jet; it was shown in Ref. 3 to be a potentially effective parameter for correlating data obtained with annular and conventional jets.

Of primary interest is the agreement between the annular and full jet data near the design pressure ratio as well as the slope of the drag curve in this region. The slope is important if the correct drag at off-design conditions is to be defined. At the design pressure ratio, agreement between the two test techniques varies from exact ($M_\infty = 1.2$, cruise nozzle) to a maximum difference of five axial-force counts ($M_\infty = 0.6$, max A/B 6.6 nozzle). For nozzle pressure ratios greater than the design value, annular jet data as a function of NPREF are in agreement with the full jet data to within six axial-force counts. It should be noted that in some cases use of the NPREF correlation procedure results in more disagreement between two points in a particular set of data than if the correlation were not used. For example, at $M_\infty = 0.8$ with the max A/B 6.6 nozzle, the two sets of data versus NPR happen to cross near $NPR = 7.2$ and therefore agree quite well, whereas when the data are presented versus NPREF, there is approximately a five-count difference in the data. The important thing to note, however, is that the slope of the correlated data at underexpanded jet pressure ratios

follows that of the full jet data, indicating that the proper plume shape effects are being simulated. This trend is generally true for all the results of this investigation, thus further substantiating the conclusion of Ref. 3 that data obtained with annular jets should be correlated versus an effective nozzle pressure ratio.

A summary of the agreement between the full jet and annular jet data at design pressure ratio is presented in Fig. 30, where results are presented for all nozzles over the complete Mach number range of this investigation. All of the data differences fall within five axial-force counts of zero, and the average of the absolute magnitude for all the ΔCA 's is 0.00023. The poorest correlation for the cruise nozzle was at $M_\infty = 0.95$; however, the disagreement was only slightly worse than at $M_\infty = 0.9$ or 1.0, indicating no severe correlation problems through the high subsonic Mach number regime.

The effect of angle of attack on the correlation between full and annular jet axial-force data at design pressure ratio is shown in Fig. 31. The data indicate no serious degradation in the comparison with the model at angle of attack on either of the nozzles except at $M_\infty = 1.0$, where a ΔCA of approximately 0.001 was obtained at $\alpha = 7$ deg. However, in view of the good agreement at other Mach numbers this difference appears to be an anomaly resulting from the overall sensitivity of the model to tunnel conditions and model attitude at this Mach number rather than from the annular jet. A similar, although not as significant, anomaly occurs in the normal-force data comparison shown in Fig. 32. A maximum ΔCN of 0.004 at $M_\infty = 1.0$ is shown for $\alpha = 0$, and a slightly larger value (0.005) is shown at $\alpha = 7$ deg, indicating no serious degrading influence of the sting and annular jet on the afterbody normal force at angles of attack up to 7 deg.

The exit diameter of the cruise nozzle was only a few thousands of an inch larger than the large sting (2.75 in.); therefore, only the small sting could be tested with this nozzle in the annular jet mode. However, tests were conducted with the cruise nozzle, the large sting being used in effect as a solid plume simulator. The increments in axial-force coefficient between the full jet configuration at design pressure ratio and both the small sting annular jet configuration and the solid plume simulator configuration are presented in Fig. 33. These results indicate a significant difference between the annular jet and the solid plume simulator data. The average increment in CA for the annular jet data over the Mach number range is -0.00017, whereas that for the solid plume simulator is -0.00084.

Pressure distributions comparing annular and full plume configurations with the cruise nozzle are presented in Figs. 34 and 35 for data at Mach numbers 0.9 and 1.2, respectively. At each Mach number data are presented for nozzle design pressure ratio and for NPREF of 1.5 times design pressure ratio.

4.2.1.2 Sting Taper Location

In planning an afterbody test utilizing the annular jet test technique, one must consider a number of potential trade-offs in designing the sting. Among these variables are model loads, nozzle weight flow, minimum nozzle size, and sting taper location. In the absence of data on the effects of sting taper location on the annular jet simulation, the present test using the small sting was planned to be conducted only at low Reynolds numbers, and the taper was placed as far aft as was consistent with sting stress requirements at these conditions. This resulted in the sting taper's beginning four body diameters aft of the nozzle exit ($X'/D_B = 4.0$, $D_B = 7.125$). The large sting was designed to obtain high Reynolds number data and had the taper beginning at $X'/D_B = 3.0$. Since for structural reasons it is desirable to locate the sting taper as close to the model as possible, a parametric study of this parameter was included in the test matrix. The results obtained on the strut-supported model with large dummy sting (see Fig. 13) are presented in Fig. 36. The incremental effects on axial force of moving the large sting taper forward from $X'/D_B = 3.0$ to $X'/D_B = 1.0$ and 1.5 are shown at angles of attack of 0 and 7 deg.

The jet-off effects on axial force at the subsonic Mach numbers (Fig. 36a) are relatively small and follow the trends intuitively expected from moving a downstream blockage closer to the model. The results for jet-on conditions at Mach numbers 0.6 and 0.8 also follow expected trends but are larger in magnitude than the jet-off results. The $X'/D_B = 1.5$ position resulted in an increment of 1.7 axial-force counts at $\alpha = 7$ deg, and the $X'/D_B = 1.0$ position resulted in an increment of 5.5 counts. On the basis of the subsonic Mach number data, it is concluded that for this configuration the taper should not be located any closer to the model than the $X'/D_B = 1.5$ position. Since the location of the maximum sting diameter may be the important position parameter, rather than where the taper begins, these positions are also defined by X_1/D_M , where X_1 is the distance from the base of the model to the maximum sting diameter and D_M is the maximum sting diameter.

At Mach numbers higher than 0.8 the character of the interference appears to change somewhat, resulting in a maximum effect at $M_\infty = 1.0$ of 10 counts higher axial force with the taper in the forward position. An examination of pressure data at this sonic Mach number indicates an overall decrease in pressure over the afterbody with the taper in the forward position. This is an indication of the sensitivity of the overall flow field to model or support hardware configuration at Mach numbers close to unity. Since the effects of moving the sting taper from $X'/D_B = 3.0$ to $X'/D_B = 1.5$ are minor at all Mach numbers except 1.0, it may also be concluded that the basic taper position chosen for the sting support system ($X'/D_B = 3.0$) was adequate.

4.2.2 Wingtip Support System Interference

4.2.2.1 Total Wingtip Support Interference

The wingtip support system has been used as an alternate to struts for supporting nozzle-afterbody models; this support system also allows full exhaust plume simulation. The interference increments on the axial and normal forces caused by the wingtip support system are presented in Figs. 37 and 38, respectively. These data, obtained with two nozzle configurations, were deduced from measurements made during the large sting phase of testing. The increments shown were obtained by subtracting the basic aircraft model data obtained with the sting mount from measurements made with the model configured with dummy wingtip support components. The axial-force results indicate large negative interference increments (lower drag on the wingtip system) at the high subsonic Mach numbers with the maximum increments at $M_\infty = 0.95$ and significant positive interference increments at the supersonic Mach numbers. The variations with Mach number are similar for each of the two nozzle configurations; however, the magnitude of the interference is generally greater for the cruise 3.4 nozzle. This is as would be expected since the cruise nozzle has more axial projected area, thereby amplifying the interference compared to the other nozzles. The variations at $\alpha = 7$ deg (Fig. 37b) are similar to those at $\alpha = 0$, although the magnitude of the interference at subsonic Mach numbers is generally larger at $\alpha = 7$ deg than at $\alpha = 0$.

The normal-force data (Fig. 38) indicate minor effects of the wingtip system at $\alpha = 0$ except at $M_\infty = 1.0$, where an increment of 0.01 in CN was obtained. At 7 deg angle of attack there are significant effects at all Mach numbers above 0.9. Analysis of pressure data indicates that the positive increments in CN result primarily from lower pressure on the upper surface of the afterbody.

4.2.2.2 Support Blade

The effects of the aft-support blade were defined by testing with and without the dummy blade in conjunction with the modified wing planform. As illustrated in Fig. 39, the effects of the aft-support blade on axial-force coefficient are quite large at the high subsonic Mach numbers, reaching a maximum at $M_\infty = 1.0$. These negative interference increments represent a significant portion of the total wingtip support interference at subsonic Mach numbers. This decrease in axial force is caused by increasing pressure on the afterbody resulting from the forward propagation of pressure disturbances by the blade. These trends with Mach number follow somewhat the Prandtl-Glanert similarity parameter, $1/\sqrt{1-M_\infty^2}$, which is illustrated on each plot. The Prandtl-Glanert curves were generated from the

interference measured at $M_\infty = 0.6$. As would be expected, the blade effects at the supersonic Mach numbers are negligible, falling within the data repeatability. Angle of attack had negligible effect on the value of the interference. The influence of the blade on the afterbody normal force is illustrated in Fig. 40 for $\alpha =$ both 0 and 7 deg. The effects are negligible at $\alpha = 0$ and small at $\alpha = 7$ deg with a maximum increment of -0.002 occurring at $M_\infty = 0.95$.

In addition to defining the total blade increment, configurations were tested to evaluate the sensitivity of this interference to the axial position of the blade. During the wingtip-supported phase of testing the dummy support blade was installed 10.6 in. forward of the actual support blade, and during the sting-supported phase of testing the dummy support blade was moved 6.75 in. aft of the basic position. The change in interference as a result of each of these blade movements is shown in Fig. 41. In each case the increment in axial force is calculated by subtracting data from the standard blade location from the results obtained at the alternate location. Data variations with Mach number are as would be anticipated from the results shown in Fig. 39. Whereas forward blade movement significantly increased the interference, aft blade movement tended to relieve the blade interference. These results at $\alpha = 0$ are presented in a different form in Fig. 42. In this figure interference increments in axial force which result from moving the blade from the basic position to each of the other positions is plotted as a function of $\Delta X/t$ for each Mach number. The increase in interference sensitivity with Mach number in the Mach number range from 0.6 to 1.0 is clearly demonstrated. The increments obtained by completely removing the blade are shown at the right-hand side of the figure. By extrapolation of the curve for a given Mach number from the aft position to the blade-off interference value, an approximation of the support blade position required for interference-free data may be inferred. This position varies somewhat with Mach number, but an average minimum interference position appears to be between five and six blade thicknesses aft of where the basic position was located. This location corresponds to approximately 26.8 blade thicknesses or 4.75 blade equivalent body diameters downstream of the nozzle exit plane.

4.2.2.3 Wingtip Booms

Data illustrating the effects of the booms on axial force and normal force are presented in Figs. 43 and 44, respectively. At $\alpha = 0$ the wingtip booms apparently contribute little to the interference at subsonic Mach numbers, but they are a major source of the interference at Mach numbers 1.0 and above. Moving the model to an angle of attack of 7 deg had little effect on the shape of the interference curve over the Mach number range; however, the values were shifted, resulting in negative interference increments at subsonic Mach numbers and essentially zero interference at Mach numbers above 1.0. The booms caused a positive

increment in normal force (Fig. 44) of approximately 0.05 for most Mach numbers at $\alpha = 0$. The effect of the booms was larger at $\alpha = 7$ deg, resulting in a maximum increment of 0.016 at $M_\infty = 1.0$. The effects of the booms alone are larger at several Mach numbers, particularly at $\alpha = 0$, than the effects shown for the total wingtip interference (Fig. 38). Apparently, compensating effects from other components of the wingtip system are present.

Selection of the geometry and axial location of the boom tips is a design decision that generally can be based upon interference considerations, since forward of the wing leading edge no structural considerations are involved. The basic boom tips for this test were located such that shocks from the conical tips would intersect the model just upstream of the instrumented afterbody at $M_\infty = 1.5$. Data were also obtained with the boom tips extended to the model nose, to determine whether the afterbody pressures were sensitive to the shock location forward of the afterbody. These resulting axial-force coefficients (Fig. 45) indicate very little effect of the boom tip forward movement, except at $M_\infty = 1.0$. At $M_\infty = 1.0$, the forward boom tip location resulted in approximately nine counts lower axial force. It was at $M_\infty = 1.0$ that the maximum positive axial-force increment occurred (Fig. 43) for the total boom interference. Thus, it can be concluded that at $M_\infty = 1.0$ the interference may be relieved somewhat by locating the boom tip in a more forward location. However, the location for minimum interference is probably model configuration dependent. Although the results are not shown, there were no appreciable effects on normal force of moving the boom tips forward.

The centerline of the wingtip booms for the basic wingtip system was located laterally at a position corresponding to the tip of the basic aircraft wing. This position was somewhat arbitrarily chosen, however, since the wing planform was modified outboard of B.L. 12. To aid design of future wingtip systems, tests were conducted to evaluate the sensitivity of the afterbody forces to the boom lateral spacing. The effects of the lateral spacing on axial force are presented in Fig. 46. The wider spacing (6 in. outboard of standard position) is seen to have more interference at the high subsonic Mach numbers and significantly greater interference at the supersonic Mach numbers. The greater subsonic interference is attributed to the larger downstream blockage of the wider support blade. The altered interference at the supersonic Mach numbers is thought to result from the shock and subsequent expansions from the conical boom tips impinging farther aft on the model as spacing increased, influencing more of the model afterbody. Illustrated in Figs. 47 and 48 are shock and expansion fan interactions with the model for Mach numbers 1.2 and 1.5. At Mach numbers up to 1.2 the shock from the boom tip is ahead of the instrumented portion of the afterbody even with the booms at the outboard position. The expansions around the shoulder of the conical tip do, however, intersect the model on the afterbody and are believed to be responsible for the increased axial force at these Mach numbers. At $M_\infty = 1.5$ the shock

from the wide spacing intersects the instrumented portion of the afterbody, resulting in the decrease in axial force. The influence of moving the booms inboard 6 in. was insignificant, the results generally being within the range of data repeatability of the standard position. The data trends are similar for $\alpha = 5$ deg and $\alpha = 0$. It is concluded from these results that within the range of lateral positions tested, the lateral proximity of the booms to the afterbody is not particularly critical; however, the boom tip location is critical and should be located so that the compression and expansion regions from the tips intersect the model ahead of the instrumented section. The effects of boom lateral spacing on afterbody normal force are illustrated in Fig. 49 for angles of attack of 0 and 5 deg. The data indicate that the lateral spacing of the booms can have significant effects upon the afterbody normal force, particularly at angle of attack. At $\alpha = 5$ deg there is a consistent trend at Mach numbers of 0.9 and higher of increasing normal force with increasing boom spacing.

Boom diameter for a given test installation must be determined from a consideration of model loads, aft-support blade location, airflow requirements, and space required for instrumentation leads. From a structural standpoint there are obviously some design trades that may be made between boom diameter and aft support blade location. The effects of a 50-percent increase in boom diameter are illustrated in Fig. 50 for both the cruise 3.4 and max A/B 6.6 nozzles. Although the data obtained with the cruise nozzle are affected significantly, the data obtained with the max A/B 6.6 nozzle remain relatively unaffected. An examination of the pressure data indicates that the interference on the cruise nozzle configuration occurs primarily in the recompression region of the model. The cruise nozzle, which has more closure and a steeper boattail angle, is apparently more sensitive to the flow-field changes induced by the booms. As shown in Fig. 51, the boom diameter had relatively minor effects on normal force at $\alpha =$ both 0 and 7 deg.

4.2.2.4 Distorted Planform

Structural integrity and area requirements for high-pressure air and instrumentation leads for the wingtip support system necessitated modifying the aircraft wing planform to a constant chord outboard of BL 12.0 (55-percent span). The change in afterbody axial force caused by the modified wing planform is illustrated in Fig. 52. Increments in axial force between the modified wing configuration and the actual aircraft wing configuration are shown. The largest effect produced a negative increment in axial force at $M_\infty = 0.95$ and $\alpha = 0$ of approximately nine counts. At supersonic Mach numbers there is a positive increment, resulting from the modified wing. The data variations at $\alpha = 7$ deg are generally similar to those at $\alpha = 0$; however, the increments tend to be larger. The high increments at subsonic Mach numbers, which indicate lower axial force with the modified wing configuration, are probably caused by an altered location of the wing shock.

The effects of the distorted planform on the afterbody normal force are shown in Fig. 53. The effects are largest at subsonic Mach numbers and indicate additional downwash on the afterbody with the distorted planform.

4.2.2.5 Comparison of Wingtip Component Interference with Total Interference Increment

A composite plot showing axial-force interference from each component of the wingtip system along with the total wingtip system interference is shown in Fig. 54. The largest contributor to the axial-force interference at subsonic Mach numbers is the aft-support blade; the modified wing planform also becomes significant at $M_\infty = 0.95$, where the largest total interference occurred. At the supersonic Mach numbers the wingtip booms and the modified wing planform contribute almost equally to the total interference at $\alpha = 0$. At $\alpha = 7$ deg, however, the modified planform is essentially the sole contributor to the total system interference.

The comparison of normal-force interference increments from the wingtip components to the total interference is presented in Fig. 55. The results reveal compensating effects from the booms and modified wing planform over most of the Mach number range at $\alpha = 0$ and at subsonic Mach numbers for $\alpha = 7$ deg. These advantageous compensating effects are probably configuration dependent and should not necessarily be expected for all models.

4.2.3 Strut Interference

The strut is a support system used extensively for nozzle-afterbody testing. It has the advantage of high strength and allows complete simulation of the aircraft afterbody contour along with full plume jet simulation. However, it causes significant interference, as shown in Fig. 56, for both the cruise 3.4 and max A/B 6.6 nozzles. Although the data show relatively minimal interference at low subsonic Mach numbers, there is a large amount of interference through the transonic and supersonic regimes up to $M_\infty = 1.5$, where the low interference may be fortuitous. The maximum measured interference was 74.5 axial-force counts at $M_\infty = 1.0$. Although this Mach number is generally avoided as a test condition for nozzle-afterbody tests, it is viewed as a worse case situation and serves to document what can occur should test requirements be identified there. While the variation of interference with Mach number is similar for each nozzle, there is a notable configuration dependency at some of the higher interference conditions. Increasing angle of attack to 7 deg (Fig. 56b) tended to alleviate interference at the high subsonic Mach numbers but aggravated the interference near $M_\infty = 1.2$. It is evident from these data that the flow field induced by a strut support can have large influences on data in the Mach number regime from 0.9 to 1.2.

The interference effects from the strut on afterbody normal force are presented in Fig. 57. These results indicate a negative increment in normal force on the order of 0.01 over much of the Mach number range. The strut was mounted through the canopy region of the forebody. Thus, the net effect of the strut on normal force was to induce a force in the direction away from the strut.

4.2.4 Comparison of Support System Interference

A comparison of the interference on axial force induced by each of the three basic support systems is presented in Fig. 58. The interference from a sting-supported model is inferred from the annular jet comparison obtained on the wingtip support system. These results were obtained with the 2.4-in.-diam sting with the nozzle operating at design pressure ratio. The interference from the wingtip and strut was obtained with the large sting, which completely filled the cruise nozzle exit and did not allow annular jet flow. The data clearly illustrate that for afterbody tests where model geometry and test conditions permit, sting support through the nozzle with annular plume simulation offers a minimum interference system. It also illustrates that for the hardware used for this test, the strut introduced the largest overall interference. The basic wingtip system as designed for these tests had the most interference at subsonic Mach numbers of any of the three supports; however, as discussed in Section 4.2.2.2, this interference comes primarily from the support blade location. Future designs could reduce the blade portion of the interference, resulting in a system with a maximum interference of approximately ten axial-force counts. A comparison of the interference with normal-force results from the three systems is shown in Fig. 59. At $\alpha = 0$ the strut had the largest effect, with the interference from the annular jet and wingtip systems being negligible except at $M_\infty = 0.95$. At $\alpha = 7$ deg, however, the wingtip system also had significant interference at Mach numbers above 0.9.

Nozzle-afterbody wind tunnel tests are typically conducted for the purpose of obtaining axial-force increments between a reference nozzle (duplicating the basic aerodynamic model nozzle contour) and an actual air vehicle nozzle configuration with jet effects. It is important to determine what influence the presence of support interference might have on the increment in axial force between two such nozzle configurations. Presented in Fig. 60 are increments in axial-force coefficient between the cruise 3.4 nozzle (jet off) and the max A/B 6.6 nozzle (design NPR) obtained on each of the three support systems. In general, the increments at the subsonic Mach numbers are within five axial-force counts of each other with the wingtip system generally falling below the results of the sting and the strut. This is, of course, the Mach number region at which the aft support blade produces a lower axial force on the afterbody. Since the nozzle represents the nearest model component to the source of the disturbance, it is reasonable to expect that nozzles having larger projected axial

areas would be influenced more. The largest discrepancy between the data on the different support systems occurs at $M_\infty = 1.0, 1.05$, and 1.1 . These Mach numbers are typically avoided if possible in wind tunnel test programs. The results show that in the high subsonic and transonic Mach number regime large errors can be present in configuration increments as a result of support interference. The configuration increments compare well at Mach numbers 1.2 and 1.5 with a maximum difference of approximately three axial-force counts between any two support systems.

5.0 CONCLUDING REMARKS

The investigation reported herein was conducted to provide (1) a base of nozzle-afterbody data on a 1/9-scale F-16 model for comparison with planned 0.25-scale and flight test results and (2) a systematic evaluation of support system interference from sting, wingtip, and strut support systems with the same model. Data are presented for the Mach number range from 0.6 to 1.5 .

The significant results and conclusions are summarized as follows:

1. At Mach number 0.9 and below, increasing nozzle closure resulted in increased thrust on the nozzle and increased drag on the afterbody for a net effect of essentially zero. At supersonic Mach numbers there were significant increases in nozzle drag and small increases in afterbody drag resulting in a large increase in drag with increasing nozzle closure.
2. Horizontal tail deflection produced systematic increases in nozzle-afterbody axial force; the largest occurred at Mach number 0.9 , where a tail deflection of -8 deg produced an 11-count increase in axial force.
3. The sting support with annular jet flow simulation appears to offer a minimum interference support system for the type of nozzle-afterbody test described in this report. At an angle of attack of zero a maximum increment between annular and full plume jet simulation of five axial-force counts was measured with an average increment of 2.3 counts over the Mach number range of the test. There was no serious degradation in the annular/full-plume comparison at an angle of attack of 7 deg.
4. Use of the wingtip support system designed for this model resulted in lower axial force than did the sting support system at the high subsonic Mach numbers, with interference increments as high as 34 axial-force counts being measured at $M_\infty = 0.95$. Parametric studies of the aft-support blade axial position indicate that a

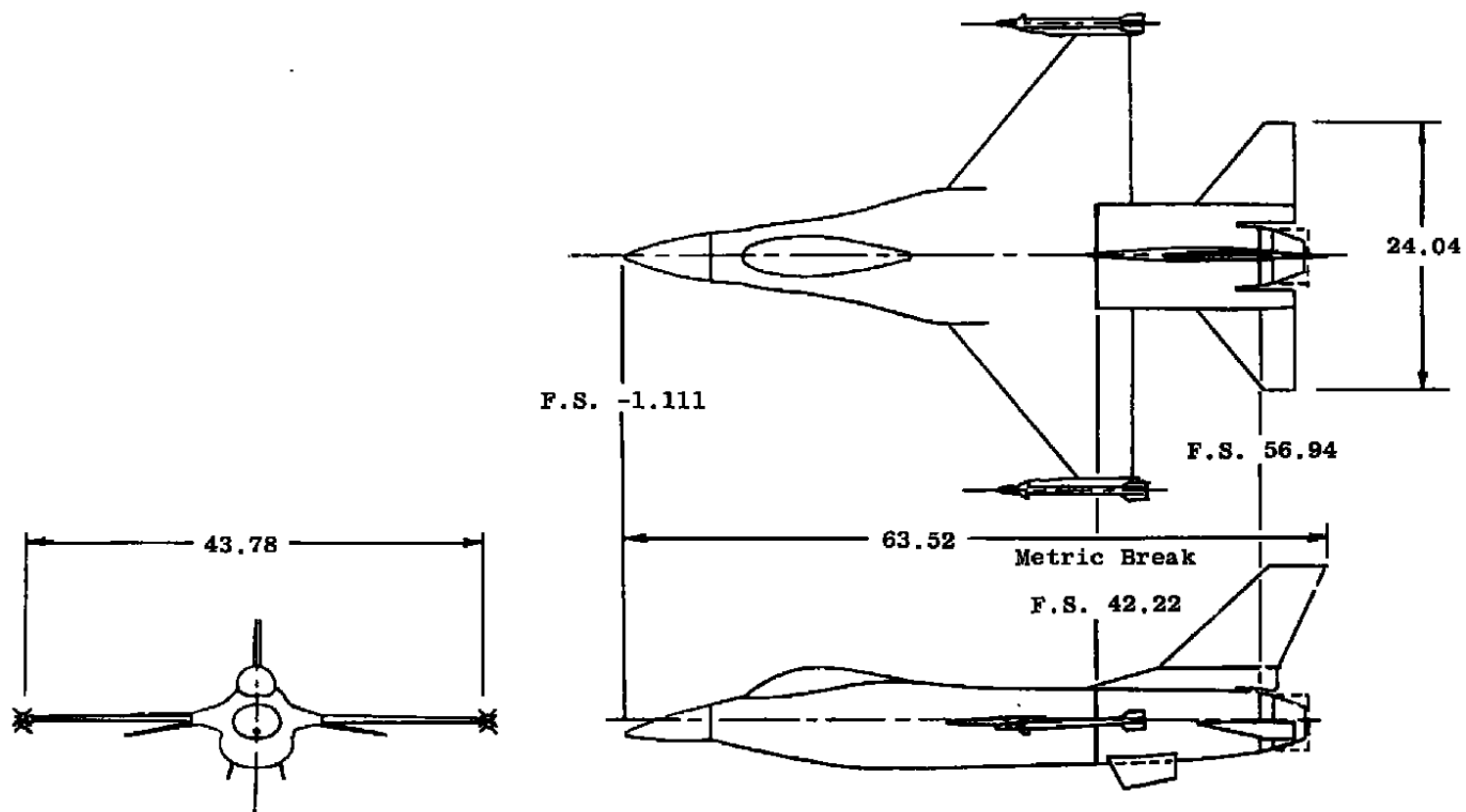
significant portion of the wingtip support system interference could be eliminated by proper blade placement. For minimum interference at supersonic Mach numbers, the boom tips should be located so that neither shock nor expansion waves from the boom tips intersect the instrumented portion of the model.

5. The interference induced by the strut support system was large in the Mach number range from 0.95 to 1.2. A maximum positive interference of 75 axial-force counts was obtained at a Mach number of 1.0, and the maximum negative interference of 31 counts was measured at a Mach number of 1.2.
6. Increments in axial force between two different nozzle configurations, obtained on each of the three support systems, compared well at all Mach numbers except in the range from 1.0 to 1.1. At these conditions support interference resulted in increments that differ by a maximum of 19 axial-force counts.

REFERENCES

1. Galigher, Lawrence L., Yaros, S. F., and Bauer, R. C. "Evaluation of Boattail Geometry and Exhaust Plume Temperature Effects on Nozzle Afterbody Drag at Transonic Mach Numbers." AEDC-TR-76-102 (AD030852), October 1976.
2. Hines, B. G., Marsh, W. H., and Wood, R. A. "Twin Jet Installation and Test Technique Improvement Test." GE-R74AEG201, January 1974.
3. Price, Earl A., Jr. "A Parametric Investigation of the Annular Jet Concept for Obtaining Afterbody Drag Data at Transonic Mach Numbers." AEDC-TR-77-104 (ADA050891), February 1978.
4. Watson, T. L. and Anderson, R. D. "Exhaust System Interaction Program: Analysis of Wind Tunnel Data on a 4.7 Percent Scale F-15 Jet Effects Model in the McDonnell Polysonic Wind Tunnel, PSWT 319." MDCA2135, McDonnell Douglas Corporation, St. Louis, Missouri, January 1973.
5. Bowers, Douglas L. "Investigation of the Annular Sting Support Concept for Aftbody Nozzle Testing." AIAA Paper No. 77-961, July 1977.
6. *Test Facilities Handbook* (Eleventh Edition). "Propulsion Wind Tunnel Facility, Vol. 4." Arnold Engineering Development Center, June 1979.
7. Abernethy, R. B. and Thompson, J. W., Jr. "Handbook - Uncertainty in Gas Turbine Measurements." AEDC-TR-73-5 (AD755356), February 1973.

8. Finnerty, Christopher S. and Price, Earl A., Jr. "A Parametric Study of Support System Interference Effects on Nozzle/Afterbody Throttle-Dependent Drag in Wind Tunnel Testing." AIAA Paper No. 79-1168, June 1979.
9. Glidewell, R. J., Stevens, H. L., and Presz, W. M. "Effects of Reynolds Number and Other Parameters on the Throttle-Dependent, Nozzle/Afterbody Drag of an 0.11-Scale Single-Engine Aircraft Model." AIAA Paper No. 79-1167, June 1979.



All Stations and Dimensions in Inches

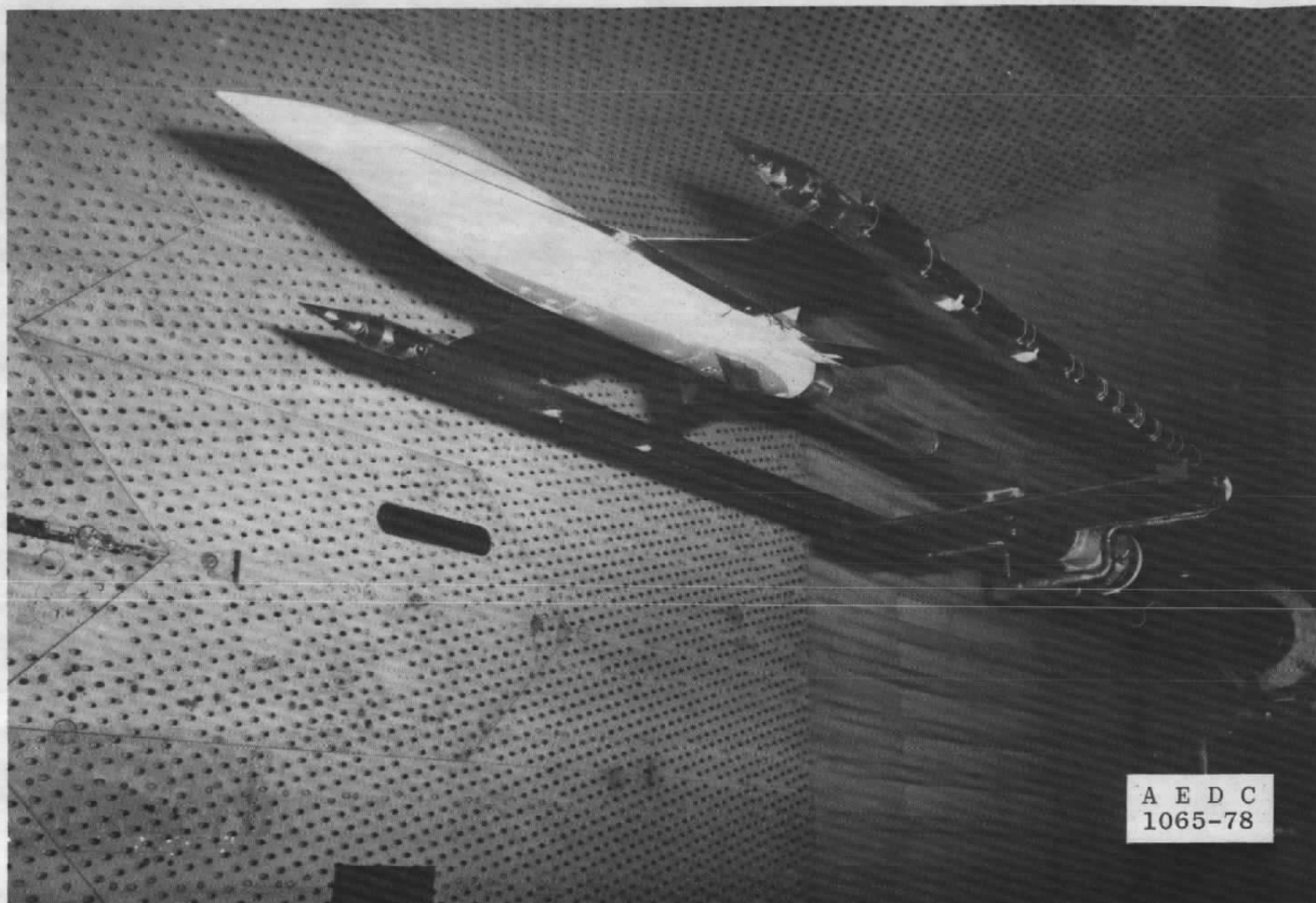
Figure 1. General arrangement of F-16A fighter aircraft.



a. Small sting installation
Figure 2. Model installation in Tunnel 16T.

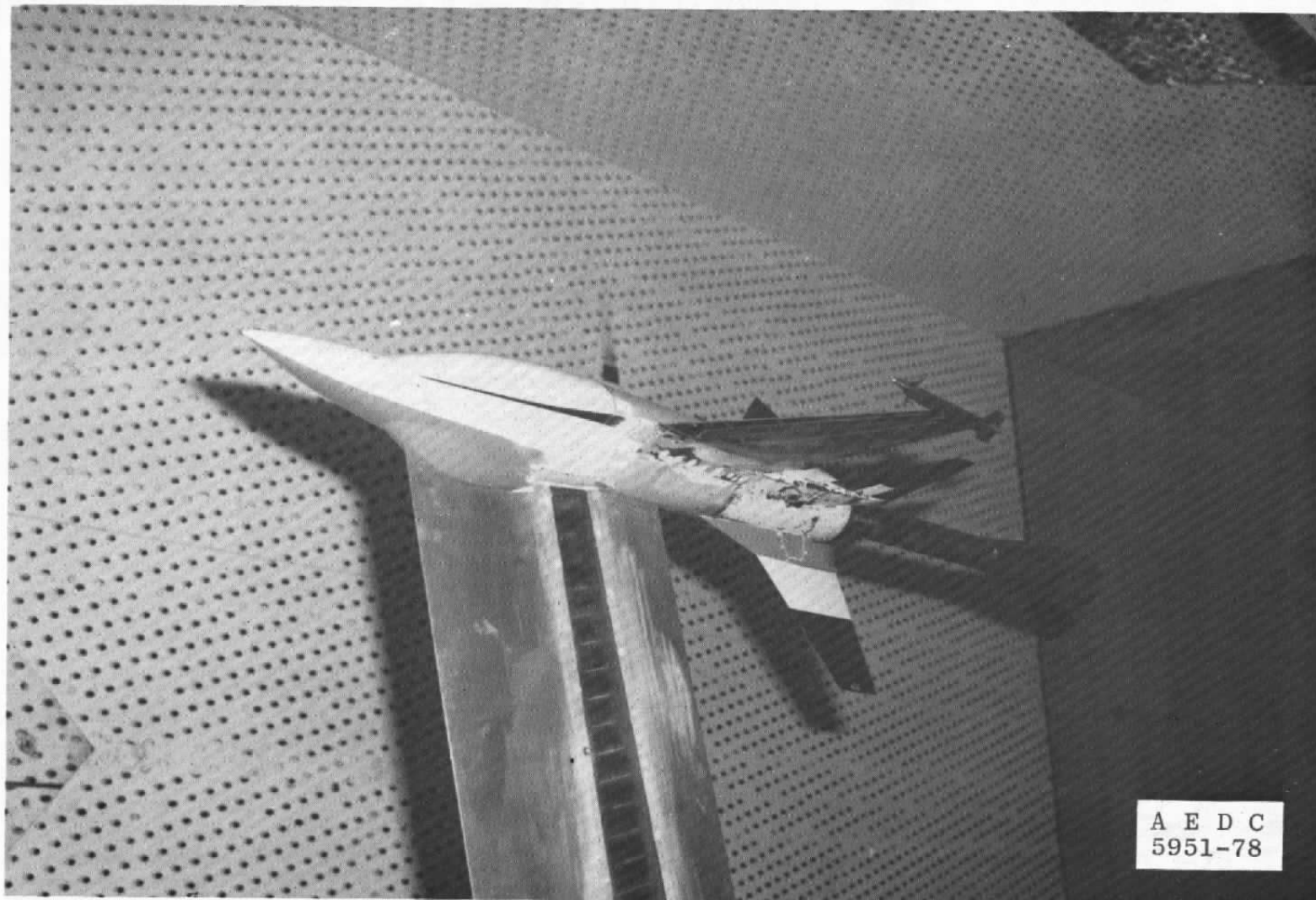


b. Large sting installation
Figure 2. Continued.



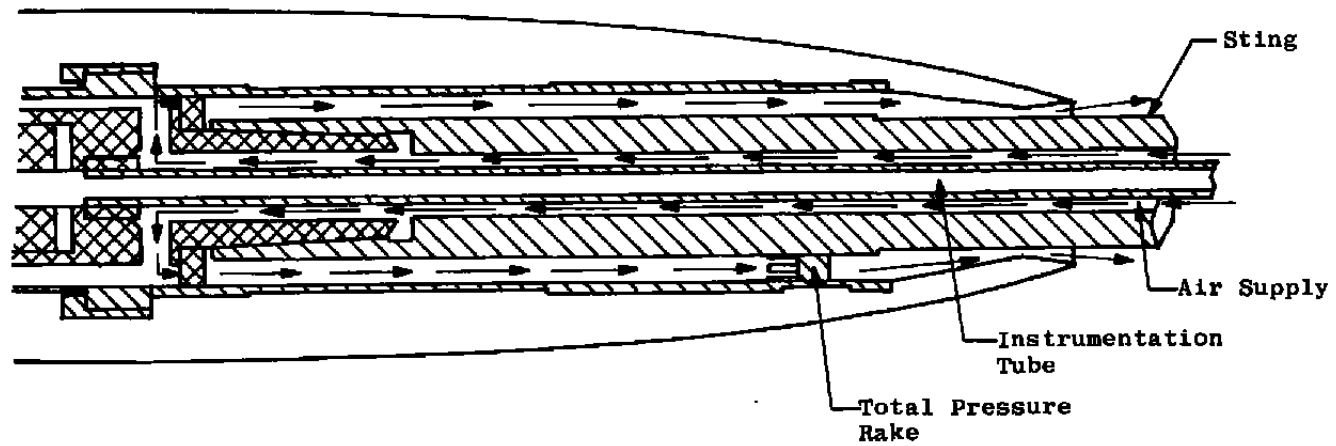
A E D C
1065-78

c. Wingtip installation
Figure 2. Continued.



d. Strut installation
Figure 2. Concluded.

Airflow System for Sting Supports



Airflow System for Wingtip and Strut Supports

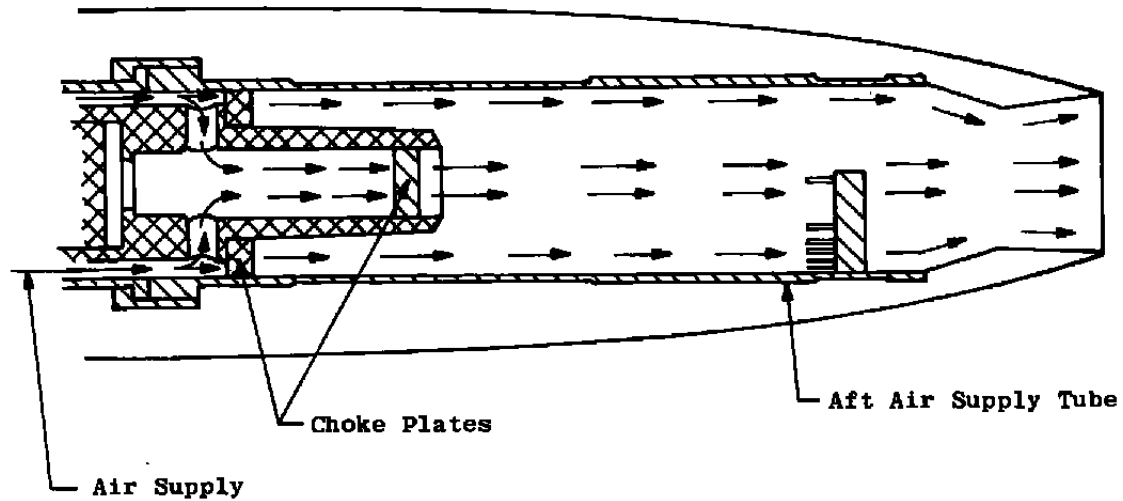
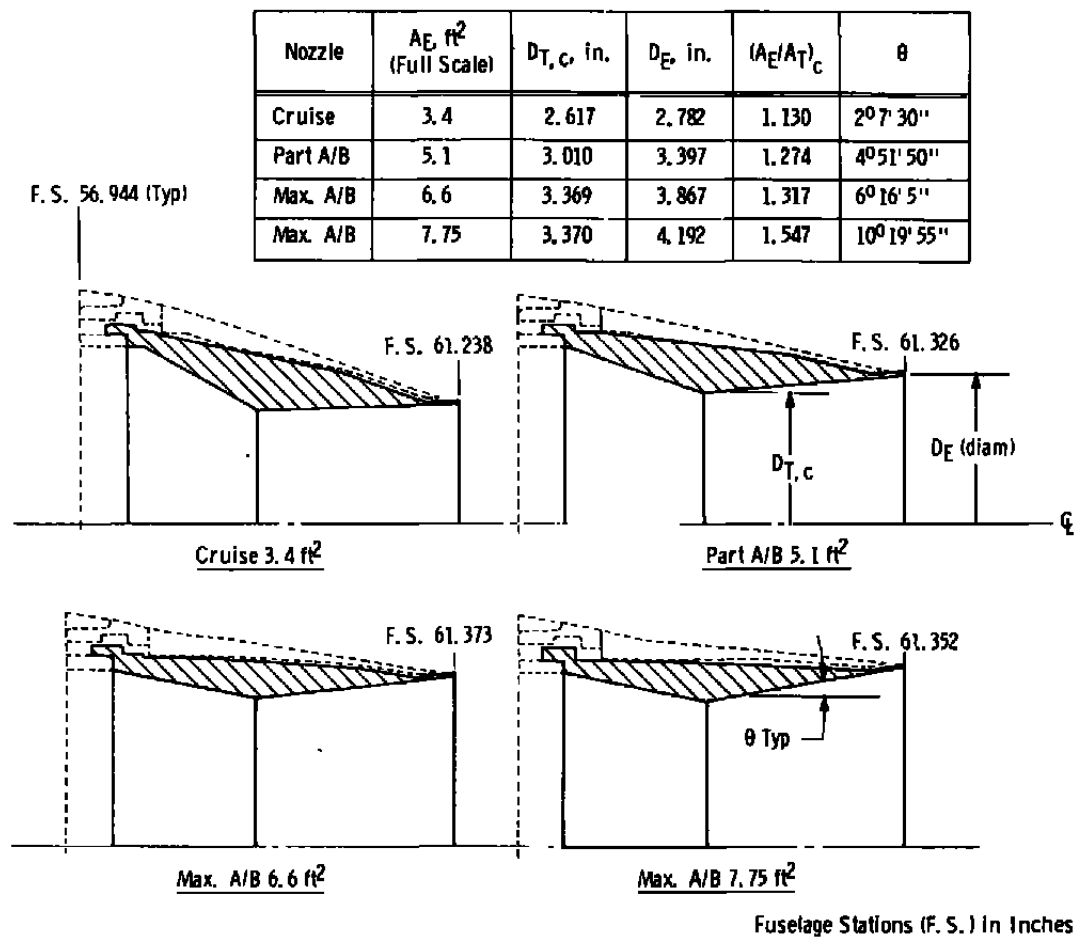
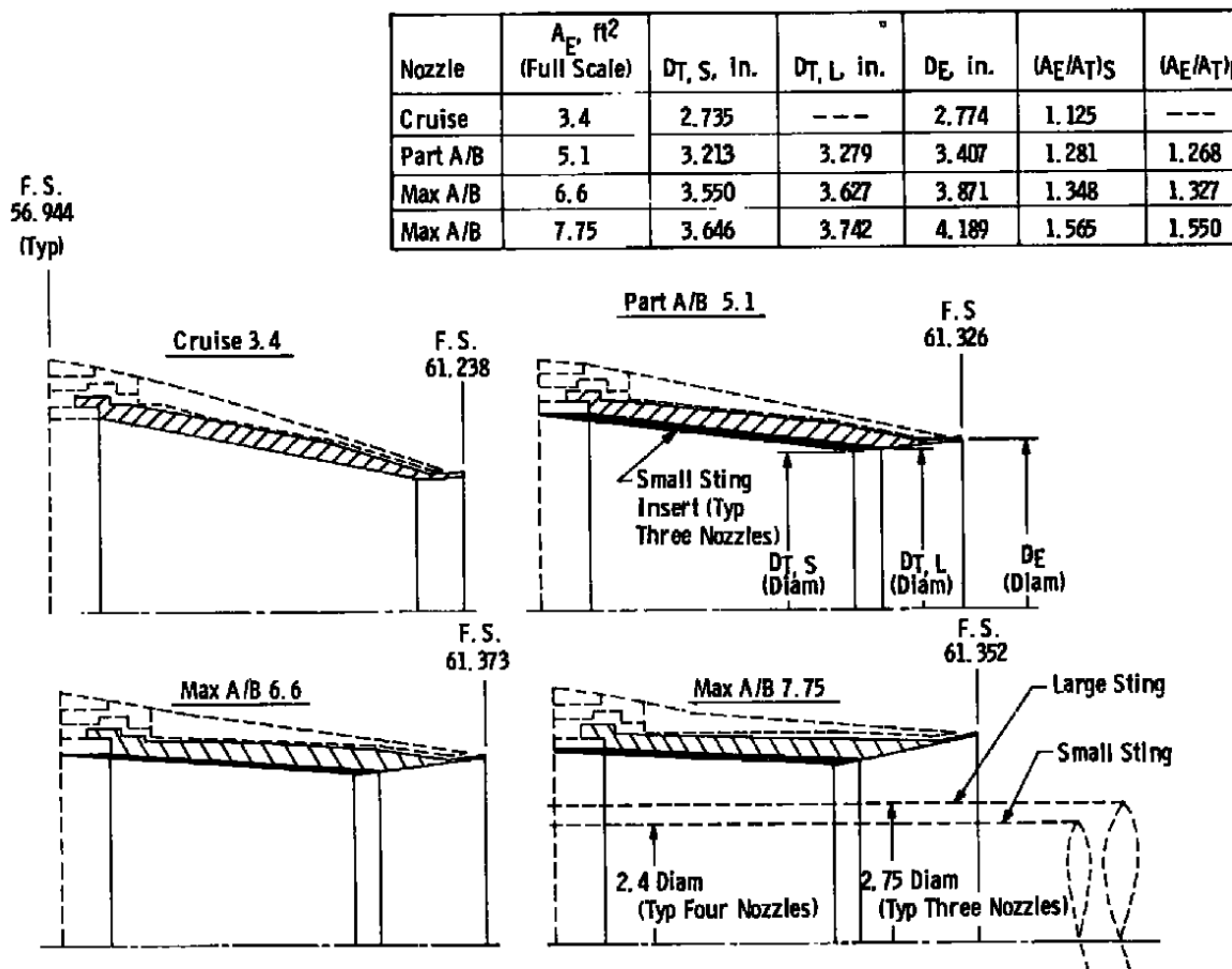


Figure 3. Air supply arrangement to model aft air supply tube.



a. Full jet nozzles
Figure 4. Air vehicle nozzles.



All Dimensions in Inches

b. Annular jet nozzles
Figure 4. Concluded.

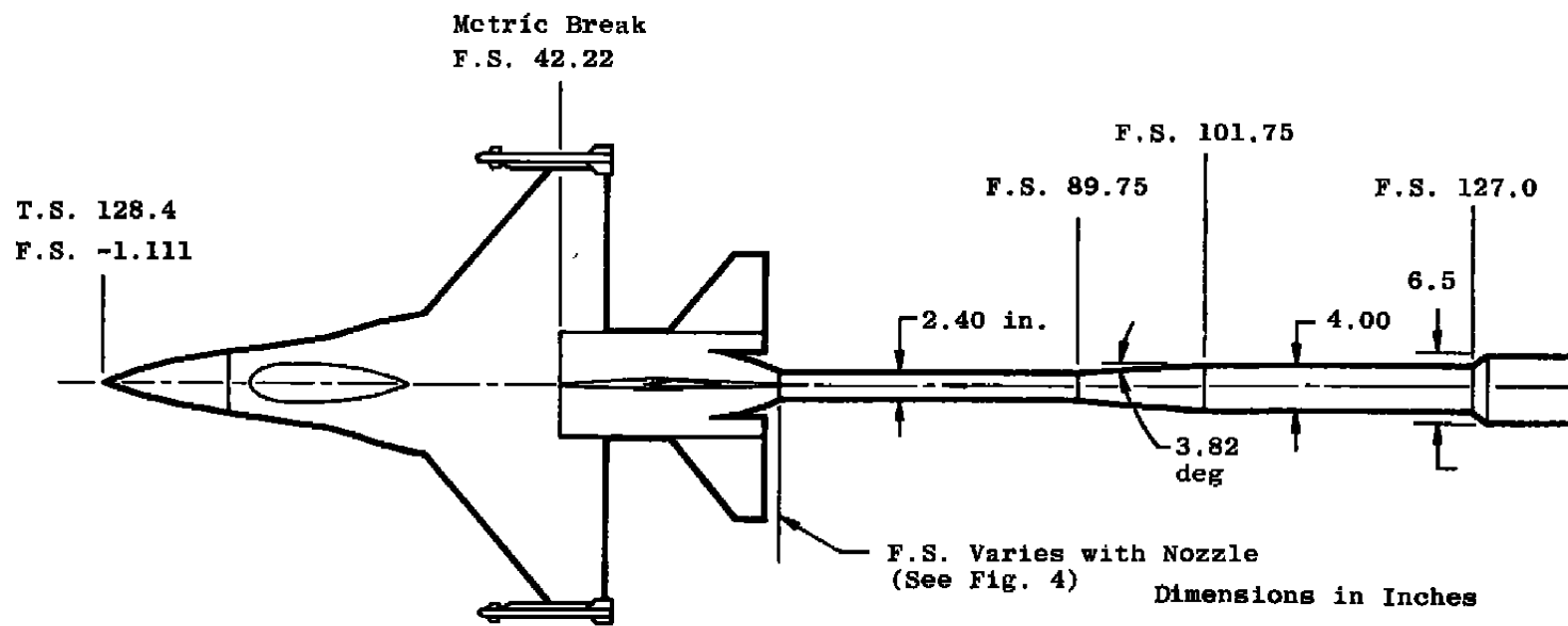


Figure 5. Small sting support installation.

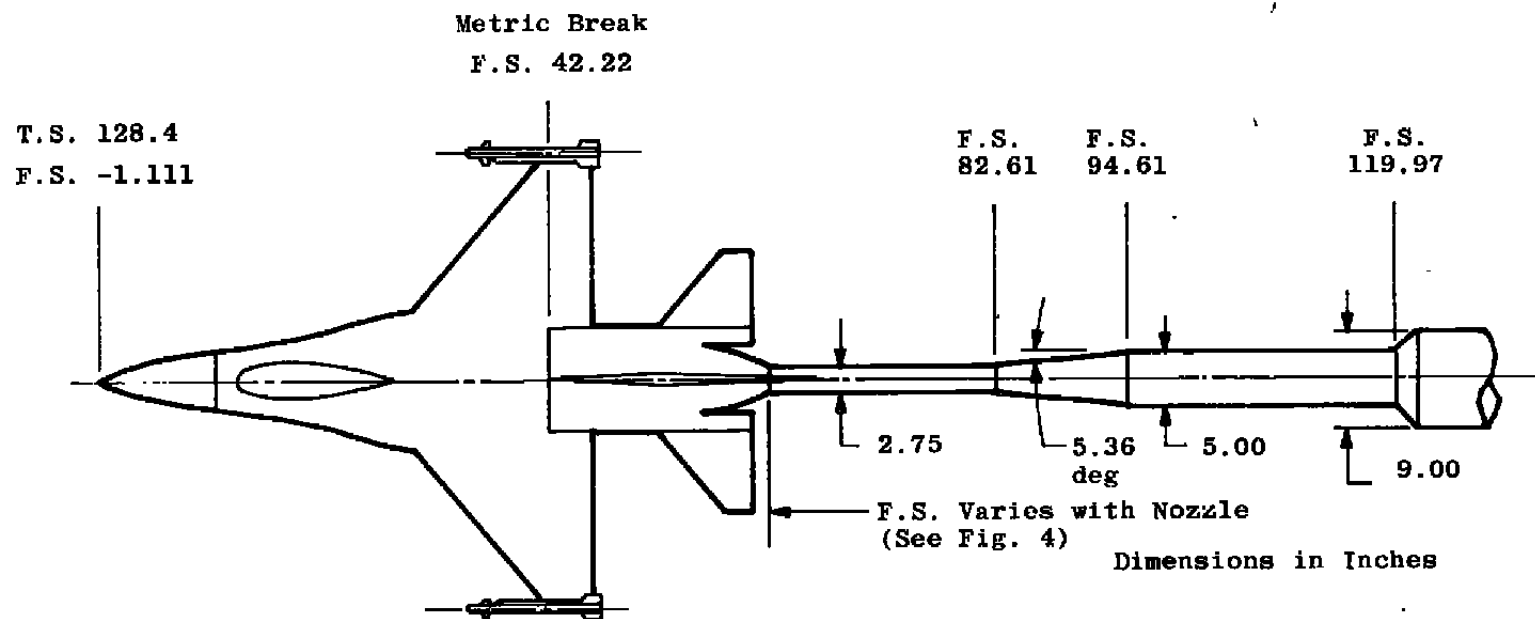


Figure 6. Large sting support installation.

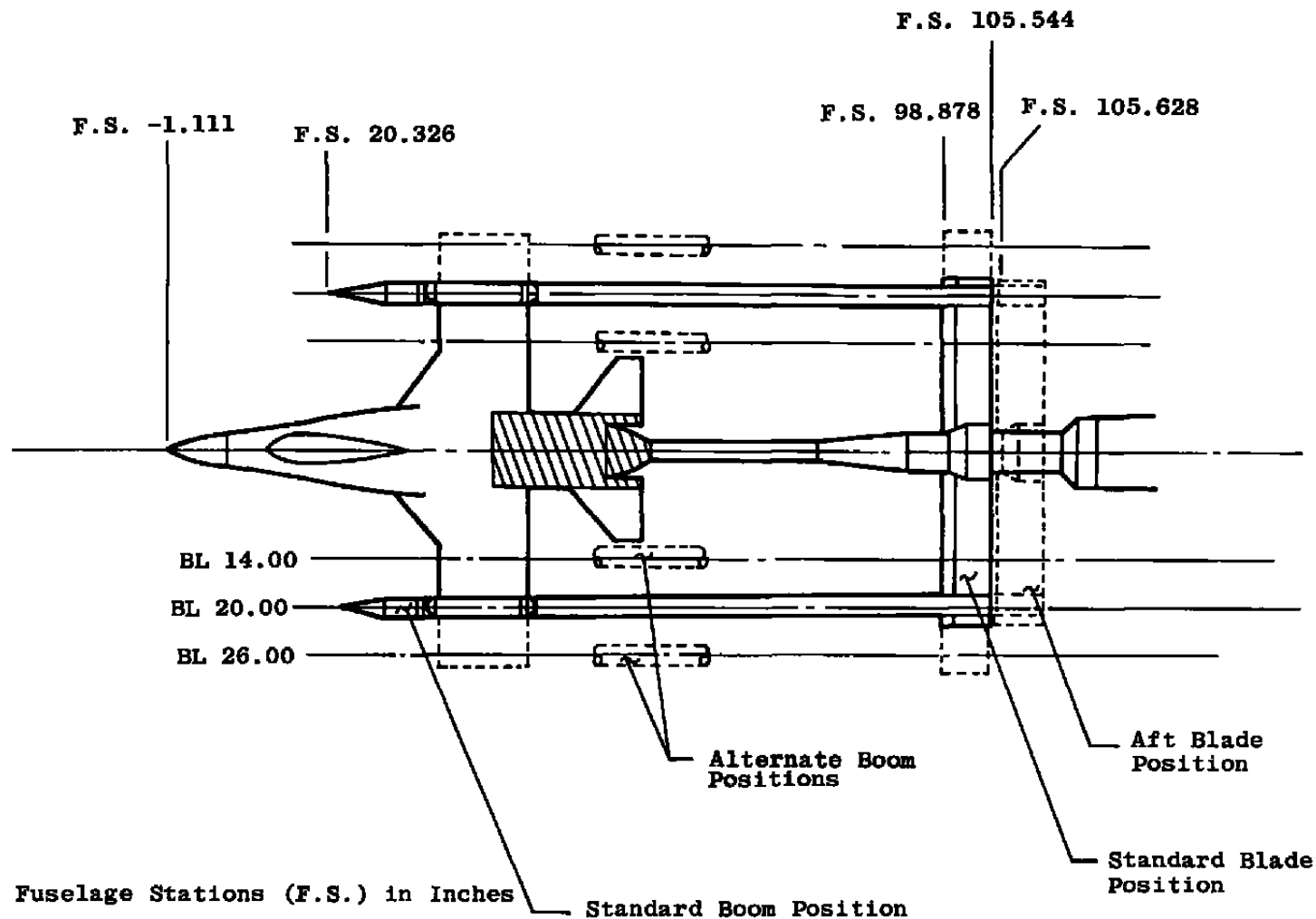
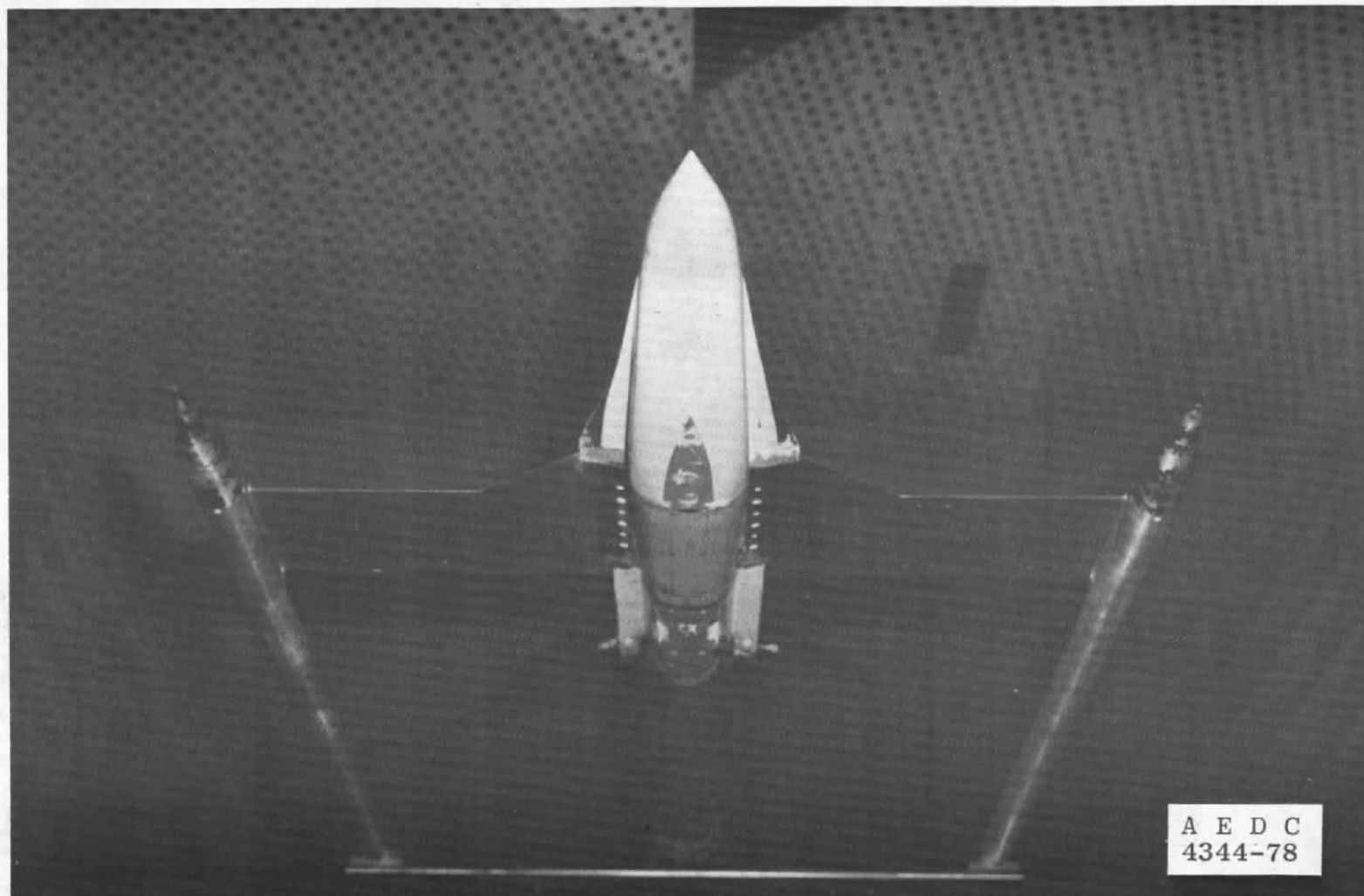
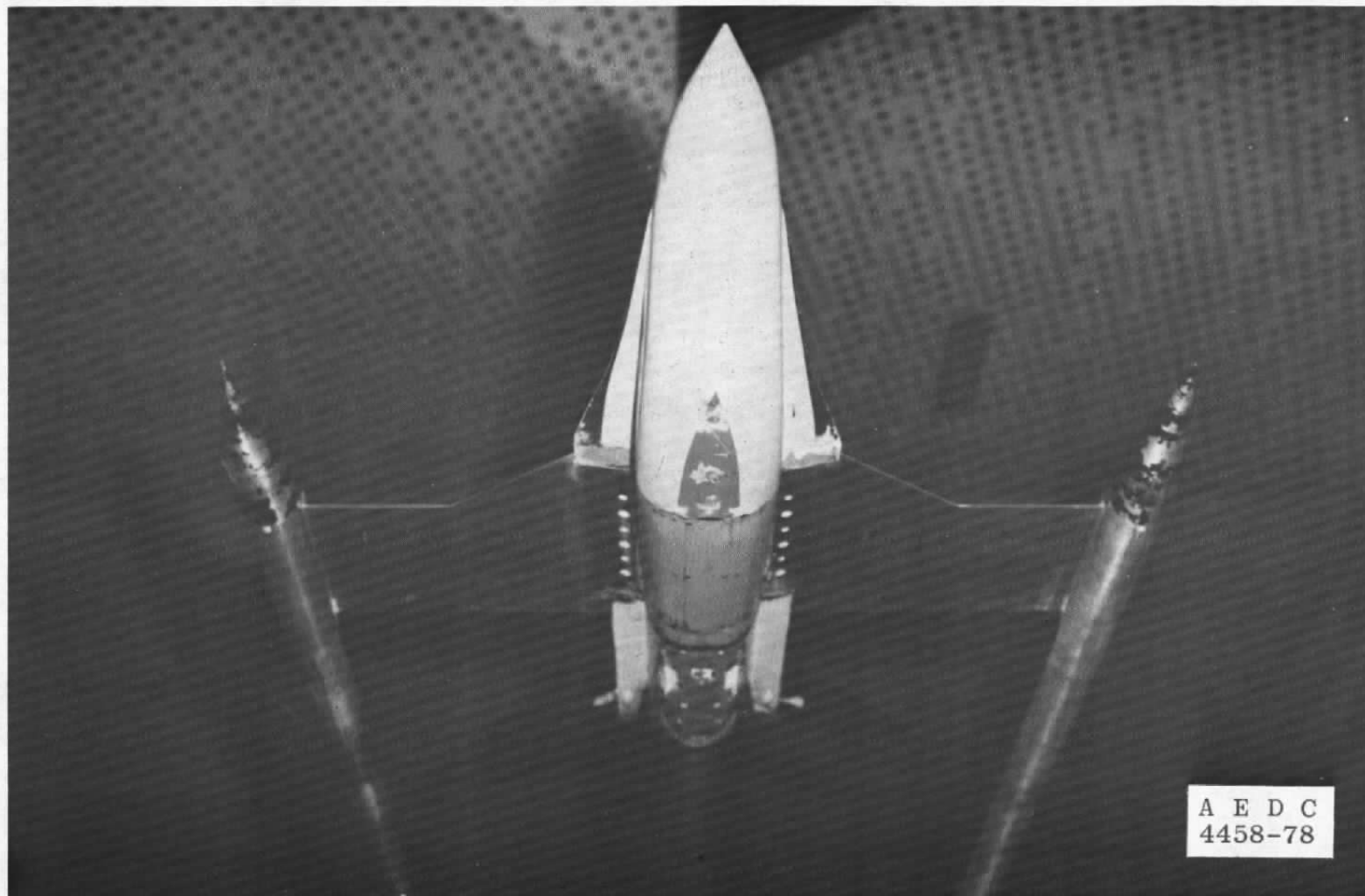


Figure 7. Hardware utilized on large sting support system for interference studies.

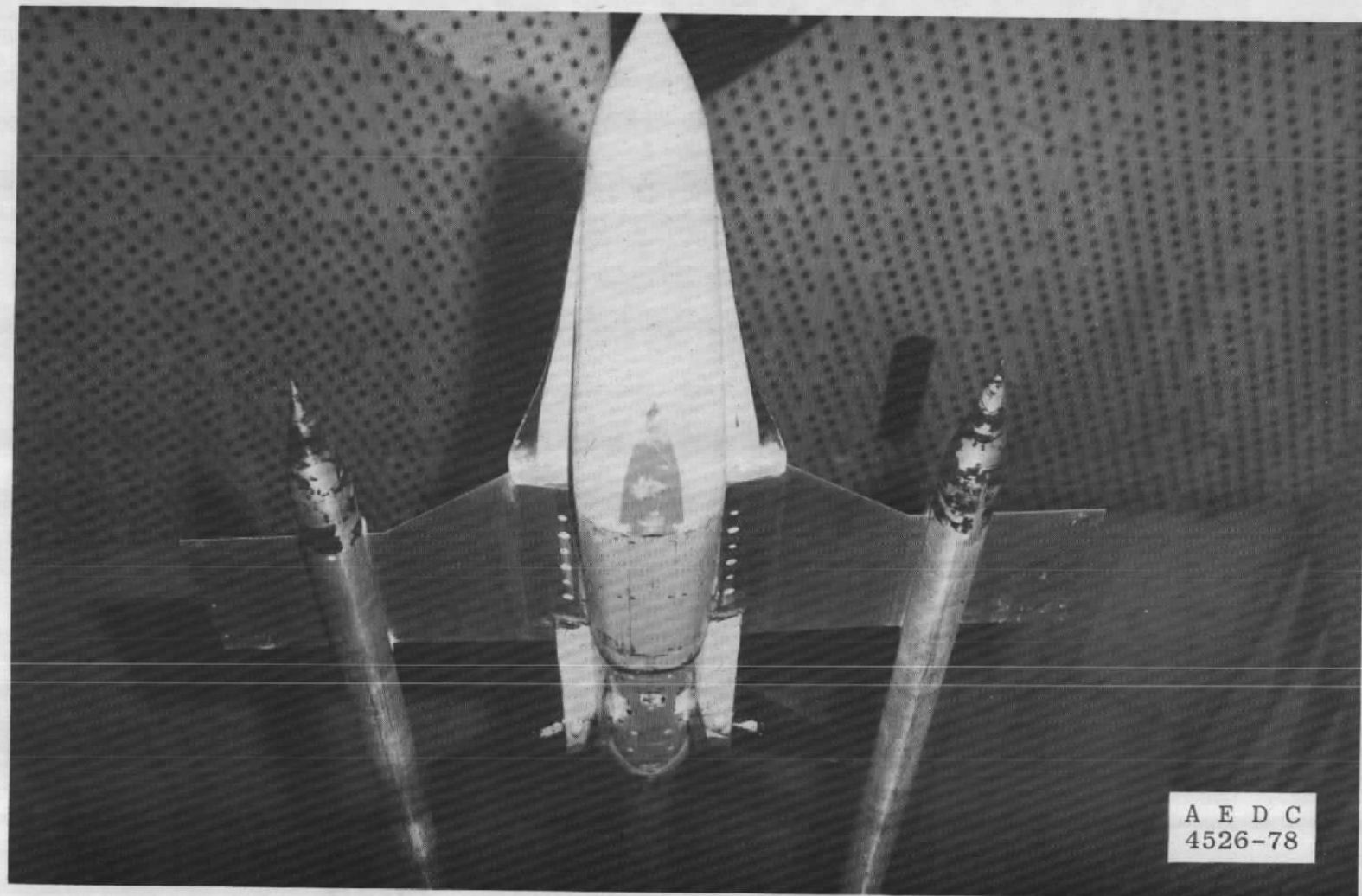


a. Outboard boom position

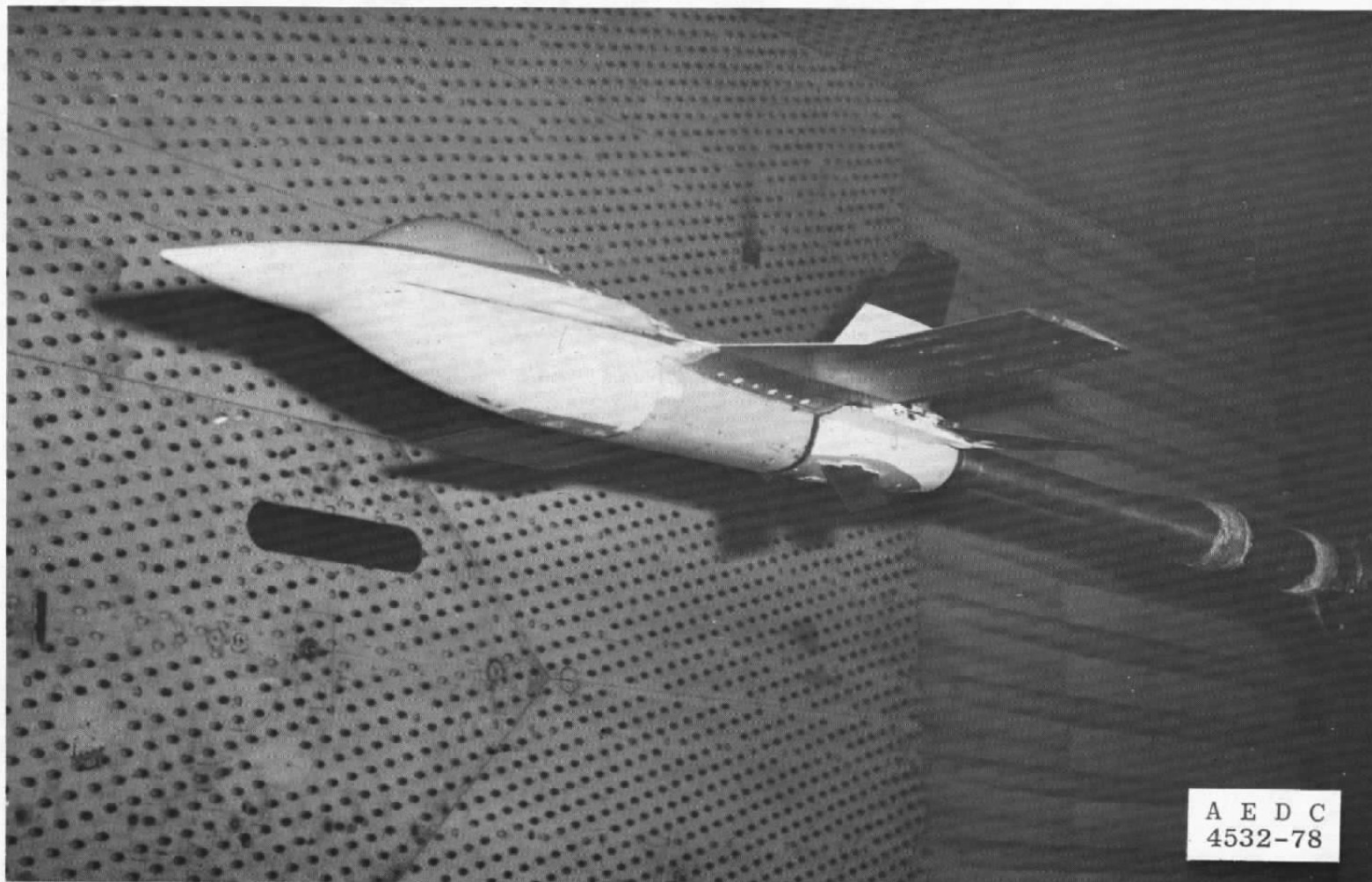
Figure 8. Model with wingtip booms installed in Tunnel 16T.



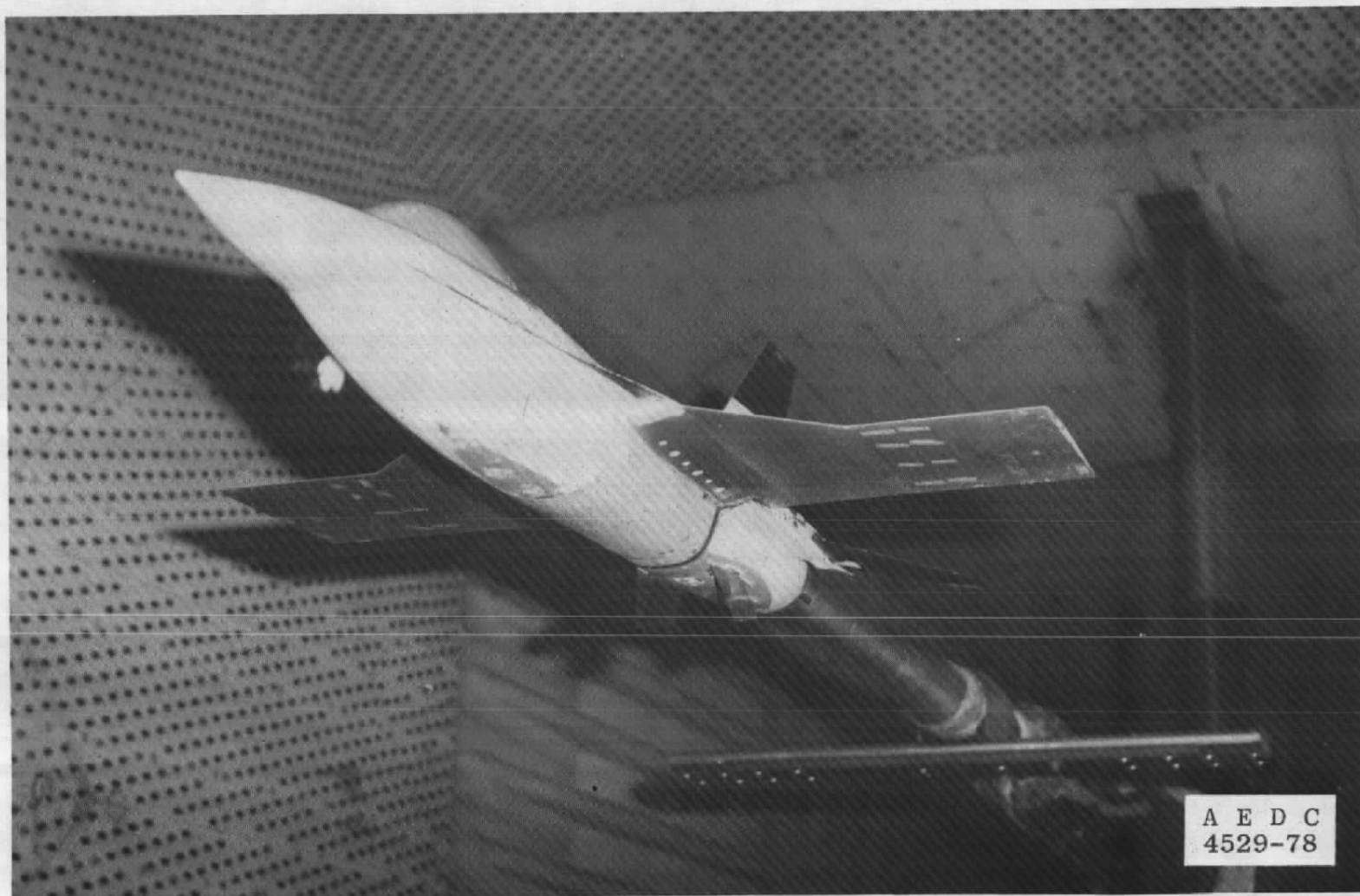
b. Standard boom position
Figure 8. Continued.



c. Inboard boom position
Figure 8. Concluded.



a. Modified wing alone
Figure 9. Modified wing configurations in Tunnel 16T.



b. Modified wing with aft dummy blade
Figure 9. Concluded.

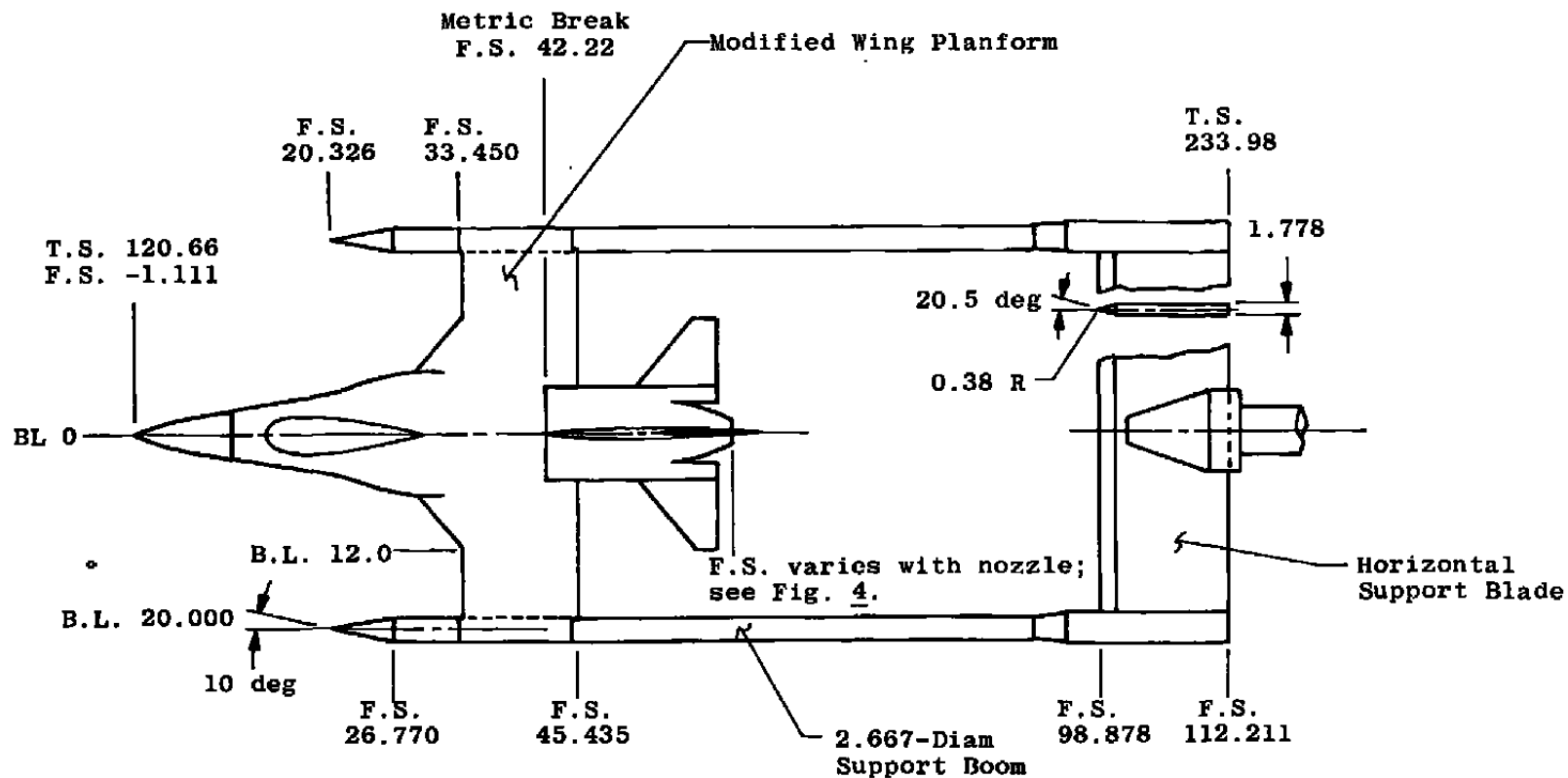


Figure 10. Wingtip support installation.

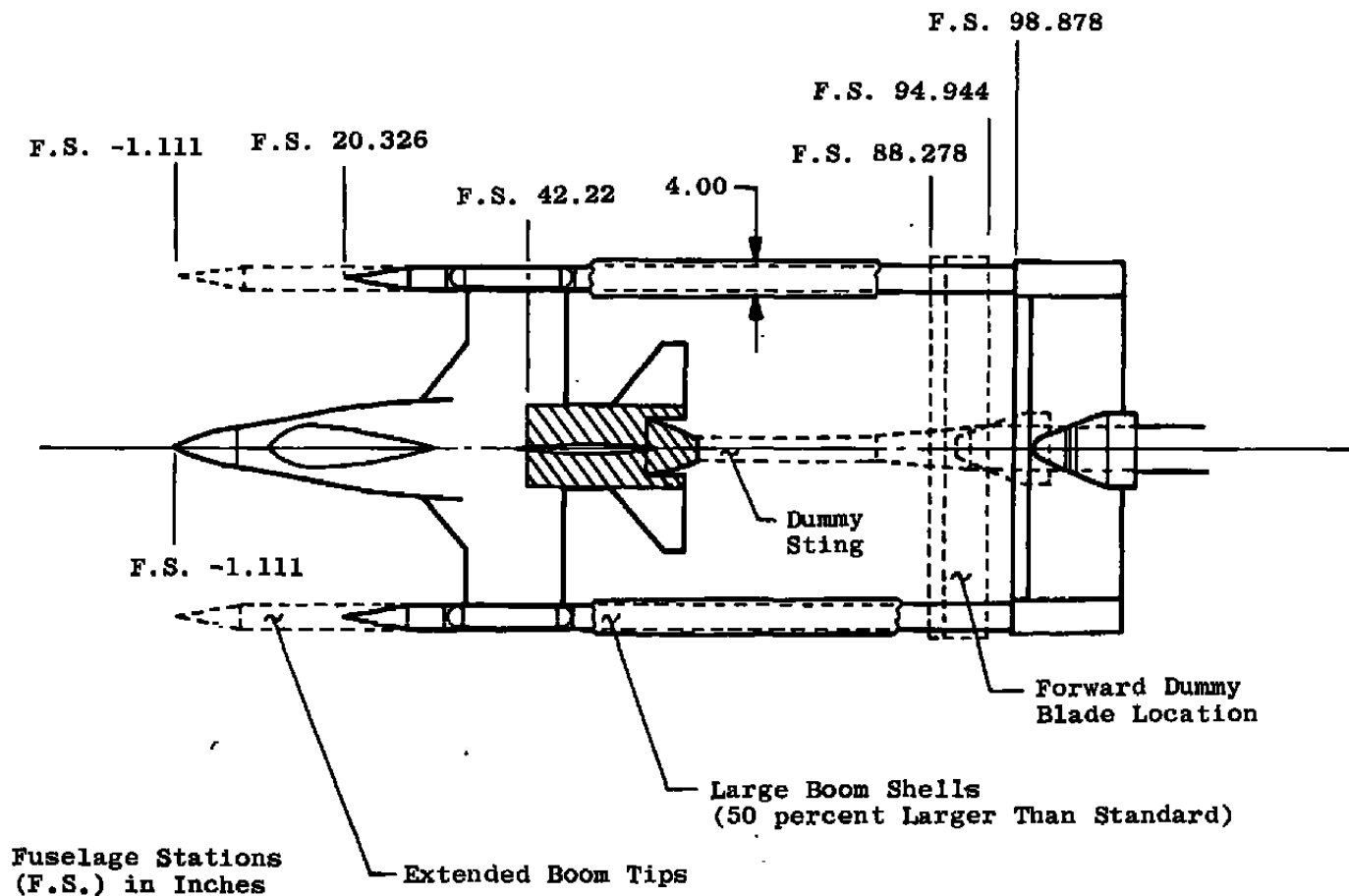


Figure 11. Hardware utilized on wingtip support system for interference studies.

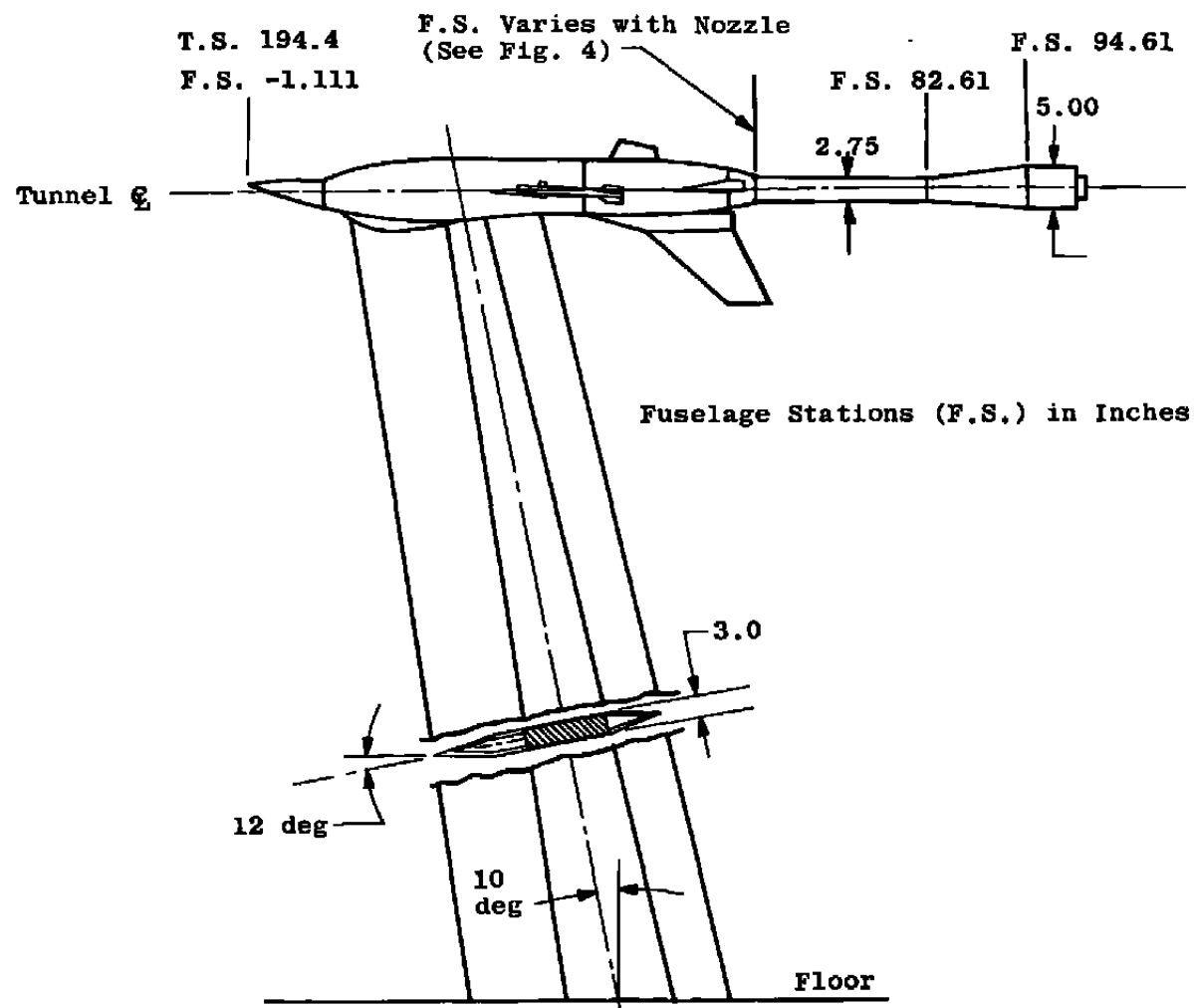


Figure 12. Strut support installation.

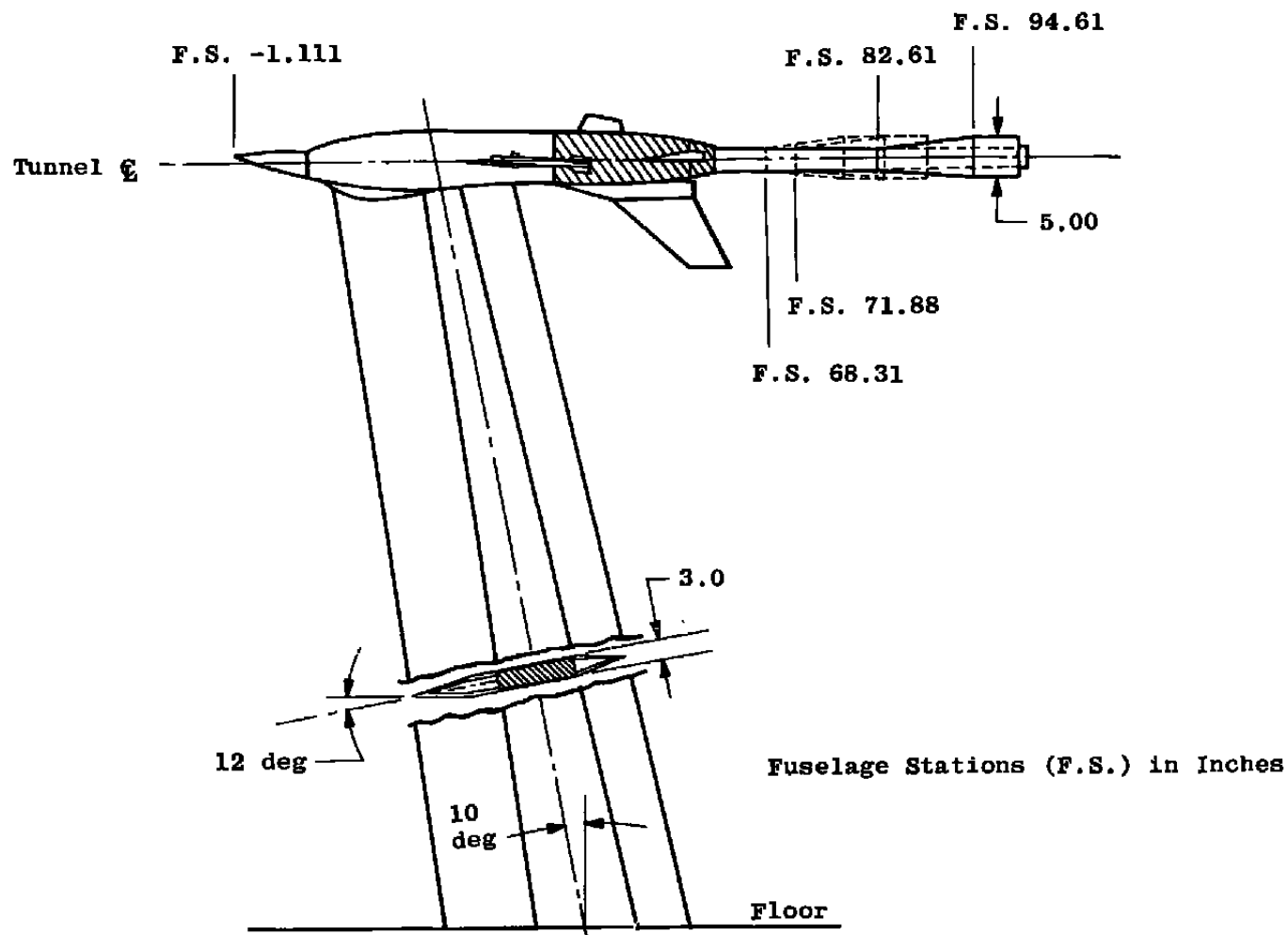


Figure 13. Sting taper locations investigated on the strut support system.

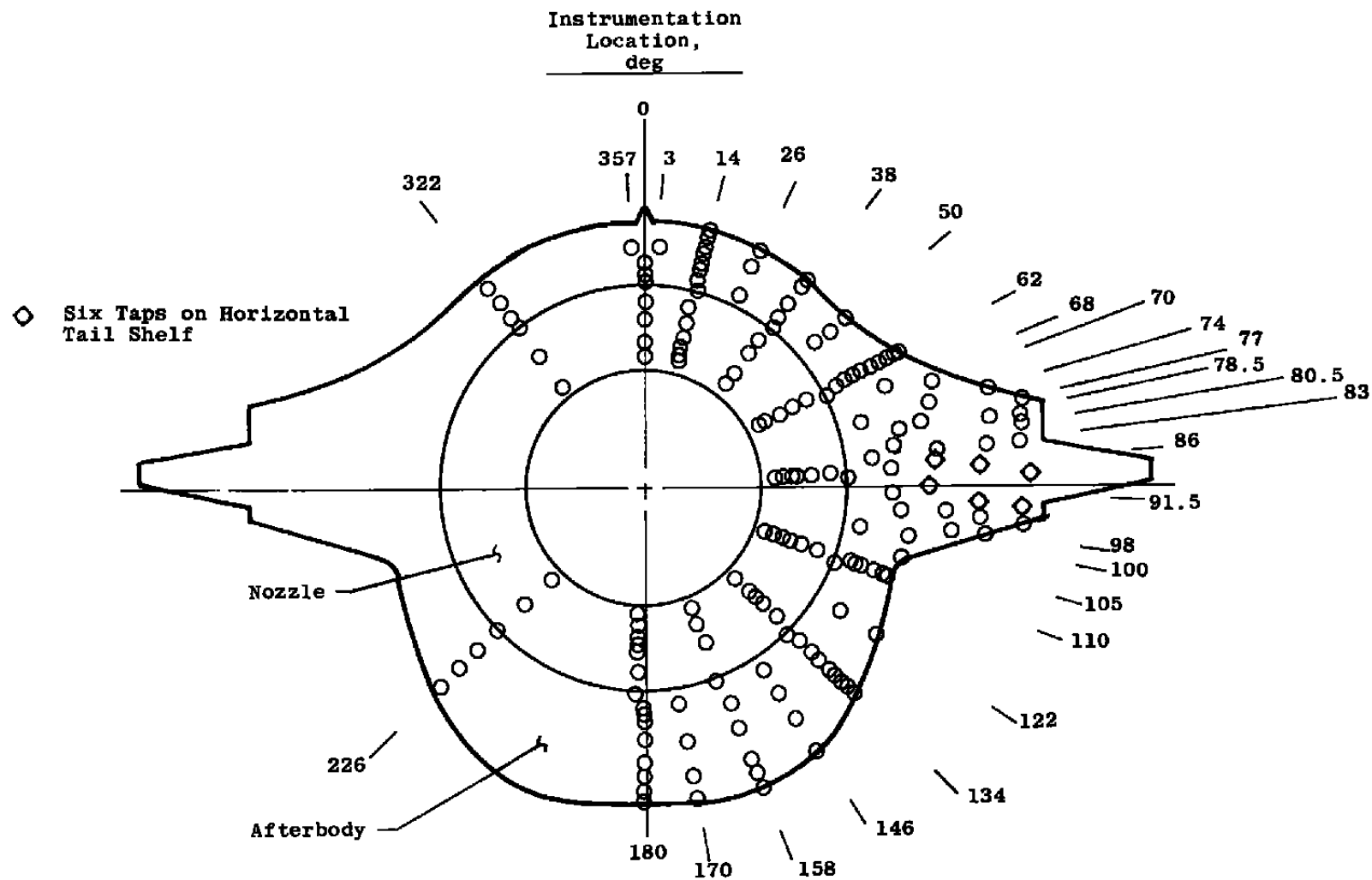


Figure 14. Nozzle and afterbody static pressure instrumentation.

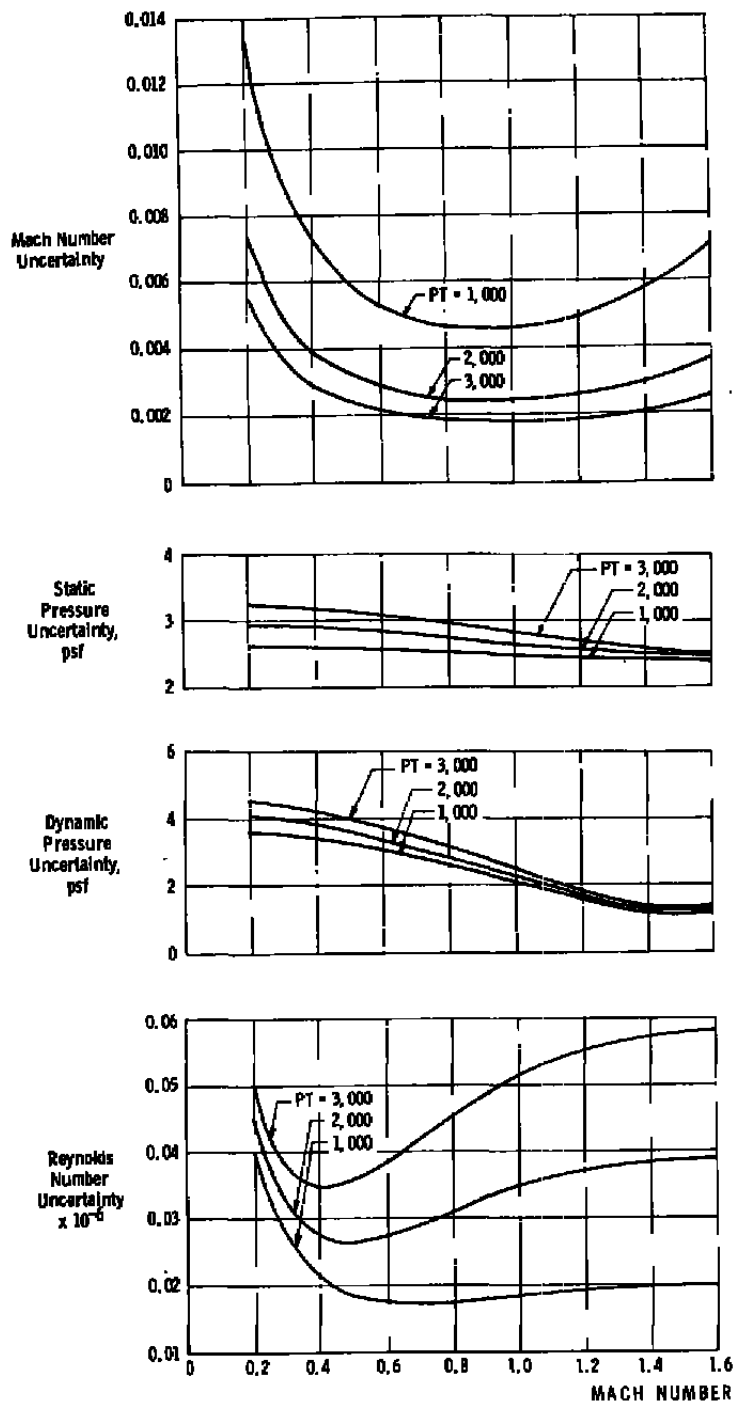
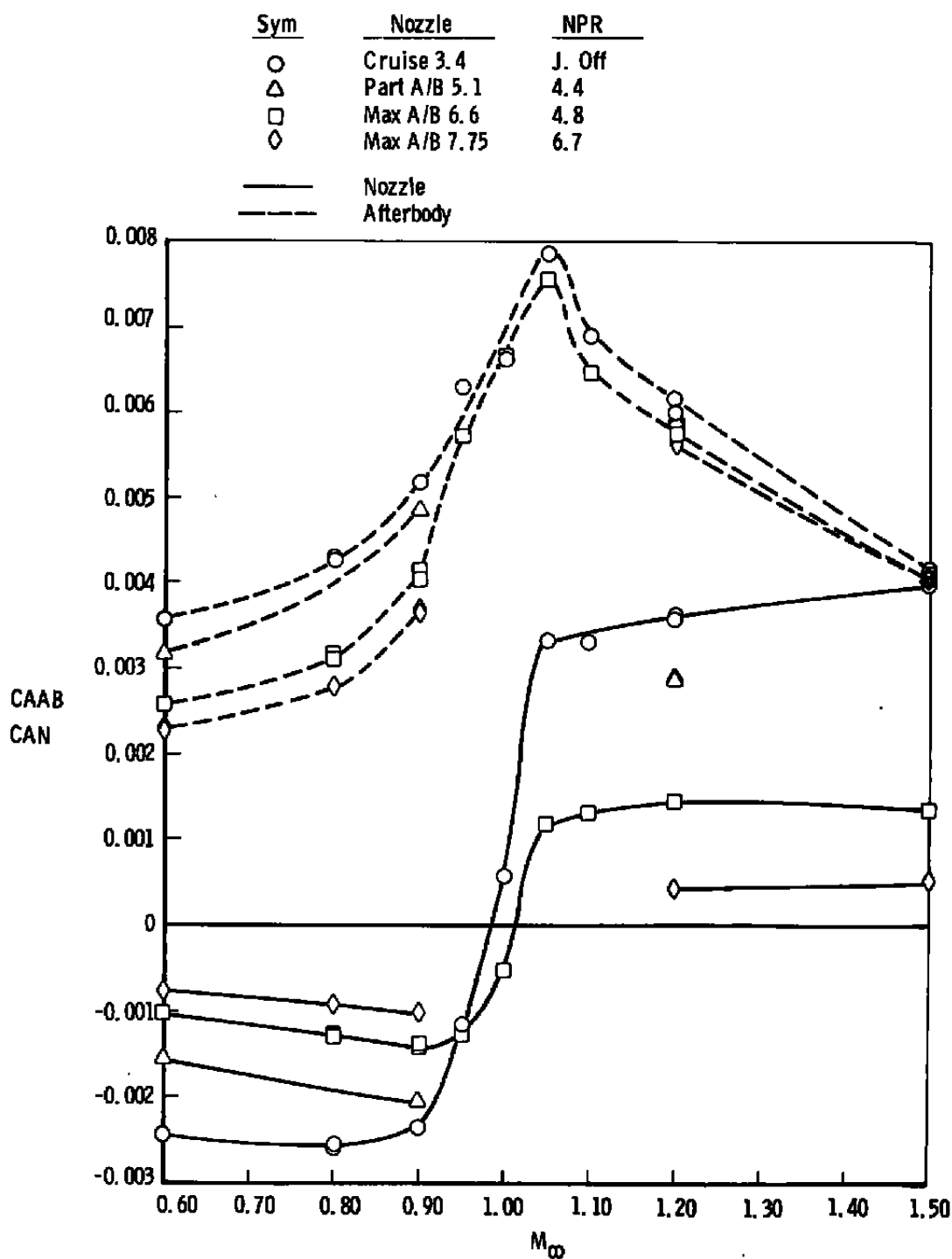


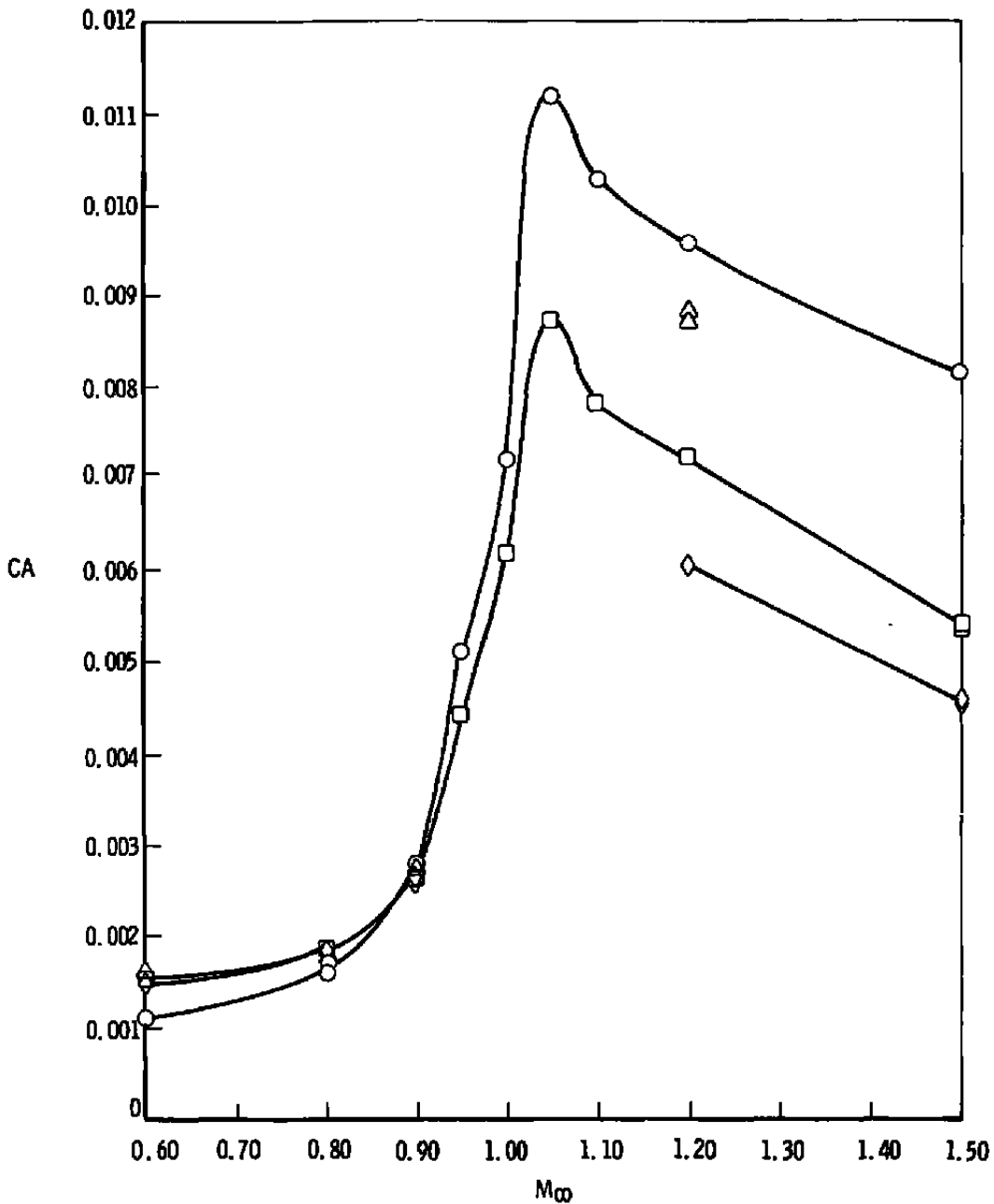
Figure 15. Estimated uncertainties in wind tunnel parameters.



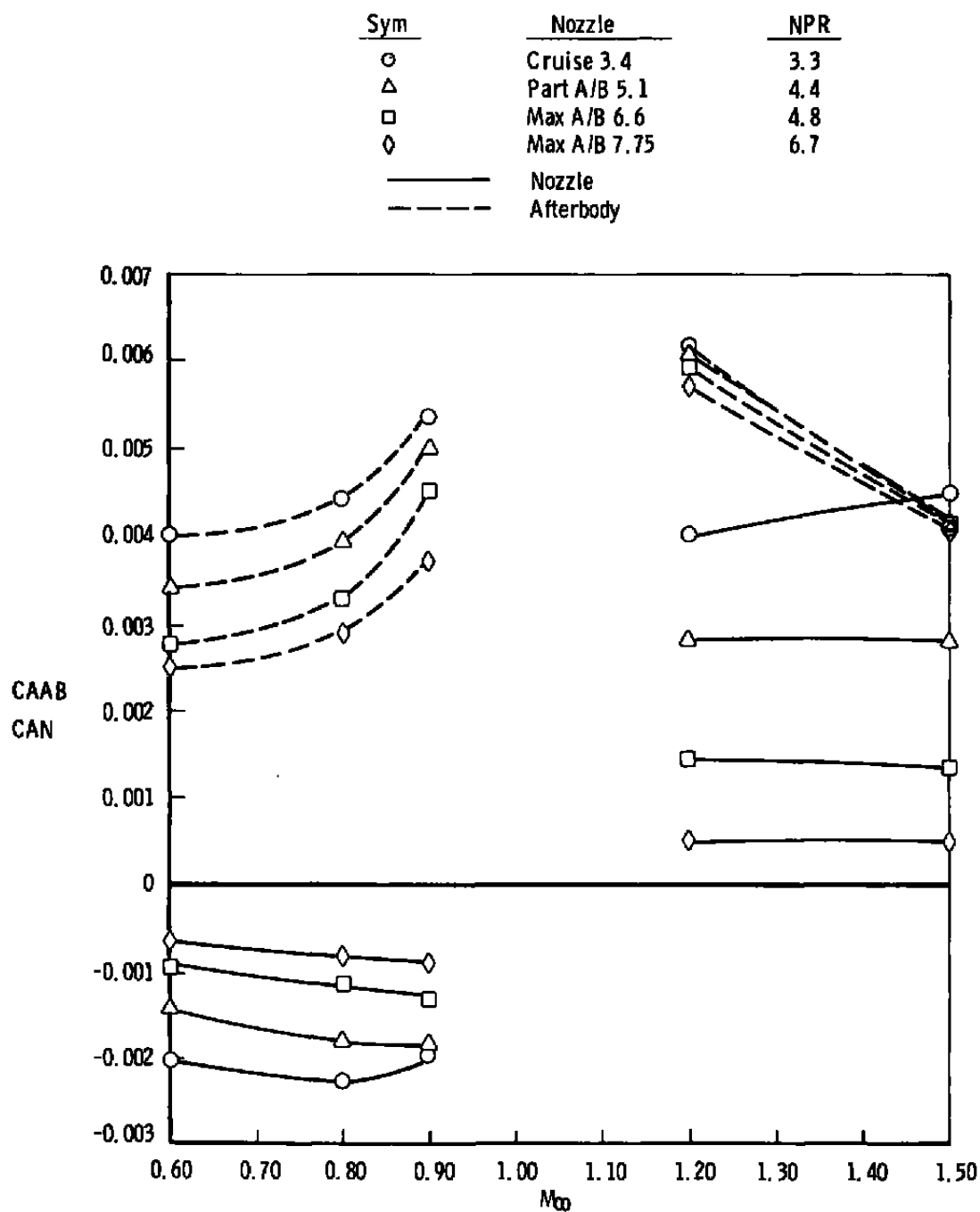
a. Afterbody and nozzle

Figure 16. Variation of axial-force coefficients with Mach number for various nozzle configurations, large sting support system, $Re = 3.4 \times 10^6$, $\alpha = 0$.

Sym	Nozzle	NPR	Config
○	Cruise 3.4	J. Off	36
△	Part A/B 5.1	4.4	41
□	Max A/B 6.6	4.8	42
◇	Max A/B 7.75	6.7	47



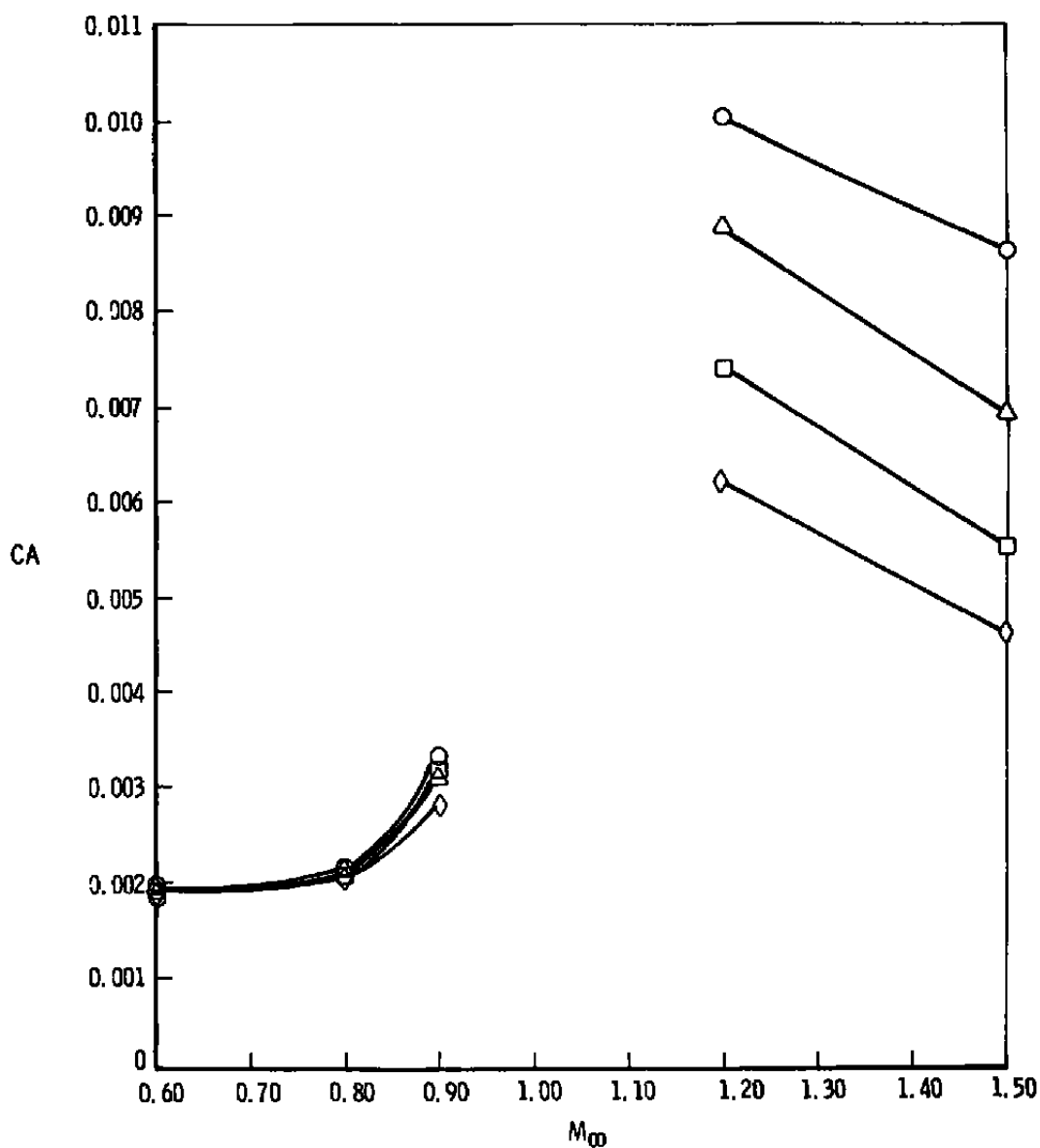
b. Complete aft nacelle
Figure 16. Concluded.



a. Afterbody and nozzle

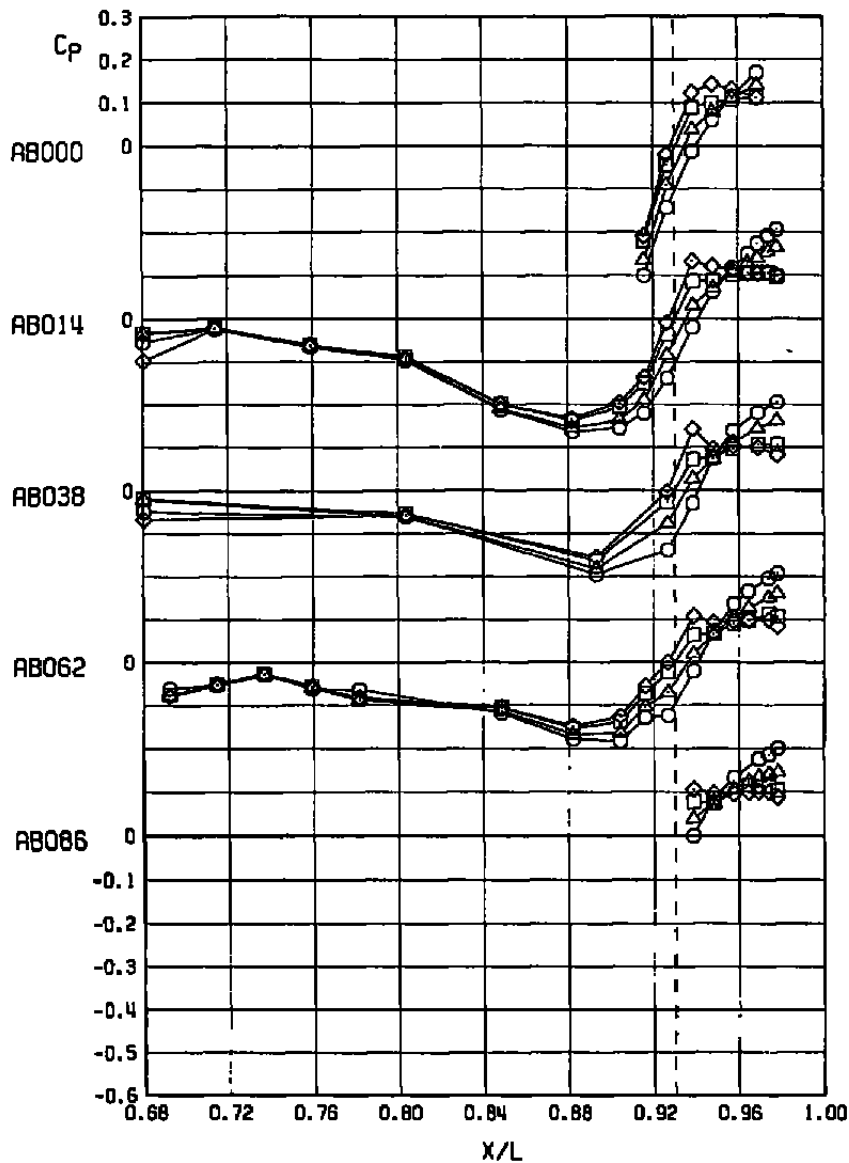
Figure 17. Variation of axial-force coefficients with Mach number for various nozzle configurations, small sting support system, $RN = 2.1 \times 10^6$, $\alpha = 0$.

Sym	Nozzle	NPR
○	Cruise	3.3
△	Part A/B 5.1	4.4
□	Max A/B 6.6	4.8
◇	Max A/B 7.75	6.7
—	Nozzle and Afterbody	



b. Complete aft nacelle
Figure 17. Concluded.

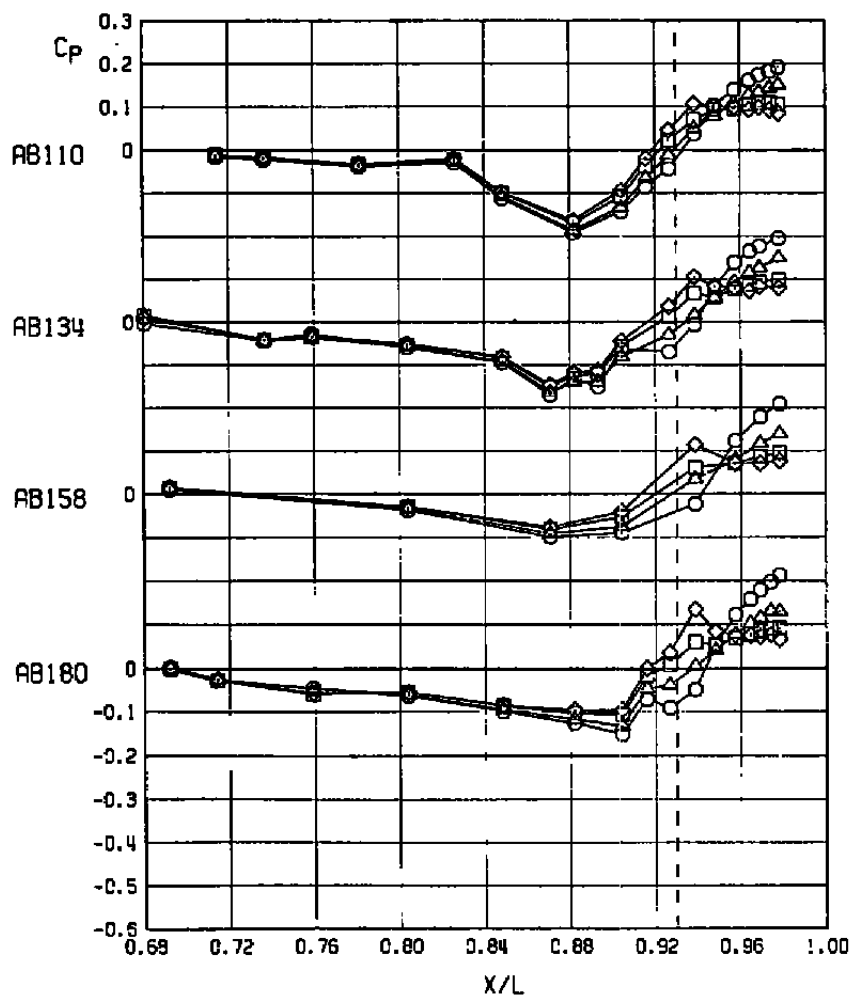
SYM	ALPHA	NPR	NPREF	DELTA	CONF	M _∞	ANX10 ⁻⁶	CA	PN.PT
○	-0.03	1.06	1.06	-0.27	36	0.60	3.41	0.00113	827.04
△	0.10	4.42	4.51	0.00	41	0.60	3.41	0.00159	1147.03
□	-0.09	4.76	4.75	0.00	42	0.60	3.41	0.00155	1105.01
◇	0.25	6.75	6.66	-0.03	47	0.60	3.41	0.00156	849.03



a. $M_{\infty} = 0.60$

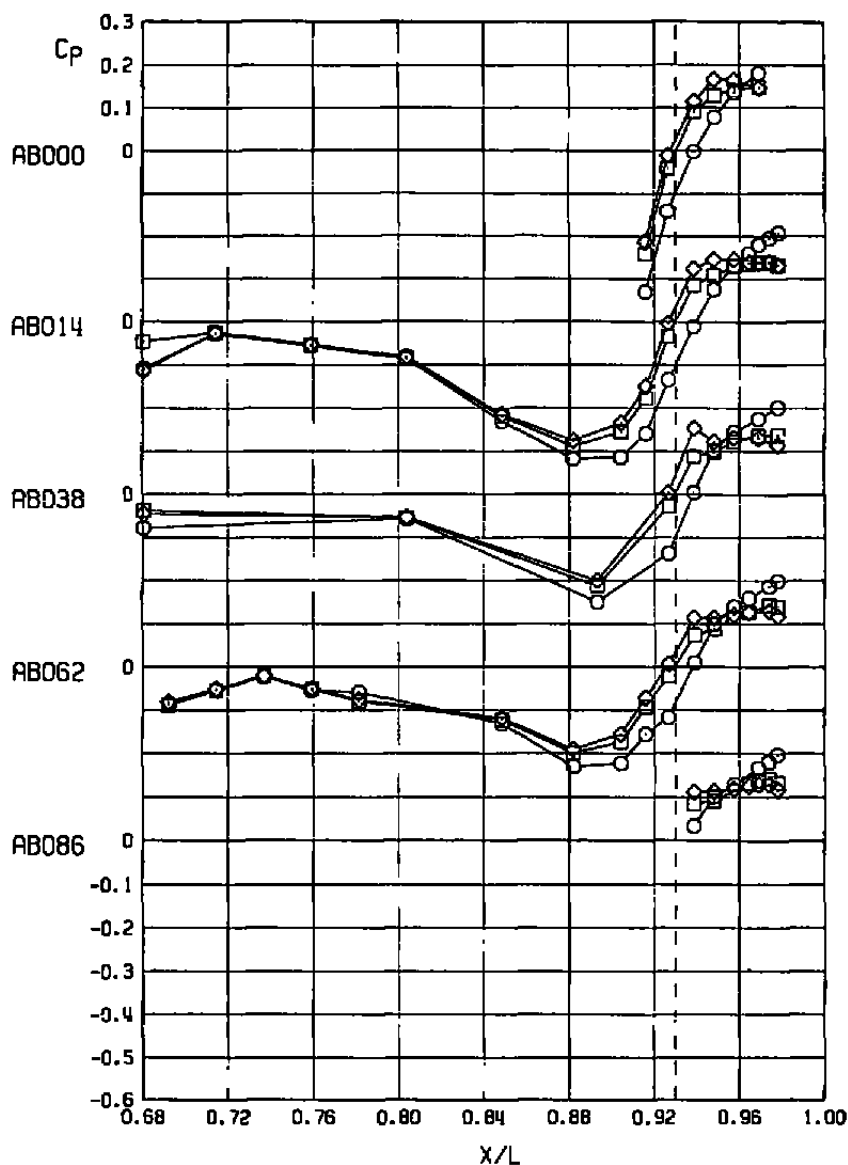
Figure 18. Effect of nozzle configuration on the nozzle and after-body static pressure distribution, large sting support system, $RN = 3.4 \times 10^6$, $\alpha = 0$.

SYM	ALPHA	NPR	NPREFF	DELTA	CONF	M _∞	RNX10 ⁻⁵	CA	PN,PT
○	-0.03	1.06	1.06	-0.27	36	0.60	3.41	0.00113	827.04
△	0.10	4.42	4.51	0.00	41	0.60	3.41	0.00159	1147.03
□	-0.09	4.76	4.75	0.00	42	0.60	3.41	0.00155	1105.01
◇	0.25	6.75	6.66	-0.03	47	0.60	3.41	0.00156	849.03



a. Concluded
Figure 18. Continued.

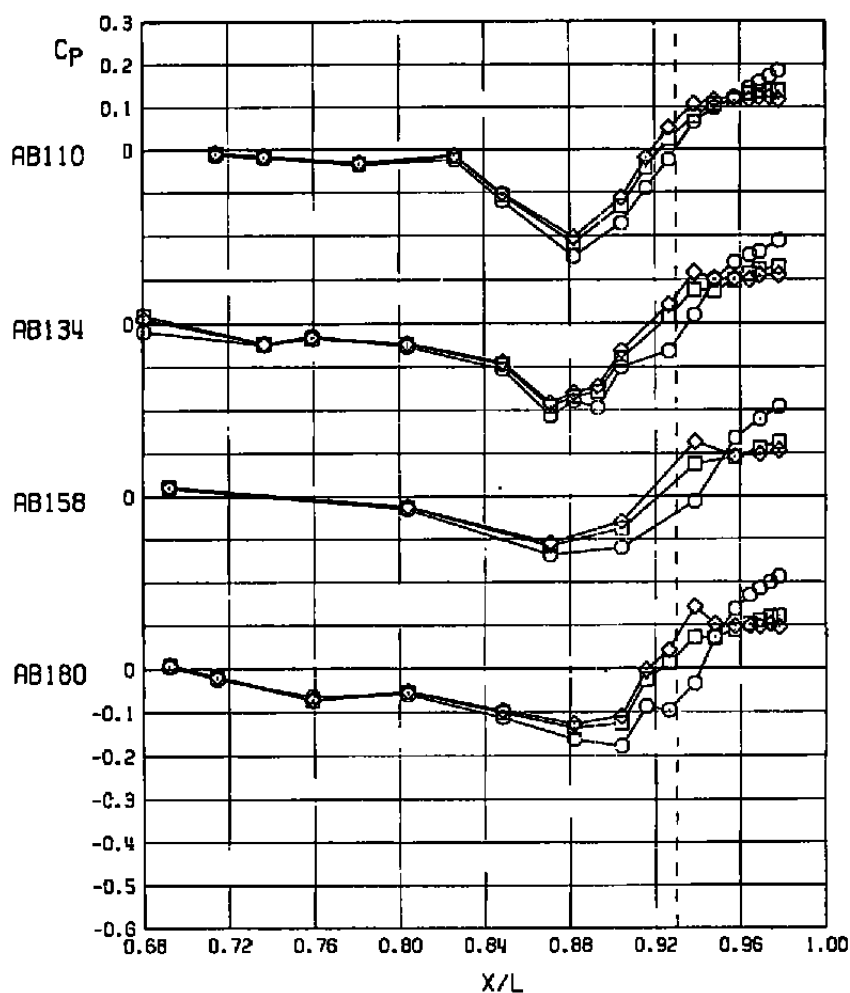
SYM	ALPHA	NPR	NPREFF	DELTA	CONF	M _∞	ANX10 ⁻⁵	CA	PN.PT
○	0.01	1.10	1.10	-0.27	36	0.80	3.40	0.00162	828.03
□	0.12	4.79	4.77	0.01	42	0.80	3.41	0.00186	1119.12
◇	0.17	6.76	6.67	-0.02	47	0.80	3.40	0.00183	858.03



b. $M_\infty = 0.80$

Figure 18. Continued.

SYM	ALPHA	NPR	NPREFF	DELTA	CONF	M _∞	ReX10 ⁻⁶	CA	PN,PT
○	0.01	1.10	1.10	-0.27	36	0.80	3.40	0.00162	828.03
□	0.12	4.79	4.77	0.01	42	0.80	3.41	0.00186	1119.12
◇	0.17	6.76	6.67	-0.02	47	0.80	3.40	0.00183	858.03



b. Concluded
Figure 18. Continued.

SYM	ALPHA	NPR	NPREF	DELHR	CONF	M _∞	RNX10 ⁻⁶	CA	PN,PT
○	0.02	1.12	1.12	-0.27	36	0.90	3.40	0.00280	829.03
△	0.11	4.38	4.49	0.03	41	0.90	3.40	0.00279	1162.03
□	0.06	4.77	4.76	-0.01	42	0.90	3.41	0.00264	1127.03
◇	0.11	6.76	6.67	0.02	47	0.90	3.40	0.00258	876.05

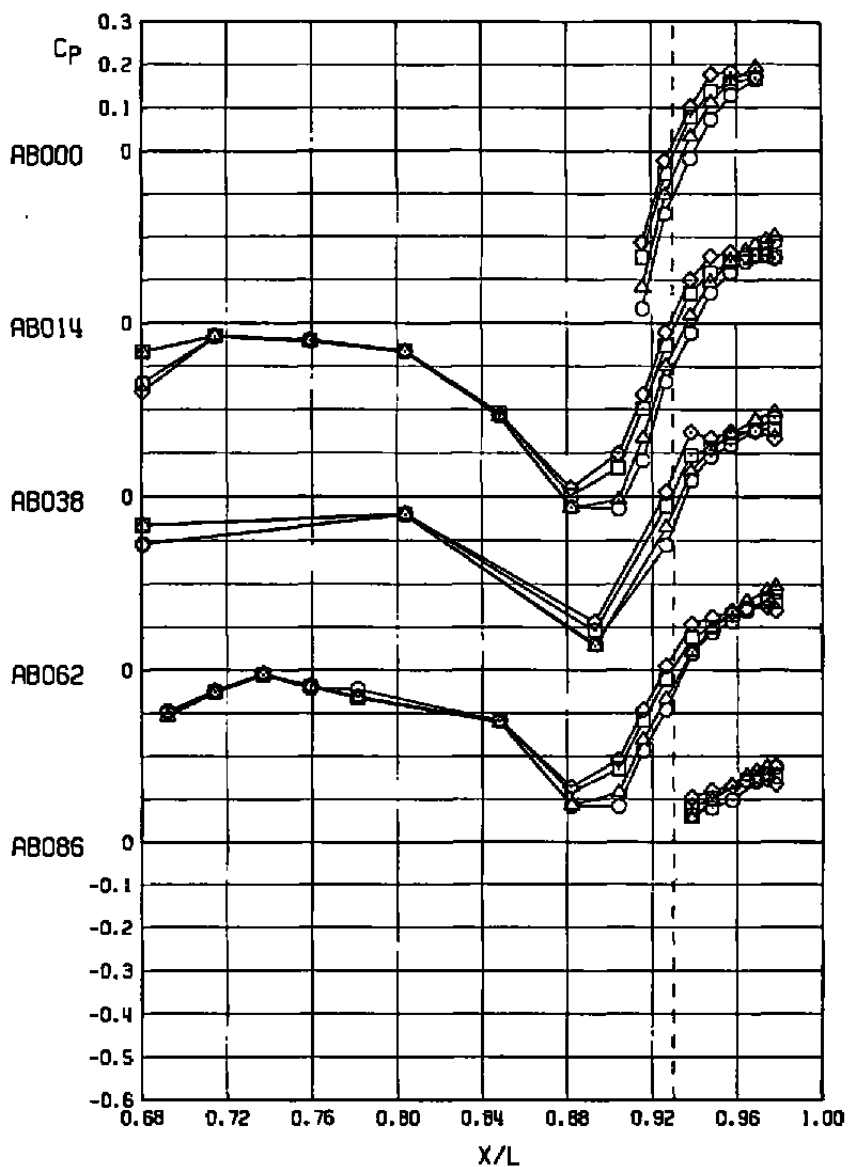
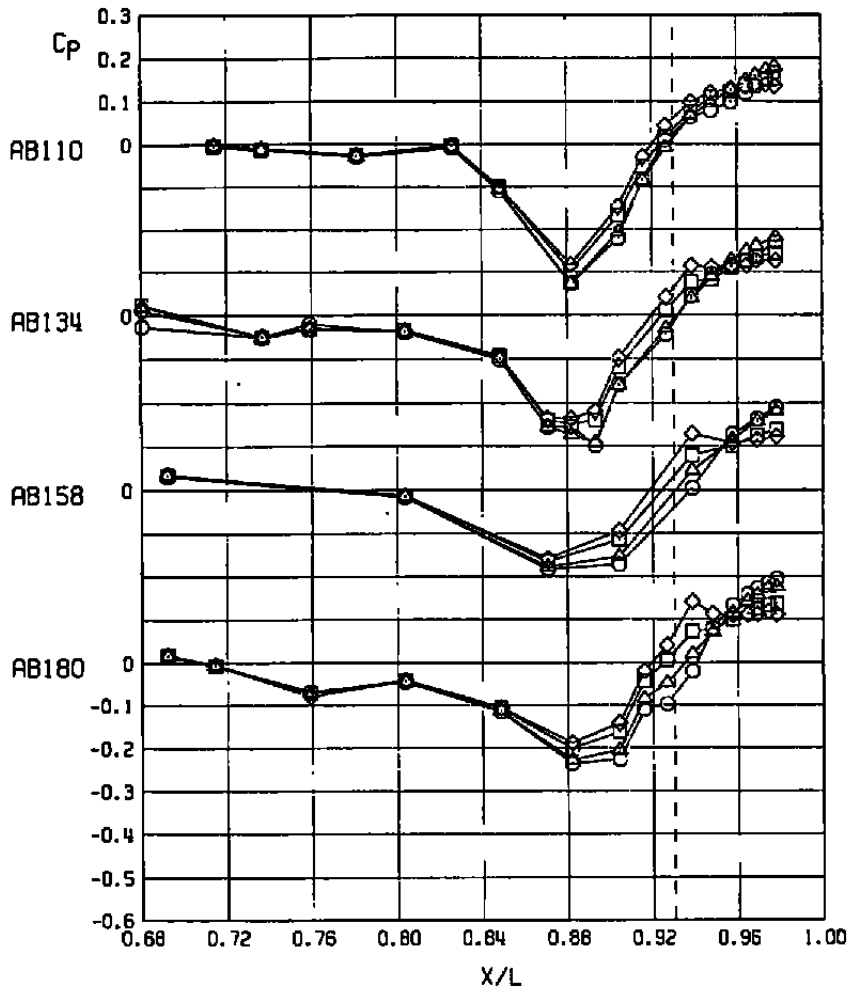
c. $M_\infty = 0.90$

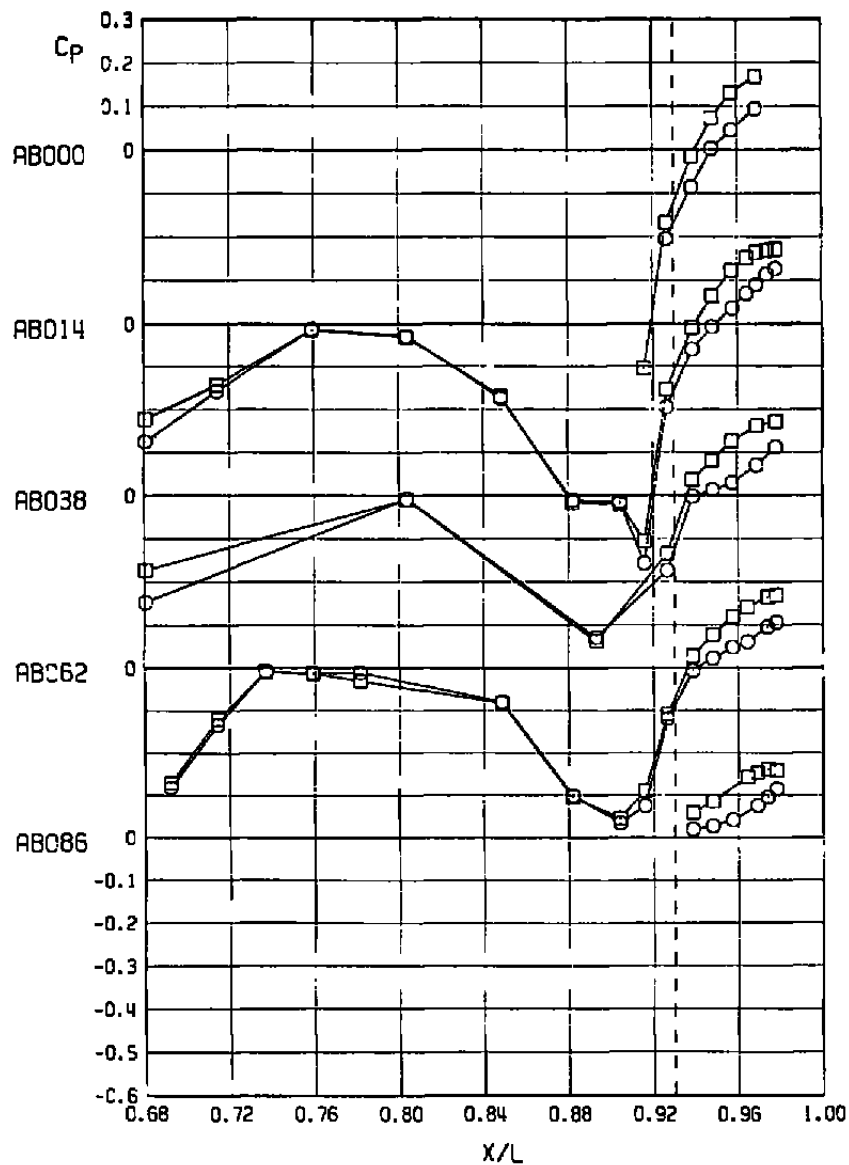
Figure 18. Continued.

SYM	ALPHA	NPR	NPREFF	DELTA	CONF	M _∞	ANX10 ⁻⁶	CA	PN.PT
○	0.02	1.12	1.12	-0.27	36	0.90	3.40	0.00280	829.03
△	0.11	4.38	4.49	0.03	41	0.90	3.40	0.00279	1162.03
□	0.06	4.77	4.76	-0.01	42	0.90	3.41	0.00264	1127.03
◇	0.11	6.76	6.67	0.02	47	0.90	3.40	0.00258	876.05



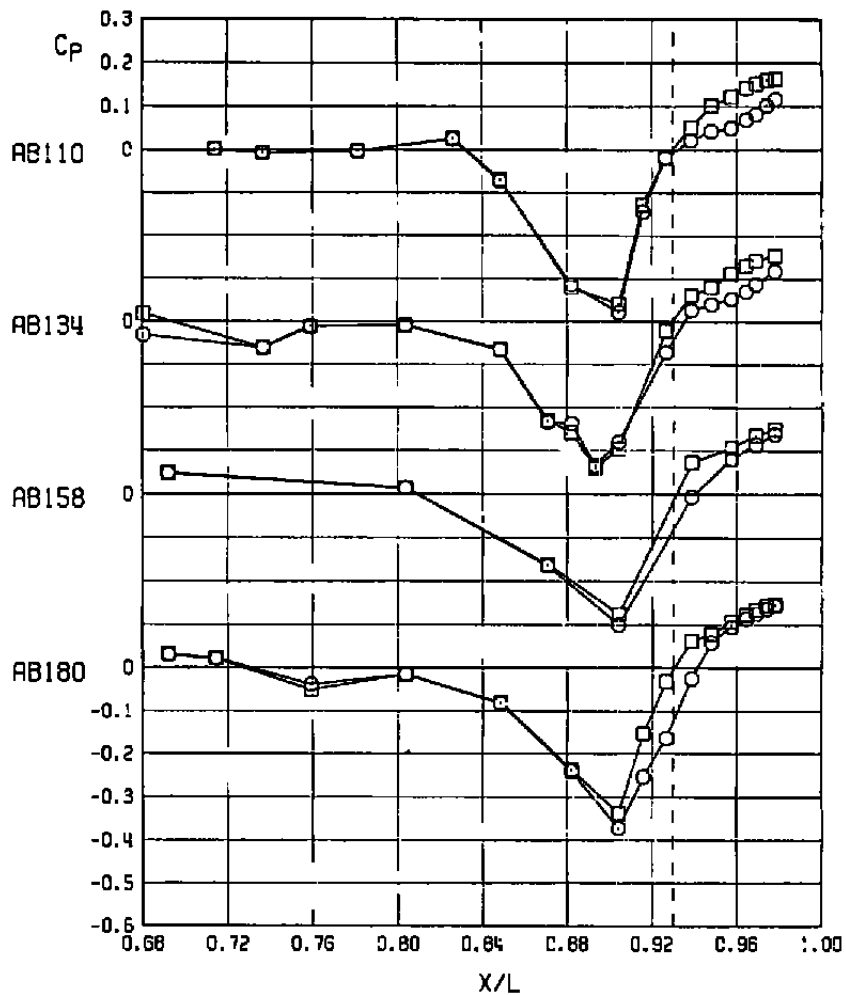
c. Concluded
Figure 18. Continued.

SYM	ALPHA	NPR	NPREF	DELTA	CONF	M _∞	RNX10 ⁻⁶	CA	PN,PT
○	0.05	1.10	1.10	-3.27	36	0.95	3.39	0.00513	830.03
□	0.02	4.82	4.78	-0.06	42	0.95	3.40	0.00442	1074.03



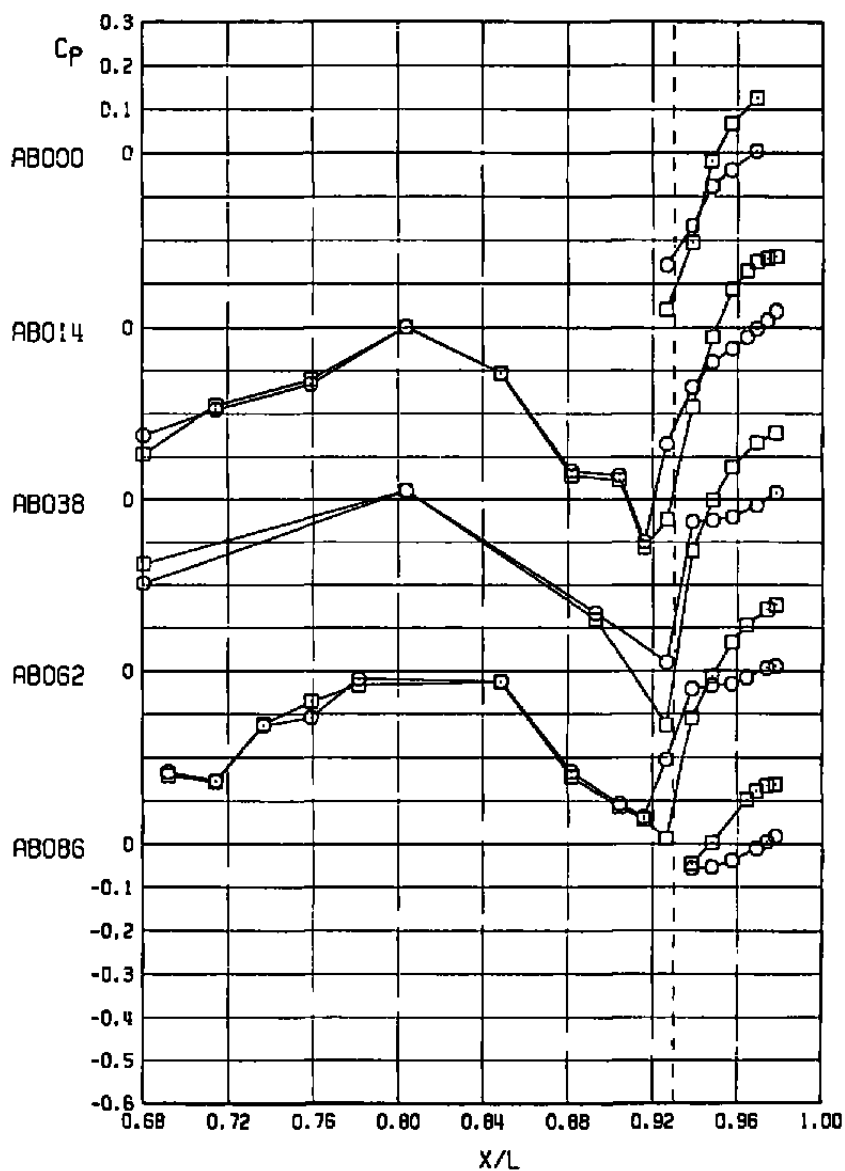
d. $M_\infty = 0.95$
Figure 18. Continued.

SYM	ALPHA	NPR	NPREFF	DELTA	CONF	M _∞	RNX10 ⁻⁶	CA	PN,PT
○	0.05	1.10	1.10	-0.27	36	0.95	3.39	0.00513	830.03
□	0.02	4.82	4.78	-0.06	42	0.95	3.40	0.00442	1074.03



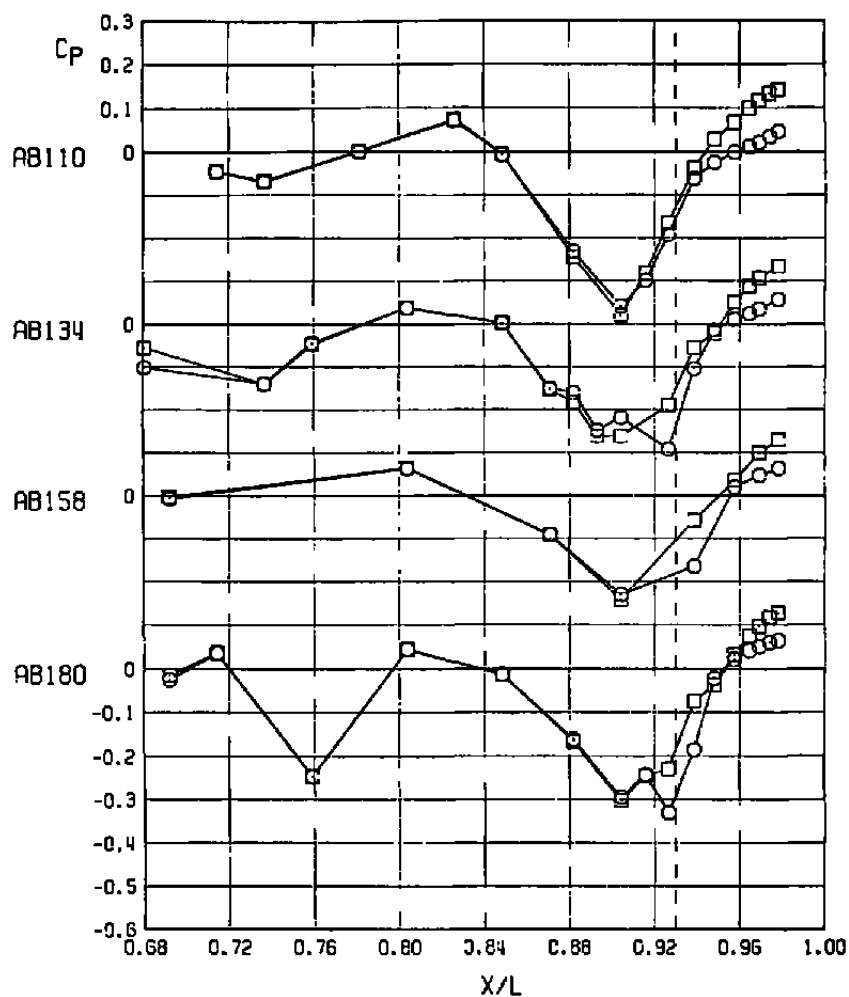
d. Concluded
Figure 18. Continued.

SYM	ALPHA	NPR	NPREFF	DELTA	CONF	M _∞	ANX10 ⁻⁶	CA	PN,PT
○	0.08	1.07	1.07	-0.27	36	1.00	3.40	0.00720	831.03
□	0.02	4.82	4.78	-0.06	42	1.00	3.38	0.00618	1073.10



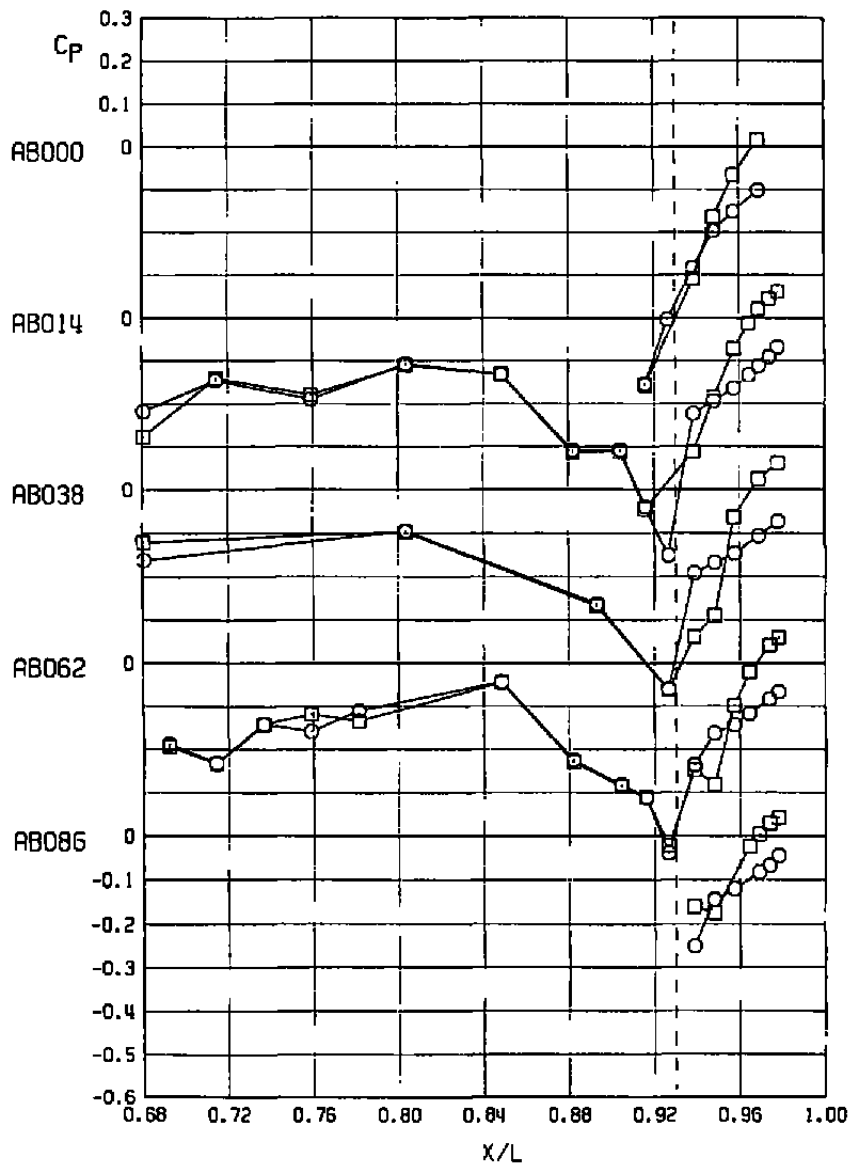
e. $M_\infty = 1.00$
Figure 18. Continued.

SYM	ALPHA	NPR	NPREFF	DELTA	CONF	M _∞	RNX:0-8	CA	PN,PT
○	0.08	1.07	1.07	-0.27	36	1.00	3.40	0.00720	831.03
□	0.02	4.82	4.78	-0.06	42	1.00	3.38	0.00618	1073.10



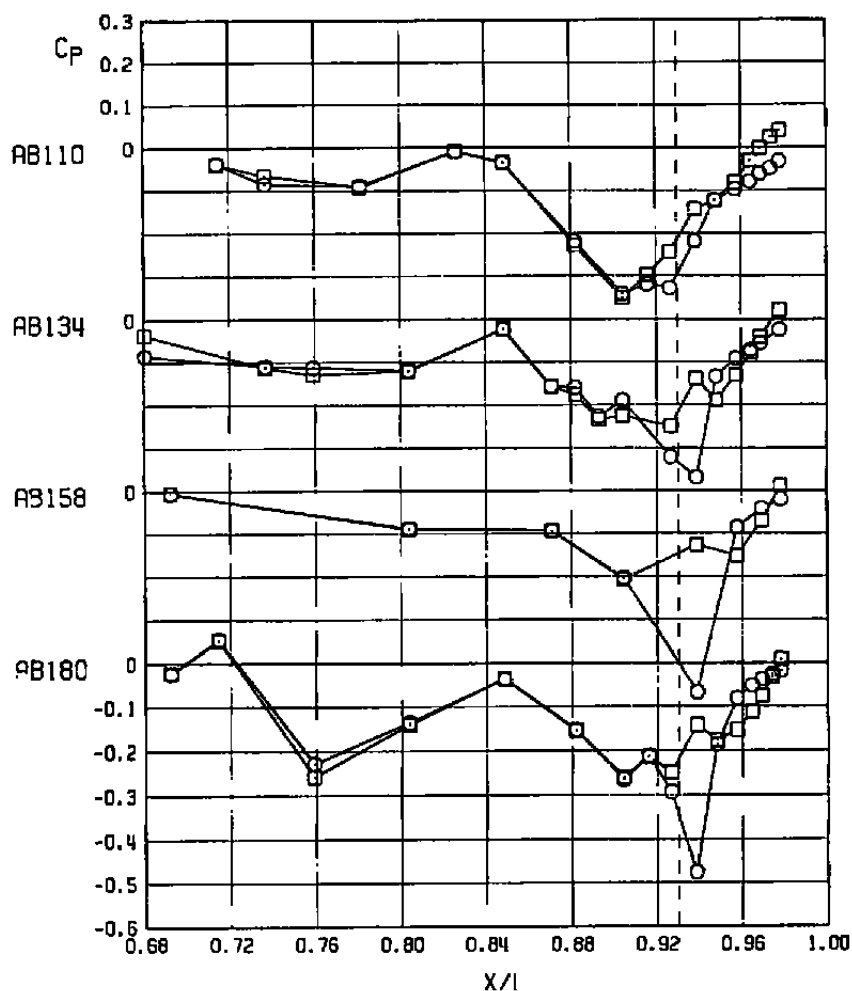
e. Concluded
Figure 18. Continued.

SYM	ALPHA	NPR	NPREF	DELTA	CONF	M _∞	RNX10 ⁻⁶	CA	PN,PT
○	0.06	1.00	1.00	-0.27	36	1.05	3.40	0.01120	832.03
□	-0.01	4.71	4.73	-0.06	42	1.05	3.39	0.00875	1072.03



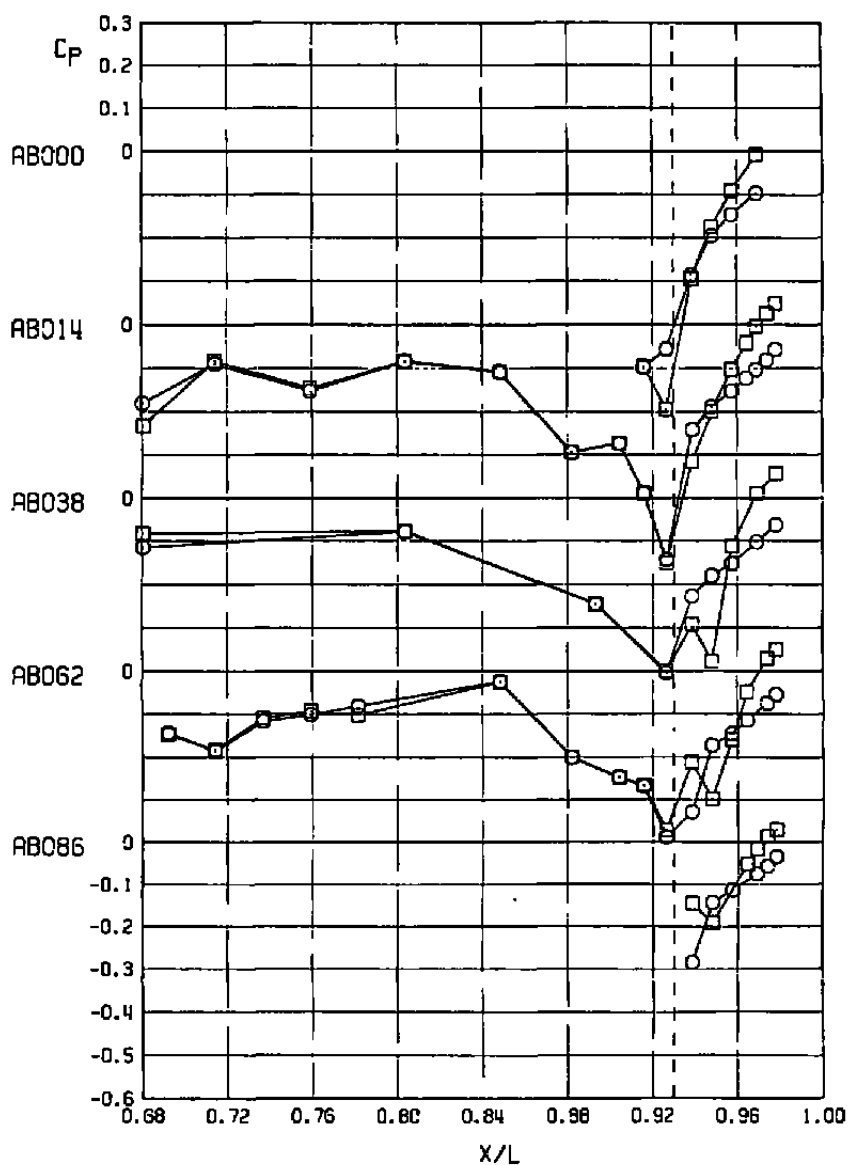
f. $M_\infty = 1.05$
Figure 18. Continued.

SYM	ALPHA	NPR	NPREF	DELTA	CONF	M _∞	RNX10 ⁻⁶	CA	PN,PT
○	0.06	1.00	1.00	-0.27	36	1.05	3.40	0.01120	832.03
□	-0.01	4.71	4.73	-0.06	42	1.05	3.39	0.00875	1072.03



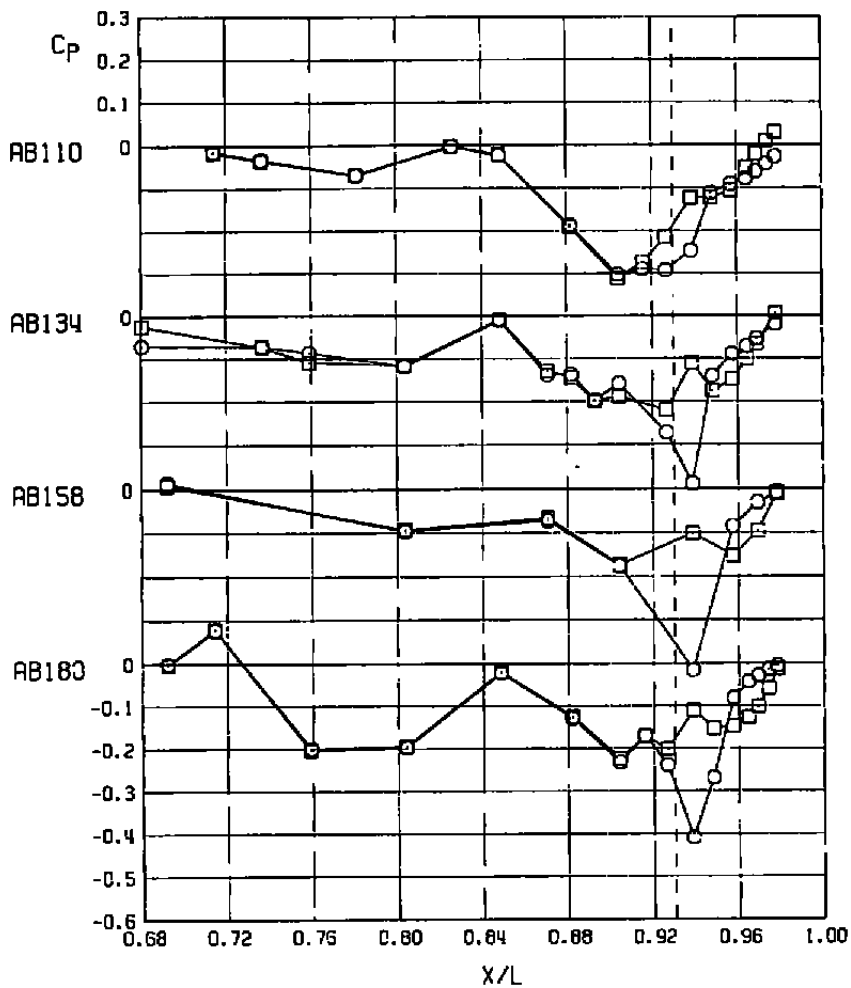
f. Concluded
Figure 18. Continued.

SYM	ALPHA	NPR	NPREFF	DELTA	CONF	M _∞	RNX10 ⁻⁵	CA	PN,PT
○	0.07	1.01	1.01	-0.27	36	1.10	3.40	0.01027	833.03
□	0.01	4.73	4.74	-0.06	42	1.10	3.42	0.00781	1071.03



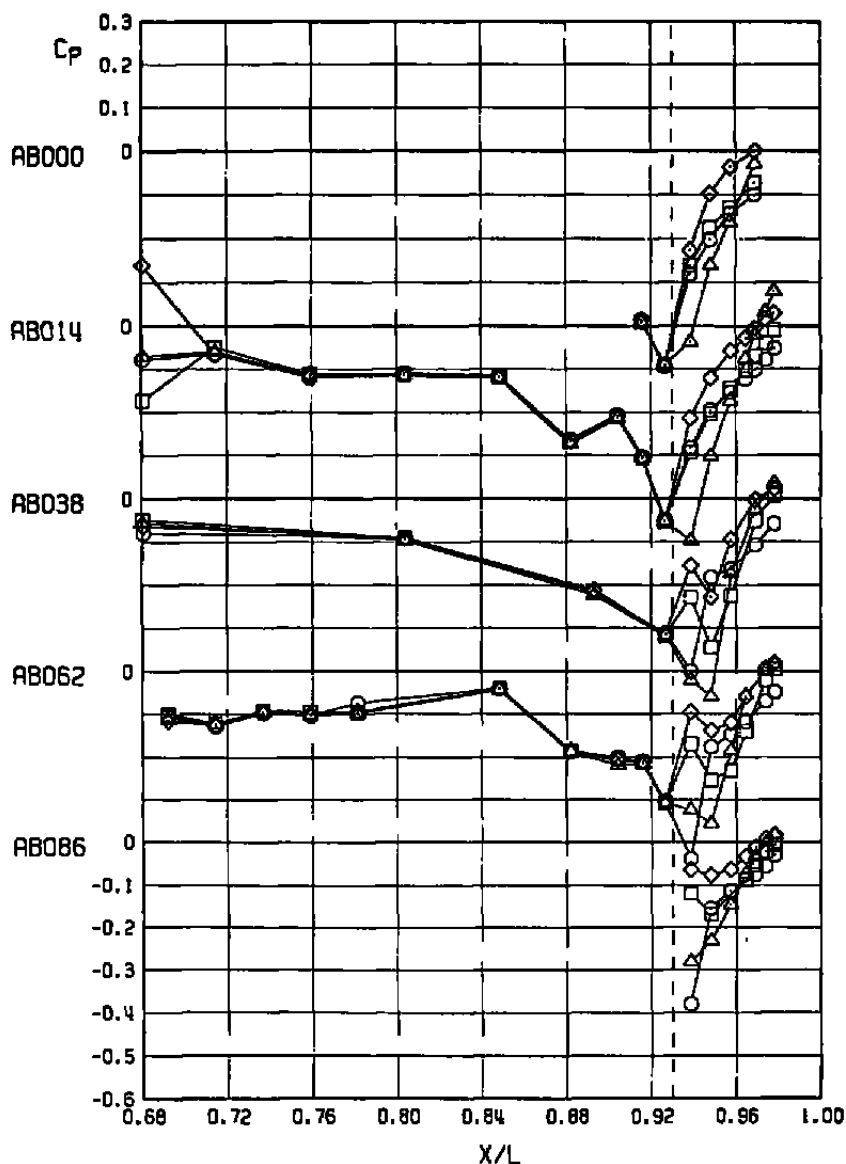
g. $M_\infty = 1.10$
Figure 18. Continued.

SYM	ALPHA	NPR	NPREFF	DELHR	CONF	M _∞	RNX10 ⁻⁶	CA	PN,PT
○	0.07	1.01	1.01	-0.27	36	1.10	3.40	0.01027	833.03
□	0.01	4.73	4.74	-0.06	42	1.10	3.42	0.00781	1071.03



g. Concluded
Figure 18. Continued.

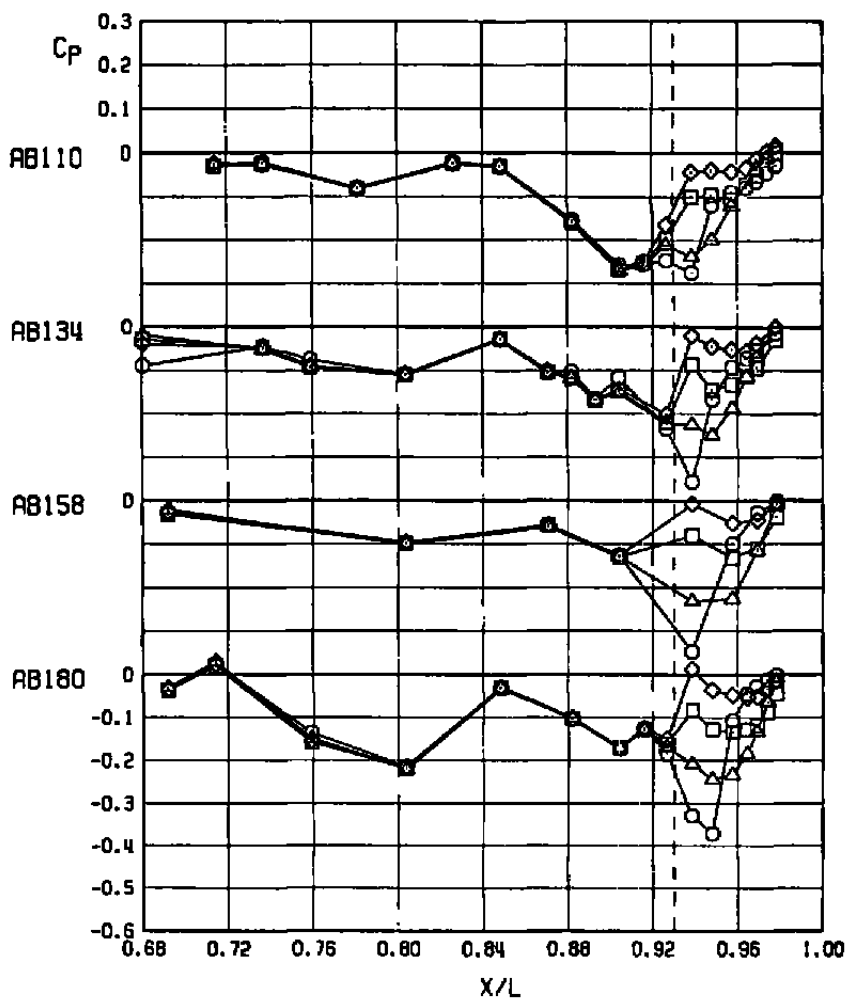
SYM	ALPHA	NPR	NPREFF	DELTA	CONF	M _∞	ANX10 ⁻⁵	CA	PN,PT
○	0.04	1.02	1.02	-0.27	36	1.20	3.39	0.00958	834.03
△	0.03	4.41	4.50	-0.08	41	1.20	3.39	0.00886	1240.09
□	-0.10	4.79	4.77	-0.14	42	1.20	3.41	0.00724	1051.03
◇	0.01	6.71	6.64	-0.02	47	1.20	3.40	0.00604	901.03



h. $M_\infty = 1.20$

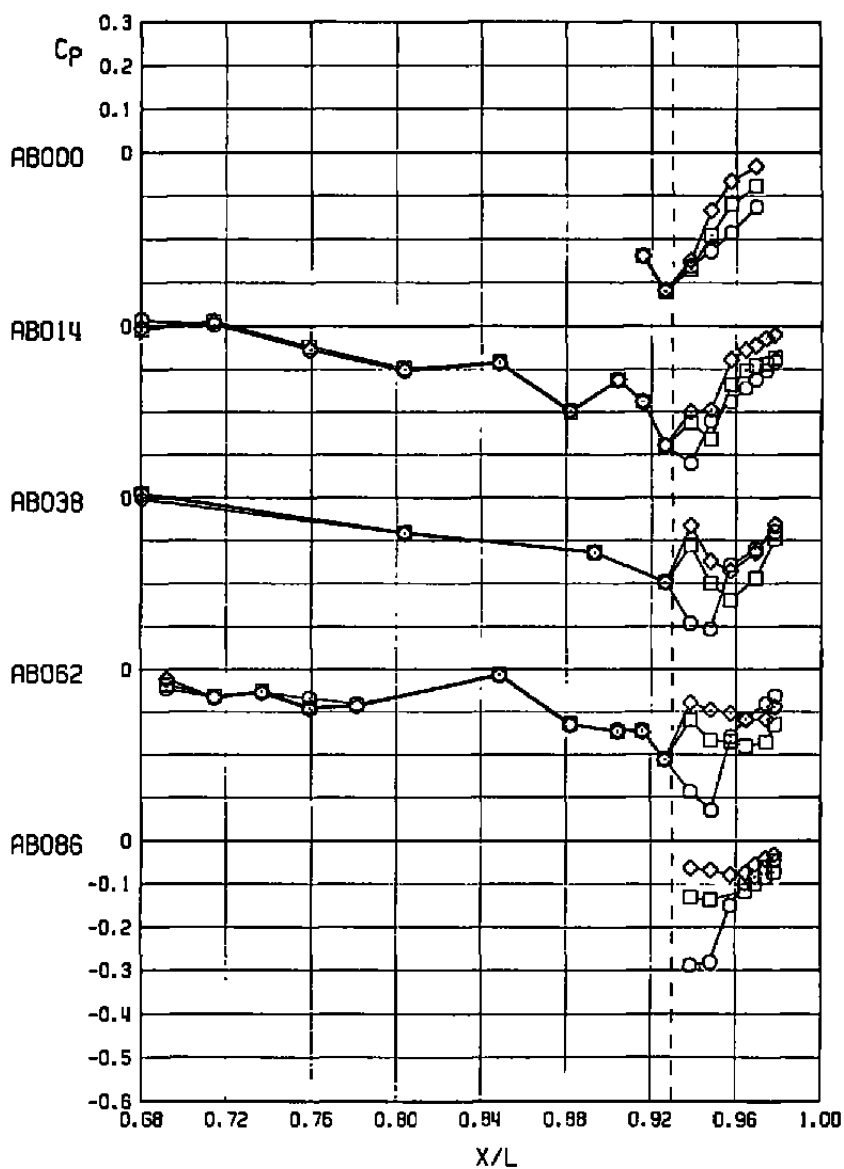
Figure 18. Continued.

SYM	ALPHA	NPR	NPREFF	DELTA	CONF	M _∞	RNX10 ⁻⁸	CA	PN,PT
○	0.04	1.02	1.02	-0.27	36	1.20	3.39	0.00958	834.03
△	0.03	4.41	4.50	-0.08	41	1.20	3.39	0.00886	1240.09
□	-0.10	4.79	4.77	-0.14	42	1.20	3.41	0.00724	1051.03
◇	0.01	6.71	6.64	-0.02	47	1.20	3.40	0.00604	901.03



h. Concluded
Figure 18. Continued.

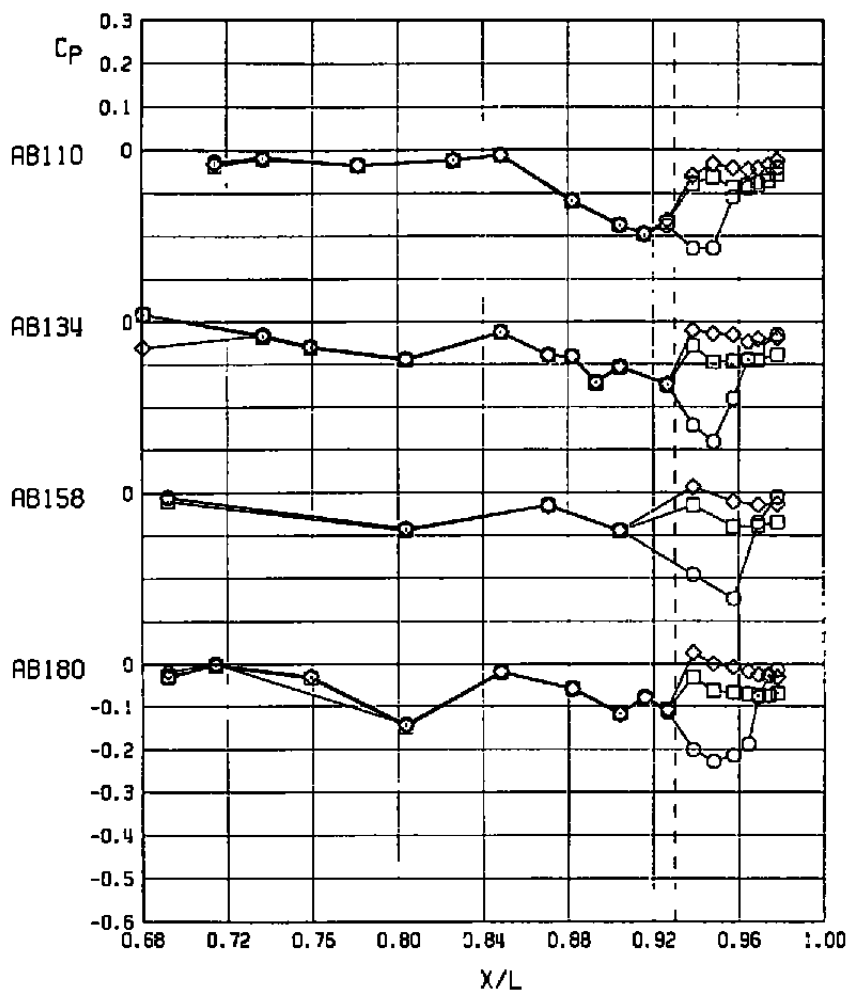
SYM	ALPHA	NPA	NPREF	DELTA	CONF	M _∞	ANX10 ⁻⁶	CA	PN,PT
○	0.07	0.99	0.99	-0.04	36	1.50	3.40	0.00816	1183.03
□	-0.14	4.83	4.79	-0.00	42	1.50	3.39	0.00543	1047.03
◇	0.08	5.77	6.68	-0.11	47	1.50	3.40	0.00460	965.03



i. $M_\infty = 1.50$

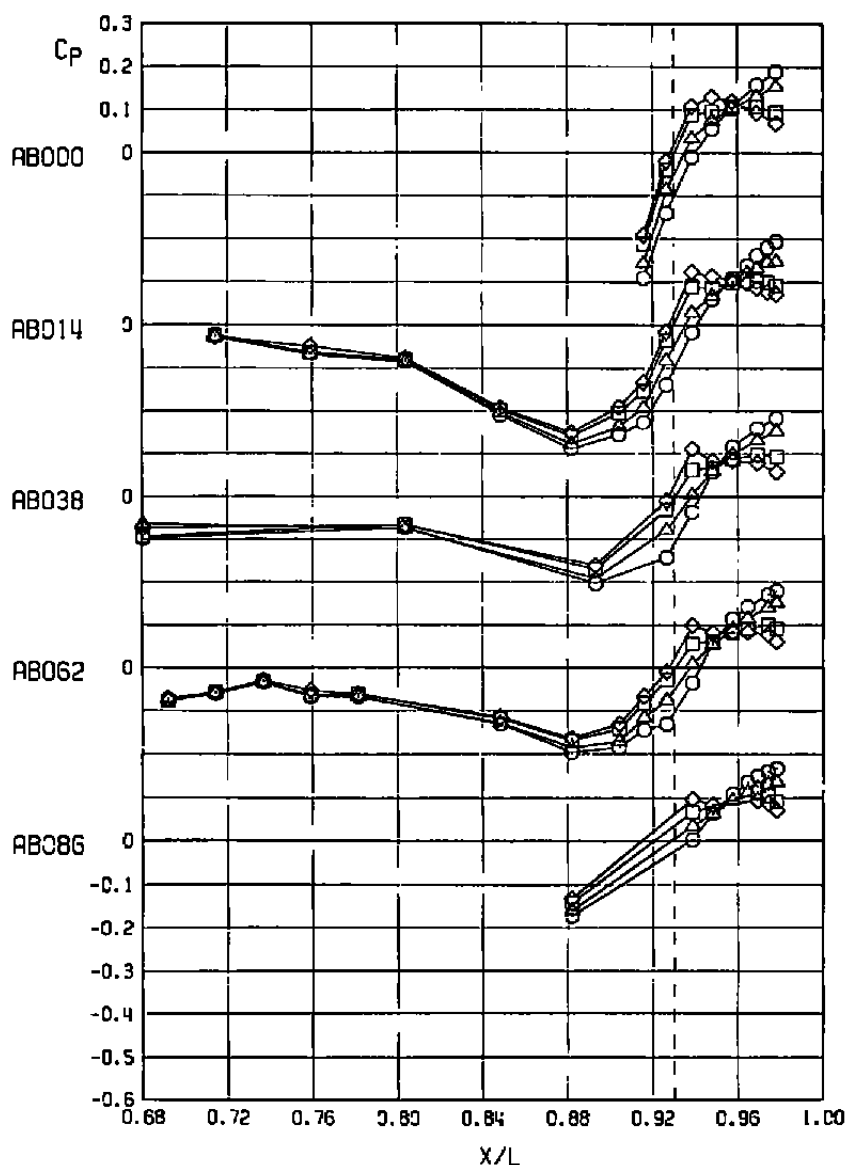
Figure 18. Continued.

SYM	ALP4P	NPR	NPREF	DELHR	CONF	M _∞	PNX10 ⁻⁶	CA	PN.PT
○	0.07	0.99	0.99	-0.04	36	1.50	3.40	0.00816	1183.03
□	-0.14	4.83	4.79	-0.00	42	1.50	3.39	0.00543	1047.03
◇	0.08	6.77	6.68	-0.11	47	1.50	3.40	0.00460	965.03



i. Concluded
Figure 18. Concluded.

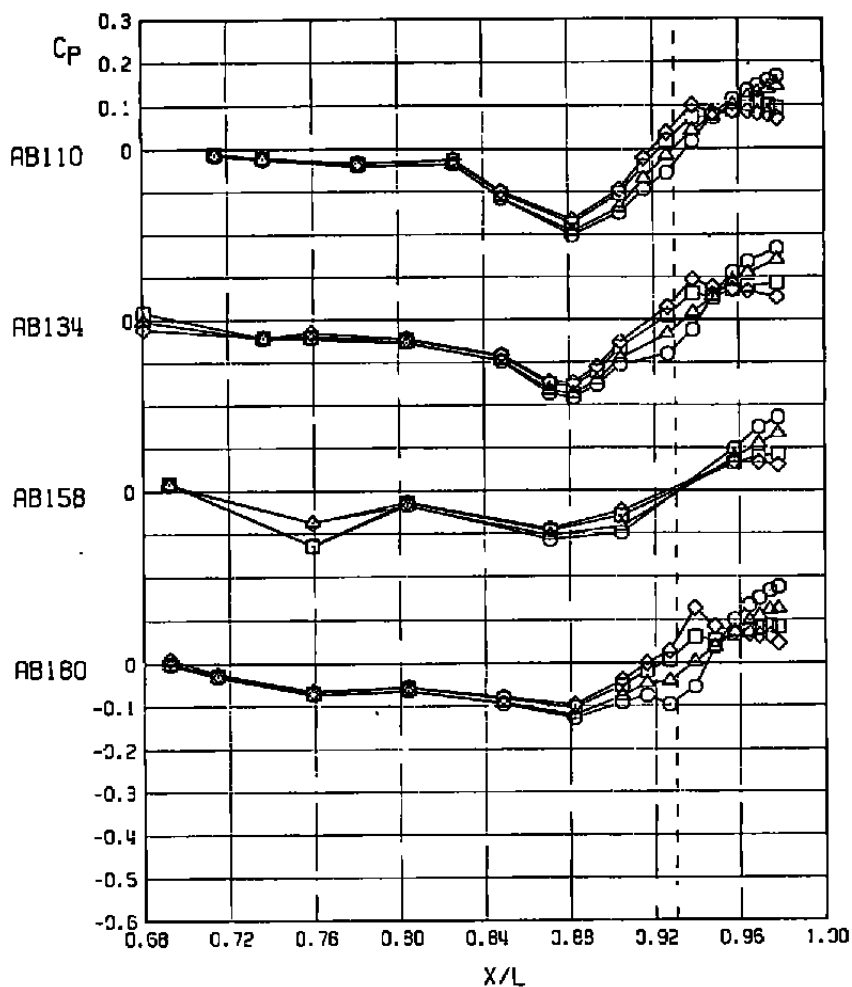
SYM	ALPHA	NPR	NPREF	DELTA	CONF	M _∞	RNX10 ⁻⁶	CA	PN.PT
○	-0.02	3.24	3.25	0.00	30	0.60	2.10	0.00198	636.10
△	-0.05	4.36	4.44	-0.03	31	0.60	2.10	0.00197	746.03
□	0.01	4.78	4.66	0.00	32	0.60	2.10	0.00184	772.03
◇	0.03	6.71	5.59	-0.01	33	0.60	2.10	0.00183	719.03



a. $M_{\infty} = 0.60$

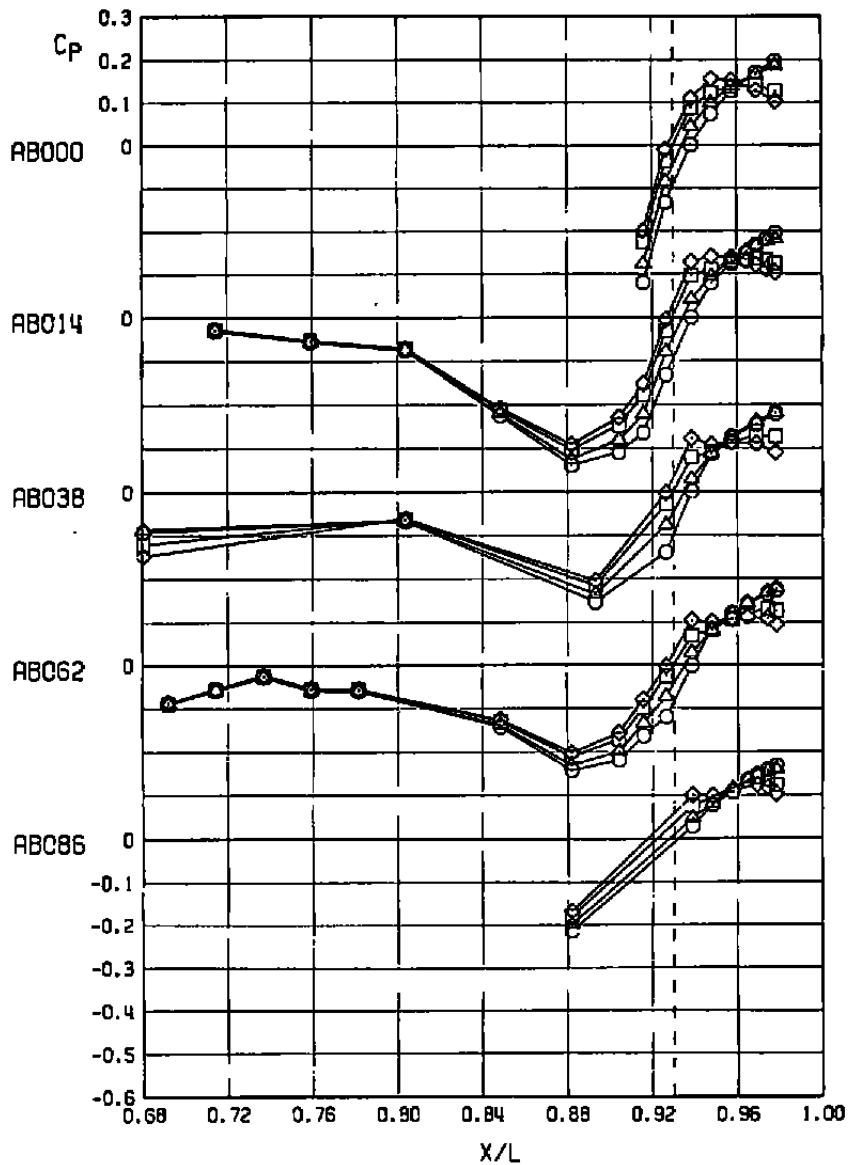
Figure 19. Effect of nozzle configuration on the nozzle and afterbody static pressure distribution, small sting support system, $RN = 2.1 \times 10^6$, $\alpha = 0$.

SYM	ALPHA	NPR	NPREFF	DELHR	CONF	M _∞	RN $\times 10^{-6}$	CA	PN,PT
○	-0.02	3.24	3.25	0.00	30	0.60	2.10	0.00198	636.10
△	-0.05	4.36	4.44	-0.03	31	0.60	2.10	0.00197	746.03
□	0.01	4.78	4.66	0.00	32	0.60	2.10	0.00184	772.03
◇	0.03	6.71	6.59	-0.01	33	0.60	2.10	0.00183	719.03



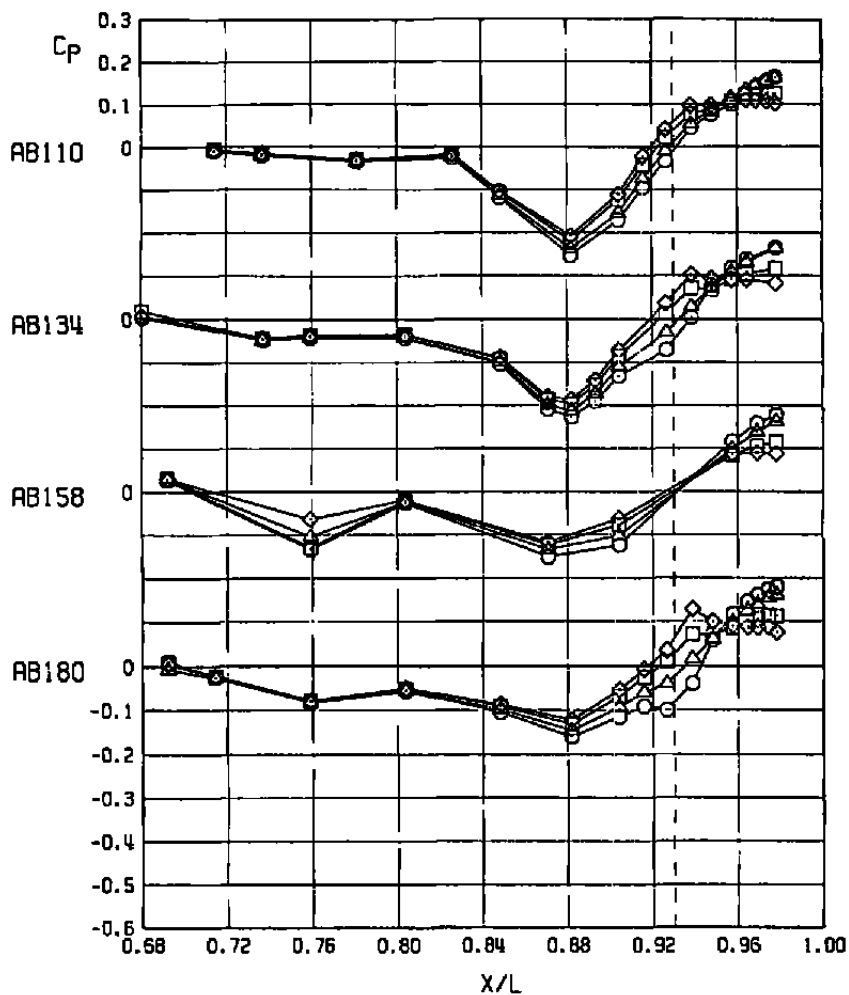
a. Concluded
Figure 19. Continued.

SYM	ALPHA	NPR	NPREF	DELTA	CONF	M _∞	RNX10 ⁻⁶	CA	PN.PT
○	-0.01	3.27	3.26	-0.01	30	0.80	2.10	0.00211	665.11
△	0.00	4.40	4.46	0.00	31	0.80	2.10	0.00211	751.03
□	0.03	4.76	4.65	-0.02	32	0.80	2.10	0.00206	777.03
◇	-0.00	6.69	6.58	-0.03	33	0.80	2.10	0.00204	724.03



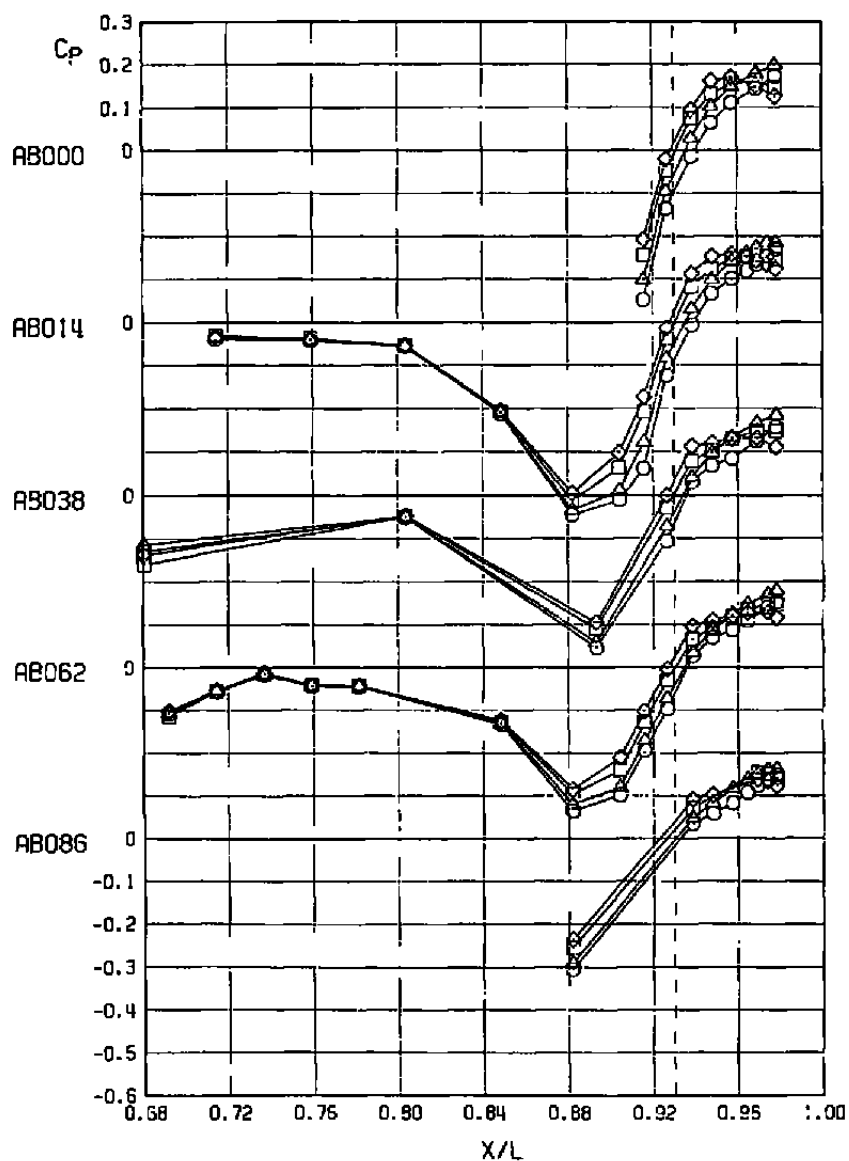
b. $M_\infty = 0.80$
Figure 19. Continued.

SYM	ALPHA	NPR	NPREFF	DELHA	CONF	M _∞	RNX10 ⁻⁶	CA	PN,PT
○	-0.01	3.27	3.26	-0.01	30	0.80	2.10	0.00211	665.11
△	0.00	4.40	4.46	0.00	31	0.80	2.10	0.00211	751.03
□	0.03	4.76	4.65	-0.02	32	0.80	2.10	0.00206	777.03
◇	-0.00	6.69	5.58	-0.03	33	0.80	2.10	0.00204	724.03



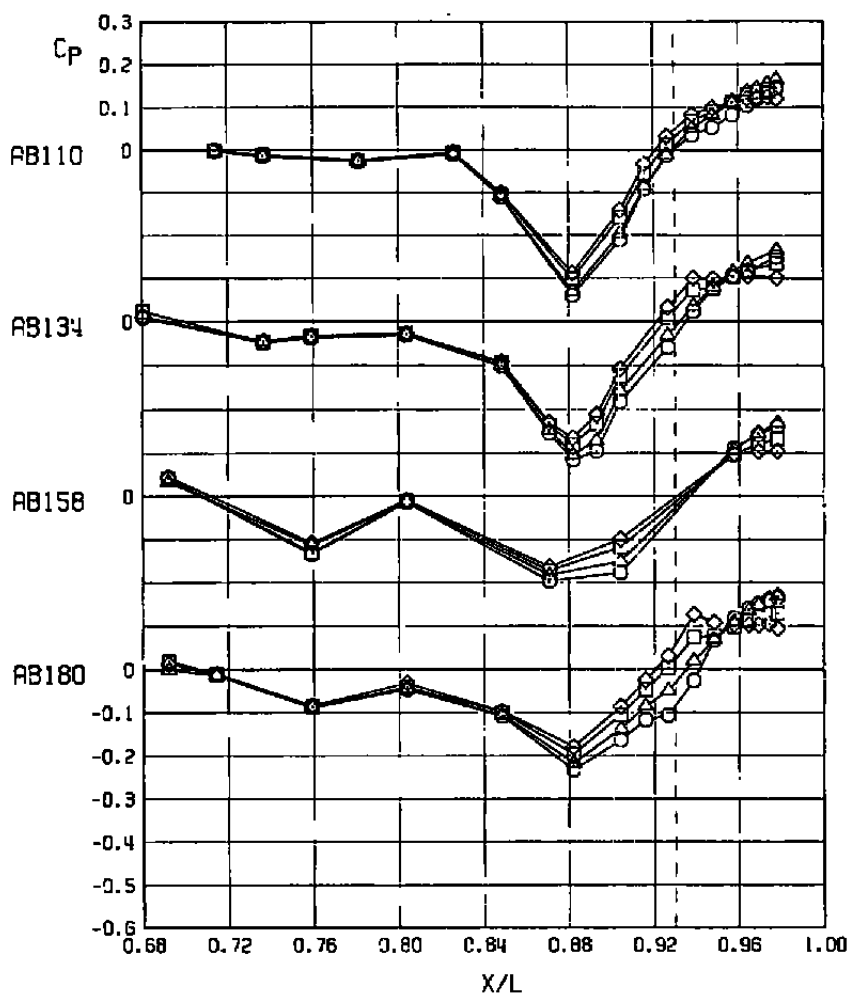
b. Concluded
Figure 19. Continued.

SYM	ALPHA	NPR	NPREFF	DELHA	CONF	M _∞	RNX10 ⁻⁶	CA	PN.PT
○	-0.02	3.32	3.27	-0.00	30	0.90	2.09	0.00334	688.11
△	-0.01	4.38	4.45	0.00	31	0.90	2.10	0.00310	754.03
□	0.02	4.79	4.67	-0.02	32	0.90	2.10	0.00318	780.03
◇	-0.00	6.67	6.57	0.00	33	0.90	2.10	0.00280	732.03



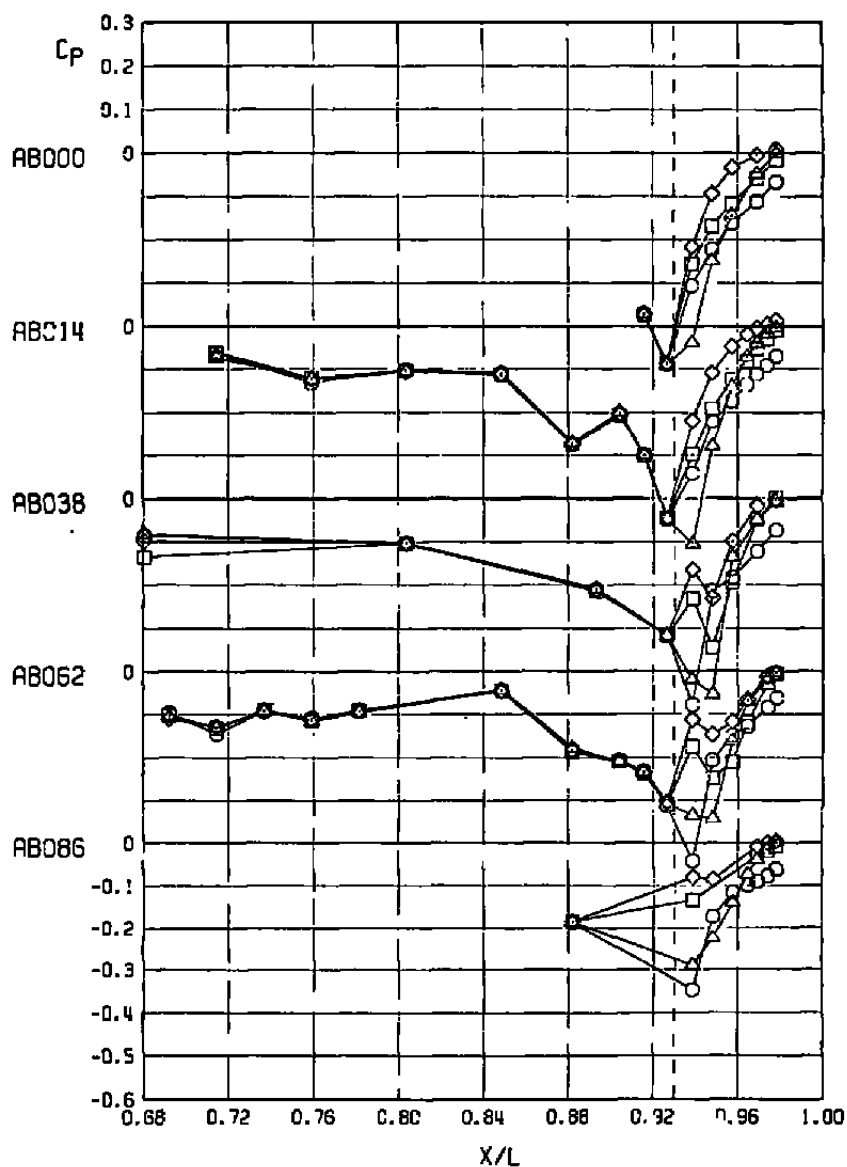
c. $M_\infty = 0.90$
Figure 19. Continued.

SYM	ALPHA	NPR	NPREF	DELHR	CONF	M _∞	RNX10 ⁻⁶	CA	PN.PT
○	-0.02	3.32	3.27	-0.00	30	0.90	2.09	0.00334	688.11
△	-0.01	4.38	4.45	0.00	31	0.90	2.10	0.00310	754.03
□	0.02	4.79	4.67	-0.02	32	0.90	2.10	0.00318	780.03
◇	-0.00	6.67	6.57	0.00	33	0.90	2.13	0.00280	732.03



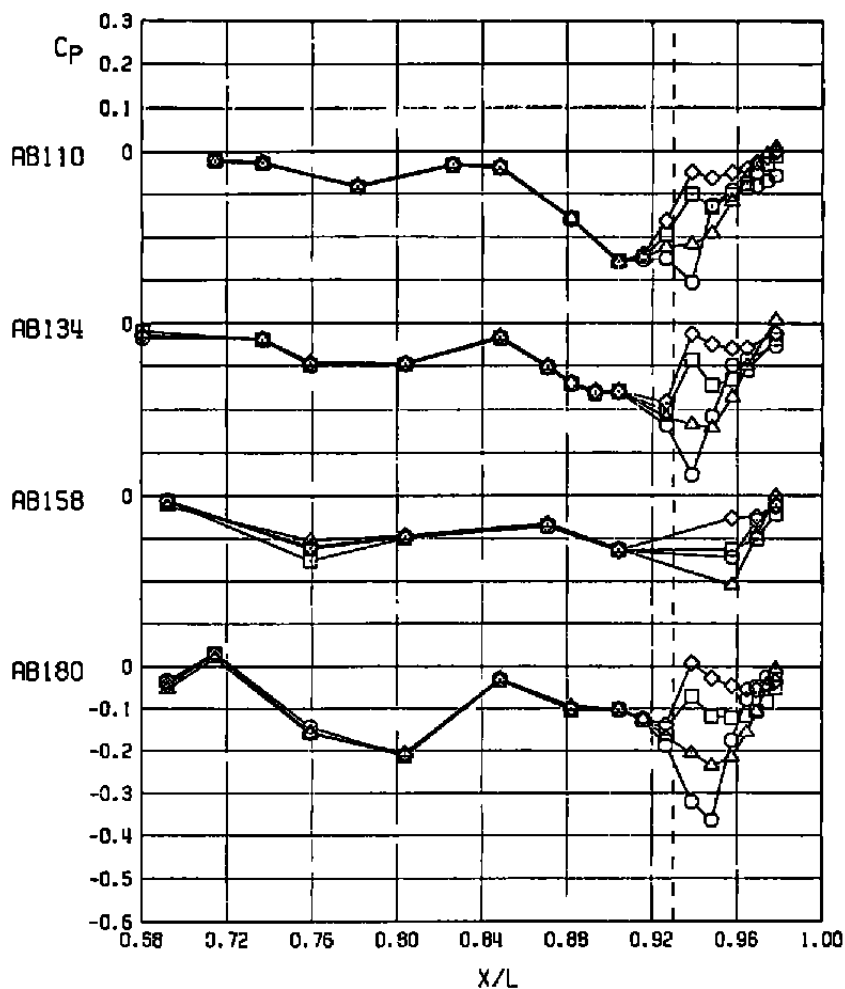
c. Concluded
Figure 19. Continued.

SYM	ALPHA	NPR	NPREFF	DELTA	CONF	M _∞	RNX10 ⁻⁶	CA	PN,PT
○	-0.01	3.18	3.24	-0.01	3C	1.20	2.10	0.01013	693.08
△	-0.01	4.37	4.44	-0.01	31	1.20	2.10	0.00888	759.03
□	-0.00	4.72	4.63	0.02	32	1.20	2.10	0.00740	785.03
◇	-0.00	6.66	6.56	-0.00	33	1.20	2.10	0.00620	735.03



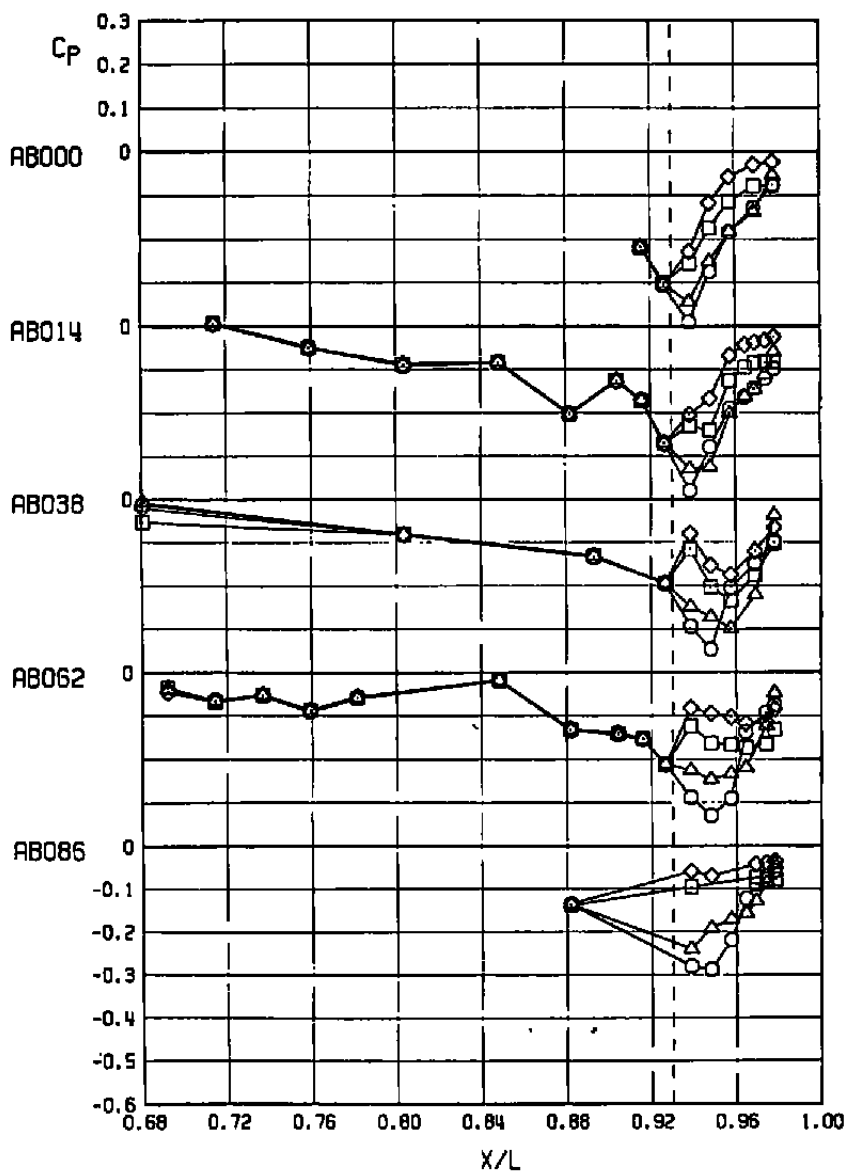
d. $M_\infty = 1.20$
Figure 19. Continued

SYM	ALPHA	NPR	NPREFF	DELTA	CONF	M _∞	ANX10 ⁻⁸	CA	PN,PT
○	-0.01	3.18	3.24	-0.01	30	1.20	2.10	0.01013	693.08
△	-0.01	4.37	4.44	-0.01	31	1.20	2.10	0.00888	759.03
□	-0.00	4.72	4.63	0.02	32	1.20	2.10	0.00740	785.03
◇	-0.00	6.66	6.56	-0.00	33	1.20	2.10	0.00620	735.03



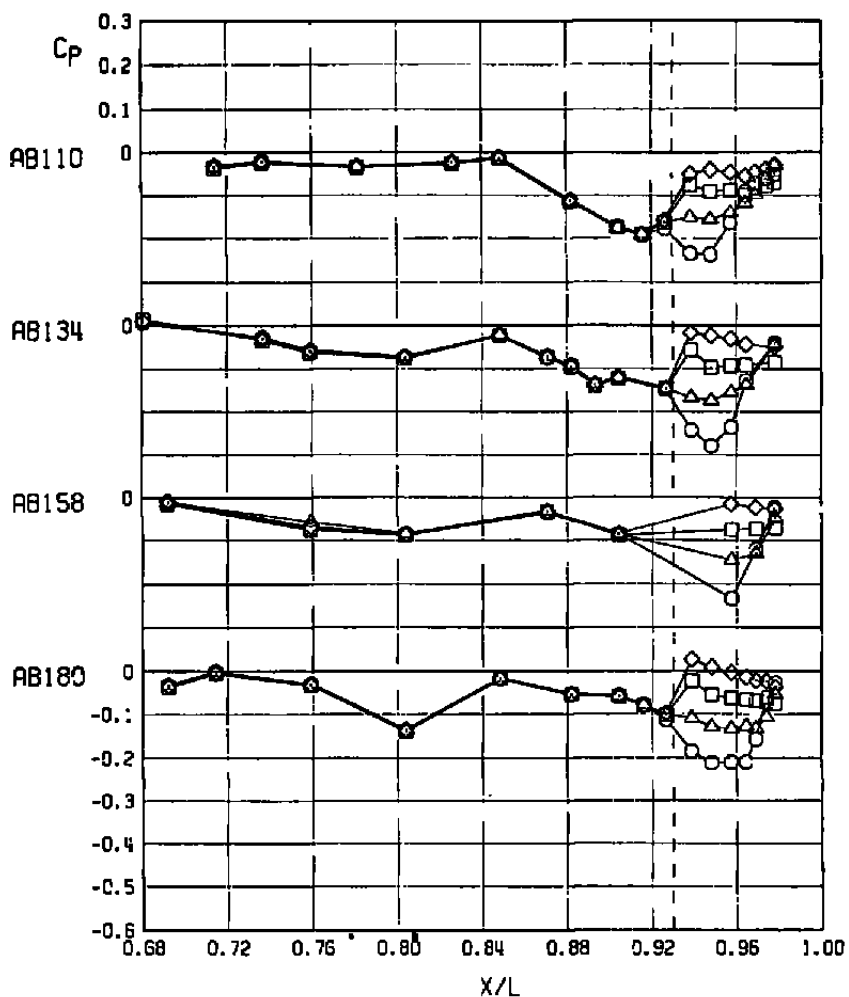
d. Concluded
Figure 19. Continued.

SYM	ALPHA	NPR	NPREF	DELHR	CONF	M _∞	ANX10 ⁻⁸	CA	PN.PT
○	-0.00	3.17	3.23	-0.03	30	1.50	2.10	0.00862	703.08
△	-0.01	4.29	4.41	-0.02	31	1.50	2.10	0.00695	762.03
□	-0.08	4.78	4.66	0.00	32	1.50	2.09	0.00552	788.03
◇	0.00	6.66	6.56	0.00	33	1.50	2.10	0.00459	740.03



e. $M_\infty = 1.50$
Figure 19. Continued.

SYM	ALPHA	NPR	NPREFF	DELTA	CONF	M _L	RNX10 ⁻⁶	CA	PN.PT
○	-0.00	3.17	3.23	-0.03	30	1.50	2.10	0.00862	703.08
△	-0.01	4.29	4.41	-0.02	31	1.50	2.10	0.00695	762.03
□	-0.08	4.78	4.66	0.00	32	1.50	2.09	0.00552	788.03
◇	0.00	6.66	6.56	0.00	33	1.50	2.10	0.00459	740.03



e. Concluded
Figure 19. Concluded.

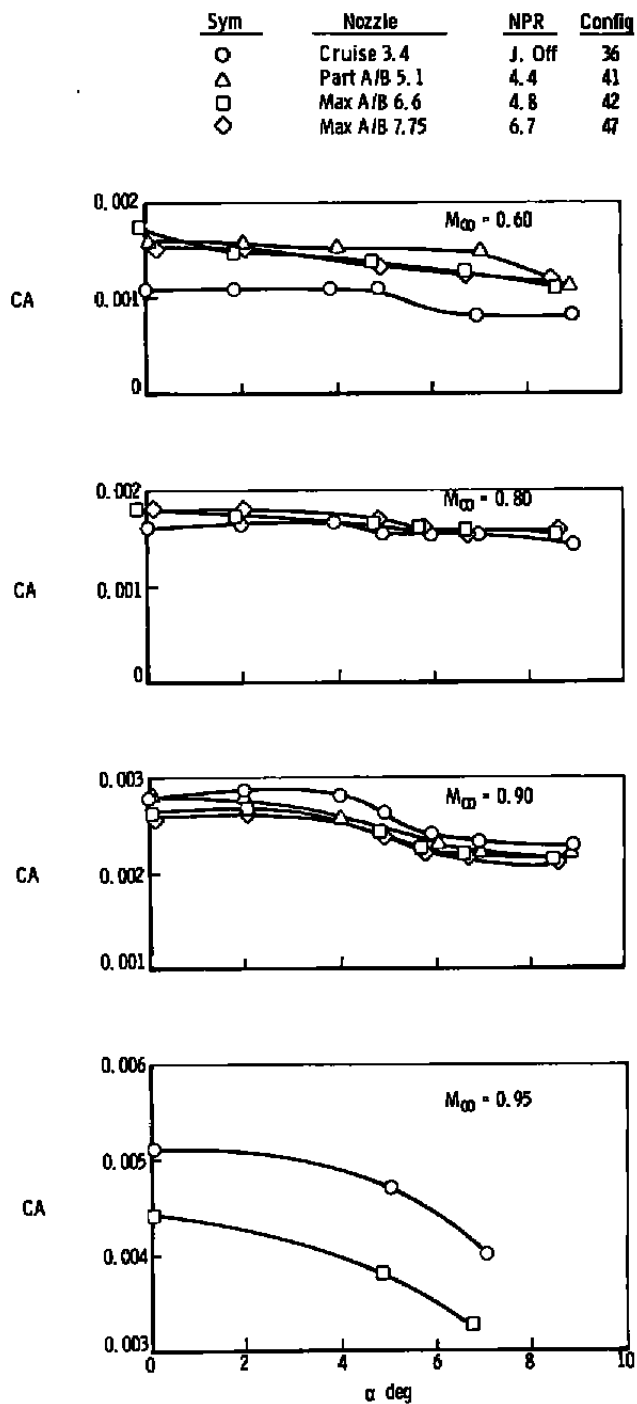


Figure 20. Variation of nozzle-afterbody axial-force coefficient with angle of attack for various nozzle configurations, large sting support system.

Sym	Nozzle	NPR	Config
○	Cruise 3.4	J. Off	36
△	Part A/B 5.1	4.4	41
□	Max A/B 6.6	4.8	42
◇	Max A/B 7.75	6.7	47

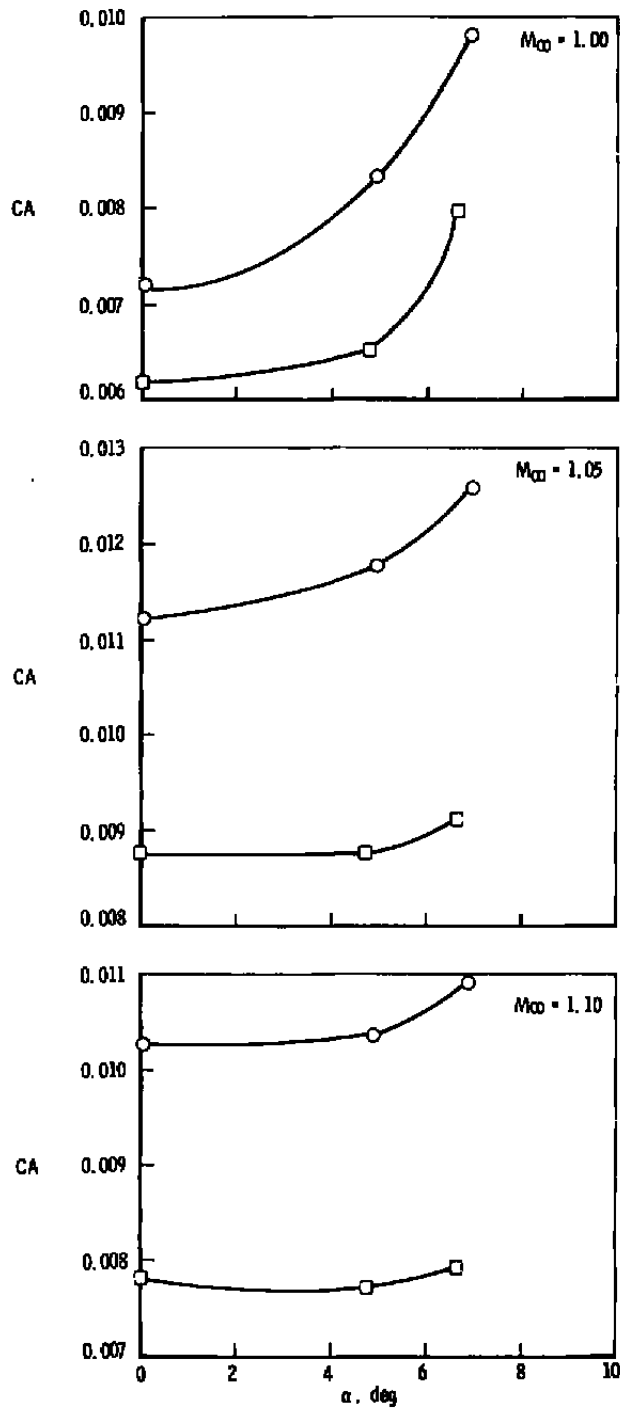


Figure 20. Continued.

Sym	Nozzle	NPR	Config
○	Cruise 3.4	J. Off	36
△	Max A/B 5.1	4.4	41
□	Max A/B 6.6	4.8	42
◇	Max A/B 7.75	6.7	47

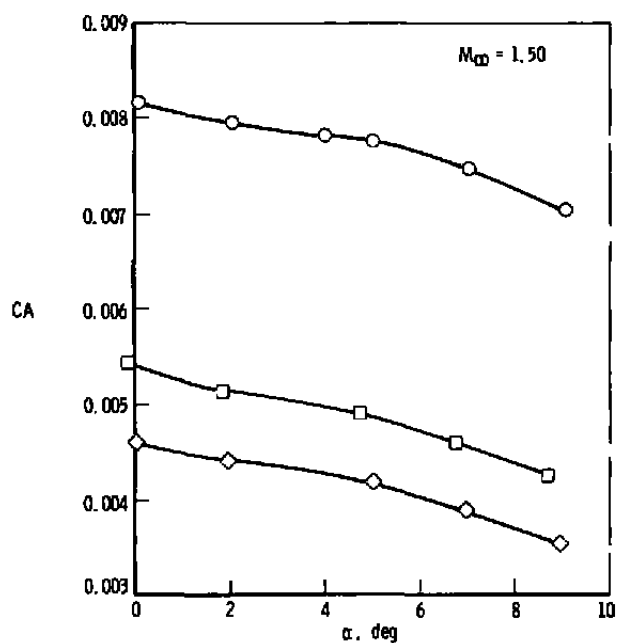
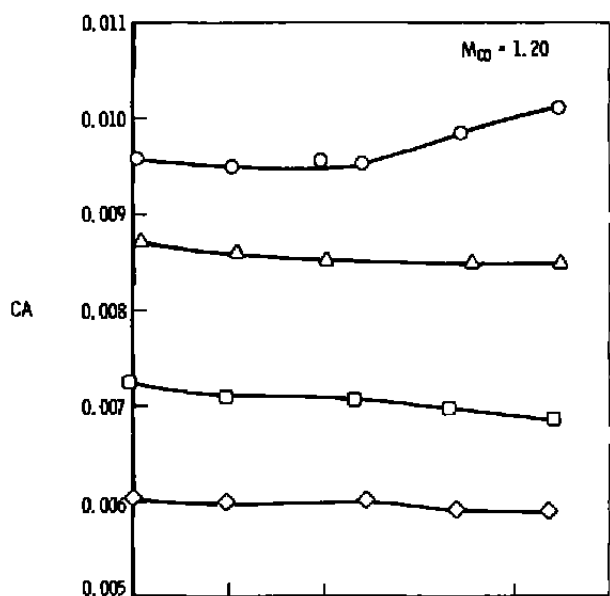


Figure 20. Concluded.

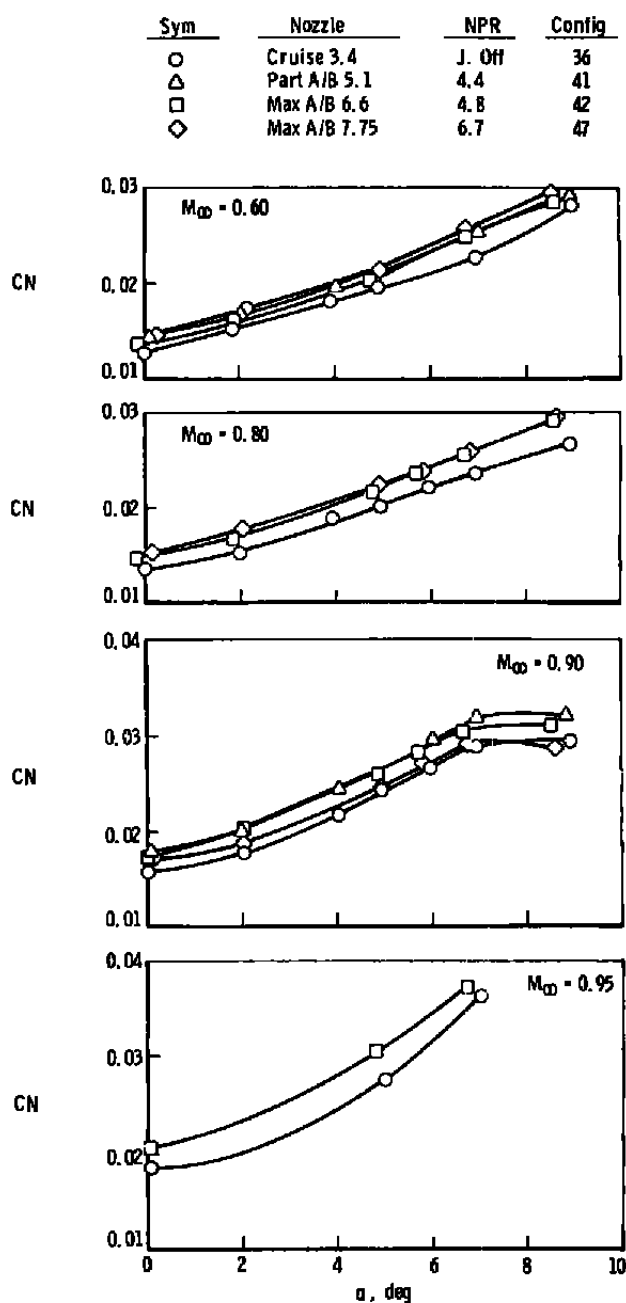


Figure 21. Variation of nozzle-afterbody normal-force coefficient with angle of attack for various nozzle configurations, large sting support system.

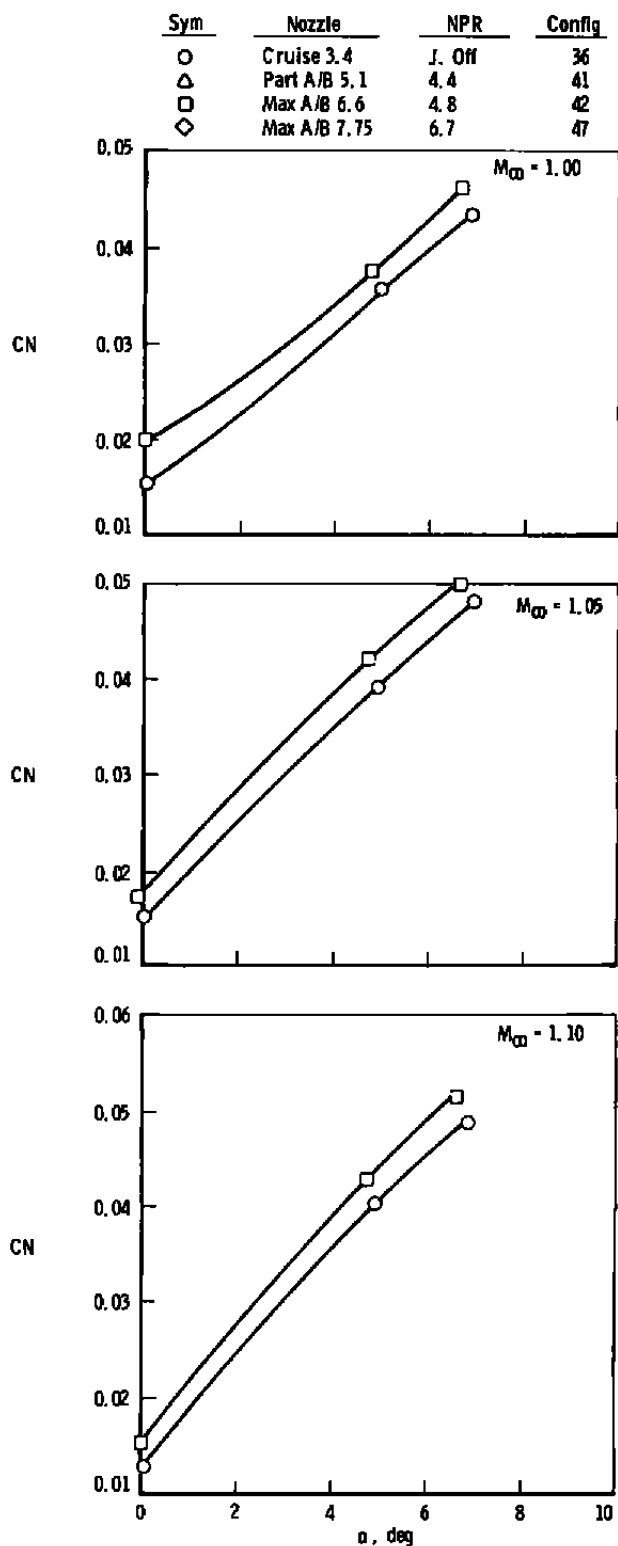


Figure 21. Continued.

Sym	Nozzle	NPR	Config
○	Cruise 3.4	J. Off	36
△	Part A/B 5.1	4.4	41
□	Max A/B 6.6	4.8	42
◇	Max A/B 7.75	6.7	47

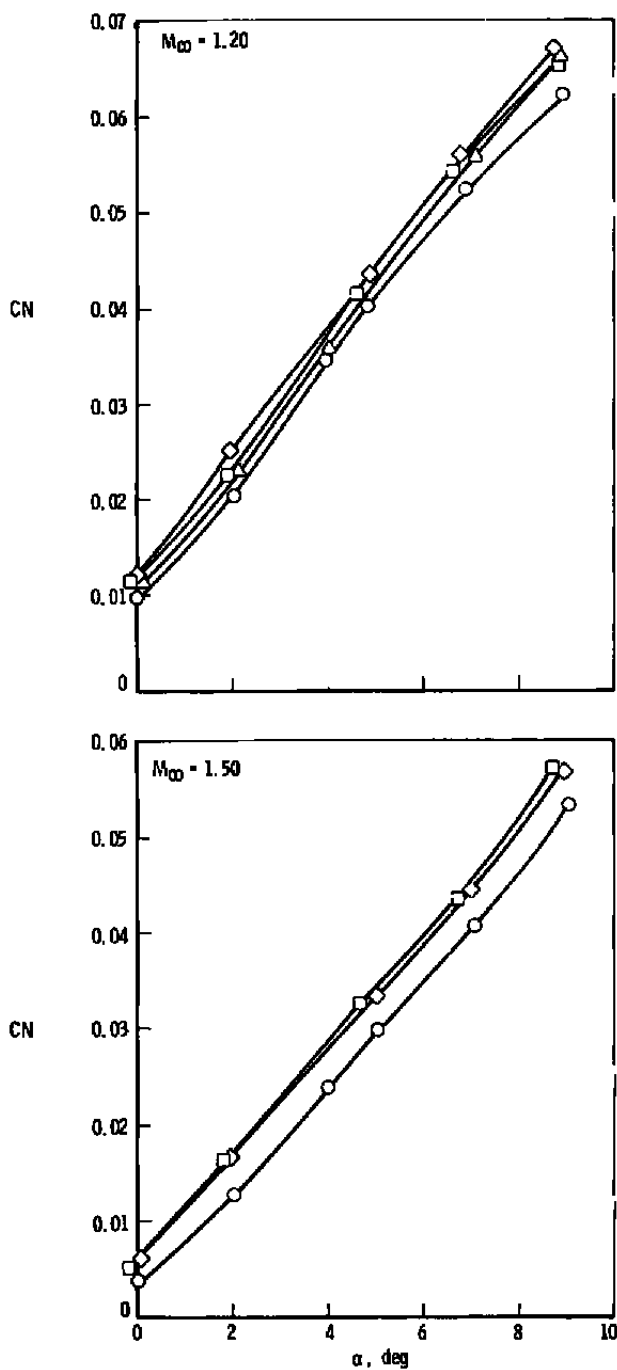
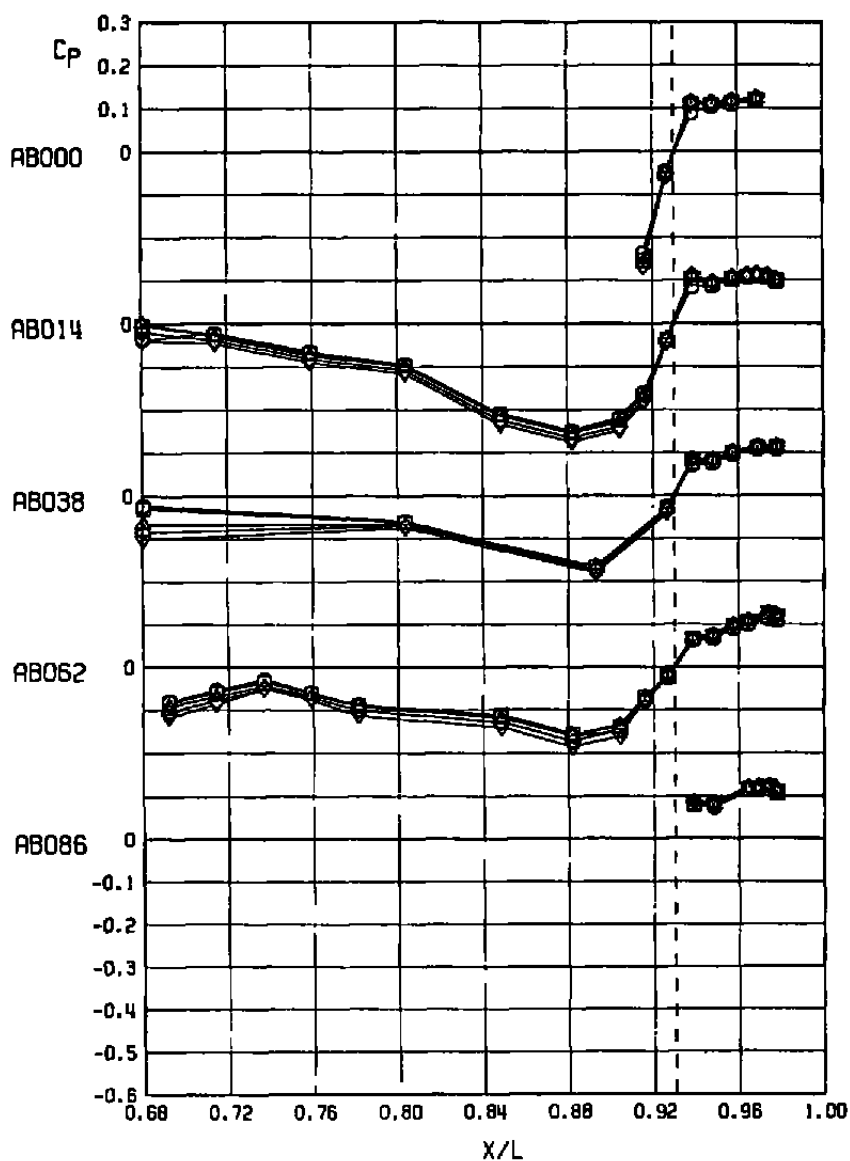


Figure 21. Concluded.

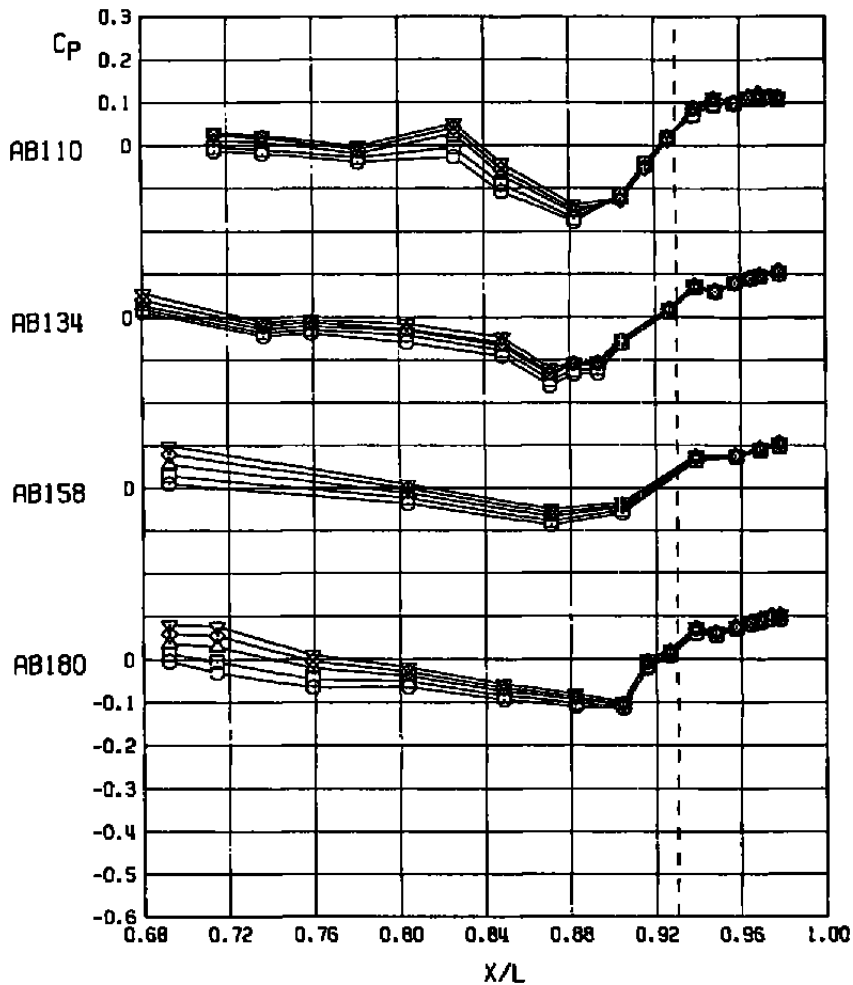
SYM	ALPHA	NPR	NPREFF	DELHR	CONF	M _∞	RNX10 ⁻⁶	CA	PN,PT
○	-0.12	4.80	4.77	0.01	42	0.60	3.40	0.00175	1107.03
□	1.89	4.79	4.77	0.01	42	0.60	3.40	0.00149	1107.06
△	4.78	4.78	4.76	0.01	42	0.60	3.41	0.00139	1107.09
◇	6.75	4.79	4.77	0.01	42	0.60	3.41	0.00129	1107.11
▽	8.67	4.78	4.76	0.01	42	0.60	3.40	0.00120	1107.13



a. $M_{\infty} = 0.60$

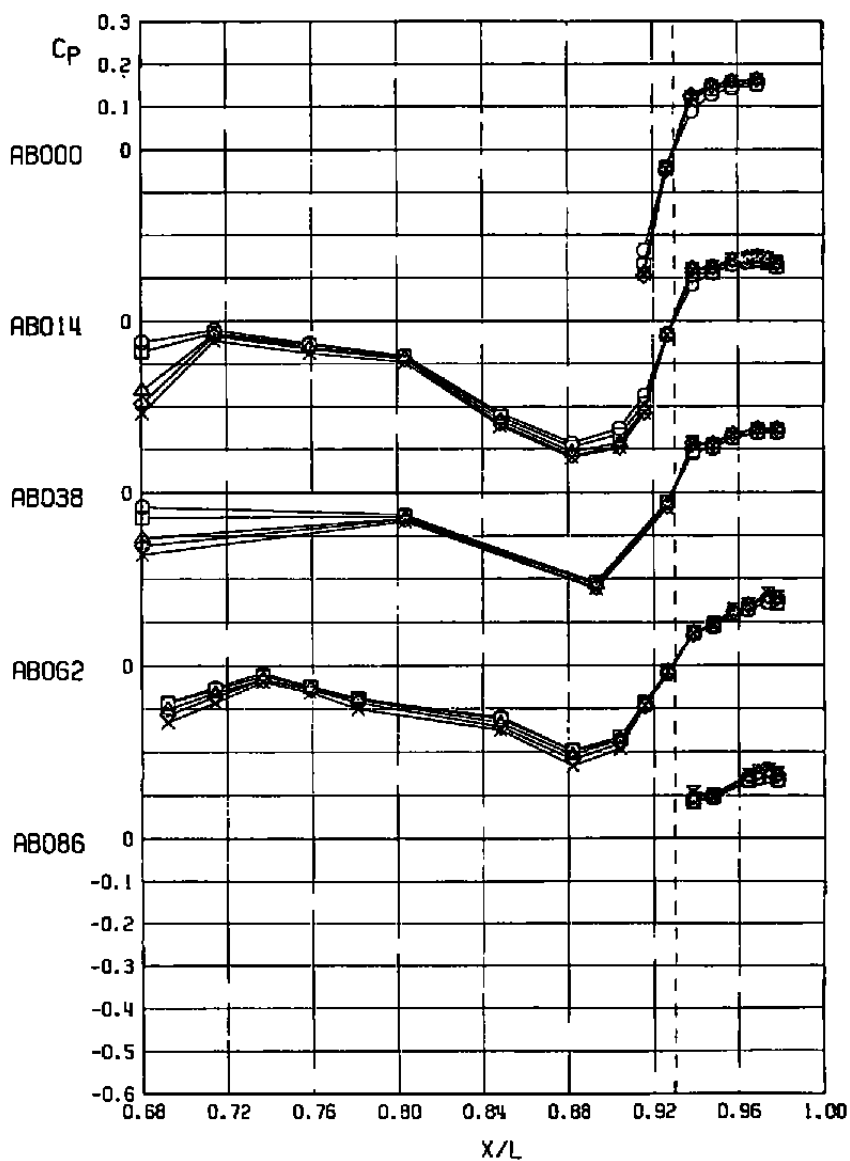
Figure 22. Effect of angle of attack on the nozzle-afterbody static pressure distribution, large sting support system, max A/B 6.6 nozzle, NPR = 4.8.

SYM	ALPHA	NPR	NPREF	DELTA	CONF	M _L	RNX10 ⁻⁶	CA	PN,PT
○	-0.12	4.80	4.77	0.01	42	0.60	3.40	0.00175	1107.03
□	1.89	4.79	4.77	0.01	42	0.60	3.40	0.00149	1107.06
△	4.78	4.78	4.76	0.01	42	0.60	3.41	0.00139	1107.09
◇	6.75	4.79	4.77	0.01	42	0.60	3.41	0.00129	1107.11
▽	8.67	4.78	4.76	0.01	42	0.60	3.40	0.00120	1107.13



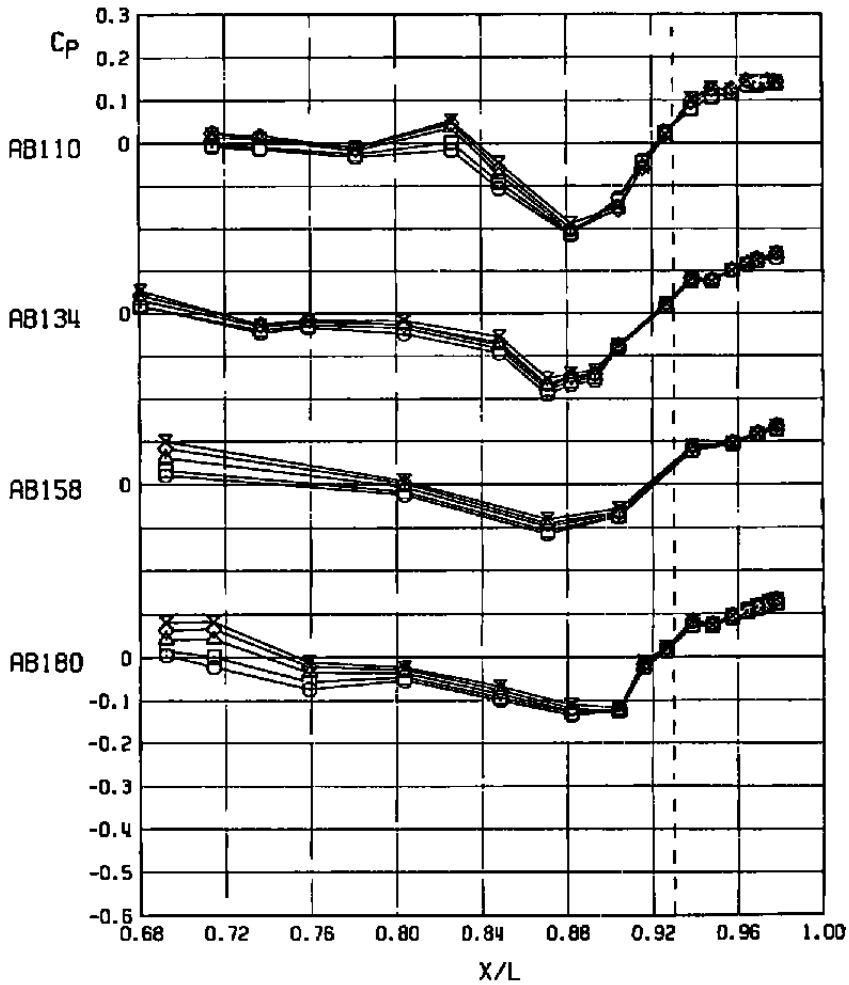
a. Concluded
Figure 22. Continued.

SYM	ALPHA	NPR	NPREFF	DELHR	CONF	M _L	ANX10 ⁻⁶	CA	PN,PT
○	-0.20	4.80	4.77	0.01	42	0.80	3.40	0.00180	1122.03
□	1.88	4.78	4.76	0.01	42	0.80	3.41	0.00172	1122.05
△	4.80	4.80	4.77	0.01	42	0.80	3.39	0.00163	1122.08
◇	6.72	4.80	4.77	0.01	42	0.80	3.40	0.00158	1122.12
x	8.61	4.79	4.77	0.01	42	0.80	3.41	0.00151	1122.15



b. $M_\infty = 0.80$
Figure 22. Continued.

SYM	ALPHA	NPR	NPREFF	DELHR	CONF	M _∞	ANX10 ⁻⁶	CA	PN.PT
○	-0.20	4.80	4.77	0.01	42	0.80	3.40	0.00180	1122.03
□	1.88	4.78	4.76	0.01	42	0.80	3.41	0.00172	1122.05
△	4.80	4.80	4.77	0.01	42	0.80	3.39	0.00163	1122.08
◇	6.72	4.80	4.77	0.01	42	0.80	3.40	0.00158	1122.12
×	8.61	4.79	4.77	0.01	42	0.80	3.41	0.00151	1122.15



b. Concluded
Figure 22. Continued.

SYM	ALPHA	NPR	NPREFF	DELTA	CONF	M _∞	RNX10 ⁻⁸	CA	PN.PT
○	0.06	4.77	4.76	-0.01	42	0.90	3.41	0.00264	1127.03
□	2.07	4.77	4.76	0.00	42	0.90	3.40	0.00268	1127.06
△	4.84	4.77	4.76	0.00	42	0.90	3.40	0.00242	1127.09
◇	6.65	4.75	4.75	-0.00	42	0.90	3.40	0.00218	1127.13
x	8.51	4.79	4.77	-0.00	42	0.90	3.40	0.00214	1127.16

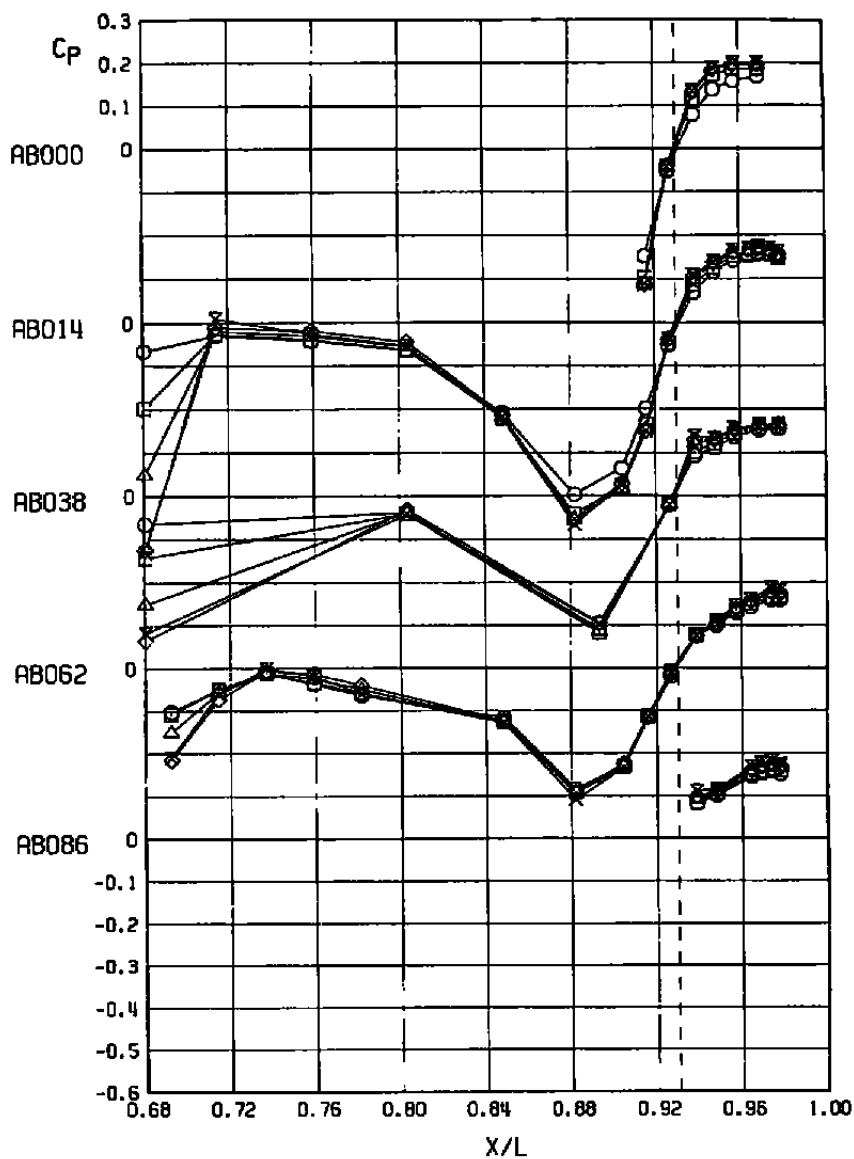
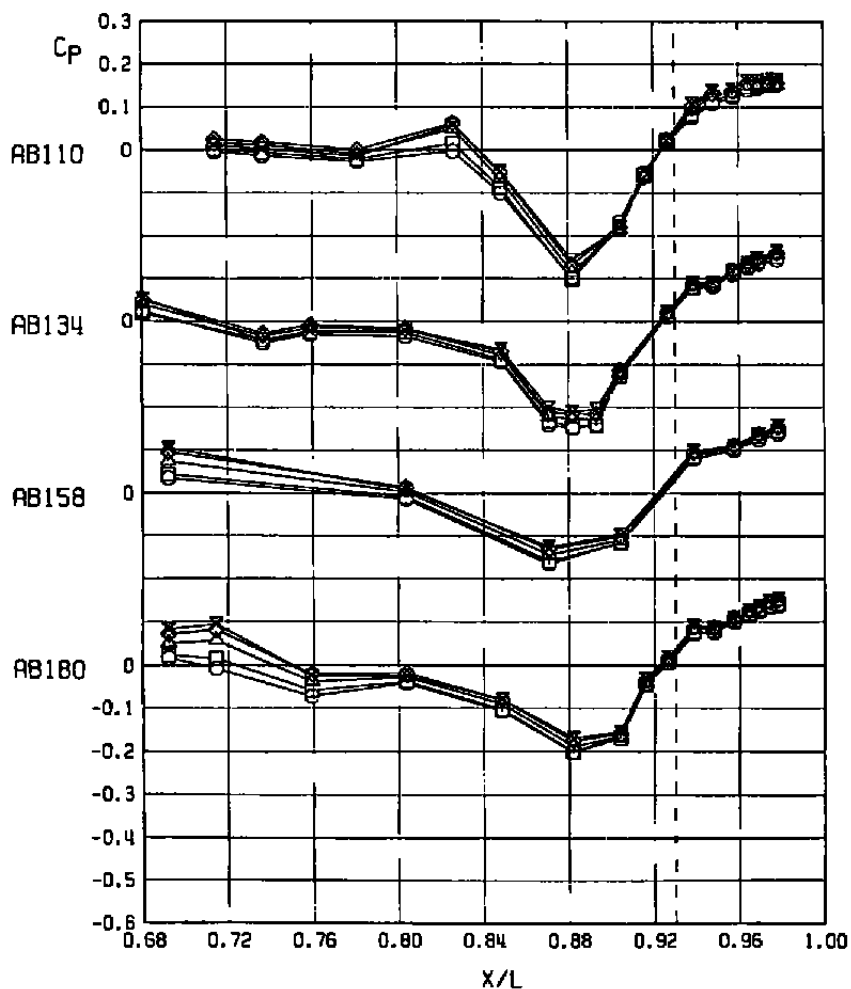
c. $M_\infty = 0.90$

Figure 22. Continued.

SYM	ALPHA	NPR	NPREF	DELHR	CONF	M _∞	ANX10 ⁻⁶	CA	PN,PT
○	0.06	4.77	4.76	-0.01	42	0.90	3.41	0.00264	1127.03
□	2.07	4.77	4.76	0.00	42	0.90	3.40	0.00268	1127.06
△	4.84	4.77	4.76	0.00	42	0.90	3.40	0.00242	1127.09
◇	6.65	4.75	4.75	-0.00	42	0.90	3.40	0.00218	1127.13
×	8.51	4.79	4.77	-0.00	42	0.90	3.40	0.00214	1127.16



c. Concluded
Figure 22. Continued.

SYM	ALPHA	NPR	NPREF	DELTA	CONF	M _∞	ANX10 ⁻⁶	CA	PN,PT
○	0.02	4.82	4.78	-0.06	42	0.95	3.40	0.00442	1074.03
△	4.82	4.81	4.78	-0.06	42	0.95	3.40	0.00380	1074.06
◇	6.75	4.81	4.78	-0.06	42	0.95	3.38	0.00322	1074.08

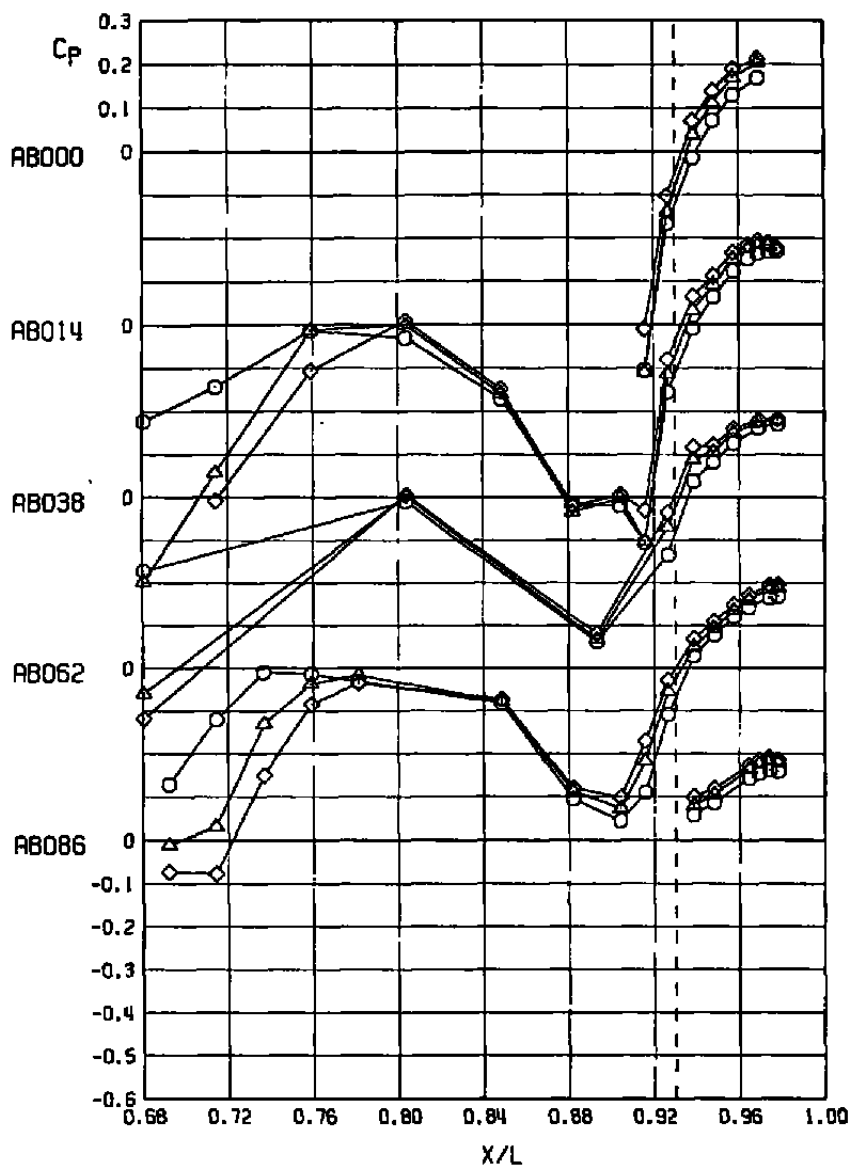
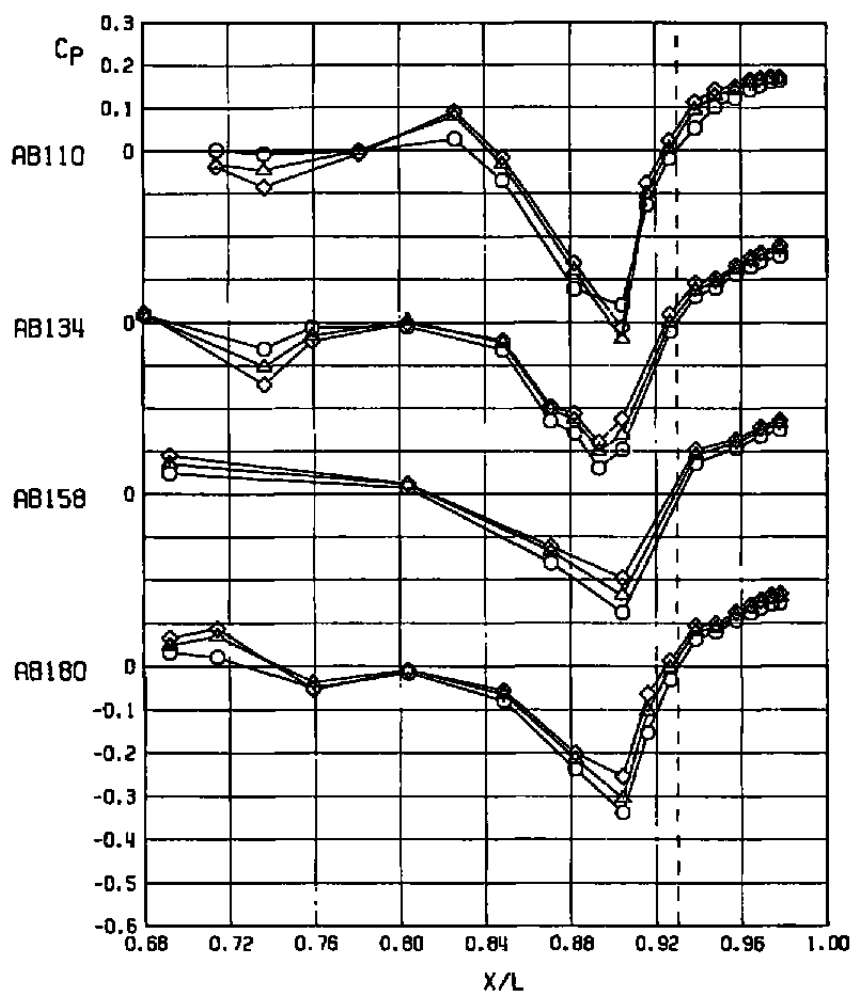
d. $M_\infty = 0.95$

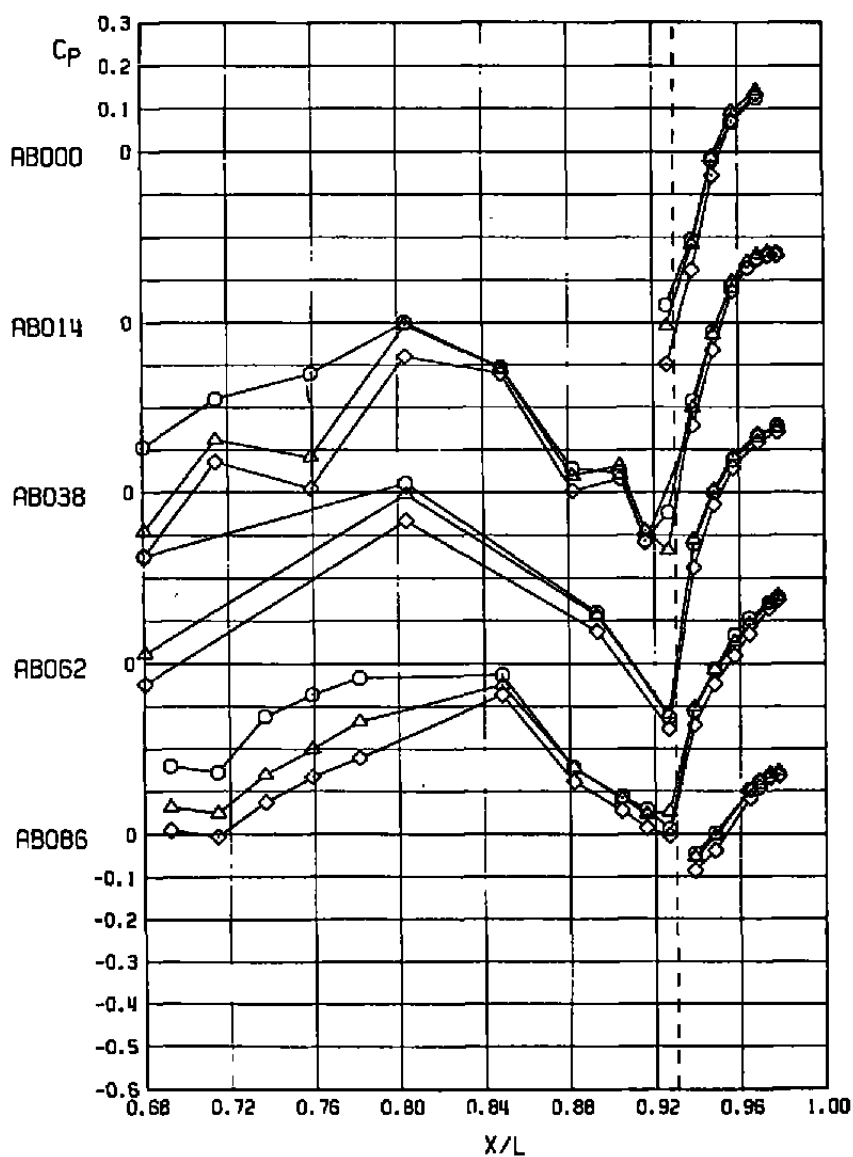
Figure 22. Continued.

SYM	ALPHA	NPR	NPREFF	DELTA	CONF	M _∞	ANX10 ⁻⁶	CA	PN.PT
⊙	0.02	4.82	4.78	-0.06	42	0.95	3.40	0.00442	1074.03
△	4.82	4.81	4.78	-0.06	42	0.95	3.40	0.00380	1074.06
◇	6.75	4.81	4.78	-0.06	42	0.95	3.38	0.00322	1074.08



d. Concluded
Figure 22. Continued.

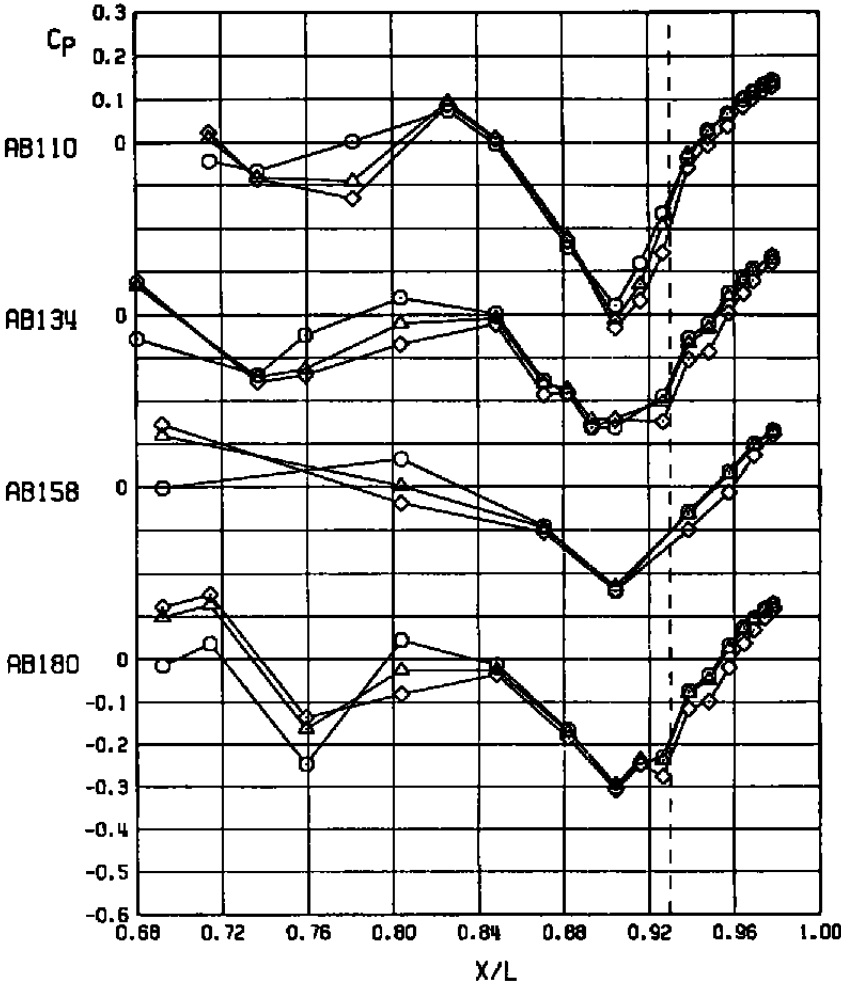
SYM	ALPHA	NPR	NPREF	DELHR	CONF	M _∞	RNX10 ⁻⁵	CA	PN,PT
○	0.02	4.82	4.78	-0.06	42	1.00	3.38	0.00618	1073.10
△	4.81	4.77	4.76	-0.06	42	1.00	3.41	0.00649	1073.06
◇	6.66	4.80	4.77	-0.06	42	1.00	3.39	0.00796	1073.09



a. $M_\infty = 1.00$

Figure 22. Continued.

SYM	ALPHA	NPR	NPREFF	DELHR	CONF	N _u	ANX10 ⁻⁶	CA	PN.PT
○	0.02	4.82	4.78	-0.06	42	1.00	3.38	0.00618	1073.10
△	4.81	4.77	4.76	-0.06	42	1.00	3.41	0.00649	1073.06
◇	6.66	4.80	4.77	-0.06	42	1.00	3.39	0.00796	1073.09



e. Concluded
Figure 22. Continued.

SYM	ALPHA	NPR	NPREF	DELHR	CONF	M _∞	RNX10 ⁻⁶	CA	PN.PT
○	-0.01	4.71	4.73	-0.06	42	1.05	3.39	0.00875	1072.03
△	4.77	4.70	4.72	-0.06	42	1.05	3.40	0.00873	1072.05
◇	6.63	4.69	4.72	-0.06	42	1.05	3.41	0.00910	1072.08

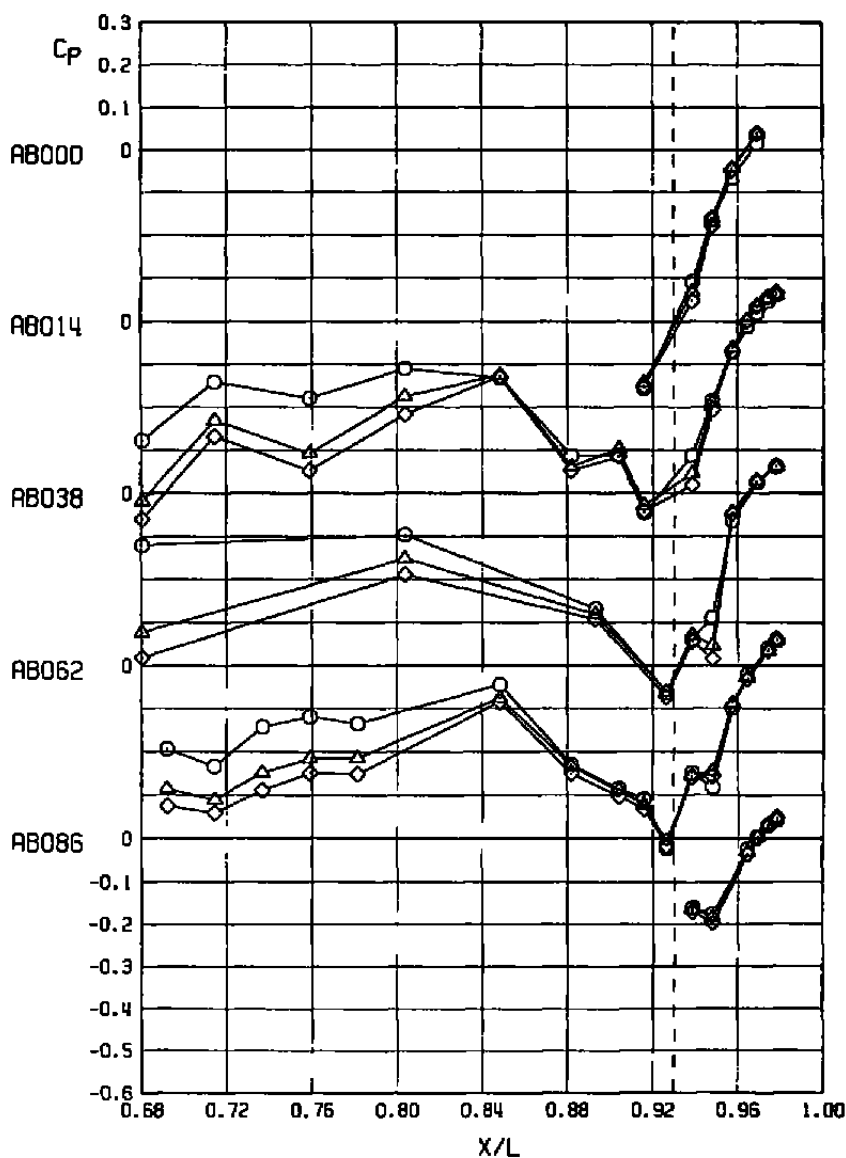
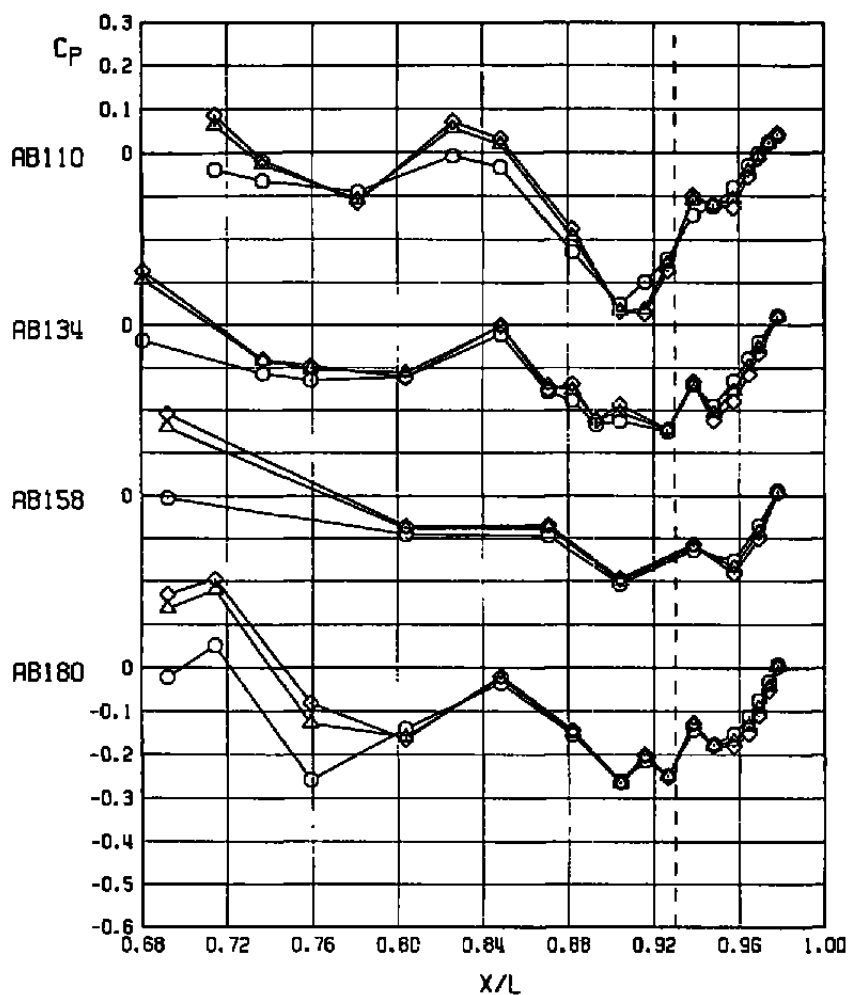
f. $M_\infty = 1.05$

Figure 22. Continued.

SYM	ALPHA	NPR	NPREF	DELTA	CONF	M _∞	ANX10 ⁻⁶	CA	PN,PT
○	-0.01	4.71	4.73	-0.06	42	1.05	3.39	0.00875	1072.03
△	4.77	4.70	4.72	-0.06	42	1.05	3.40	0.00873	1072.05
◇	6.63	4.69	4.72	-0.06	42	1.05	3.41	0.00910	1072.08



f. Concluded
Figure 22. Continued.

SYM	ALPHA	NPA	NPREF	DELTA	CONF	M _∞	RNX10 ⁻⁸	CA	PN.PT
○	0.01	4.73	4.74	-0.06	42	1.10	3.42	0.00781	1071.03
△	4.76	4.77	4.76	-0.06	42	1.10	3.40	0.00770	1071.06
◇	6.63	4.74	4.74	-0.06	42	1.10	3.41	0.00790	1071.09

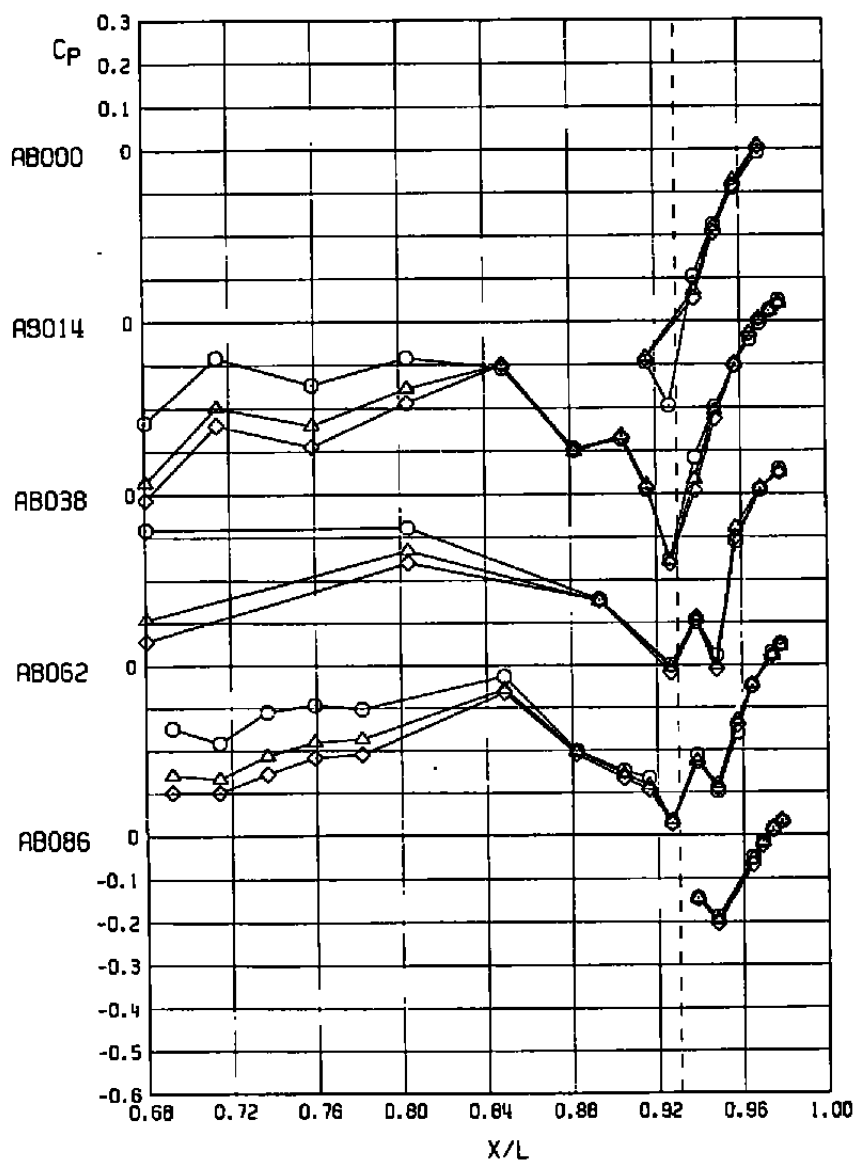
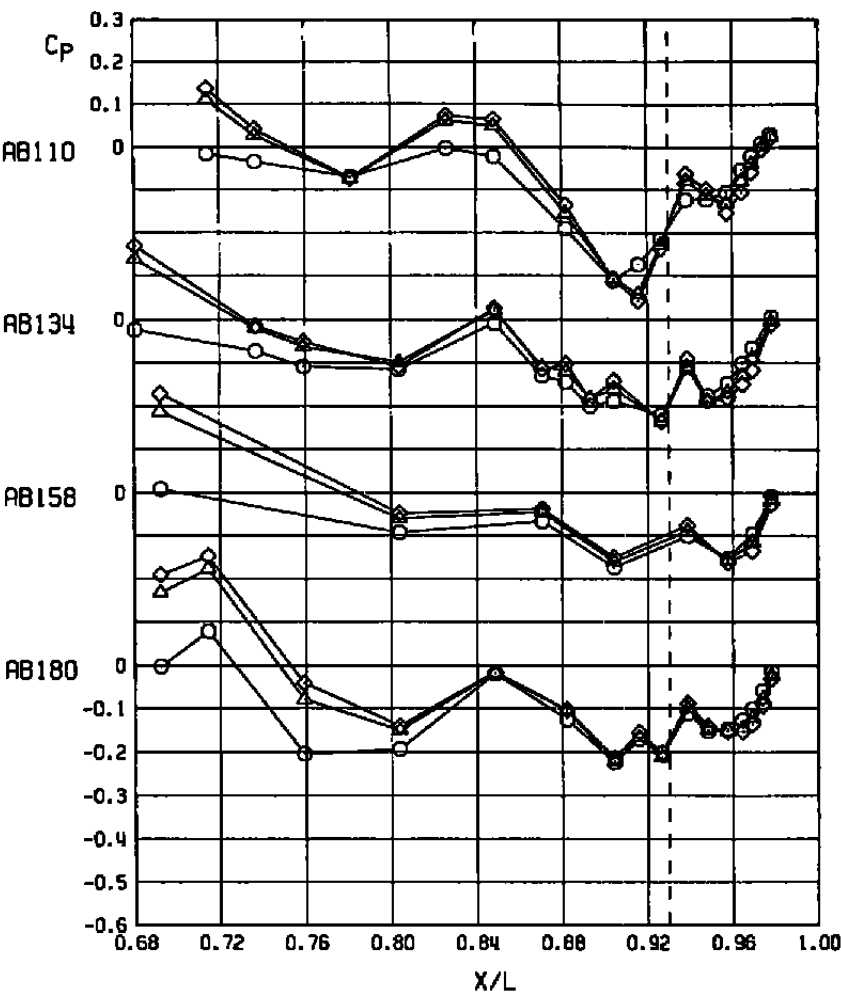
g. $M_\infty = 1.10$

Figure 22. Continued.

SYM	ALPHA	NPR	NPREF	DELHR	CONF	M _∞	RNX10 ⁻⁸	CA	PN.PT
⊙	0.01	4.73	4.74	-0.06	42	1.10	3.42	0.00781	1071.03
△	4.76	4.77	4.76	-0.06	42	1.10	3.40	0.00770	1071.06
◇	6.63	4.74	4.74	-0.06	42	1.10	3.41	0.00790	1071.09



g. Concluded.
Figure 22. Continued.

SYM	ALPHA	NPR	NPREFF	DELTA	CONF	M _∞	RNX10 ⁻⁶	CA	PN.PT
○	-0.10	4.79	4.77	-0.14	42	1.20	3.41	0.00724	1051.03
□	1.96	4.83	4.79	-0.15	42	1.20	3.40	0.00706	1051.07
△	4.67	4.79	4.77	-0.15	42	1.20	3.41	0.00707	1051.10
◇	6.62	4.81	4.78	-0.15	42	1.20	3.40	0.00695	1051.12
▽	8.51	4.80	4.77	-0.15	42	1.20	3.41	0.00686	1051.14

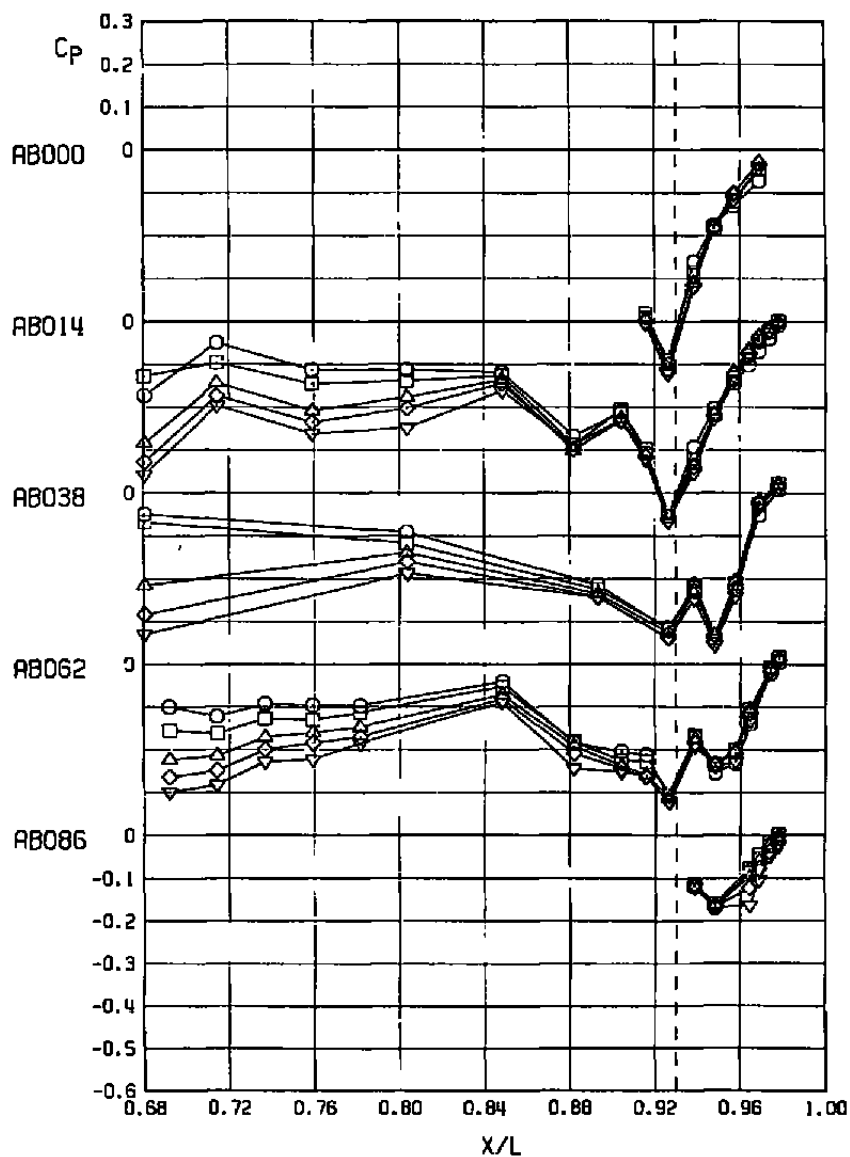
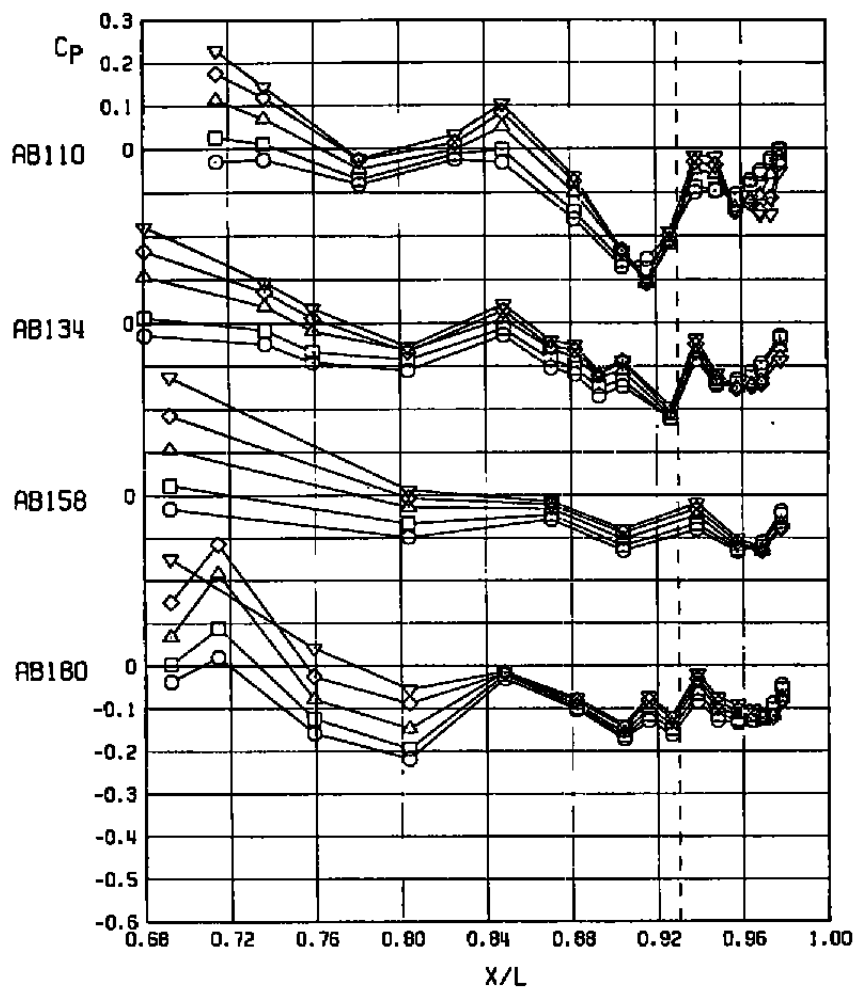
h. $M_\infty = 1.20$

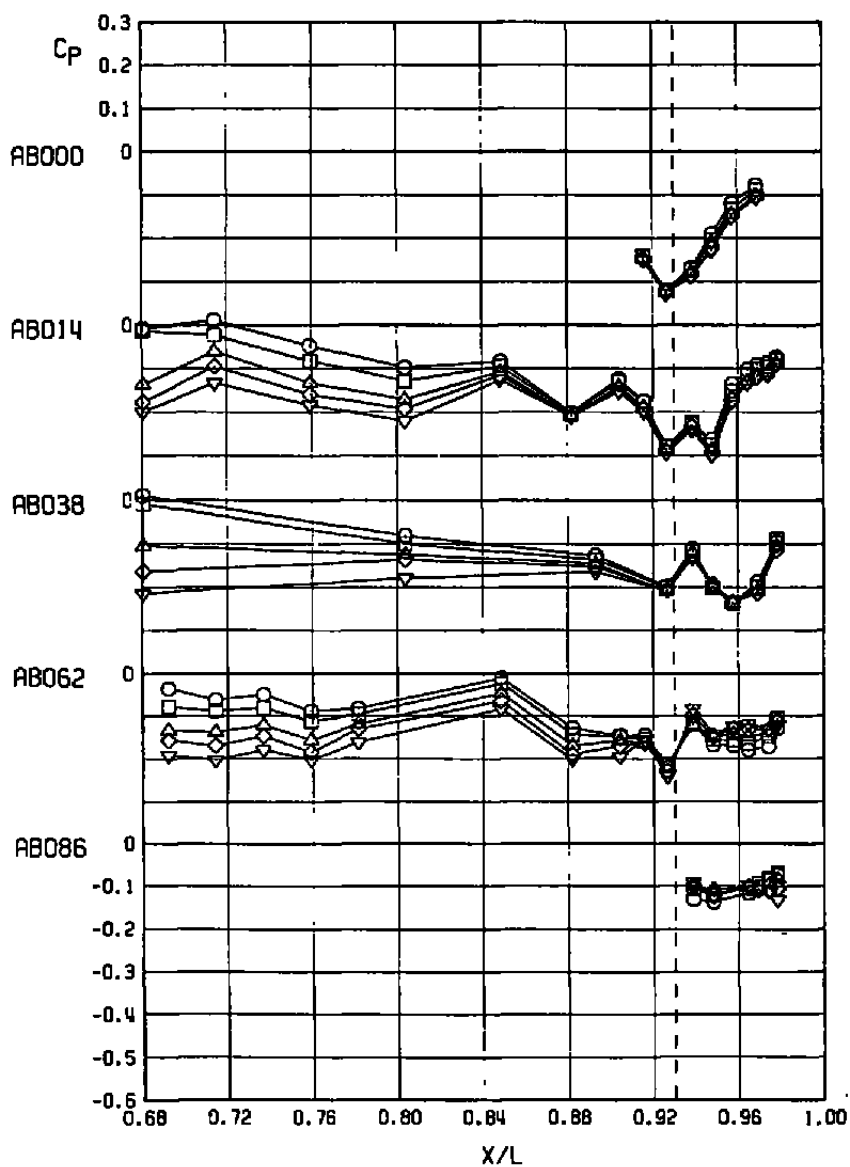
Figure 22. Continued.

SYM	ALPHA	NPR	NPREFF	DELTA	CONF	M _∞	ANX10 ⁻⁶	CA	PN.PT
○	-0.10	4.79	4.77	-0.14	42	1.20	3.41	0.00724	1051.03
□	1.96	4.83	4.79	-0.15	42	1.20	3.40	0.00706	1051.07
△	4.67	4.79	4.77	-0.15	42	1.20	3.41	0.00707	1051.10
◇	6.62	4.81	4.78	-0.15	42	1.20	3.40	0.00695	1051.12
▽	8.51	4.80	4.77	-0.15	42	1.20	3.41	0.00686	1051.14



h. Concluded
Figure 22. Continued.

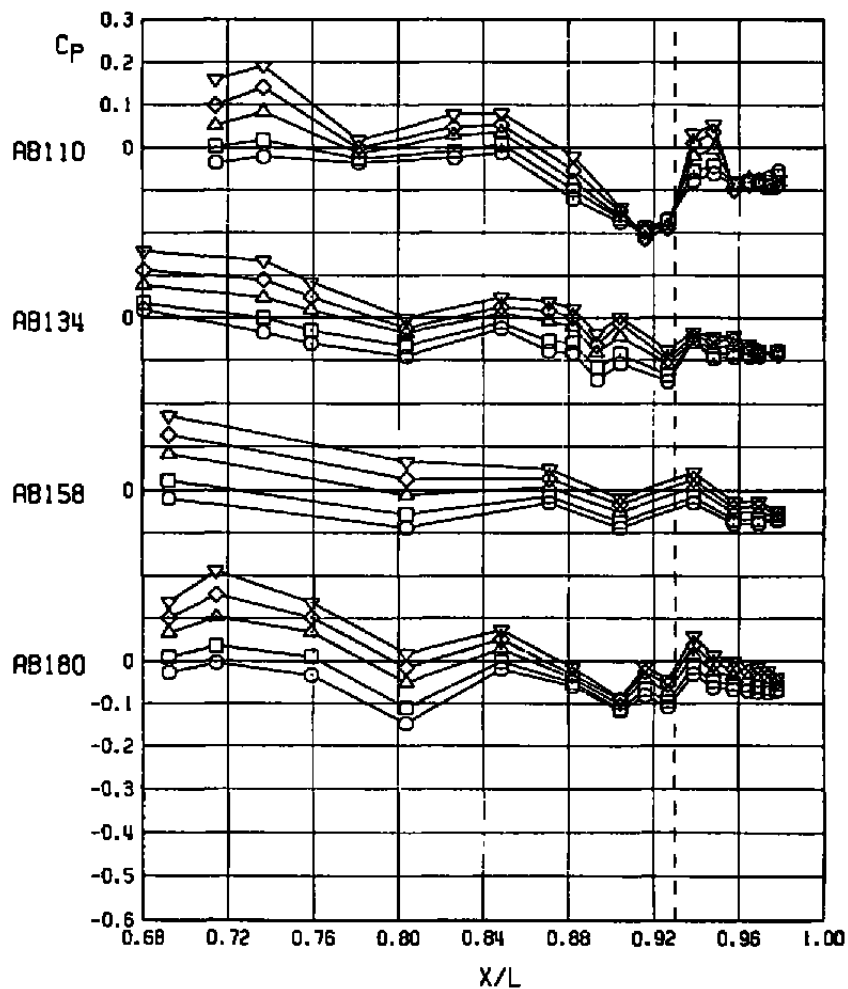
SYM	ALPHA	NPR	NPREFF	DELTA	CONF	M _∞	ANX10 ⁻⁵	CA	PN.PT
○	-0.14	4.83	4.79	-0.00	42	1.50	3.39	0.00543	1047.03
□	1.83	4.84	4.79	-0.00	42	1.50	3.40	0.00513	1047.05
△	4.71	4.82	4.78	-0.07	42	1.50	3.40	0.00491	1047.07
◇	6.75	4.80	4.77	-0.11	42	1.50	3.40	0.00460	1047.09
▽	8.70	4.82	4.78	-0.15	42	1.50	3.40	0.00425	1047.11



i. $M_{\infty} = 1.50$

Figure 22. Continued.

SYM	ALPHA	NPR	NPREFF	DELTA	CONF	M _∞	ANX10 ⁻⁸	CA	PN.PT
○	-0.14	4.83	4.79	-0.00	42	1.50	3.99	0.00543	1047.03
□	1.83	4.84	4.79	-0.00	42	1.50	3.40	0.00513	1047.05
△	4.71	4.82	4.78	-0.07	42	1.50	3.40	0.00491	1047.07
◇	6.75	4.80	4.77	-0.11	42	1.50	3.40	0.00460	1047.09
▽	8.70	4.82	4.78	-0.15	42	1.50	3.40	0.00425	1047.11



i. Concluded
Figure 22. Concluded.

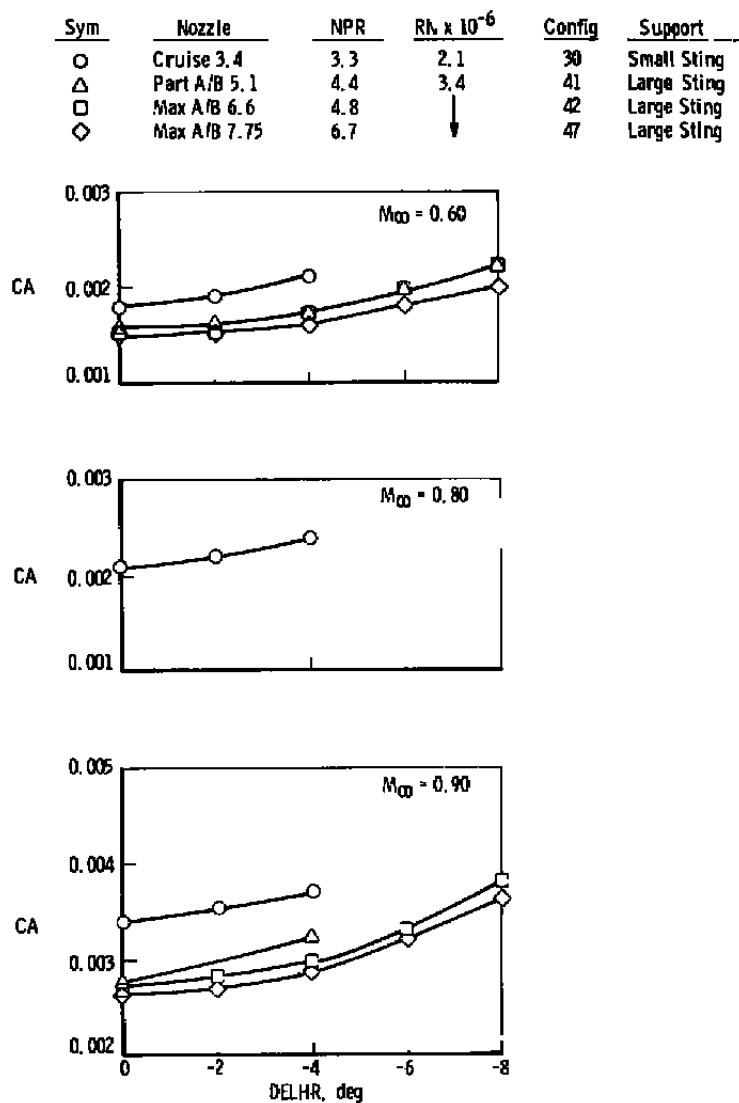


Figure 23. Effect of horizontal tail deflection on the nozzle-afterbody axial-force coefficients for various nozzle configurations, $\alpha = 0$.

Sym	Nozzle	NPR	RN x 10 ⁻⁶	Config	Support
○	Cruise 3.4	3.3	2.1	30	Small Sting
△	Part A/B 5.1	4.4	3.4	41	Large Sting
□	Max A/B 6.6	4.8		42	Large Sting
◇	Max A/B 7.75	6.7	↓	47	Large Sting

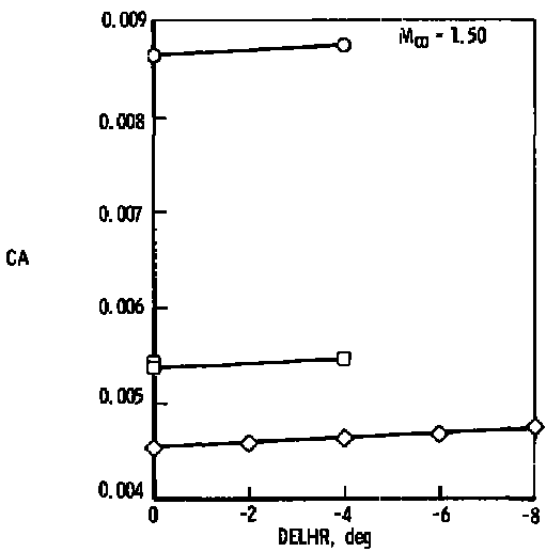
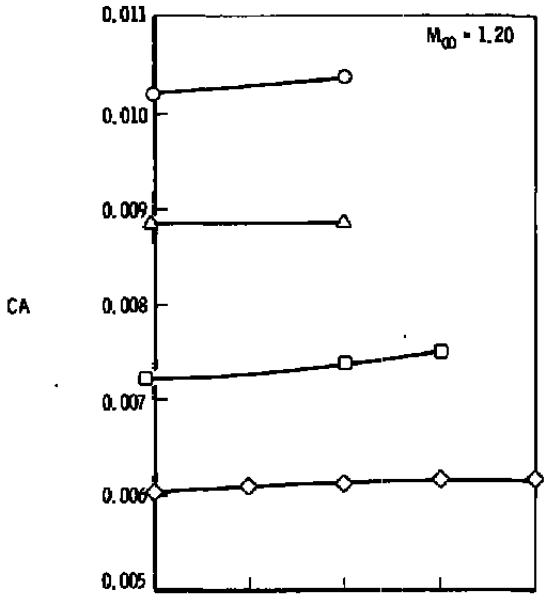


Figure 23. Concluded.

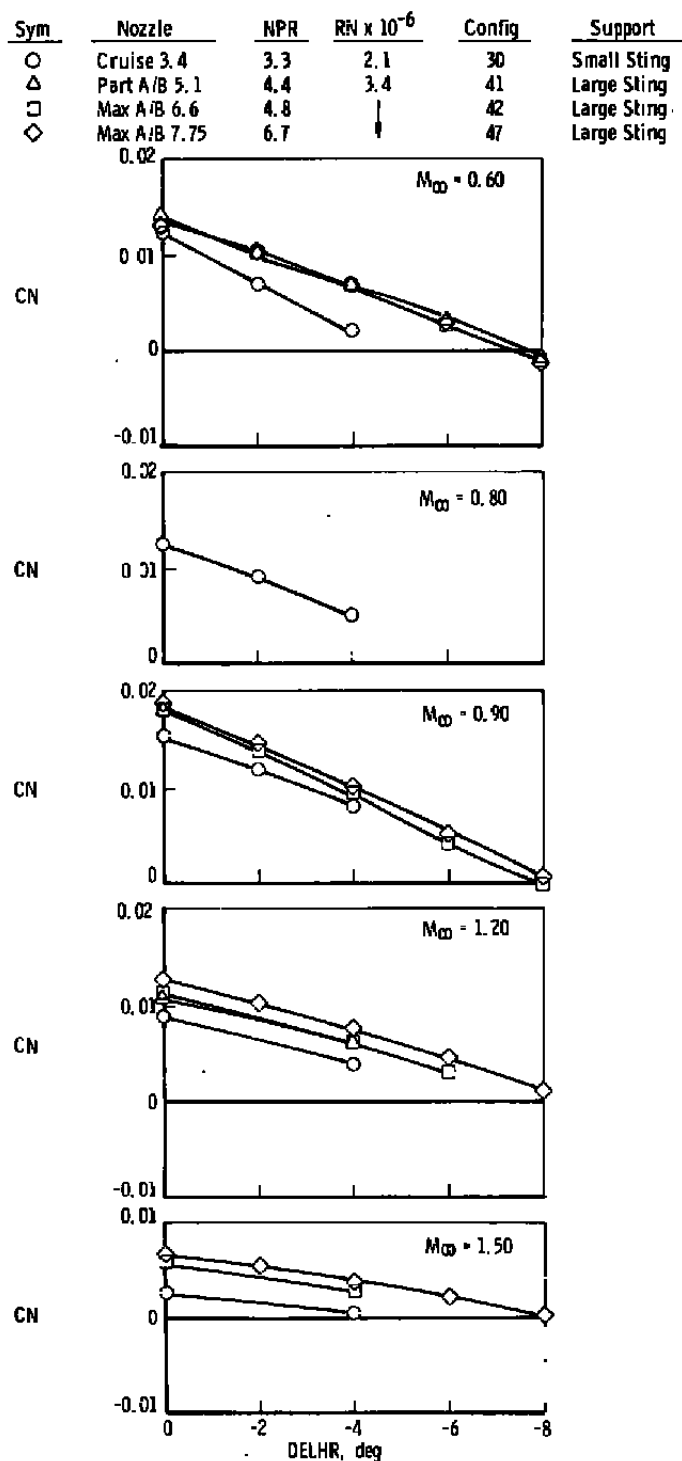
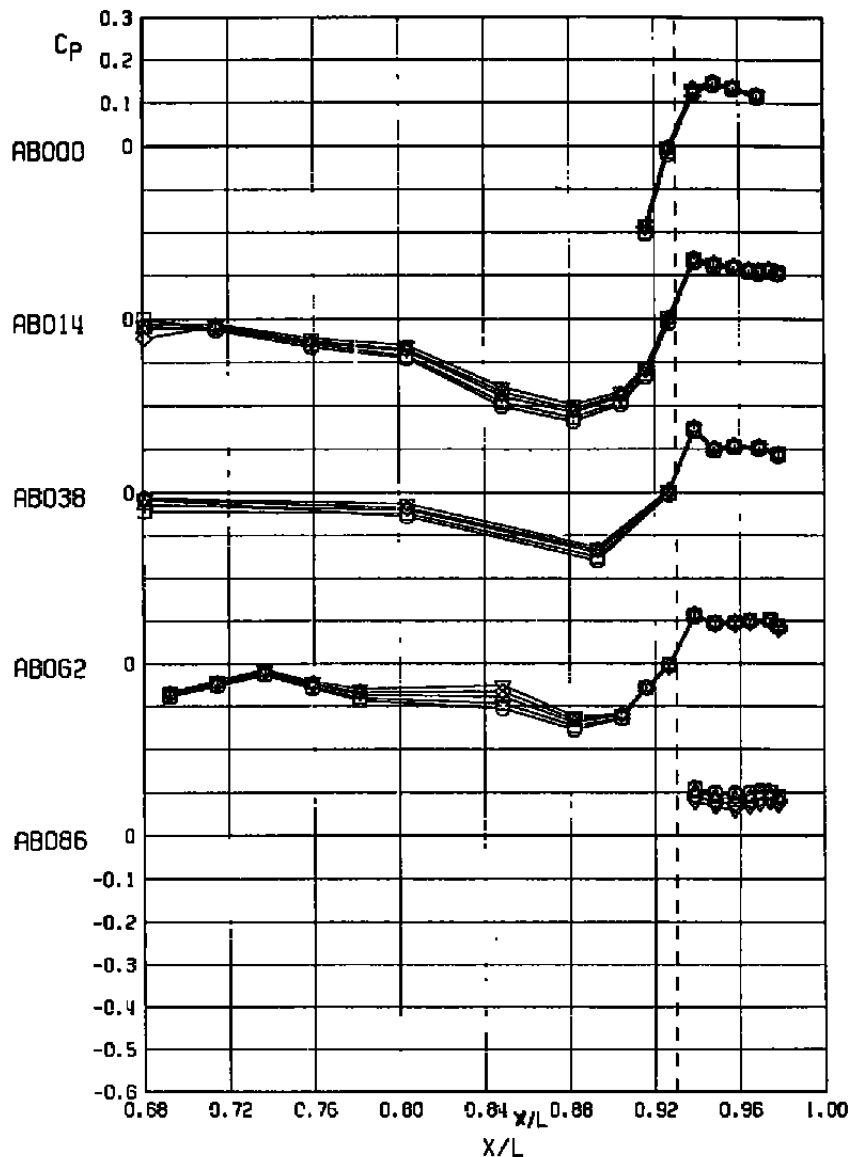


Figure 24. Effect of horizontal tail deflection on the nozzle-afterbody normal-force coefficients for various nozzle configurations, $\alpha = 0$.

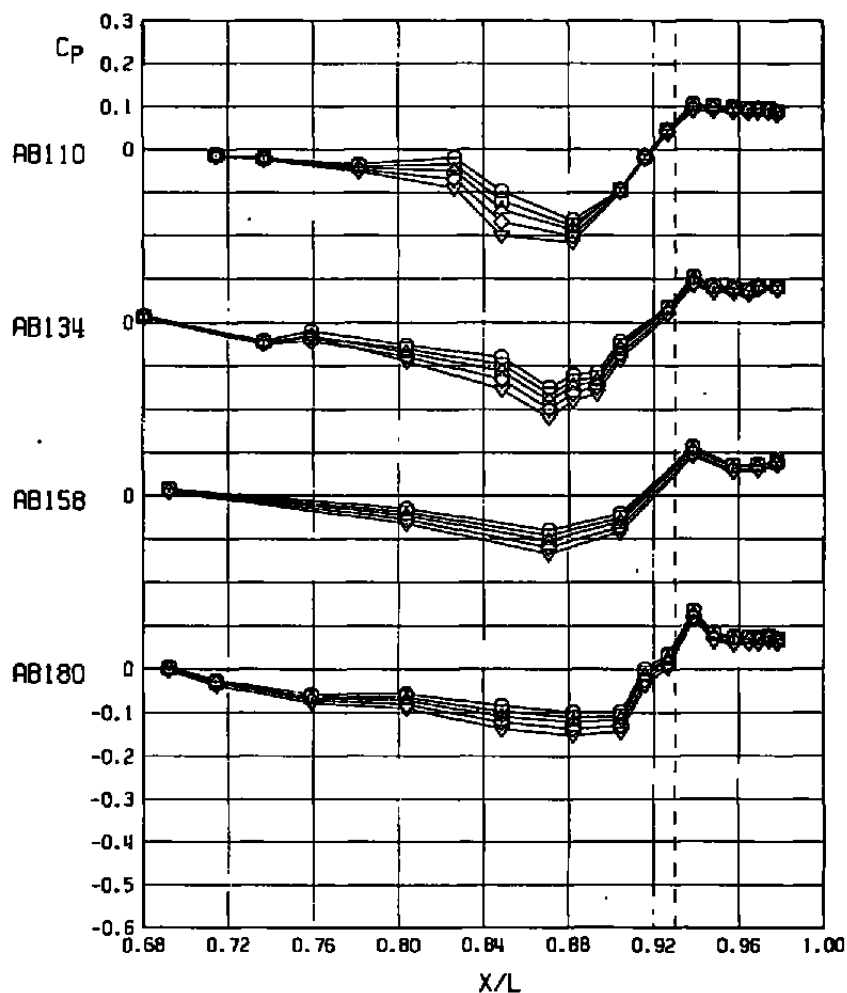
SYM	ALPHA	NPR	NPREFF	DELHA	CONF	M _∞	RNX10 ⁻⁶	CA	PN.PT
○	0.05	6.73	6.55	0.03	47	0.60	3.41	0.00148	839.01
□	0.04	6.75	6.67	-2.00	47	0.60	3.40	0.00154	839.02
△	0.03	6.76	6.67	-4.00	47	0.60	3.40	0.00160	839.03
◇	0.24	6.80	6.69	-6.00	47	0.60	3.40	0.00181	839.04
▽	0.13	6.75	6.65	-8.00	47	0.60	3.40	0.00203	839.05



a. $M_{\infty} = 0.60$

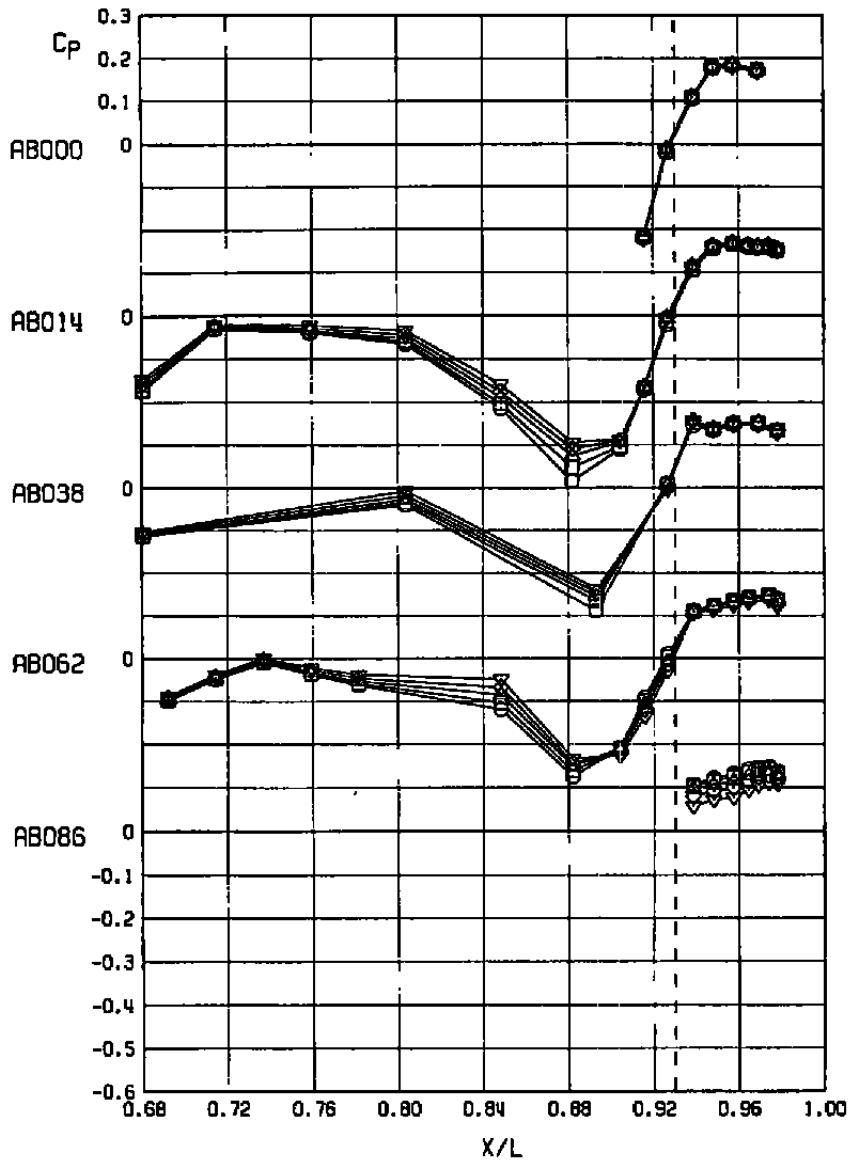
Figure 25. Influence of horizontal tail deflection on the nozzle-afterbody pressure distributions, large sting support system, max A/B 7.75 nozzle, NPR = 6.8, $\alpha = 0$.

SYM	ALPHA	NPR	NPREFF	DELHR	CONF	M _∞	RNX10 ⁻⁶	CA	PN.PT
○	0.05	6.73	6.65	0.03	47	0.60	3.41	0.00148	839.01
□	0.04	6.75	6.67	-2.00	47	0.60	3.40	0.00154	839.02
△	0.03	6.76	6.67	-4.00	47	0.60	3.40	0.00160	839.03
◇	0.24	6.80	6.69	-6.00	47	0.60	3.40	0.00181	839.04
▽	0.13	6.75	6.66	-8.00	47	0.60	3.40	0.00203	839.05



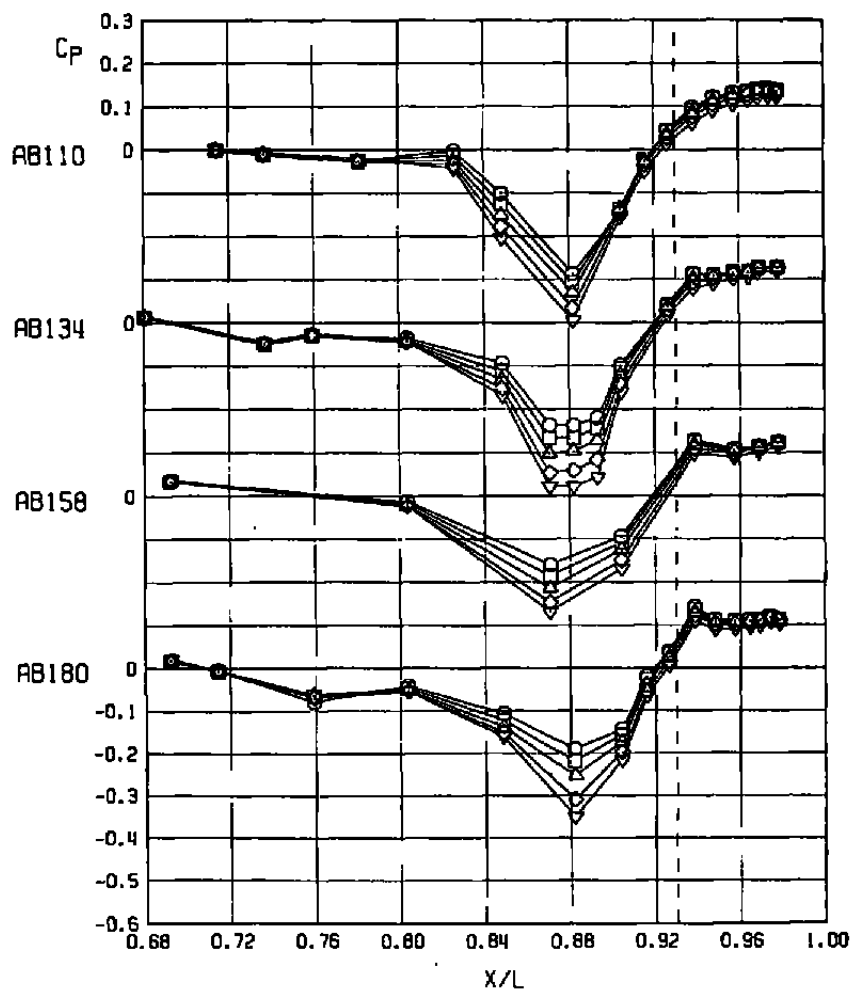
a. Concluded
Figure 25. Continued.

SYM	ALPHA	NPR	NPREF	DELTA	CONF	M _∞	RNX10 ⁻⁶	CA	PN.PT
○	0.17	6.77	6.68	0.01	47	0.90	3.39	0.00265	863.01
□	0.17	6.75	6.67	-2.04	47	0.90	3.39	0.00270	863.02
△	0.13	6.74	6.66	-3.99	47	0.90	3.39	0.00287	863.03
◇	0.09	6.74	6.66	-5.98	47	0.90	3.40	0.00321	863.04
▽	0.07	6.74	6.66	-8.01	47	0.90	3.40	0.00363	863.05



b. $M_\infty = 0.90$
Figure 25. Continued.

SYM	ALPHA	NPR	NPREF	DELTA	CONF	M _L	PNX10 ⁻⁶	CA	PN,PT
○	0.17	6.77	6.68	0.01	47	0.90	3.39	0.00265	863.01
□	0.17	6.75	6.67	-2.04	47	0.90	3.39	0.00270	863.02
△	0.13	6.74	6.66	-3.99	47	0.90	3.39	0.00287	863.03
◇	0.09	6.74	6.66	-5.98	47	0.90	3.40	0.00321	863.04
▽	0.07	6.74	6.56	-8.01	47	0.90	3.40	0.00363	863.05



b. Concluded
Figure 25. Continued.

SYM	ALPHA	NPR	NPREFF	DELHR	CONF	M _∞	ReX10 ⁻⁶	CA	PN.PT
○	0.07	6.71	6.54	0.02	47	1.20	3.41	0.00604	885.01
□	0.06	6.73	6.66	-1.96	47	1.20	3.40	0.00610	885.02
△	0.04	5.72	6.65	-3.97	47	1.20	3.40	0.00614	885.03
◇	0.02	6.74	6.66	-5.98	47	1.20	3.40	0.00617	885.04
▽	-0.05	5.72	6.65	-7.94	47	1.20	3.40	0.00619	885.05

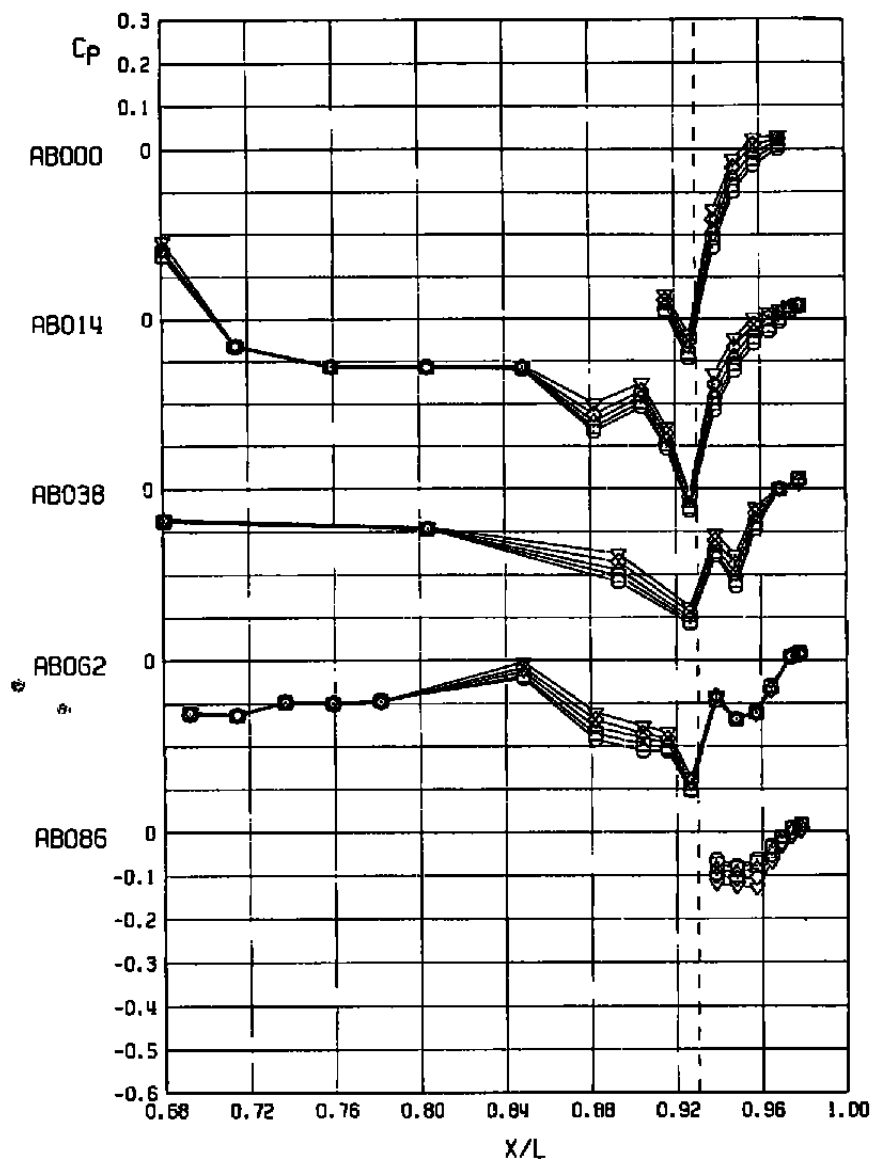
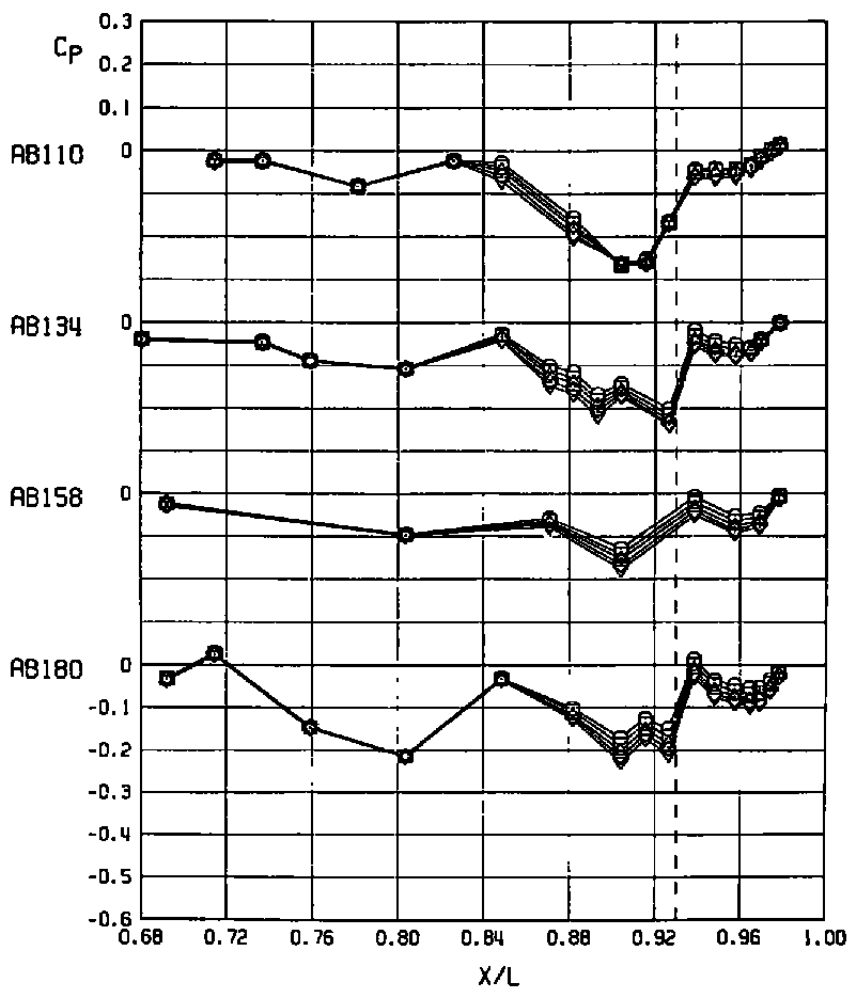
c. $M_\infty = 1.20$

Figure 25. Continued.

SYM	ALPHA	NPR	NPREF	DELTA	CONF	M _L	RNX10 ⁻⁵	CA	PN.PT
○	0.07	6.71	6.64	0.02	47	1.20	3.41	0.00604	885.01
□	0.06	6.73	6.66	-1.96	47	1.20	3.40	0.00610	885.02
△	0.04	6.72	6.65	-3.97	47	1.20	3.40	0.00614	885.03
◇	0.02	6.74	6.66	-5.98	47	1.20	3.40	0.00617	885.04
▽	-0.05	6.72	6.65	-7.94	47	1.20	3.40	0.00619	885.05



c. Concluded
Figure 25. Continued.

SYM	ALPHA	NPR	NPREF	DELHR	CCNF	M _∞	ANX10 ⁻⁵	CA	PN.PT
○	0.15	6.79	6.68	-0.02	47	1.50	3.38	0.00455	905.01
□	0.13	6.78	6.68	-2.04	47	1.50	3.38	0.00459	905.02
△	0.04	6.78	6.68	-3.96	47	1.50	3.39	0.00464	905.03
◇	0.03	6.75	6.66	-5.98	47	1.50	3.40	0.00469	905.04
▽	-0.09	6.77	6.67	-7.95	47	1.50	3.39	0.00477	905.05

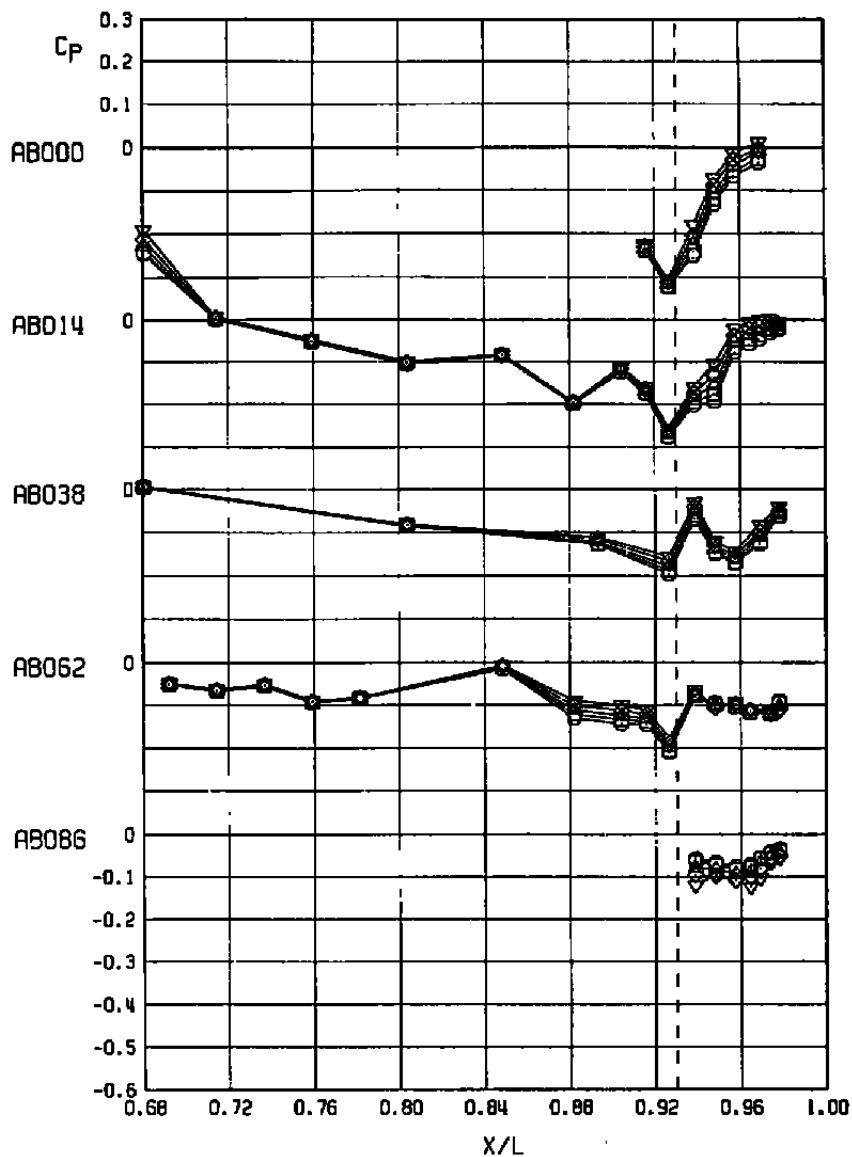
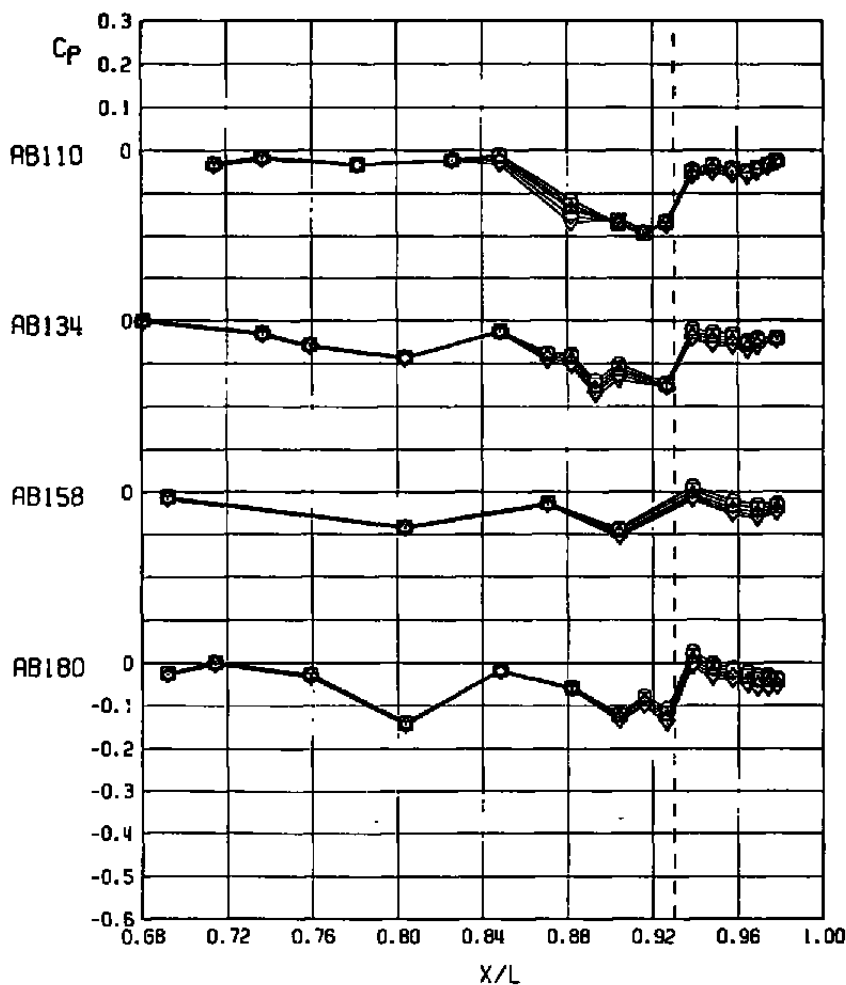
d. $M_{\infty} = 1.50$

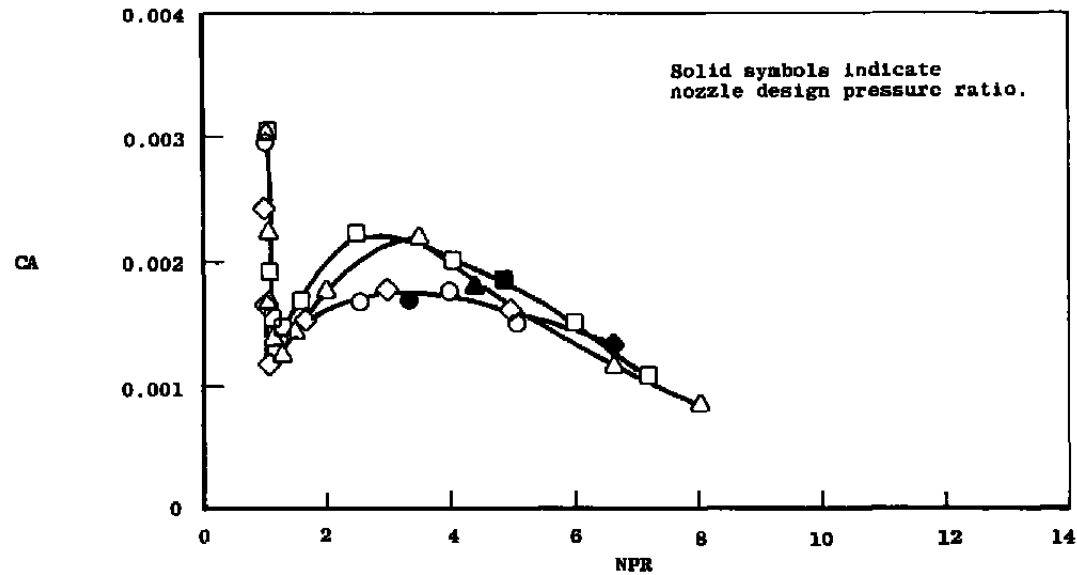
Figure 25. Continued.

SYM	ALPHA	NPA	NPREFF	DELHR	CONF	M _L	ANX10 ⁻⁶	CA	PN.PT
○	0.15	6.79	6.68	-0.02	47	1.50	3.38	0.00455	905.01
□	0.13	6.78	6.68	-2.04	47	1.50	3.38	0.00459	905.02
△	0.04	6.78	6.68	-3.96	47	1.50	3.39	0.00464	905.03
◇	0.03	6.75	6.66	-5.98	47	1.50	3.40	0.00469	905.04
▽	-0.09	6.77	6.67	-7.95	47	1.50	3.39	0.00477	905.05



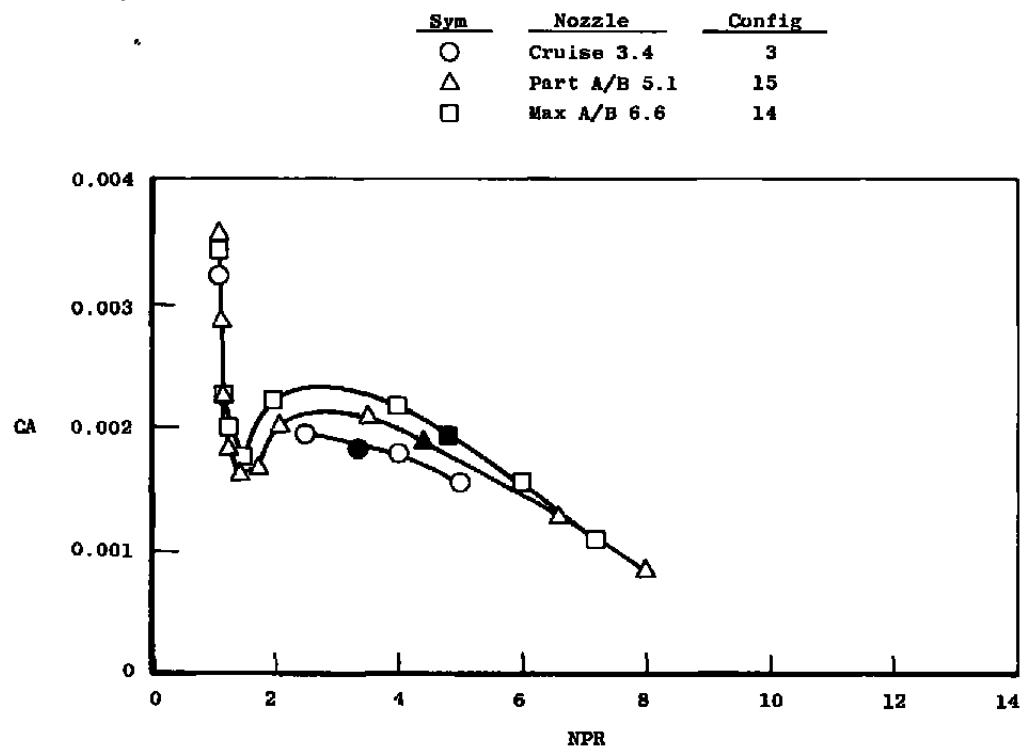
d. Concluded
Figure 25. Concluded.

Sym	Nozzle	Config
○	Cruise 3.4	3
△	Part A/B 5.1	15
□	Max A/B 6.6	14
◇	Max A/B 7.75	16



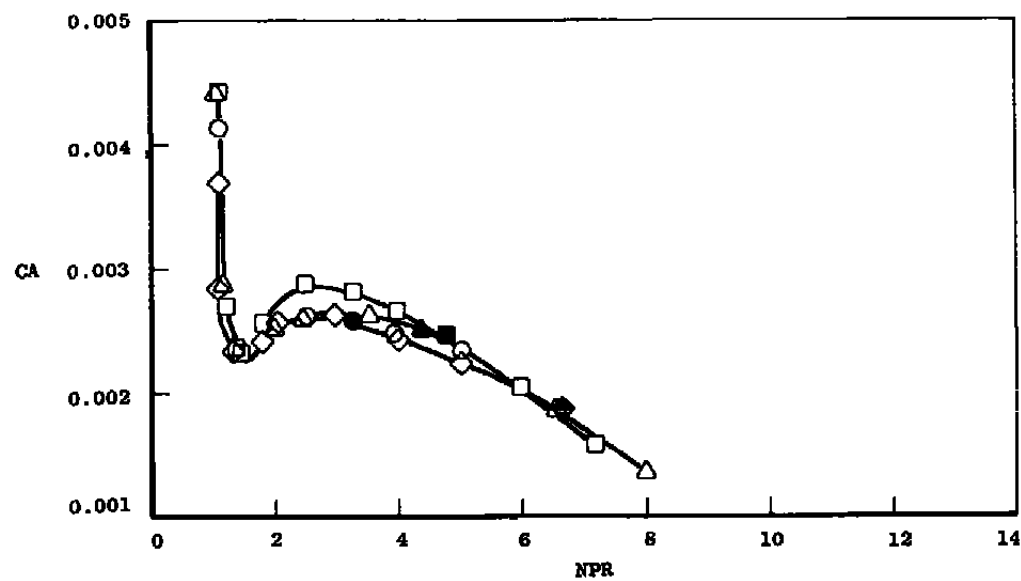
a. $M_\infty = 0.60$

Figure 26. Variation of nozzle-afterbody axial-force coefficient with NPR for various nozzle configurations, wingtip support system, $\alpha = 0$.



b. $M_\infty = 0.80$
Figure 26. Continued.

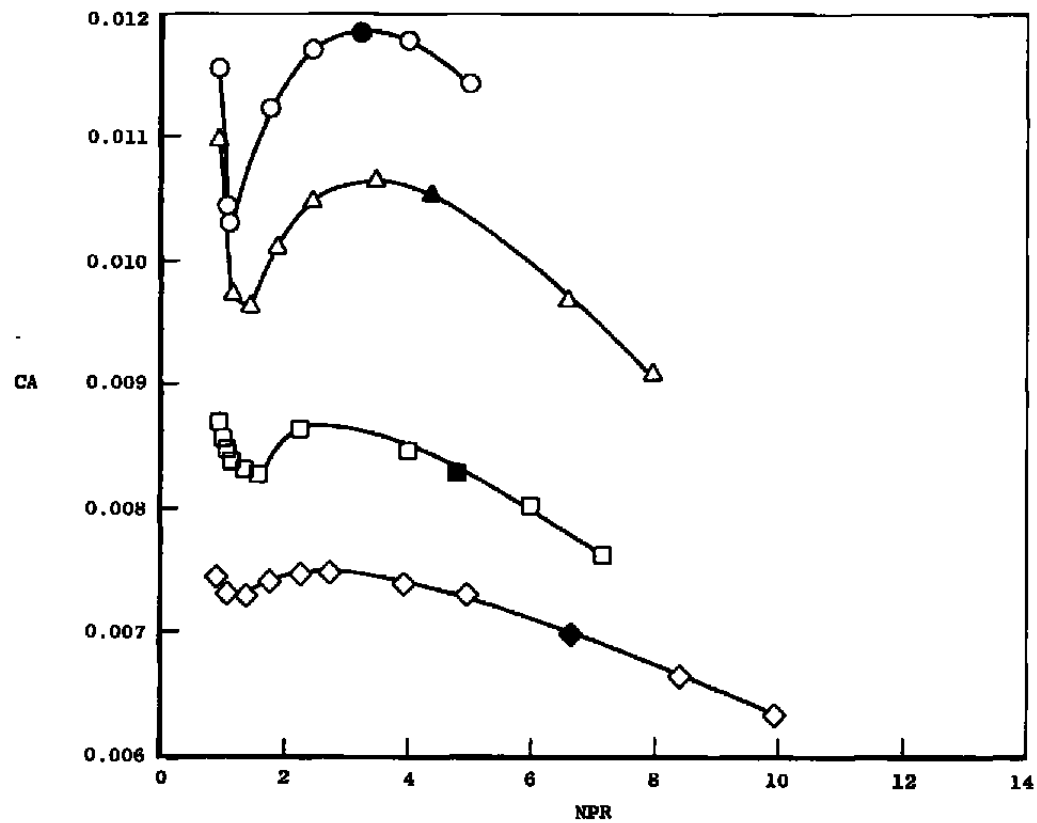
Sym	Nozzle	Config
○	Cruise 3.4	3
△	Part A/B 5.1	15
□	Max A/B 6.6	14
◇	Max A/B 7.75	16



c. $M_{\infty} = 0.90$

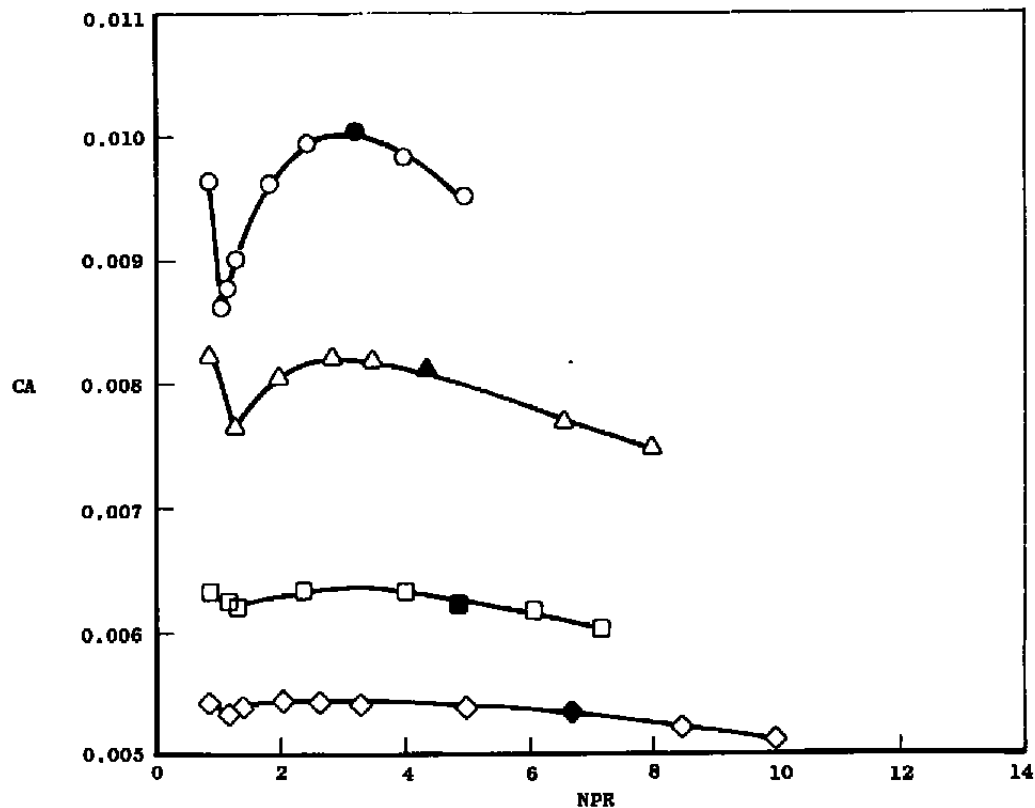
Figure 26. Continued.

Sym	Nozzle	Config
○	Cruise 3.4	3
△	Part A/B 5.1	15
□	Max A/B 6.6	14
◇	Max A/B 7.75	16



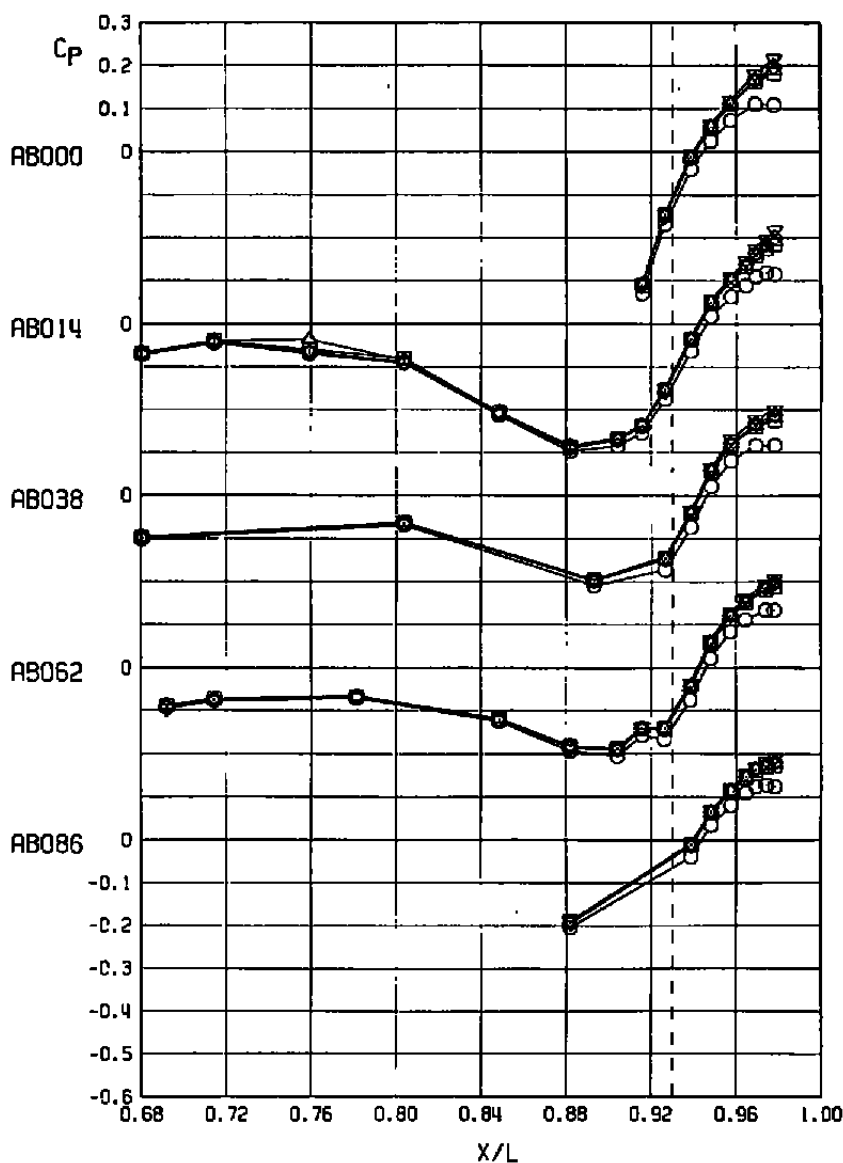
d. $M_\infty = 1.20$
Figure 26. Continued.

Sym	Nozzle	Config
○	Cruise	3
△	Part A/B 5.1	15
□	Max A/B 6.6	14
◇	Max A/B 7.75	16



e. $M_\infty = 1.50$
Figure 26. Concluded.

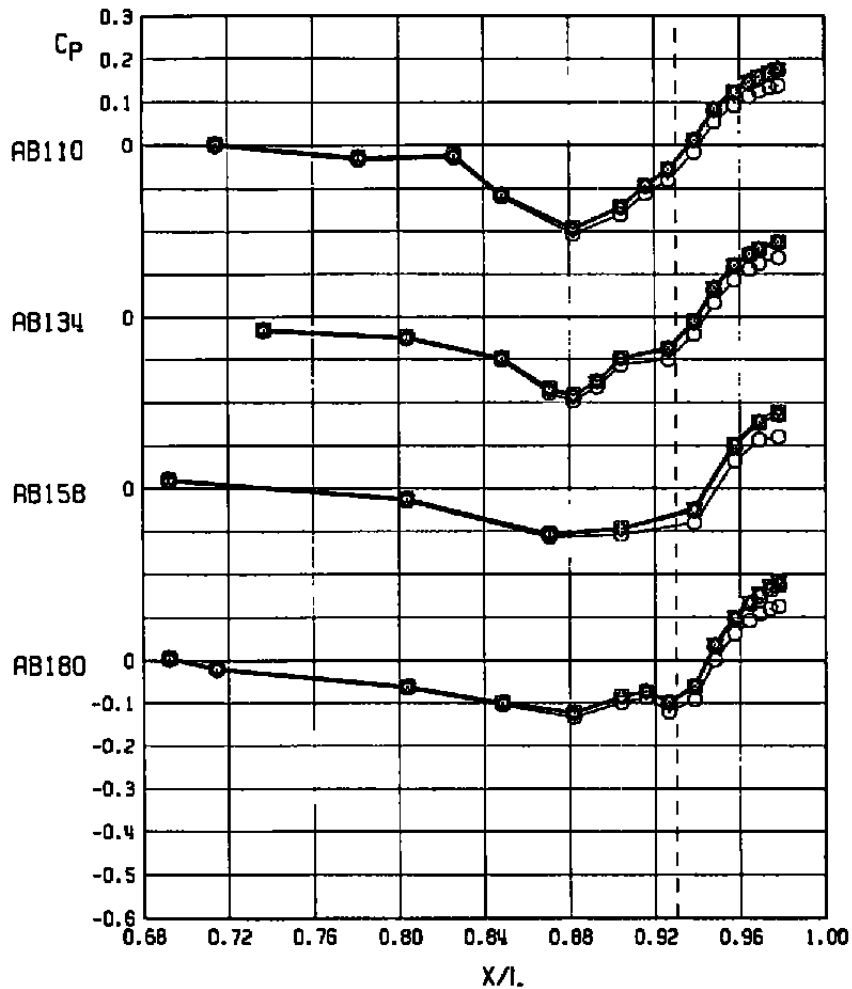
SYM	ALPHA	NPR	NPREF	DELHR	CONF	M _∞	RNX10 ⁻⁸	CA	PN,PT
○	0.02	1.04	1.04	-0.20	3	0.60	3.41	0.00297	117.04
□	0.03	2.52	2.52	-0.20	3	0.60	3.42	0.00168	118.03
△	0.02	3.33	3.33	-0.20	3	0.60	3.42	0.00168	119.03
◇	0.03	4.02	4.02	-0.20	3	0.60	3.42	0.00176	120.08
▽	0.02	5.05	5.05	-0.20	3	0.60	3.42	0.00150	121.03



a. $M_{\infty} = 0.60$

Figure 27. Effect of nozzle pressure ratio on the nozzle afterbody pressure distributions, cruise 3.4 nozzle, wingtip support system, $\alpha = 0$.

SYM	ALPHA	NPR	NPREFF	DELHR	CONF	M _∞	RNX10 ⁻⁸	CA	PN.PT
○	0.02	1.04	1.04	-0.20	3	0.60	3.41	0.00297	117.04
□	0.03	2.52	2.52	-0.20	3	0.60	3.42	0.00168	118.03
△	0.02	3.33	3.33	-0.20	3	0.60	3.42	0.00168	119.03
◇	0.03	4.02	4.02	-0.20	3	0.60	3.42	0.00176	120.08
▽	0.02	5.05	5.05	-0.20	3	0.60	3.42	0.00150	121.03



a. Concluded
Figure 27. Continued.

SYM	ALPHA	NPR	NPREFF	DELTA	CONF	M _L	ANX10 ⁻⁶	CA	PN,PT
○	0.00	1.08	1.08	-0.20	3	0.80	3.41	0.00322	111.01
□	-0.00	2.47	2.47	-0.20	3	0.80	3.40	0.00194	112.03
△	-0.00	3.31	3.31	-0.20	3	0.80	3.40	0.00182	113.03
◇	0.00	3.97	3.97	-0.20	3	0.80	3.40	0.00178	114.03
▽	-0.00	4.99	4.99	-0.20	3	0.80	3.41	0.00155	115.01

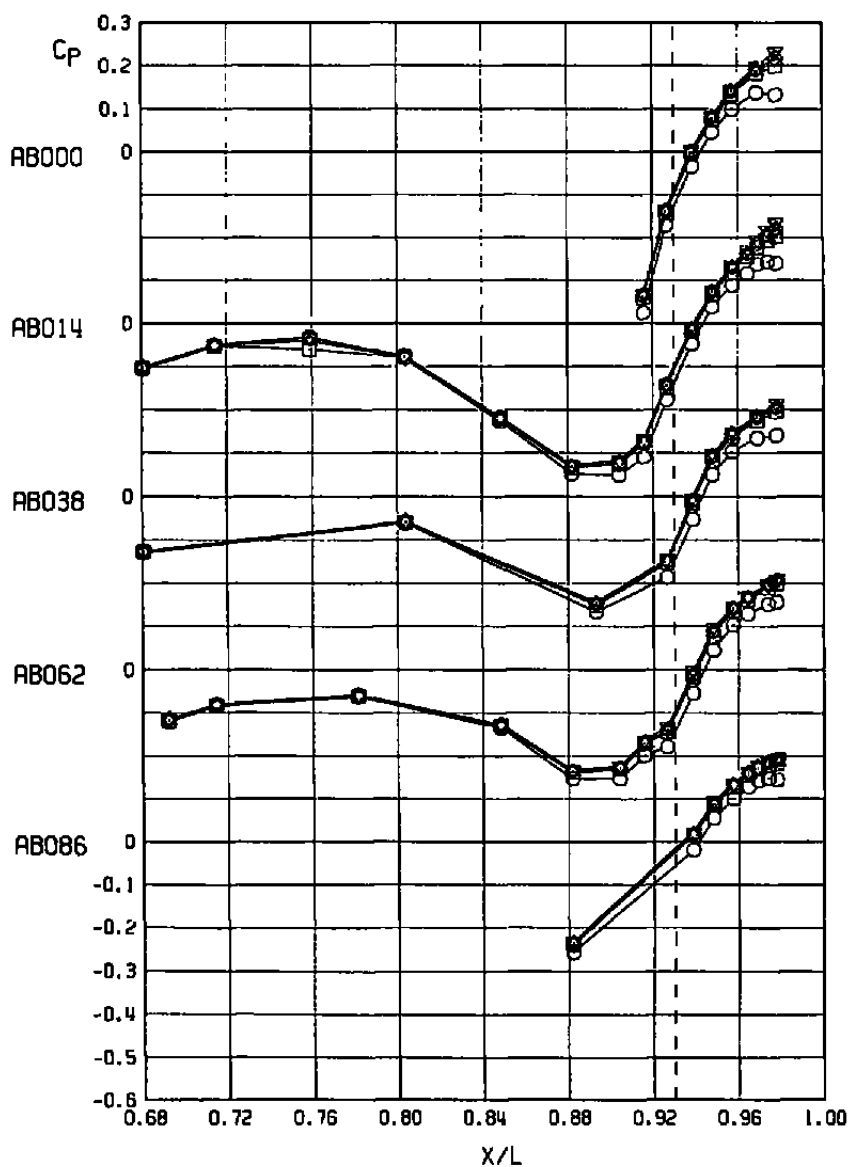
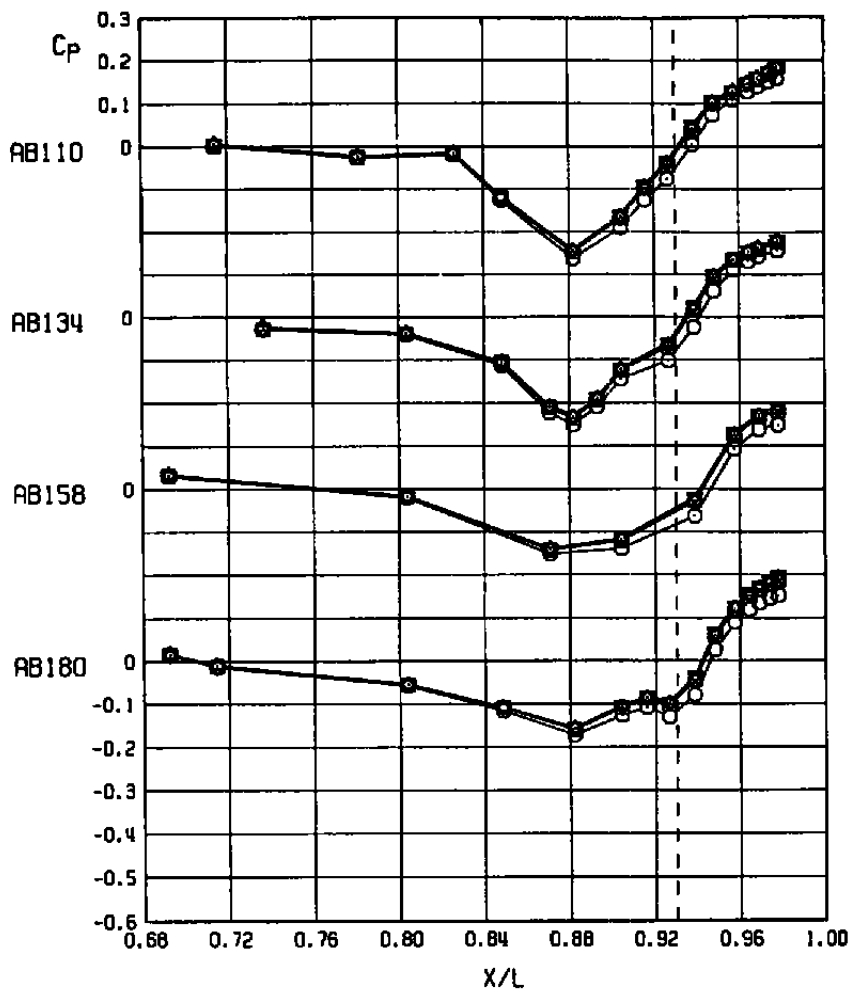
b. $M_\infty = 0.80$

Figure 27. Continued.

SYM	ALPHA	NPR	NPREF	DELTA	CONF	M _∞	RNX10 ⁻⁸	CA	PN.PT
○	0.00	1.08	1.08	-0.20	3	0.80	3.41	0.00322	111.01
□	-0.00	2.47	2.47	-0.20	3	0.80	3.40	0.00194	112.03
△	-0.00	3.31	3.31	-0.20	3	0.80	3.40	0.00182	113.03
◇	0.00	3.97	3.97	-0.20	3	0.80	3.40	0.00178	114.03
▽	-0.00	4.99	4.99	-0.20	3	0.80	3.41	0.00155	115.01



b. Concluded
Figure 27. Continued.

SYM	ALPHA	NPR	NPREF	DELTA	CONF	M _∞	RNX10 ⁻⁶	CA	PN,PT
○	0.00	1.09	1.09	-0.20	3	0.90	3.40	0.00414	109.01
□	0.03	2.51	2.51	-0.20	3	0.90	3.40	0.00260	102.03
△	0.07	3.30	3.30	-0.20	3	0.90	3.40	0.00258	103.03
◇	0.02	3.96	3.96	-0.20	3	0.90	3.40	0.00249	104.04
▽	-0.01	4.99	4.99	-0.20	3	0.90	3.41	0.00235	107.03

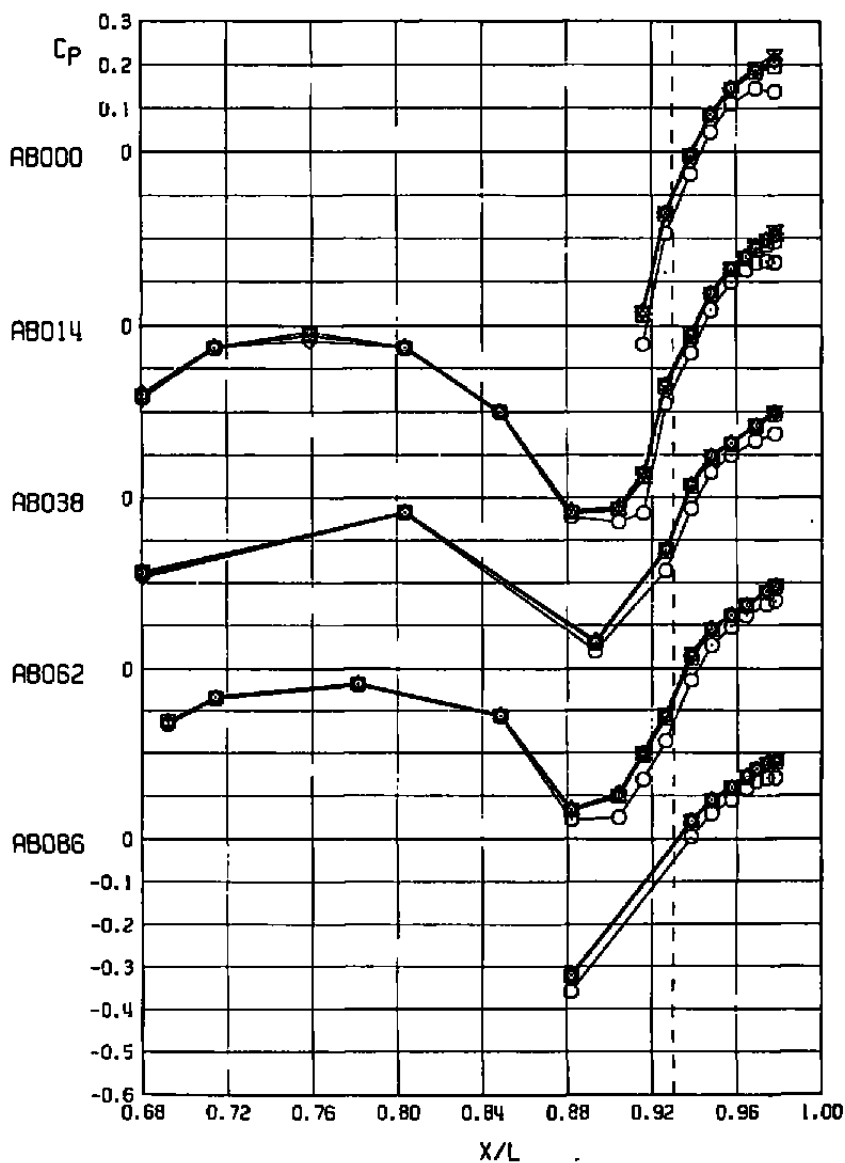
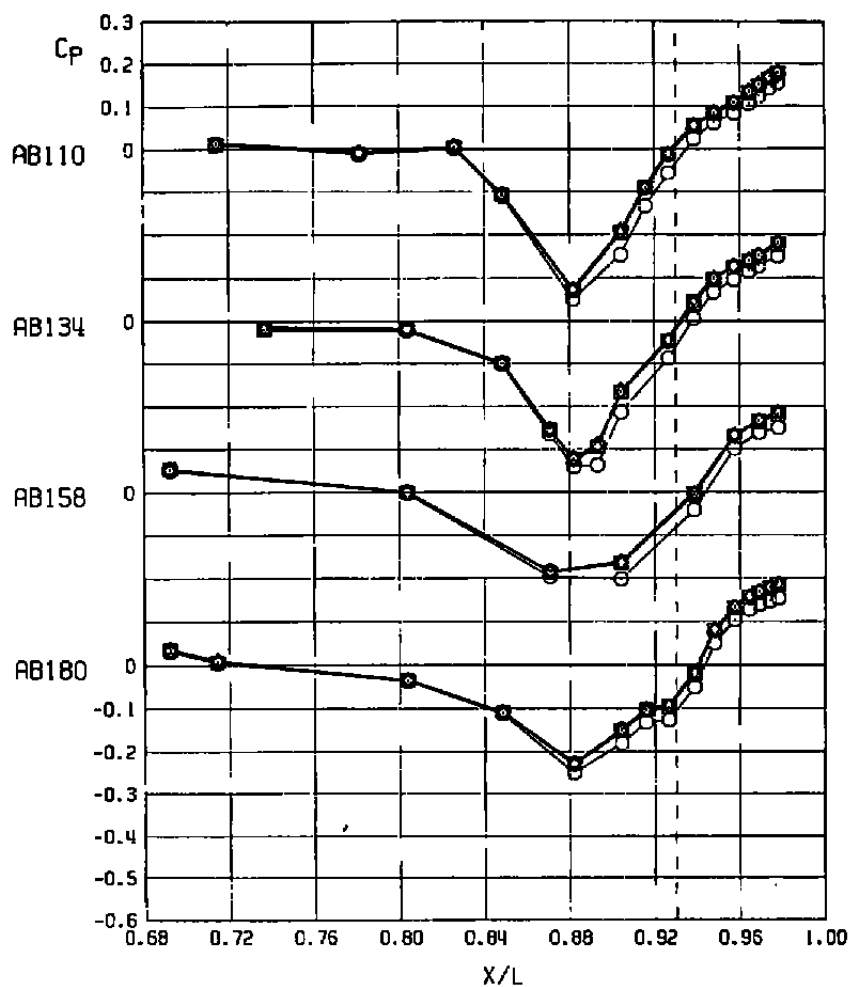
c. $M_\infty = 0.90$

Figure 27. Continued.

SYM	ALPHA	NPR	NPREF	DELHR	CONF	M _∞	RNX10 ⁻⁶	CA	PN,PT
○	0.00	1.09	1.09	-0.20	3	0.90	3.40	0.00414	109.01
□	0.03	2.51	2.51	-0.20	3	0.90	3.40	0.00260	102.03
△	0.07	3.30	3.30	-0.20	3	0.90	3.40	0.00258	103.03
◇	0.02	3.96	3.96	-0.20	3	0.90	3.40	0.00249	104.04
▽	-0.01	4.99	4.99	-0.20	3	0.90	3.41	0.00235	107.03



c. Concluded
Figure 27. Continued.

SYM	ALPHA	NPR	NPREFF	DELTA	CONF	M _∞	RNX10 ⁻⁸	CA	PN.PT
○	-0.00	0.93	0.93	-0.20	3	1.20	3.42	0.01155	93.03
□	-0.01	2.43	2.43	-0.20	3	1.20	3.40	0.01170	94.03
△	-0.02	3.22	3.22	-0.20	3	1.20	3.42	0.01184	95.03
◇	-0.02	3.99	3.99	-0.20	3	1.20	3.40	0.01178	96.04
▽	-0.02	4.97	4.97	-0.20	3	1.20	3.39	0.01141	97.03

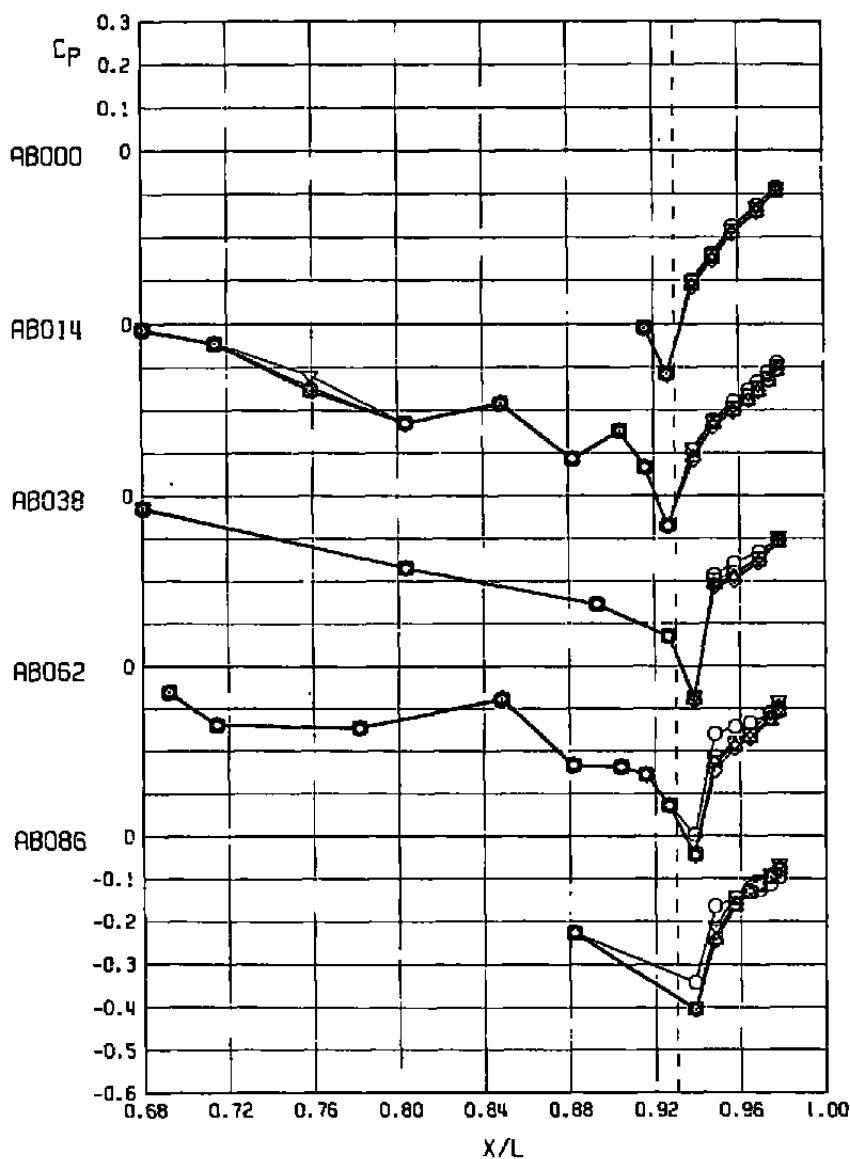
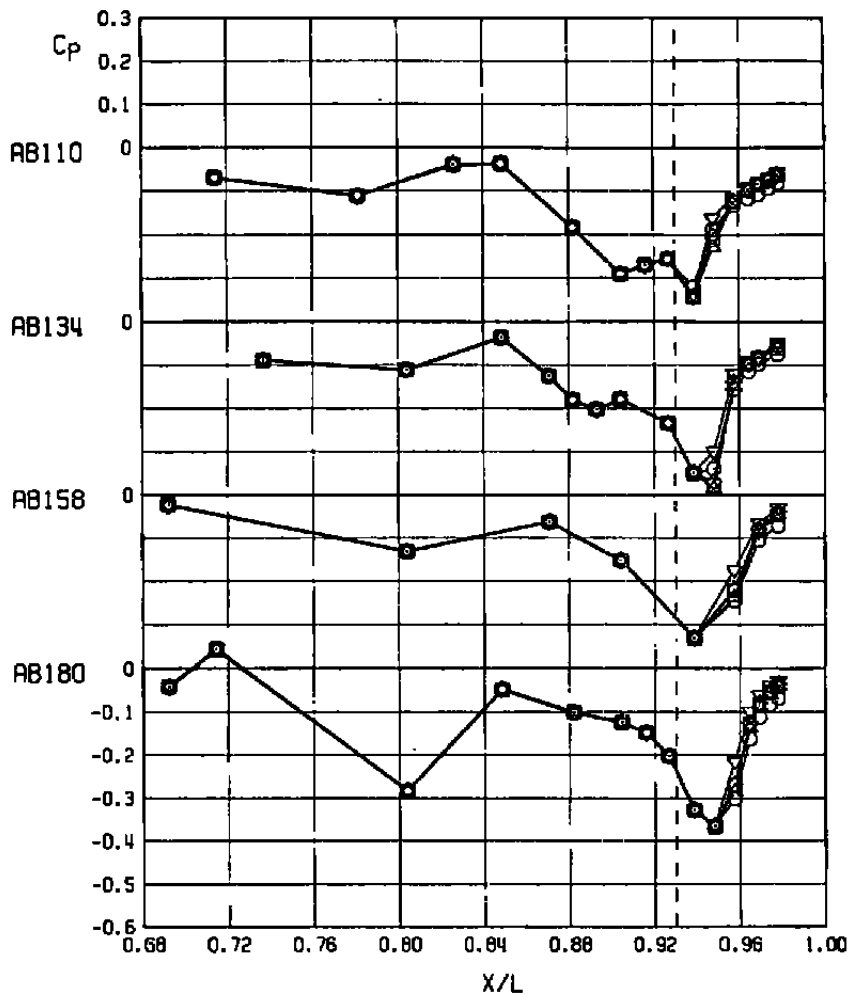
d. $M_\infty = 1.20$

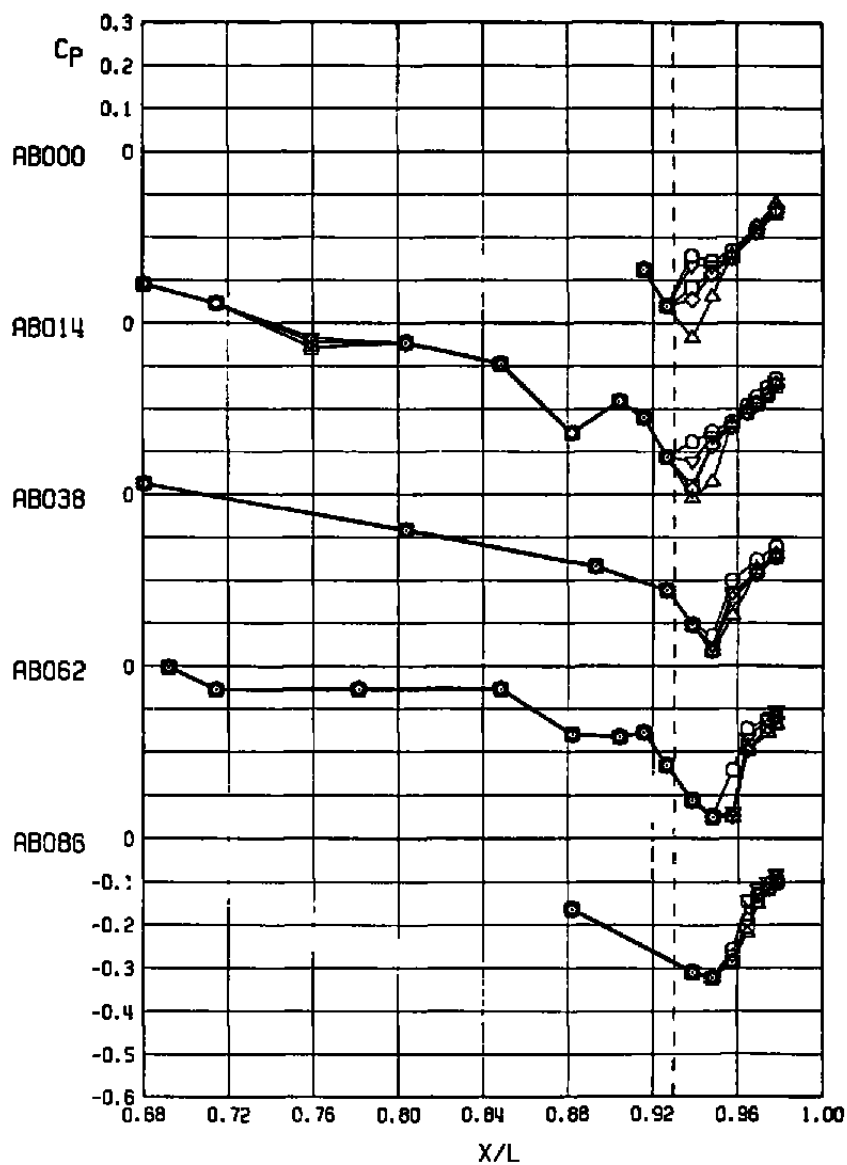
Figure 27. Continued.

SYM	ALPHA	NPR	NPREF	DELHR	CONF	M _∞	RNX10 ⁻⁸	CA	PN.PT
○	-0.00	0.93	0.93	-0.20	3	1.20	3.42	0.01155	93.03
□	-0.01	2.43	2.43	-0.20	3	1.20	3.40	0.01170	94.03
△	-0.02	3.22	3.22	-0.20	3	1.20	3.42	0.01184	95.03
◇	-0.02	3.99	3.99	-0.20	3	1.20	3.40	0.01178	96.04
▽	-0.02	4.97	4.97	-0.20	3	1.20	3.39	0.01141	97.03



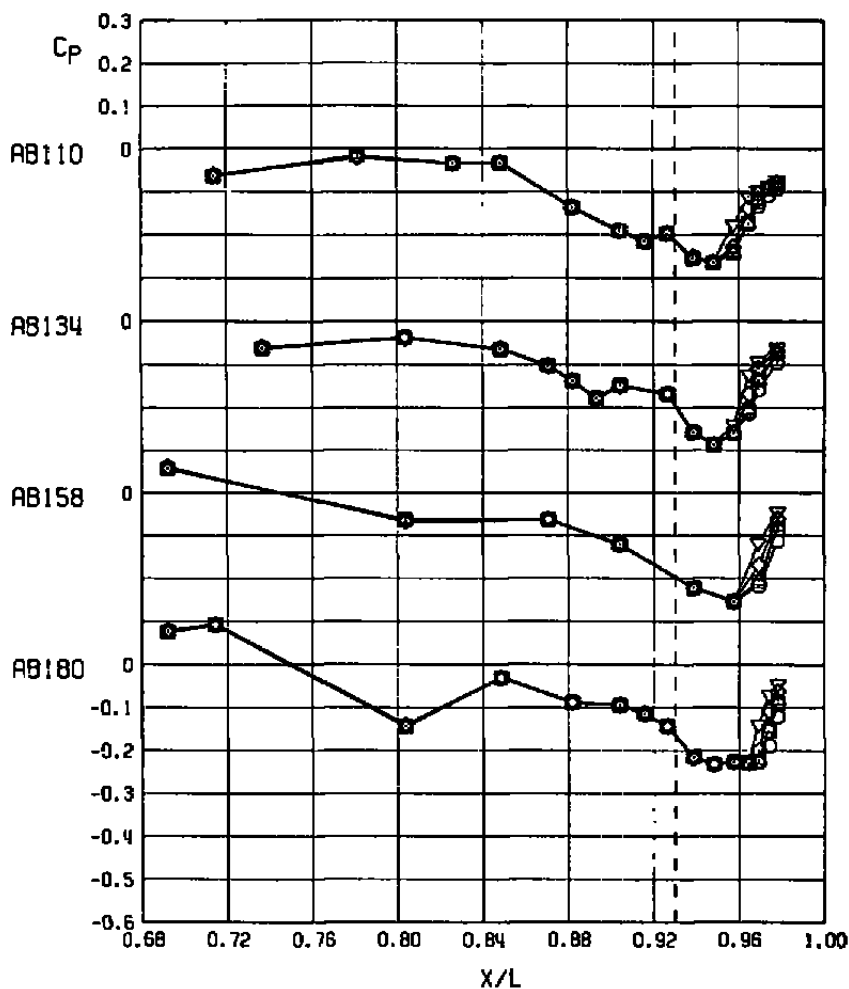
d. Concluded.
Figure 27. Continued.

SYM	ALPHA	NPR	NPREFF	DELTA	CONF	M _∞	ANX10 ⁻⁶	CA	PN,PT
⊙	-0.01	0.85	0.85	-0.20	3	1.50	3.40	0.00964	85.01
□	-0.01	2.43	2.43	-0.20	3	1.50	3.41	0.00995	85.02
△	-0.01	3.22	3.22	-0.20	3	1.50	3.41	0.01008	85.03
◇	-0.00	3.97	3.97	-0.20	3	1.50	3.40	0.00983	85.04
▽	-0.00	4.91	4.91	-0.20	3	1.50	3.40	0.00952	85.07



e. $M_\infty = 1.50$
Figure 27. Continued.

SYM	ALPHA	NPR	NPREF	DELTA	CONF	M _∞	RNX10 ⁻⁶	CA	PN.PT
○	-0.01	0.85	0.85	-0.20	3	1.50	3.40	0.00964	85.01
□	-0.01	2.43	2.43	-0.20	3	1.50	3.41	0.00995	85.02
△	-0.01	3.22	3.22	-0.20	3	1.50	3.41	0.01008	85.03
◇	-0.00	3.97	3.97	-0.20	3	1.50	3.40	0.00983	85.04
▽	-0.00	4.91	4.91	-0.20	3	1.50	3.40	0.00952	85.07



e. Concluded
Figure 27. Concluded.

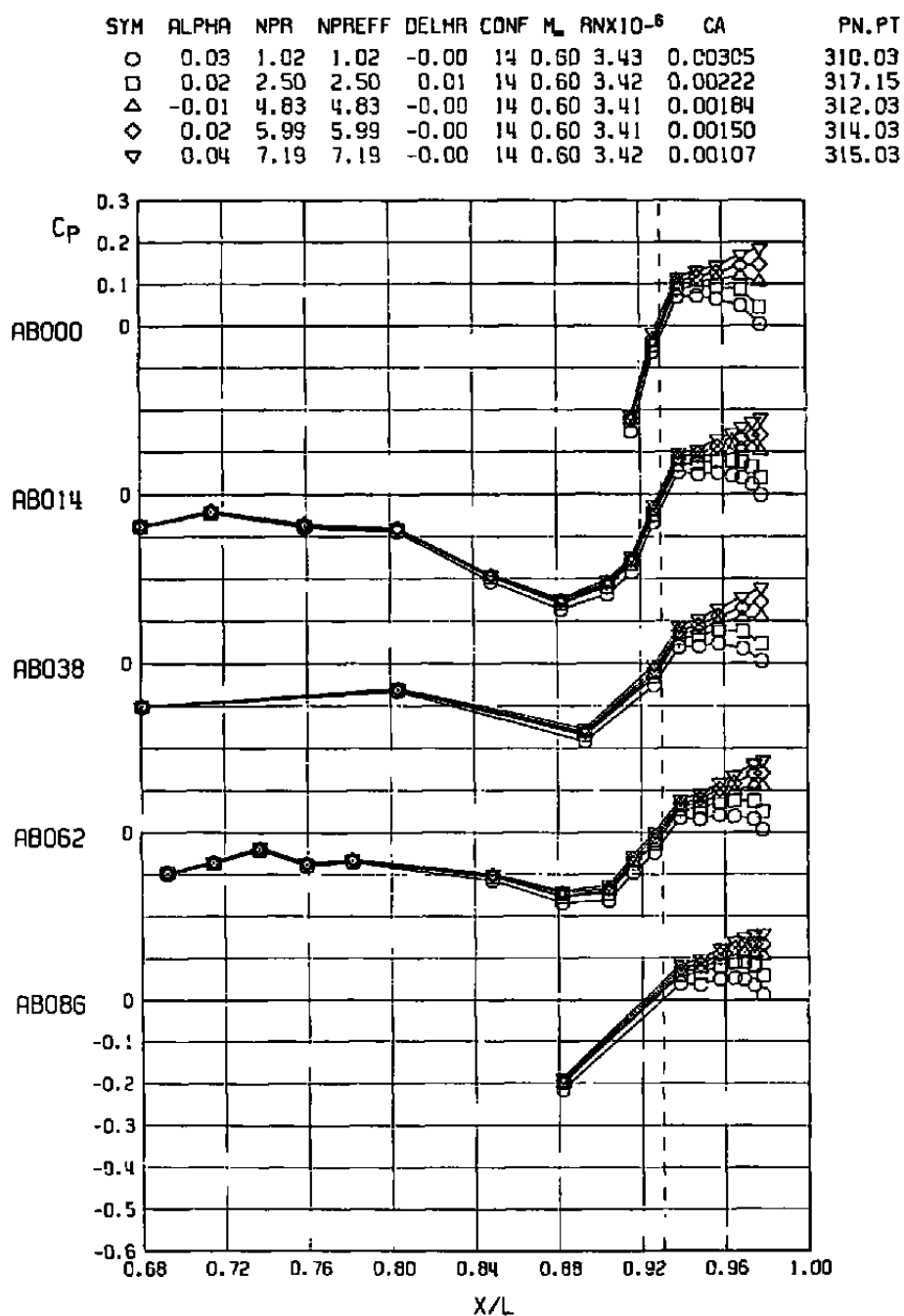
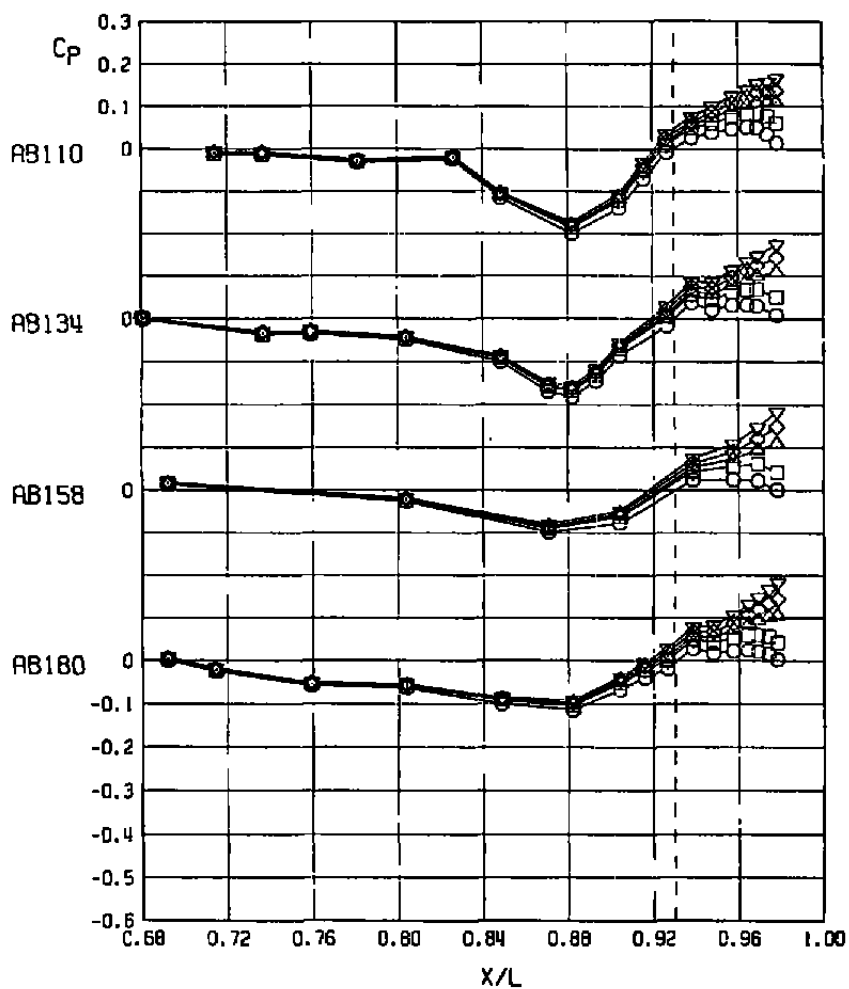
a. $M_{\infty} = 0.60$

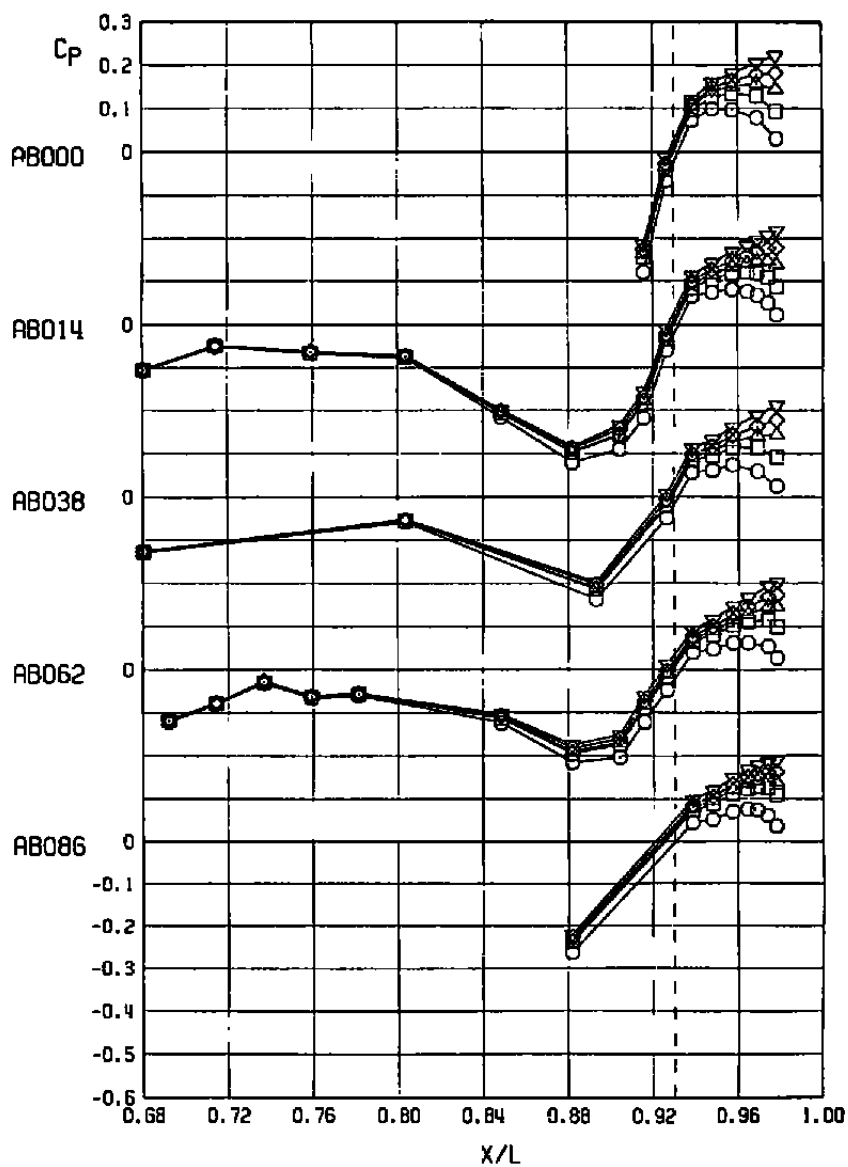
Figure 28. Effect of nozzle pressure ratio on the nozzle-afterbody pressure distributions, max A/B 6.6 nozzle, wingtip support system, $\alpha = 0$.

SYM	ALPHA	NPR	NPREFF	DELTA	CONF	M _∞	PNX10 ⁻⁶	CA	PN,PT
○	0.03	1.02	1.02	-0.00	14	0.60	3.43	0.00305	310.03
□	0.02	2.50	2.50	0.01	14	0.60	3.42	0.00222	317.15
△	-0.01	4.83	4.83	-0.00	14	0.60	3.41	0.00184	312.03
◇	0.02	5.99	5.99	-0.00	14	0.60	3.41	0.00150	314.03
▽	0.04	7.19	7.19	-0.00	14	0.60	3.42	0.00107	315.03



a. Concluded
Figure 28. Continued.

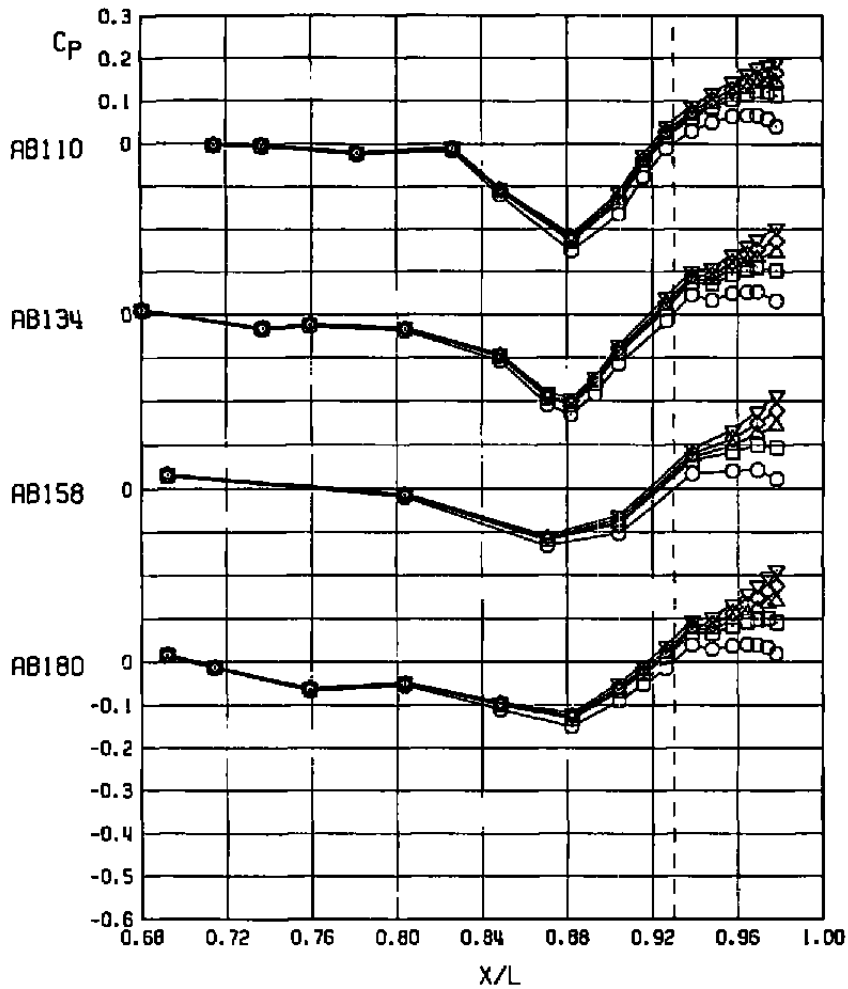
SYM	ALPHA	NPR	NPREF	DELTA	CONF	M _∞	ANX10 ⁻⁶	CA	PN,PT
○	0.02	1.04	1.04	0.00	14	0.80	3.41	0.00341	318.03
□	0.01	1.97	1.97	0.00	14	0.80	3.40	0.00222	318.18
△	0.02	4.80	4.80	0.00	14	0.80	3.39	0.00191	322.03
◇	0.02	5.96	5.96	0.00	14	0.80	3.41	0.00155	320.03
▽	0.02	7.17	7.17	0.00	14	0.80	3.39	0.00106	321.03



b. $M_\infty = 0.80$

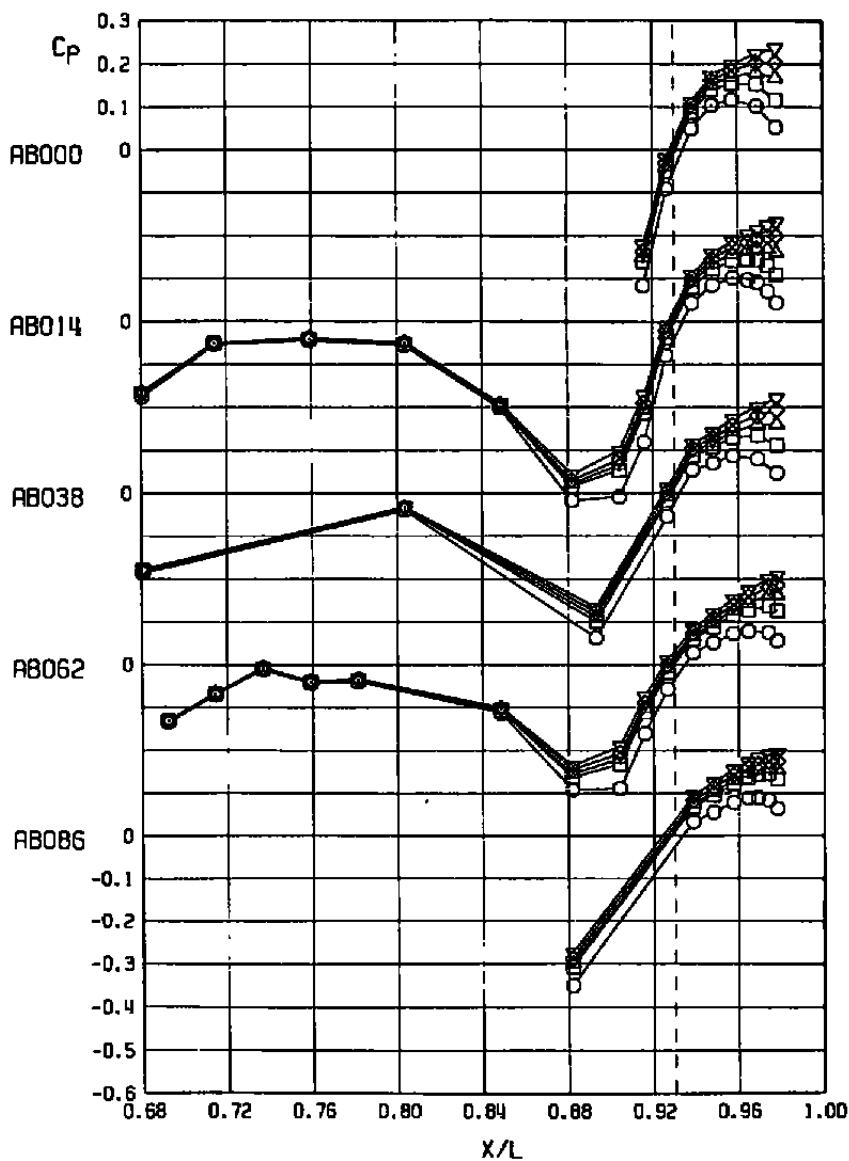
Figure 28. Continued.

SYM	ALPHA	NPR	NPREF	DELTA	CONF	M _∞	ANX10 ⁻⁶	CA	PN.PT
○	0.02	1.04	1.04	0.00	14	0.80	3.41	0.00341	318.03
□	0.01	1.97	1.97	0.00	14	0.80	3.40	0.00222	318.18
△	0.02	4.80	4.80	0.00	14	0.80	3.39	0.00191	322.03
◇	0.02	5.96	5.96	0.00	14	0.80	3.41	0.00155	320.03
▽	0.02	7.17	7.17	0.00	14	0.80	3.39	0.00106	321.03

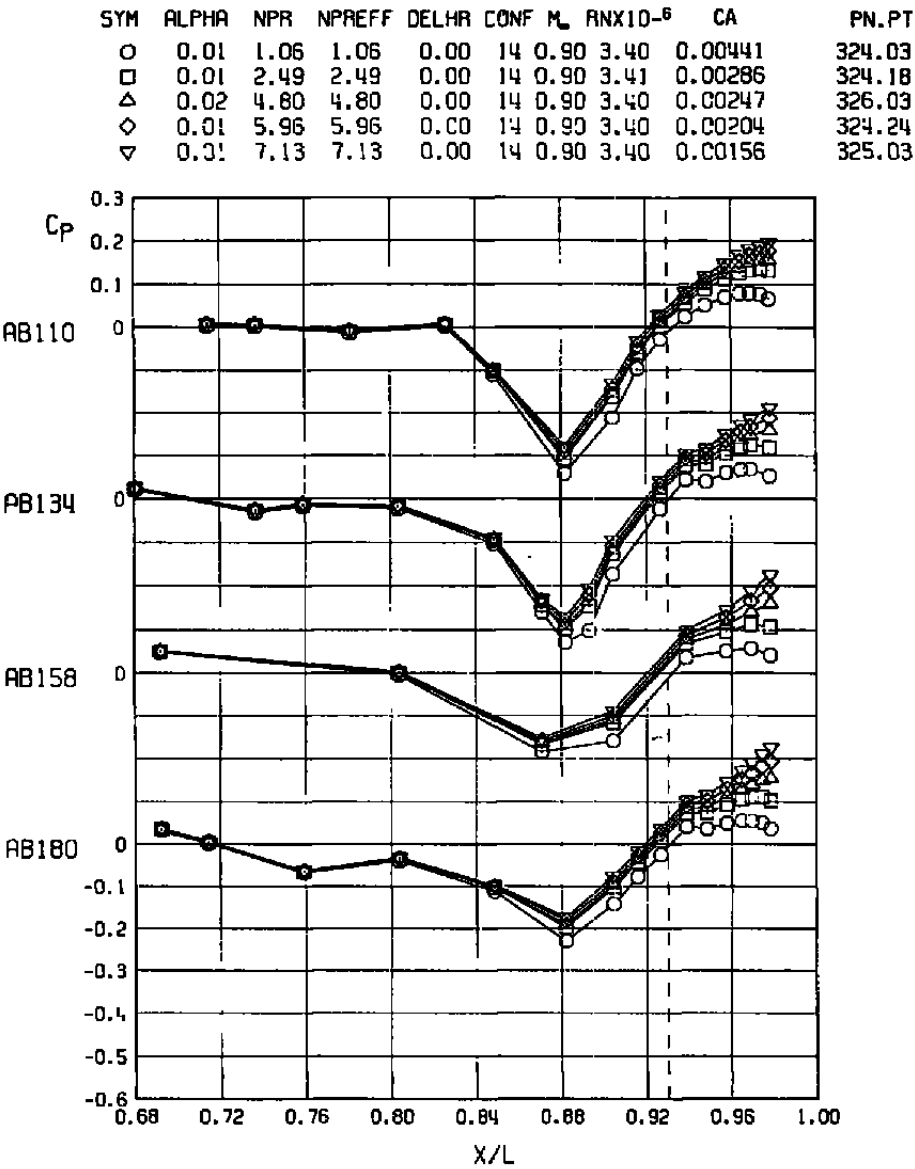


b. Concluded
Figure 28. Continued.

SYM	ALPHA	NPR	NPREFF	DELHR	CONF	M _∞	RNX10 ⁻⁶	CA	PN.PT
○	0.01	1.06	1.06	0.00	14	0.90	3.40	0.00441	324.03
□	0.01	2.49	2.49	0.00	14	0.90	3.41	0.00286	324.18
△	0.02	4.80	4.80	0.00	14	0.90	3.40	0.00247	326.03
◇	0.01	5.96	5.96	0.00	14	0.90	3.40	0.00204	324.24
▽	0.01	7.13	7.13	0.00	14	0.90	3.40	0.00156	325.03

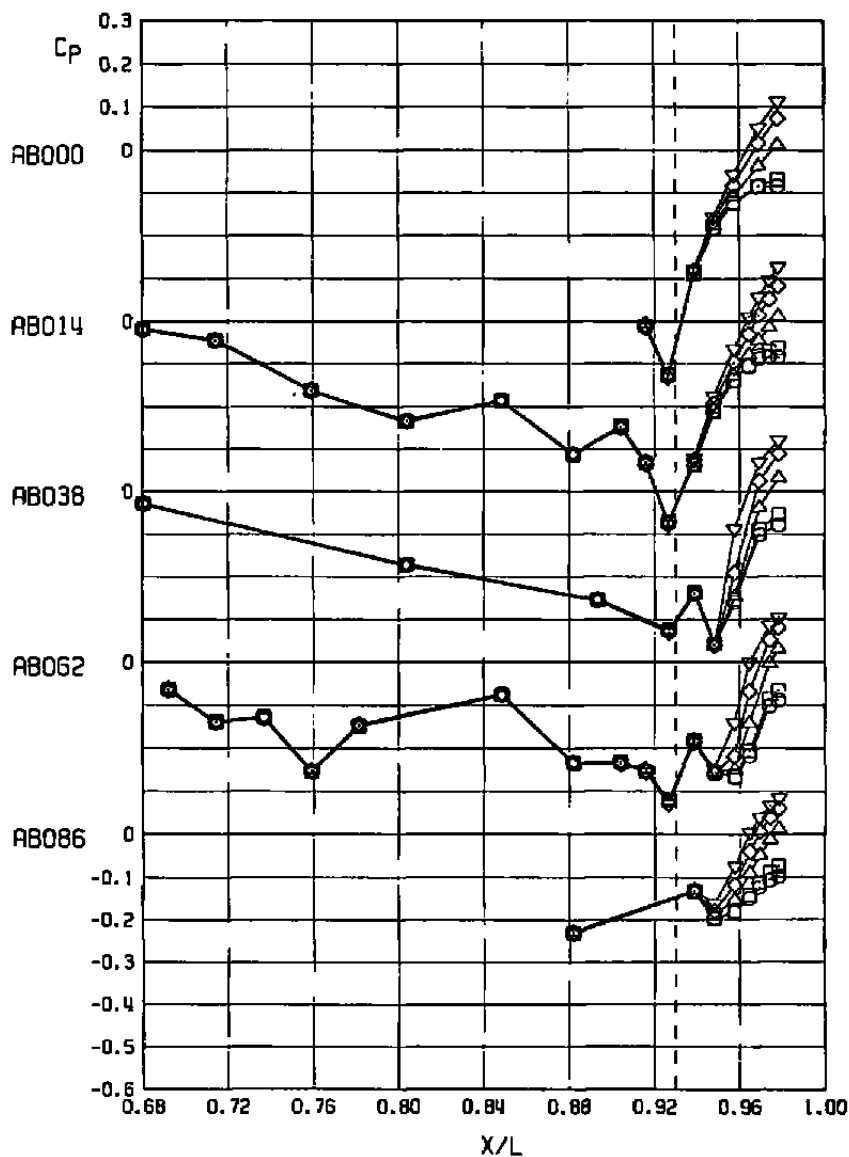


c. $M_{\infty} = 0.9$
Figure 28. Continued.



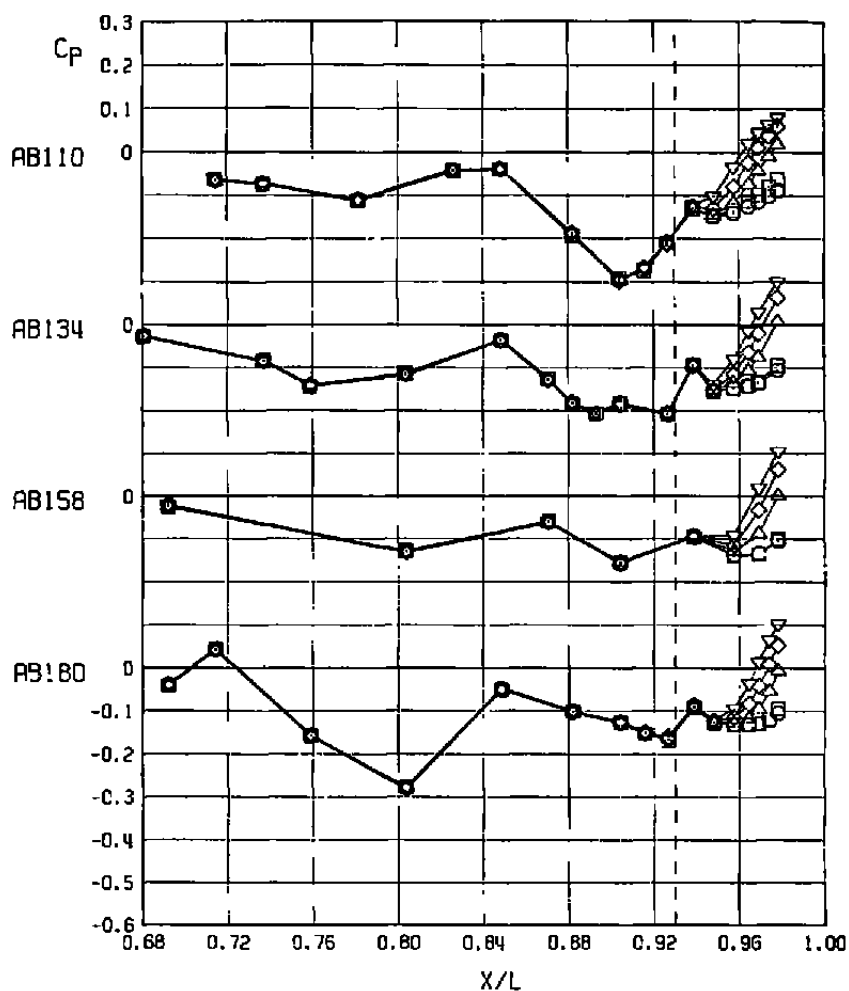
c. Concluded
Figure 28. Continued.

SYM	ALPHA	NPR	NPREFF	DELTA	CONF	M _∞	ANX10 ⁻⁶	CA	PN,PT
○	0.01	0.91	0.91	-0.01	14	1.20	3.40	0.00869	366.03
□	0.00	2.21	2.21	-0.01	14	1.20	3.40	0.00864	367.10
△	-0.01	4.78	4.78	-0.01	14	1.20	3.41	0.00827	368.03
◇	-0.00	5.97	5.97	-0.01	14	1.20	3.40	0.00801	370.01
▽	-0.01	7.13	7.13	-0.01	14	1.20	3.40	0.00762	371.03



d. $M_\infty = 1.20$
Figure 28. Continued.

SYM	ALPHA	NPR	NPREFF	DELHR	CONF	M _∞	FNX10 ⁻⁶	CA	PN,PT
○	0.01	0.91	0.91	-0.01	14	1.20	3.40	0.00869	366.03
□	0.00	2.21	2.21	-0.01	14	1.20	3.40	0.00864	367.10
△	-0.01	4.78	4.78	-0.01	14	1.20	3.41	0.00827	368.03
◇	-0.03	5.97	5.97	-0.01	14	1.20	3.40	0.00801	370.01
▽	-0.01	7.13	7.13	-0.01	14	1.20	3.40	0.00762	371.03



d. Concluded
Figure 28. Continued.

SYM	ALPHA	NPR	NPREFF	DELHR	CONF	M _∞	RNX10 ⁻⁶	CA	PN.PT
○	0.01	0.84	0.84	0.00	14	1.50	3.40	0.00632	360.03
□	-0.00	2.32	2.32	-0.01	14	1.50	3.40	0.00635	365.04
△	0.00	4.81	4.81	0.00	14	1.50	3.40	0.00622	361.03
◇	0.00	6.03	6.03	-0.00	14	1.50	3.40	0.00619	363.03
▽	0.00	7.17	7.17	-0.00	14	1.50	3.40	0.00604	364.03

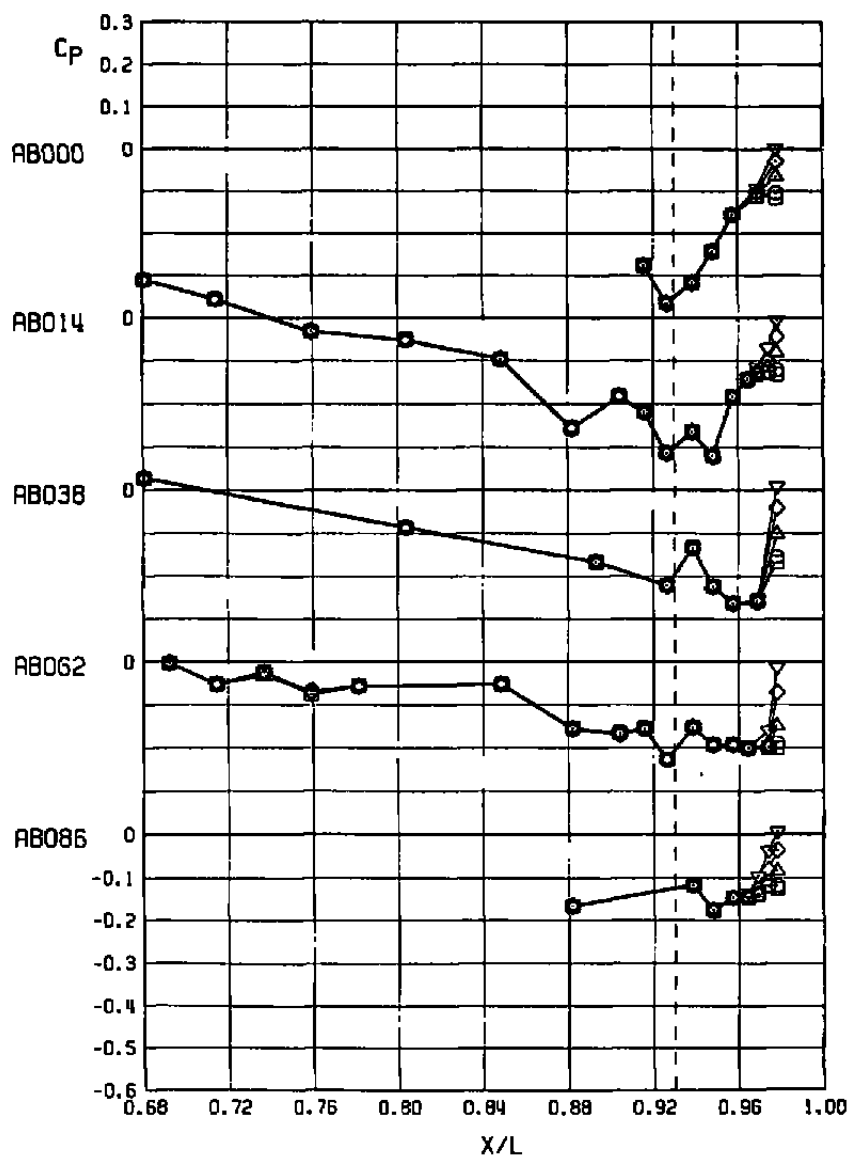
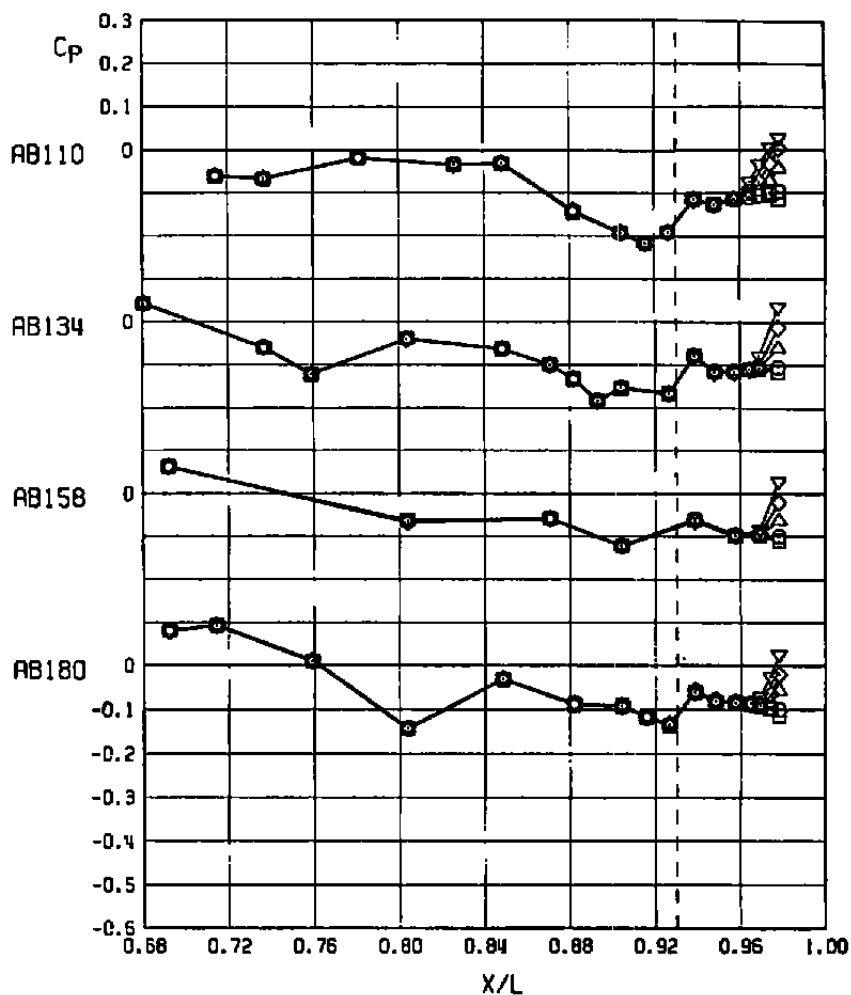
e. $M_\infty = 1.50$

Figure 28. Continued.

SYM	ALPHA	NPR	NPREF	DELTA	CONF	M _∞	ANX10 ⁻⁶	CA	PN.PT
○	0.01	0.84	0.84	0.00	14	1.50	3.40	0.00632	360.03
□	-0.00	2.32	2.32	-0.01	14	1.50	3.40	0.00635	365.04
△	0.00	4.81	4.81	0.00	14	1.50	3.40	0.00622	361.03
◇	0.00	6.03	6.03	-0.00	14	1.50	3.40	0.00619	363.03
▽	0.00	7.17	7.17	-0.00	14	1.50	3.40	0.00604	364.03



e. Concluded
Figure 28. Concluded.

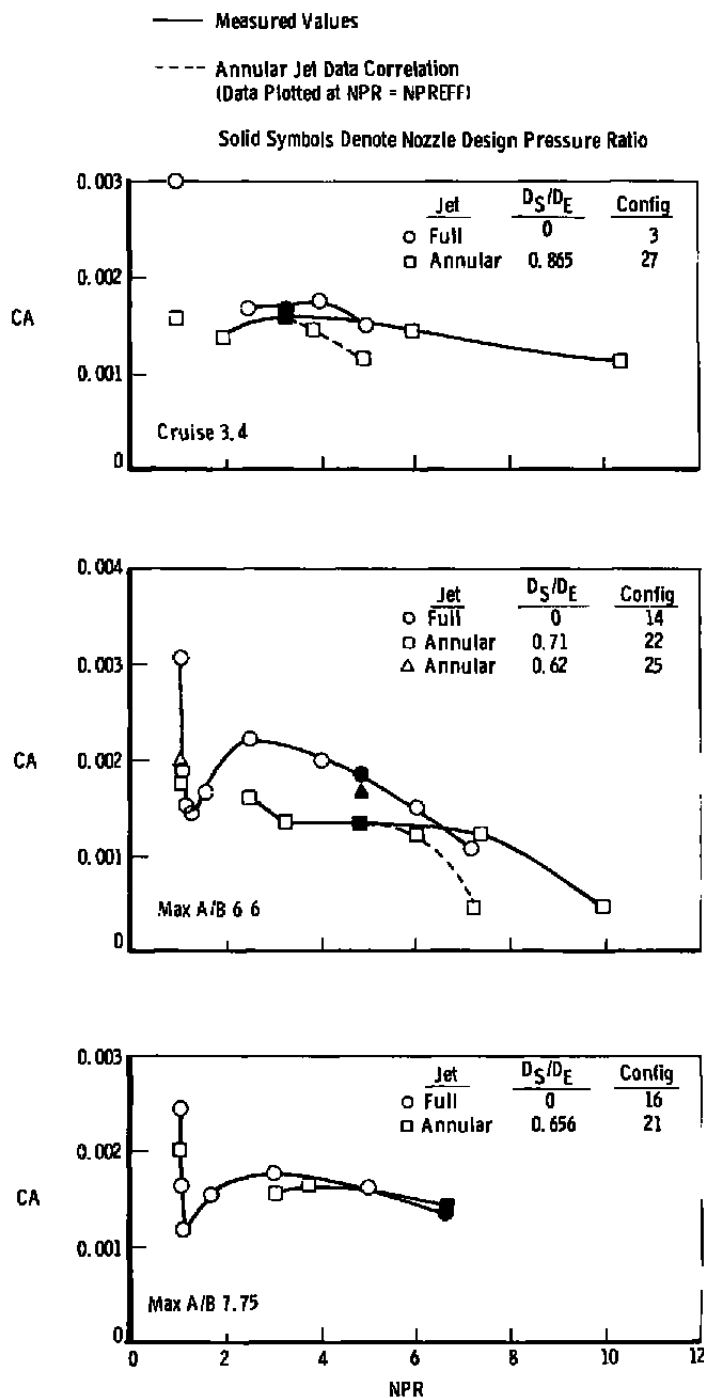
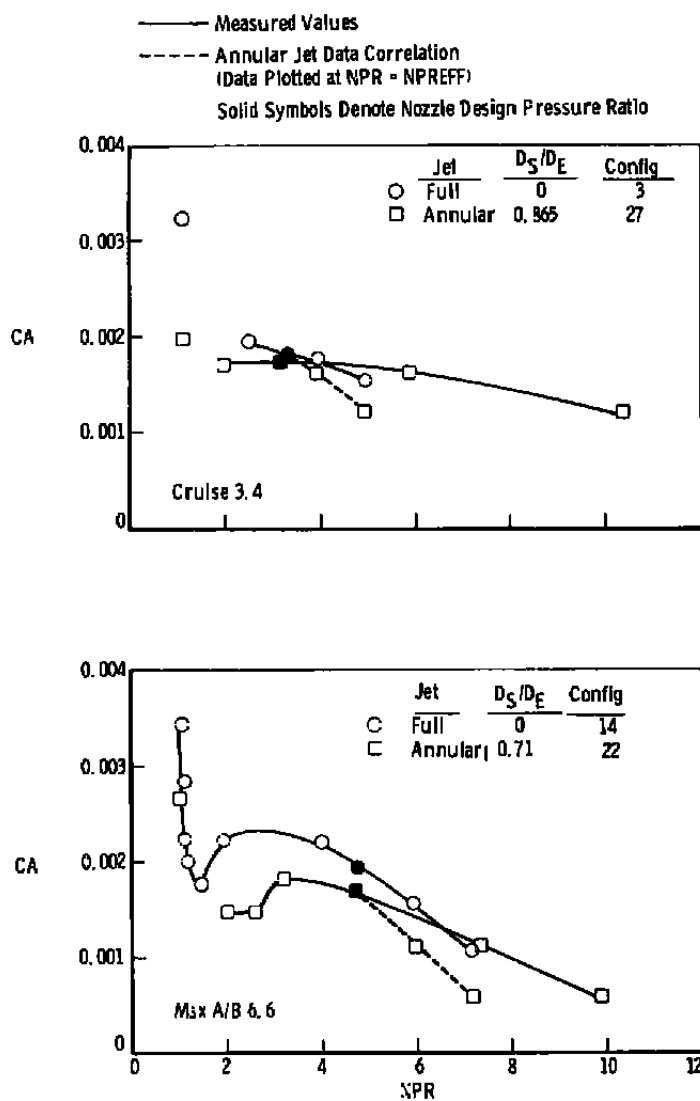
a. $M_\infty = 0.60$

Figure 29. Comparison of afterbody axial-force data from full and annular jet configurations, wingtip support system, $\alpha = 0$.



b. $M_\infty = 0.80$
 Figure 29. Continued.

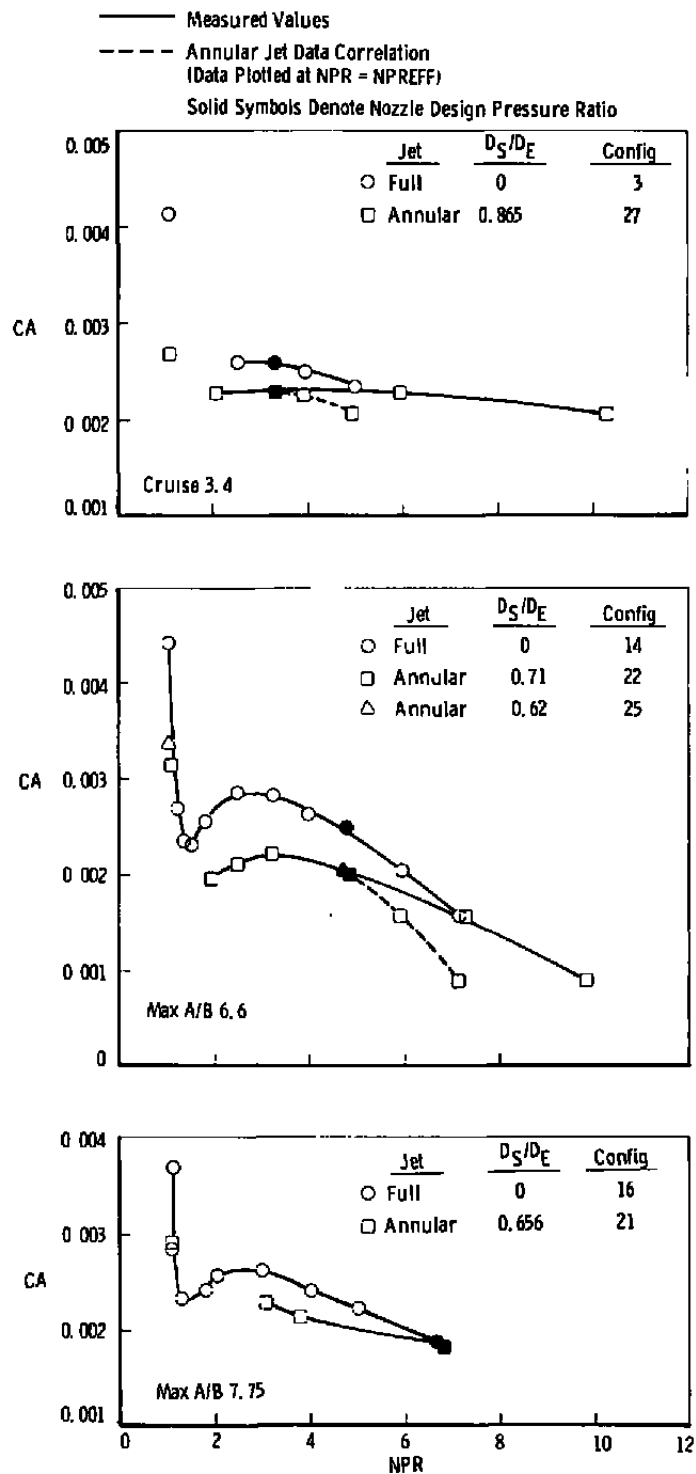
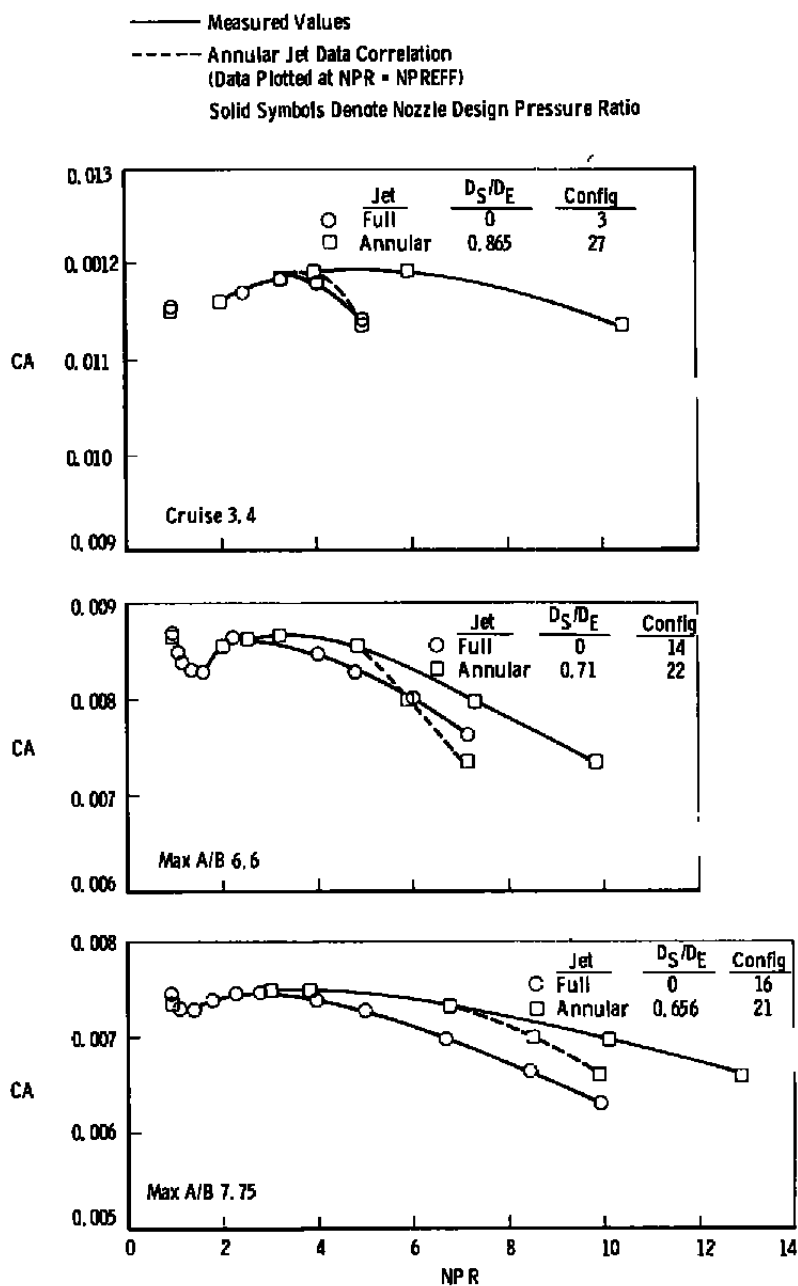
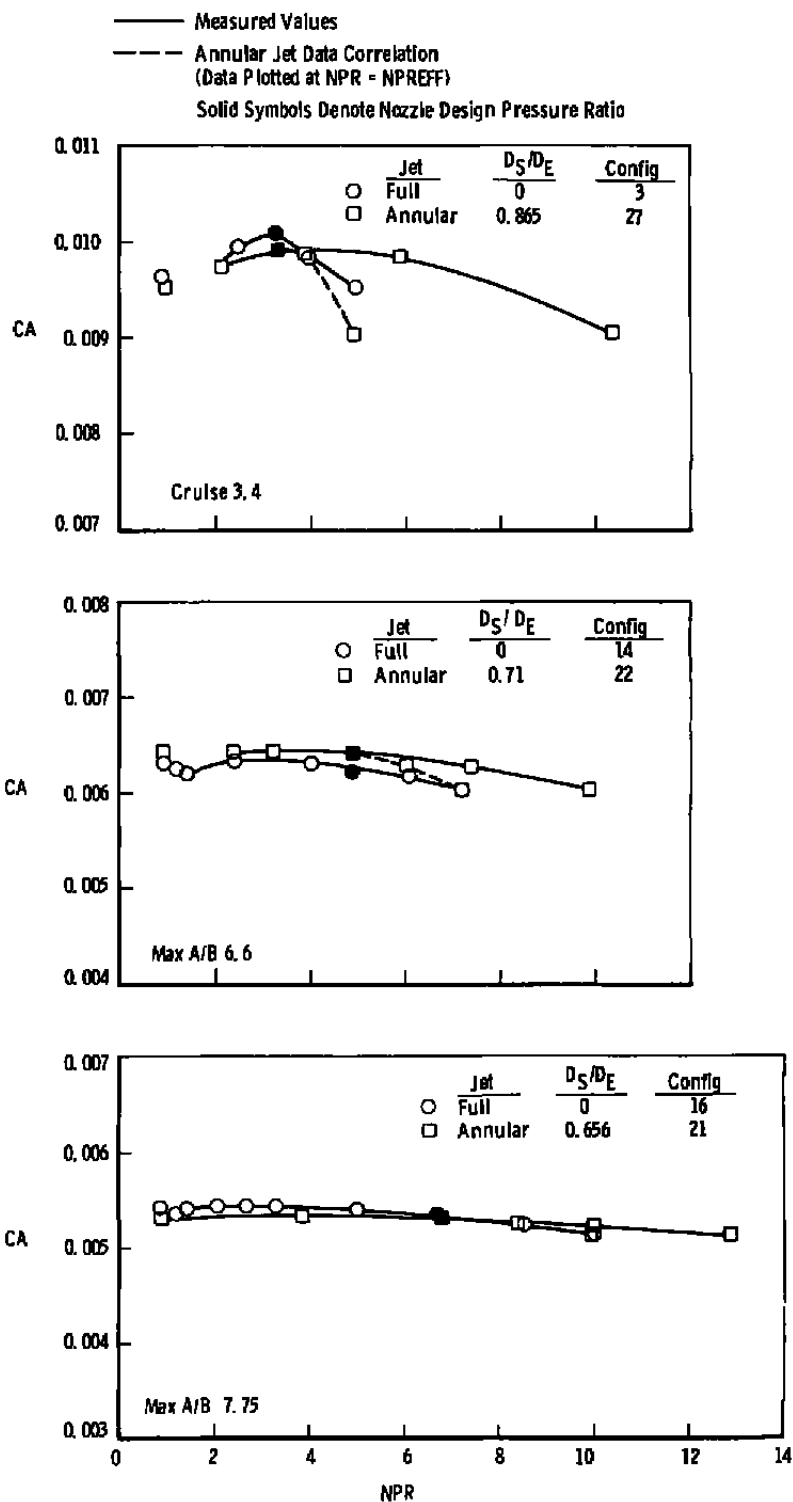
c. $M_\infty = 0.90$

Figure 29. Continued.



d. $M_\infty = 1.20$
 Figure 29. Continued.



e. $M_\infty = 1.50$
 Figure 29. Concluded.

Sym	Nozzle	D_S	D_S/D_F	Config
○	Cruise	2.4	0.865	(27) - (3)
△	Part A/B 5.1	2.75	0.807	(23) - (15)
□	Max A/B 6.6	2.75	0.710	(22) - (14)
■	Max A/B 6.6	2.40	0.620	(25) - (14)
◇	Max A/B 7.75	2.75	0.656	(21) - (16)

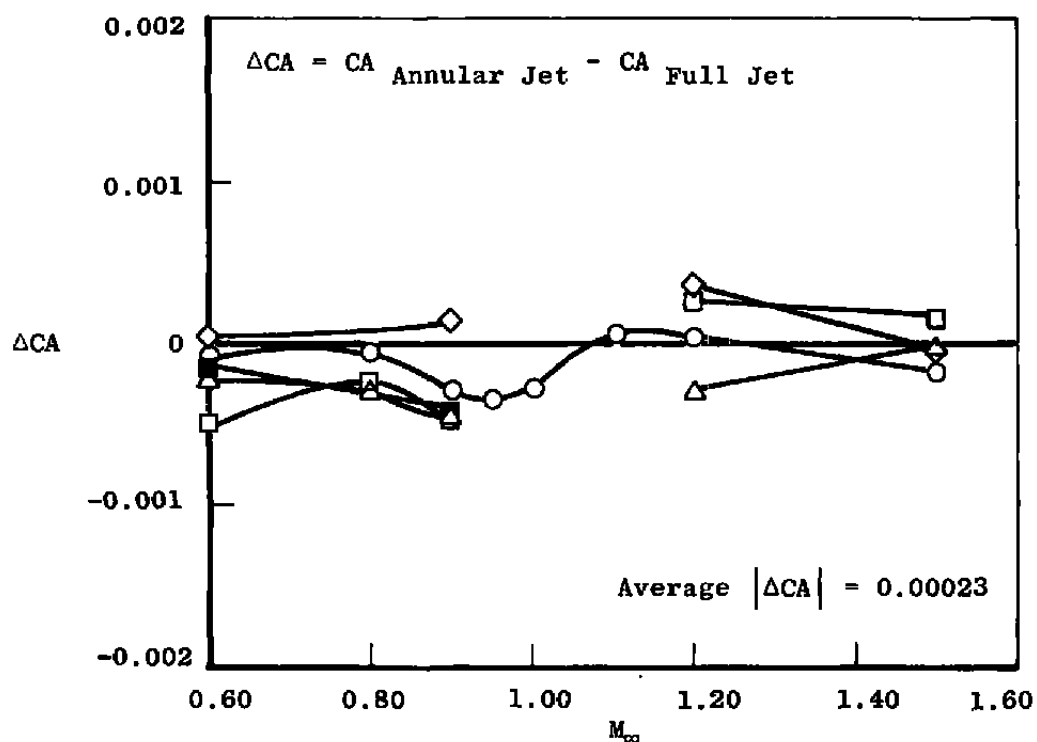


Figure 30. Summary of annular jet axial-force comparison at design NPR, wingtip support system, $\alpha = 0$.

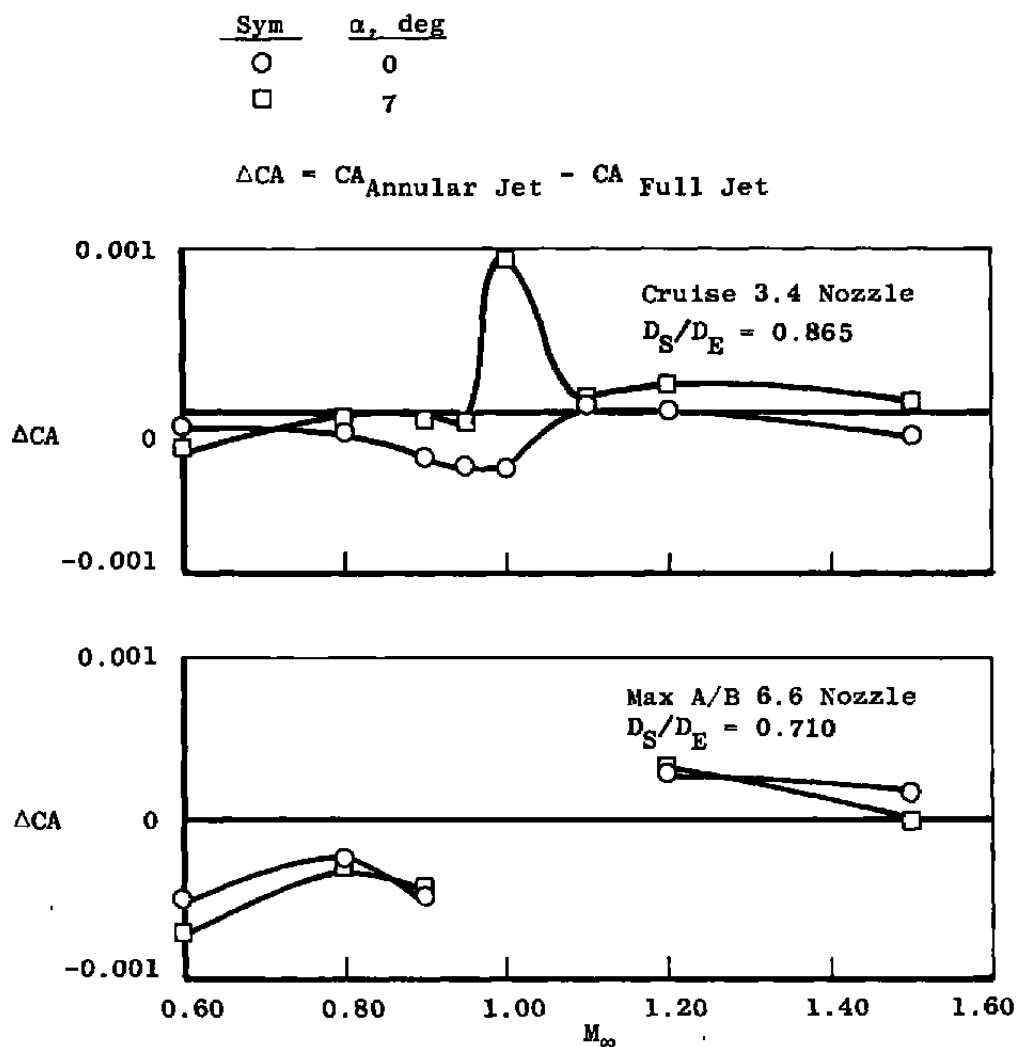


Figure 31. Effect of angle of attack on the annular and full jet comparison of axial-force results, wingtip support system, design NPR.

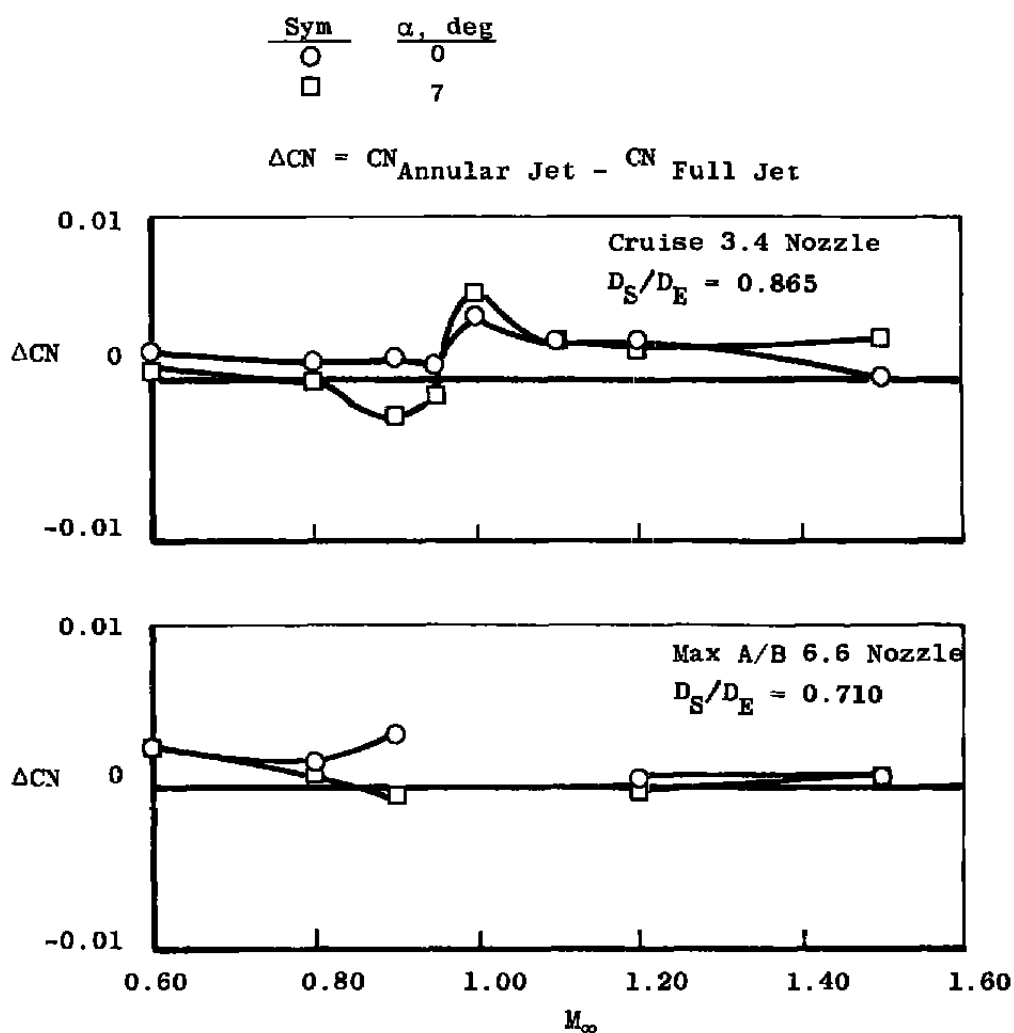


Figure 32. Effect of angle of attack on the annular and full jet comparison of normal-force results, wingtip support system, design NPR.

Sym	D_S , in.	D_S/D_E	Jet	NPR	Config
○	2.4	0.865	Annular	3.3	(27) - (3)
□	2.75	1.000	Solid Plume	---	(20) - (3)

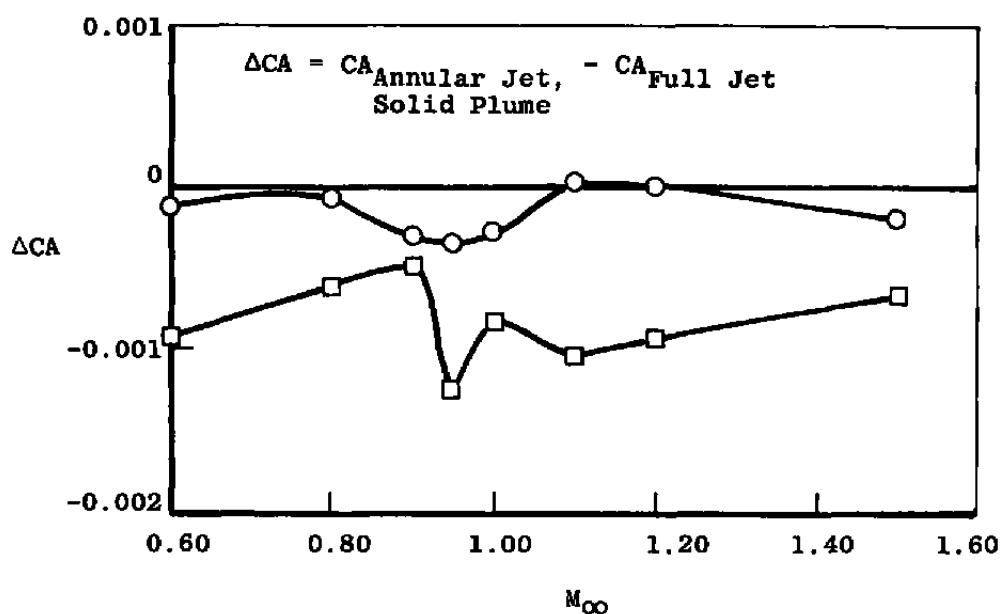
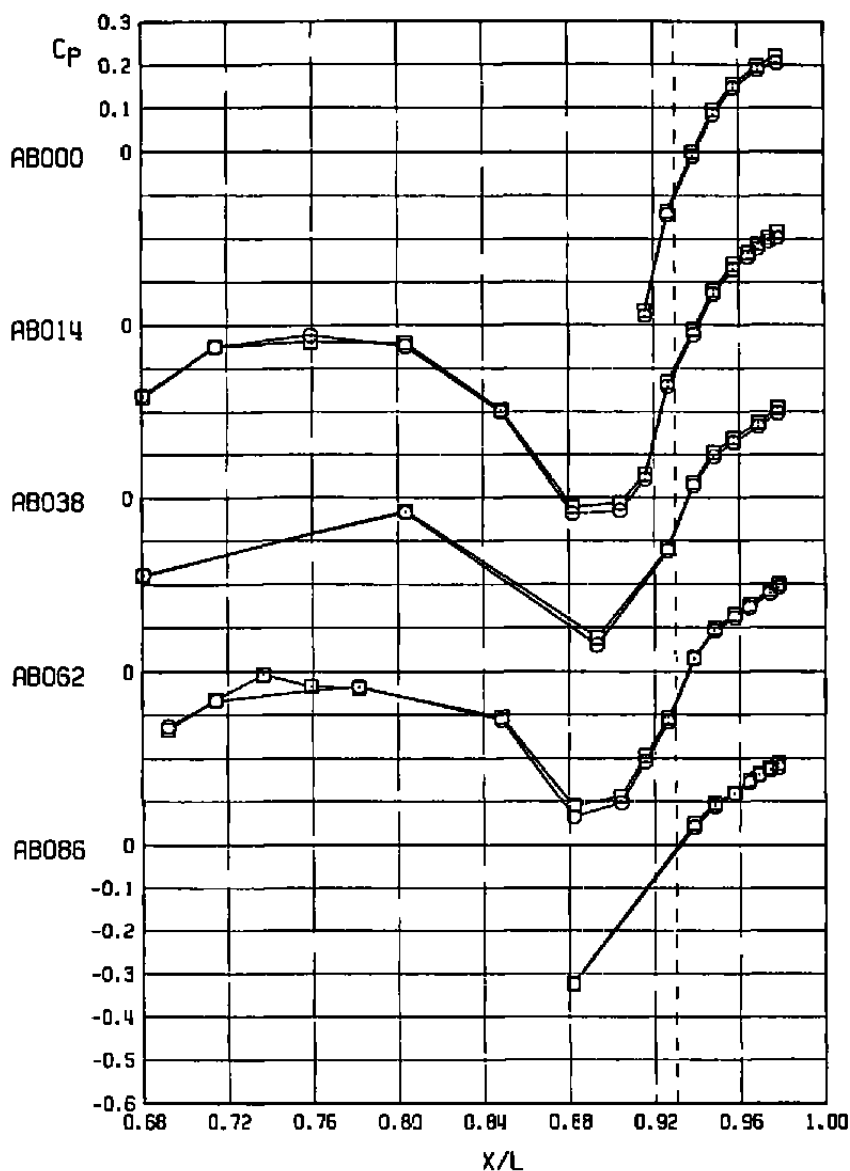


Figure 33. Comparison of annular and solid plume simulation of full plume effects on nozzle-afterbody axial-force coefficients, wingtip support system, cruise nozzle, design NPR, $\alpha = 0$.

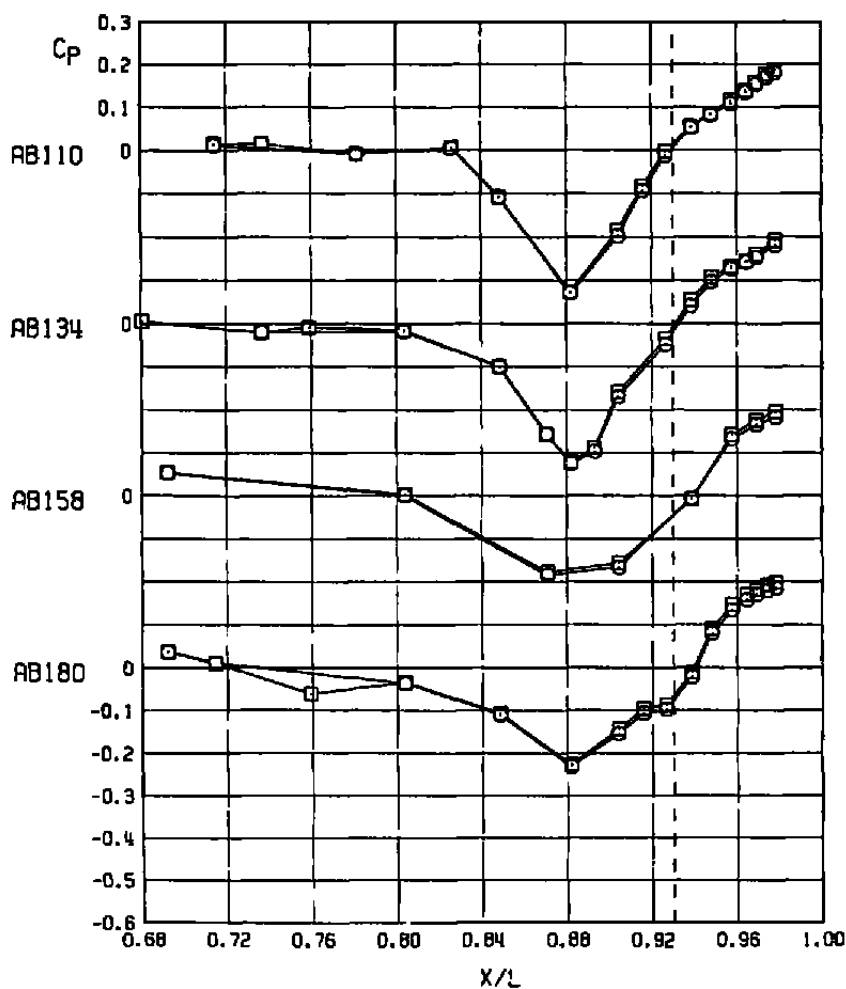
SYM	ALPHA	NPR	NPREFF	DELTA	CONF	M _∞	ANX10 ⁻⁶	CA	PN,PT
○	0.07	3.30	3.30	-0.20	3	0.90	3.40	0.00258	103.03
□	0.00	3.32	3.27	-0.00	27	0.90	3.39	0.00227	549.07



a. NPR = design

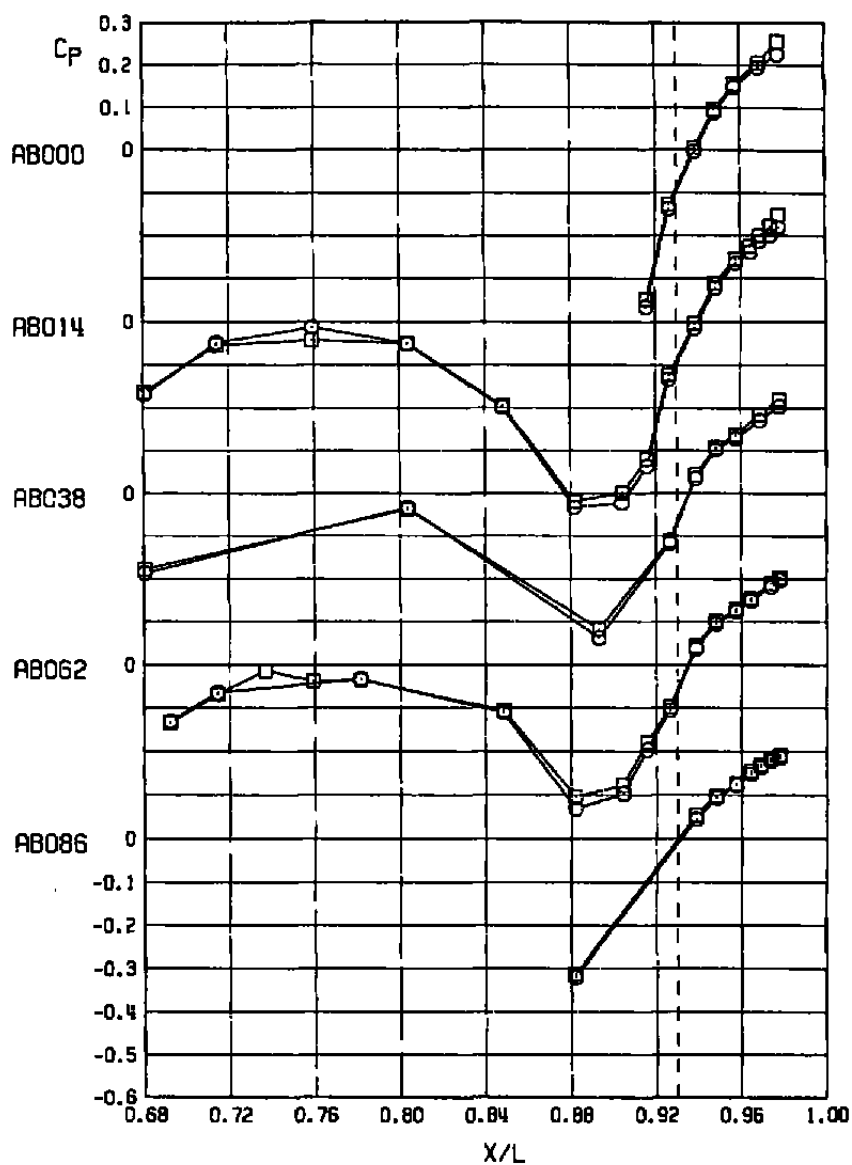
Figure 34. Pressure distributions comparing annular and full plume results, $M_{\infty} = 0.9$, wingtip support system, cruise nozzle, $\alpha = 0$.

SYM	ALPHA	NPR	NPREF	DELTA	CONF	M _∞	RNX10 ⁻⁵	CA	PN.PT
○	0.07	3.30	3.30	-0.20	3	0.90	3.40	0.00258	103.03
□	0.00	3.32	3.27	-0.00	27	0.90	3.39	0.00227	549.07



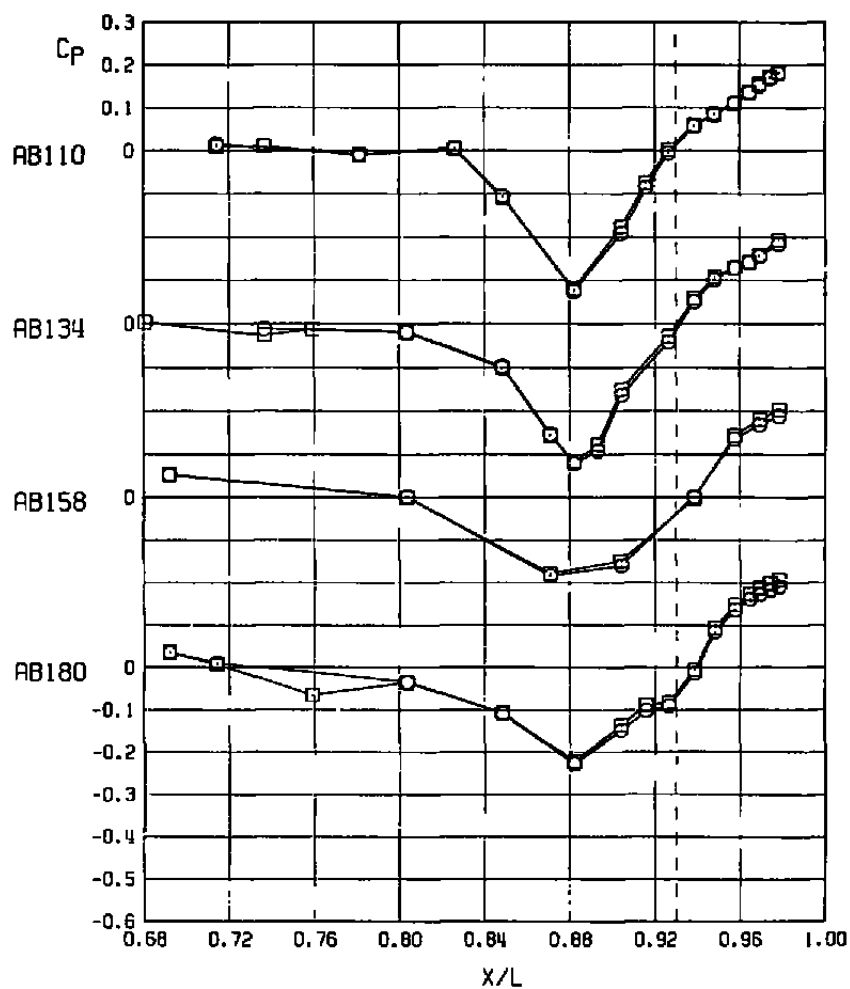
a. Concluded
Figure 34. Continued.

SYM	ALPHA	NPR	NPREFF	DELTA	CONF	M _∞	RNX10 ⁻⁶	CA	PN.PT
○	-0.01	4.99	4.99	-0.20	3	0.90	3.41	0.00235	107.03
□	-0.00	10.34	4.95	-0.00	27	0.90	3.40	0.00207	549.11



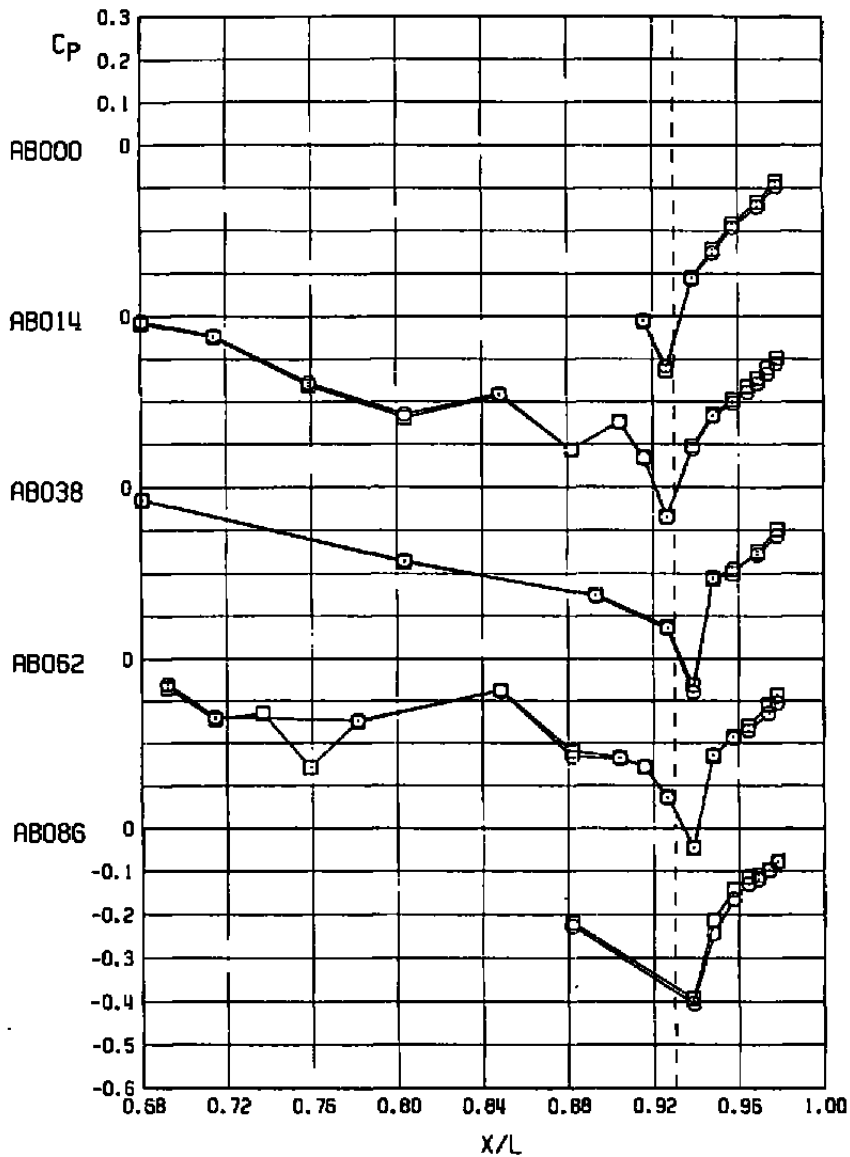
b. NPR = 1.5 x design
Figure 34. Continued.

SYM	ALPHA	NPR	NPREF	DELHR	CONF	M _L	RNX10 ⁻⁶	CA	PN.PT
○	-0.01	4.99	4.99	-0.20	3	0.90	3.41	0.00235	107.03
□	-0.00	10.34	4.95	-0.00	27	0.90	3.40	0.00207	549.11



b. Concluded
Figure 34. Concluded.

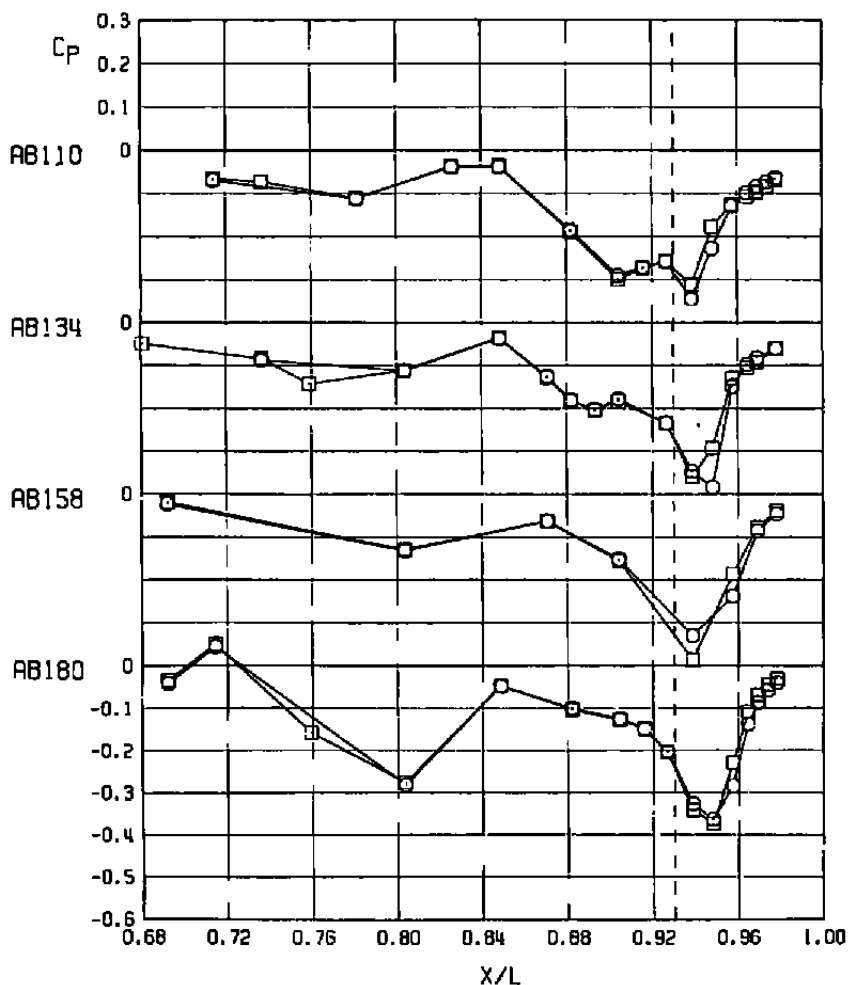
SYM	ALPHA	NPR	NPREFF	DELHR	CONF	M _∞	RNX10 ⁻⁸	CA	PN.PT
○	-0.02	3.22	3.22	-0.20	3	1.20	3.42	0.01184	95.03
□	0.05	3.22	3.25	-0.00	27	1.20	3.40	0.01186	543.11



a. NPR = design

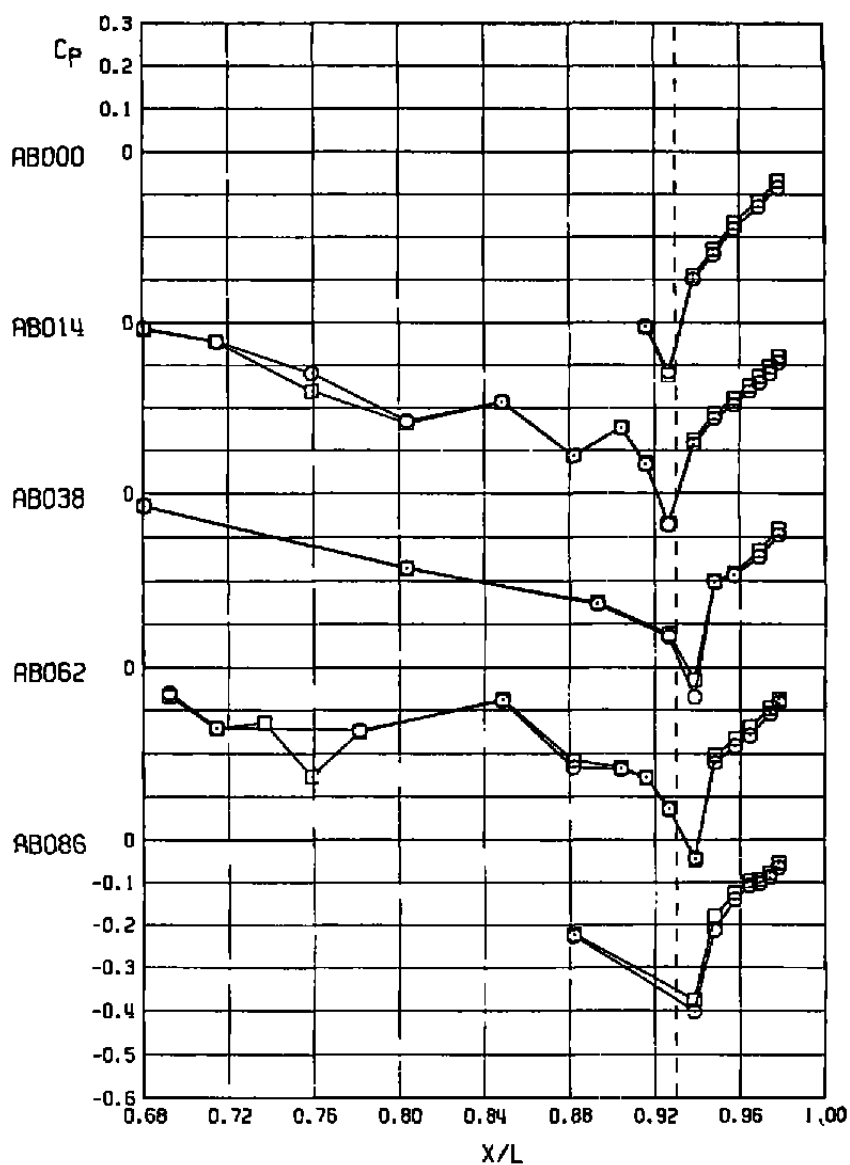
Figure 35. Pressure distributions comparing annular and full plume results, $M_{\infty} = 1.2$, wingtip support system, cruise nozzle, $\alpha = 0$.

SYM	ALPHA	NPR	NPREF	DELTA	CONF	M _∞	ANX10 ⁻⁶	CA	PN,PT
○	-0.02	3.22	3.22	-0.20	3	1.20	3.42	0.01184	95.03
□	0.05	3.22	3.25	-0.00	27	1.20	3.40	0.01185	543.11



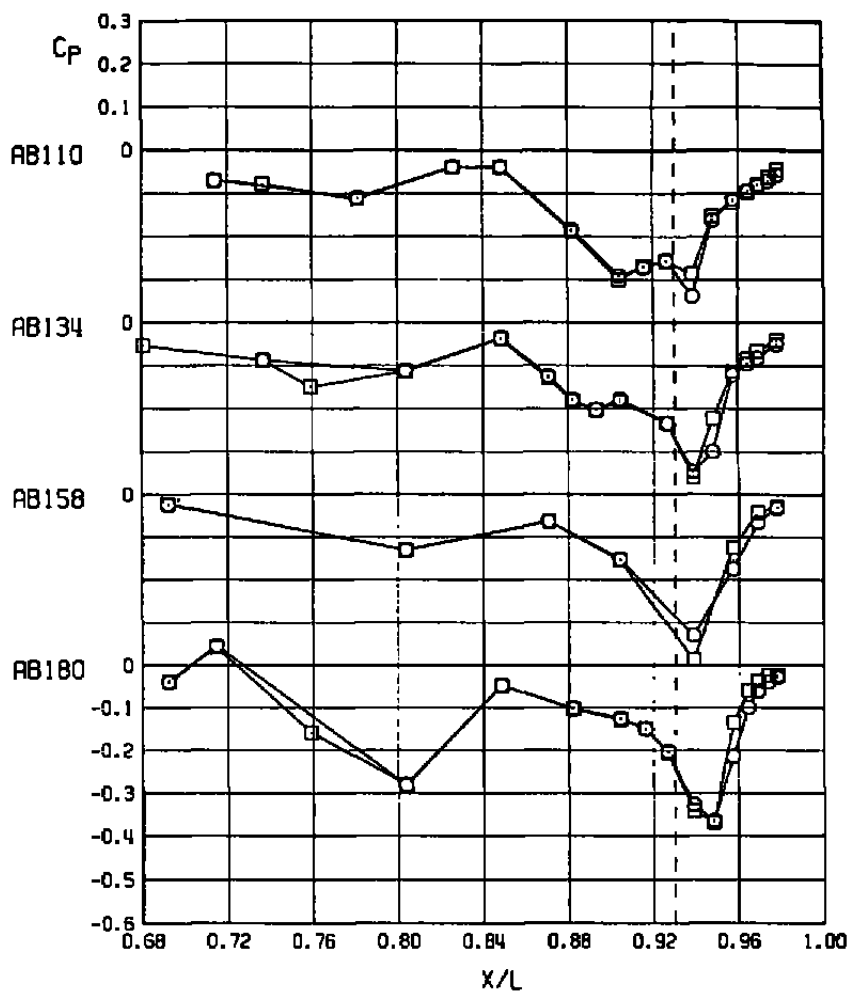
a. Concluded
Figure 35. Continued.

SYN	ALPHA	NPR	NPREF	DELTA	CONF	M _∞	ANX10-6	CA	PN.PT
○	-0.02	4.97	4.97	-0.20	3	1.20	3.39	0.01141	97.03
□	-0.06	10.43	4.97	-0.00	27	1.20	3.41	0.01137	543.15







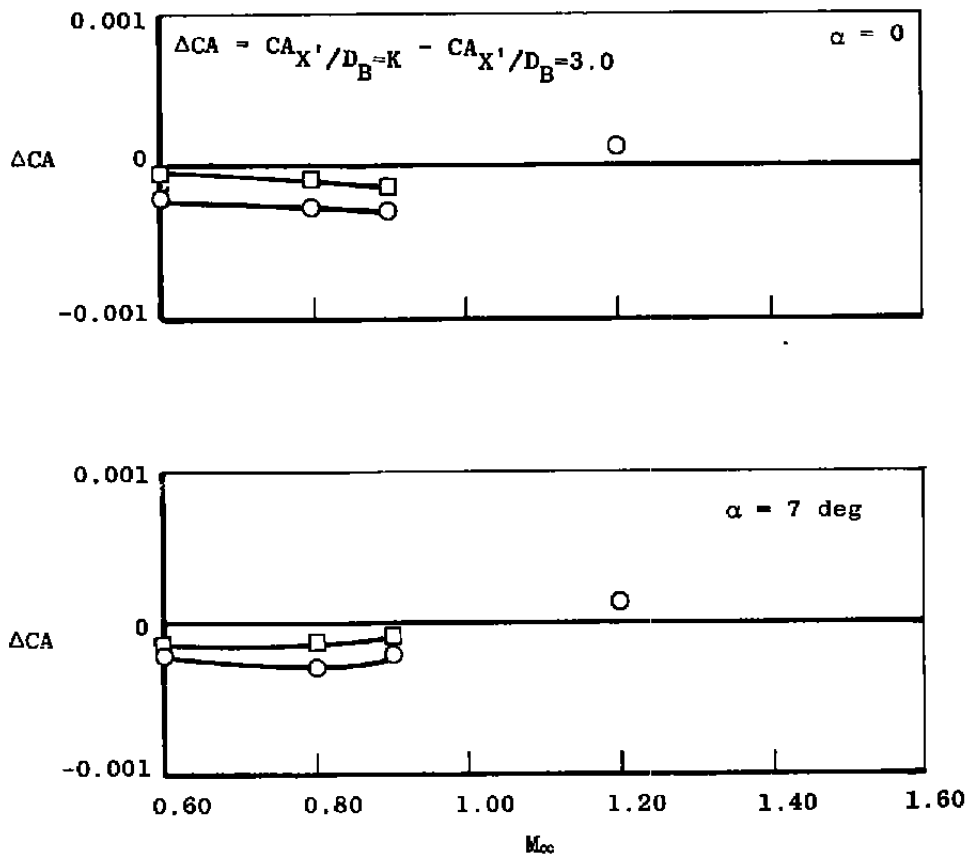
b. NPR = 1.5 x design
Figure 35. Continued.

SYM	ALPHA	NPR	NPREF	DELTA	CONF	M _∞	ANX10 ⁻⁶	CA	PN.PT
○	-0.02	4.97	4.97	-0.20	3	1.20	3.39	0.01141	97.03
□	-0.06	10.43	4.97	-0.00	27	1.20	3.41	0.01137	543.15



b. Concluded
Figure 35. Concluded.

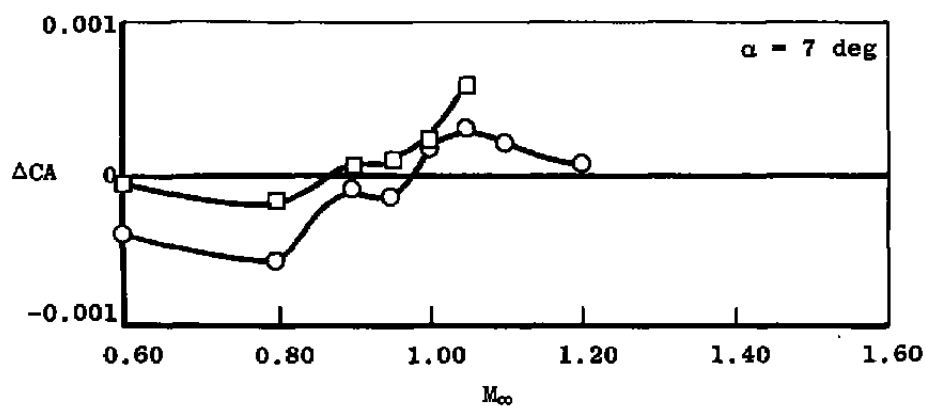
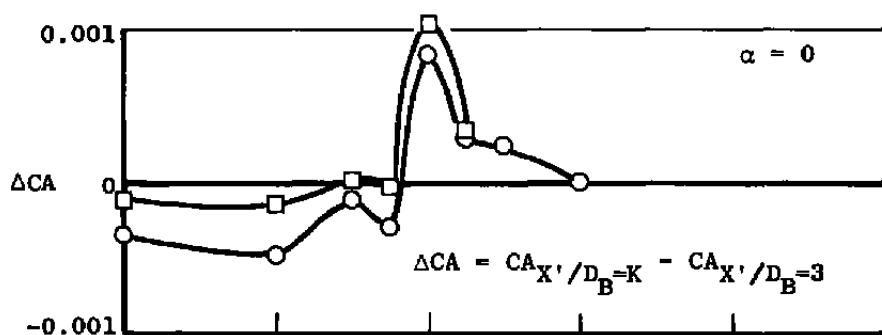
Sym	X'/D_B	Configurations		X_1/D_M
○	1.0		— 	3.825
□	1.5		— 	4.538



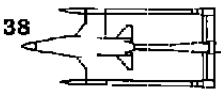
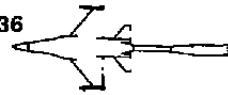
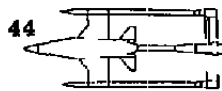
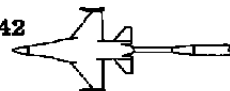
a. NPR = jet off

Figure 36. Effect of sting taper location on the nozzle-afterbody axial-force coefficients, wingtip support system, max A/B 6.6 nozzle.

Sym	X'/D_B	Configurations		$X_1 D_M$
○	1.0	60	54	3.825
□	1.5	61	54	4.538



b. NPR = 4.8
Figure 36. Concluded.

<u>Sym</u>	<u>Nozzle</u>	<u>NPR</u>	<u>Configurations</u>
○	Cruise 3.4	J. Off	38  36 
□	Max A/B 6.6	4.8	44  42 

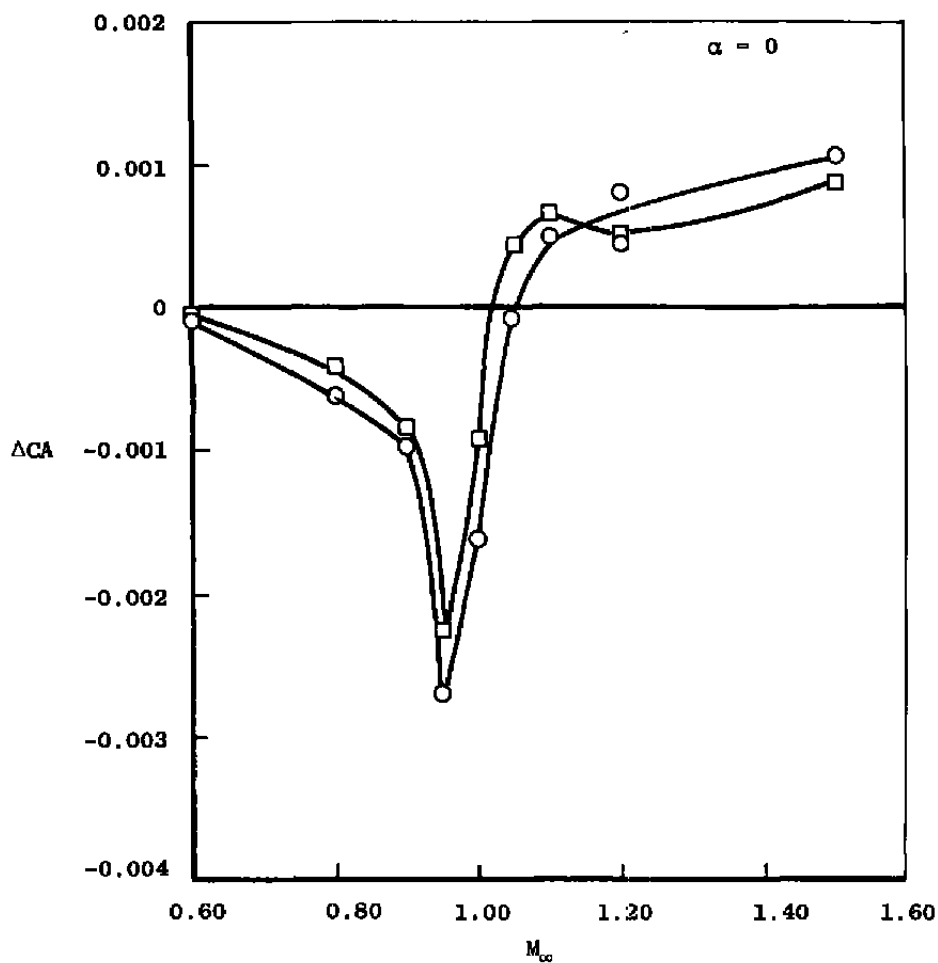
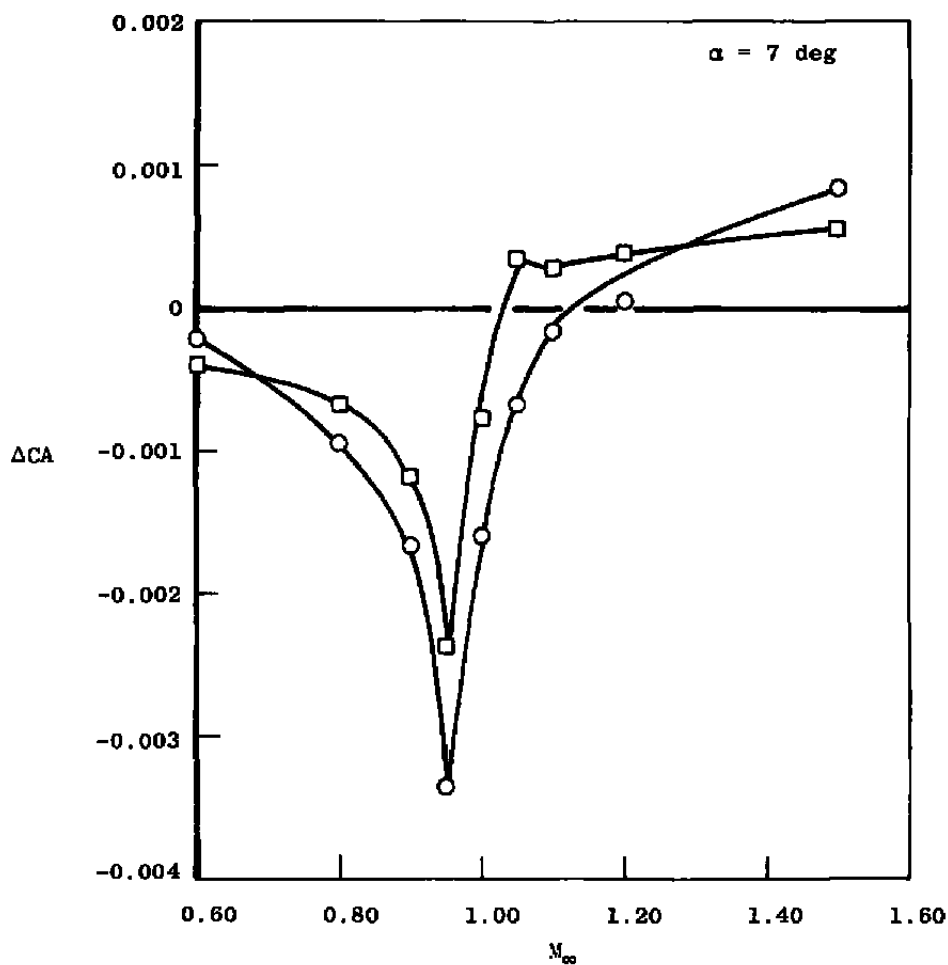
a. $\alpha = 0$

Figure 37. Total wingtip support system interference on nozzle-afterbody axial force, large sting support system.

<u>Sym</u>	<u>Nozzle</u>	<u>NPR</u>	<u>Configurations</u>	
○	Cruise 3.4	J. Off	38	36
□	Max A/B 6.6	4.8	44	42



b. $\alpha = 7 \text{ deg}$
Figure 37. Concluded.

Sym	Nozzle	NPR	Configurations	
○	Cruise 3.4	J. Of1	38	36
□	Max A/B 6.6	4.8	44	42

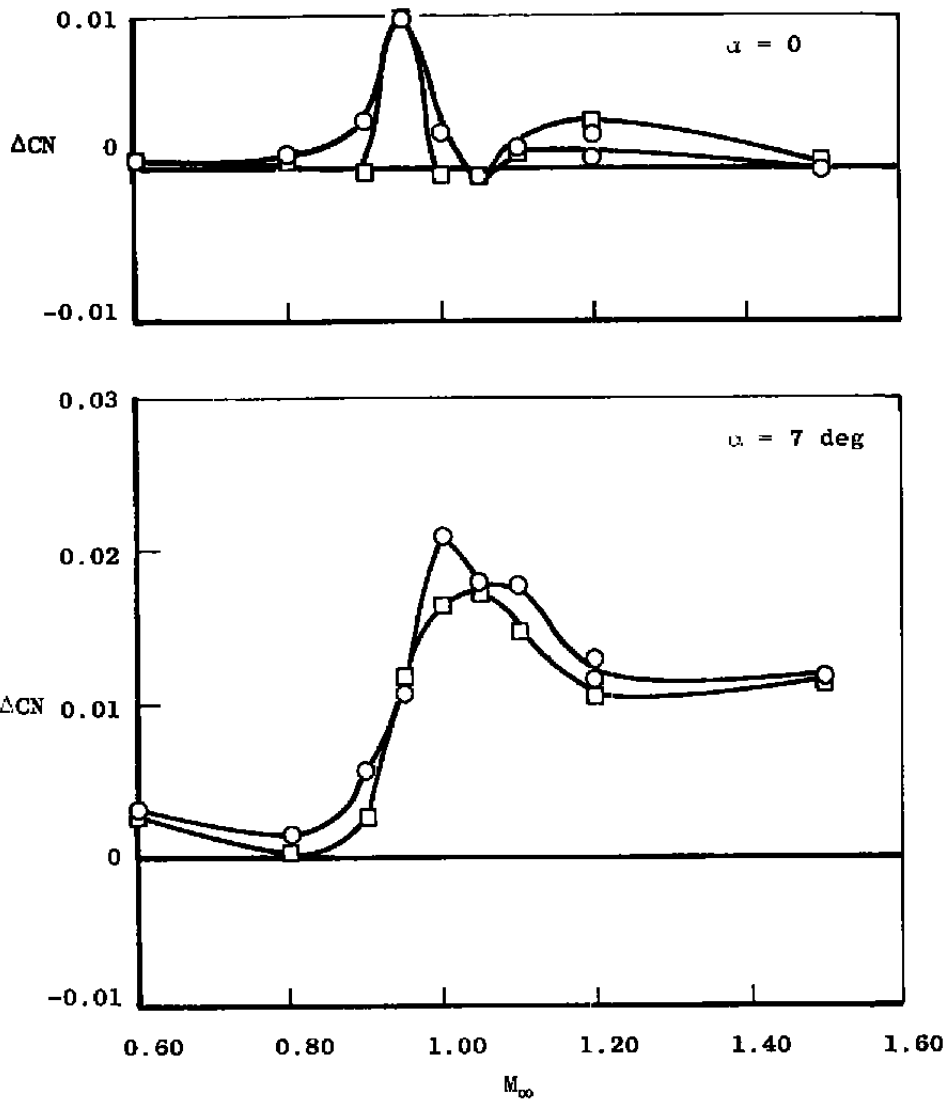


Figure 38. Total wingtip support system interference on nozzle-afterbody normal force, large sting support system.

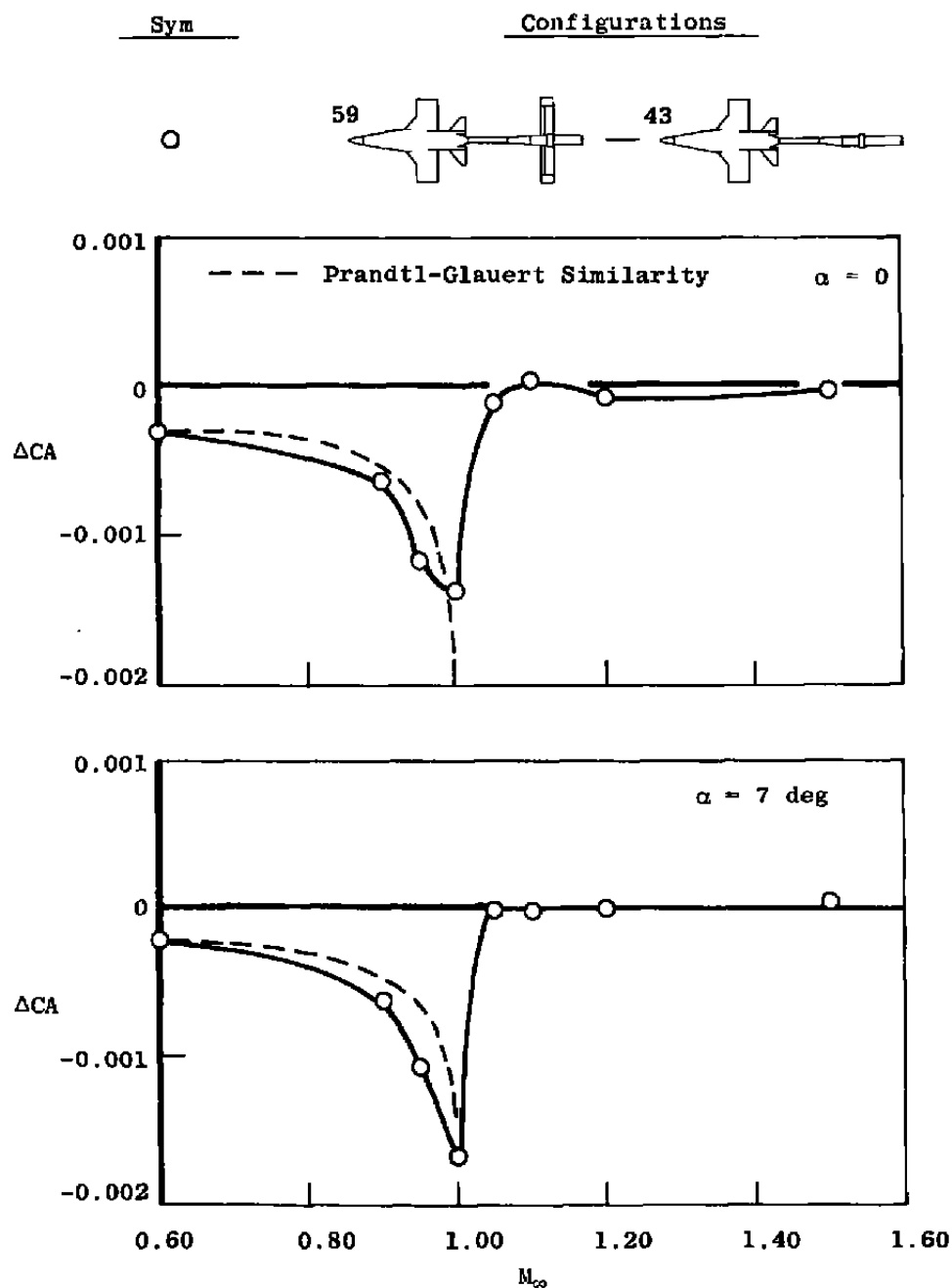


Figure 39. Aft support blade interference on nozzle-afterbody axial force, large sting support system, max A/B 6.6 nozzle, NPR = 4.8.

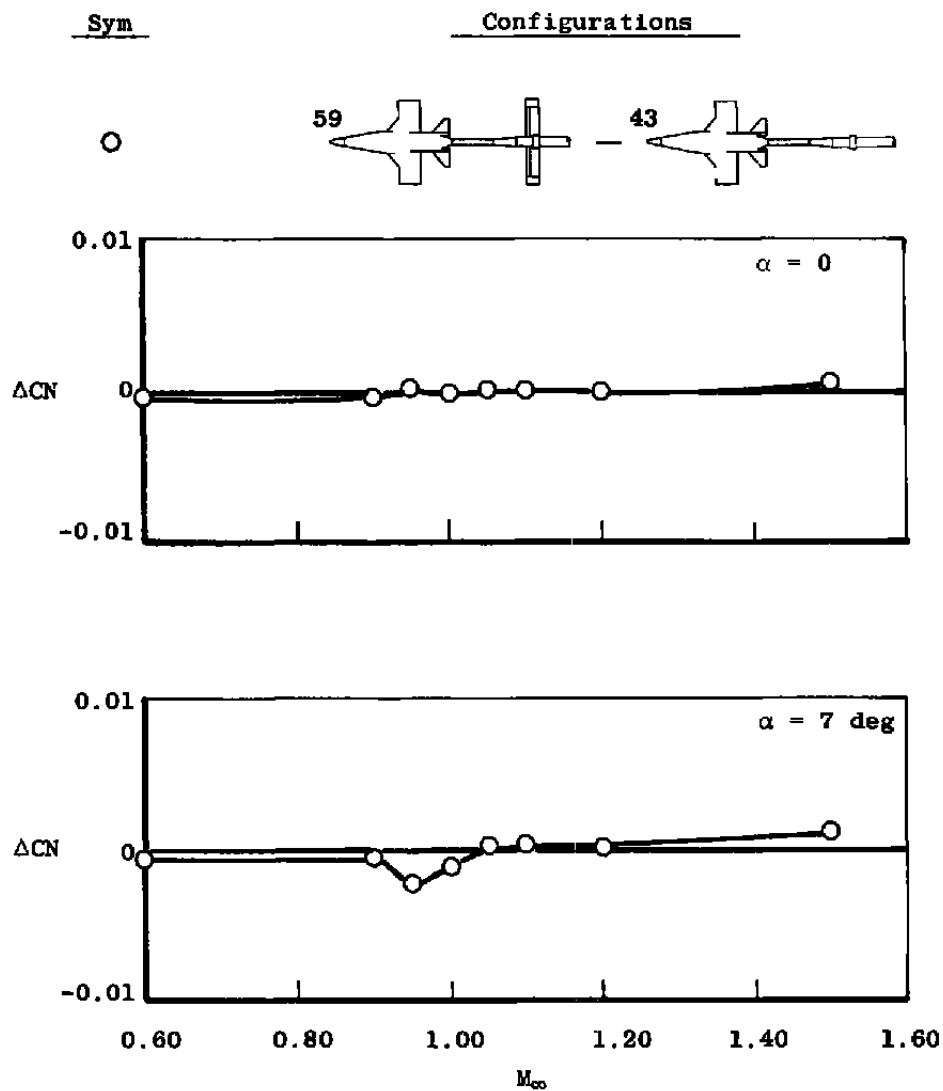


Figure 40. Aft support blade interference on nozzle-afterbody axial force, large sting support system, max A/B 6.6 nozzle, NPR = 4.8.

Sym	Blade Location	Support Systems	Configurations	
○	10.6 in. Fwd	Wingtip	10	14
□	6.75 in. Aft	Large Sting	58	44

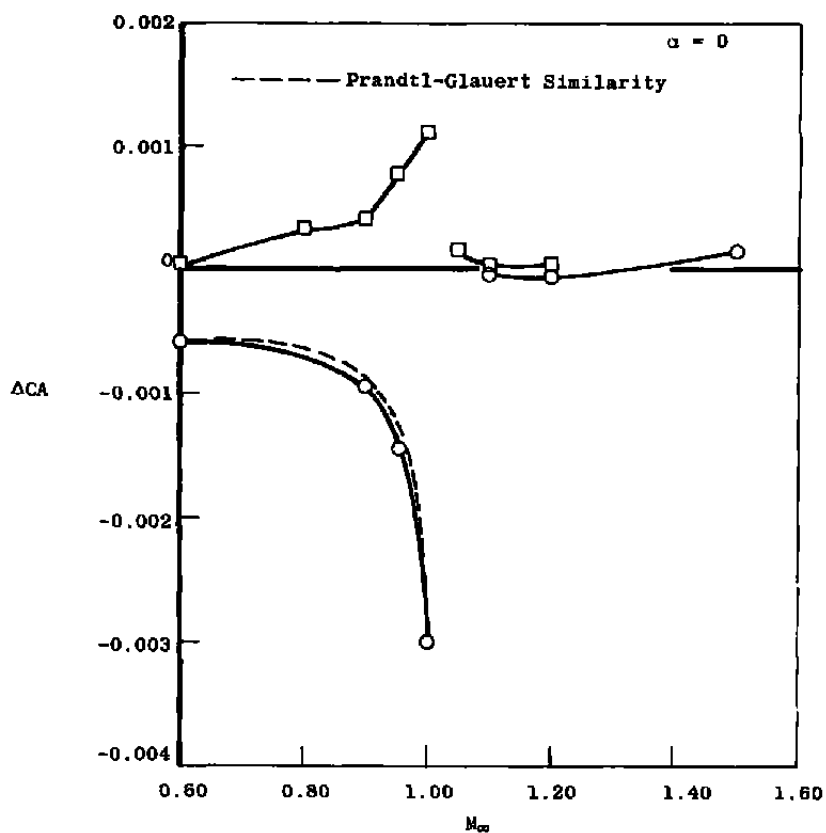
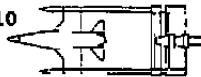
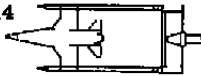
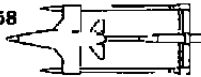
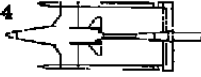
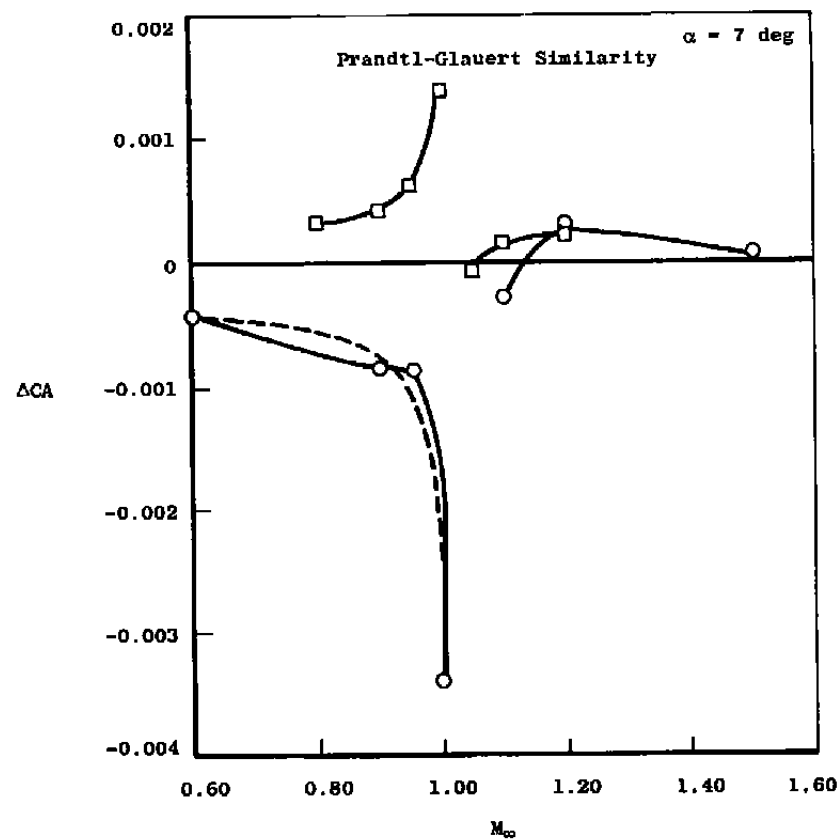
a. $\alpha = 0$

Figure 41. Effect of aft support blade movement on nozzle-afterbody axial force, max A/B 6.6 nozzle, NPR = 4.8.

<u>Sym</u>	<u>Blade Locations</u>	<u>Support Systems</u>	<u>Configurations</u>
○	10.6 in. Fwd	Wingtip	10  - 14 
□	6.75 in. Aft	Large Sting	58  - 44 



b. $\alpha = 7 \text{ deg}$
Figure 41. Concluded.

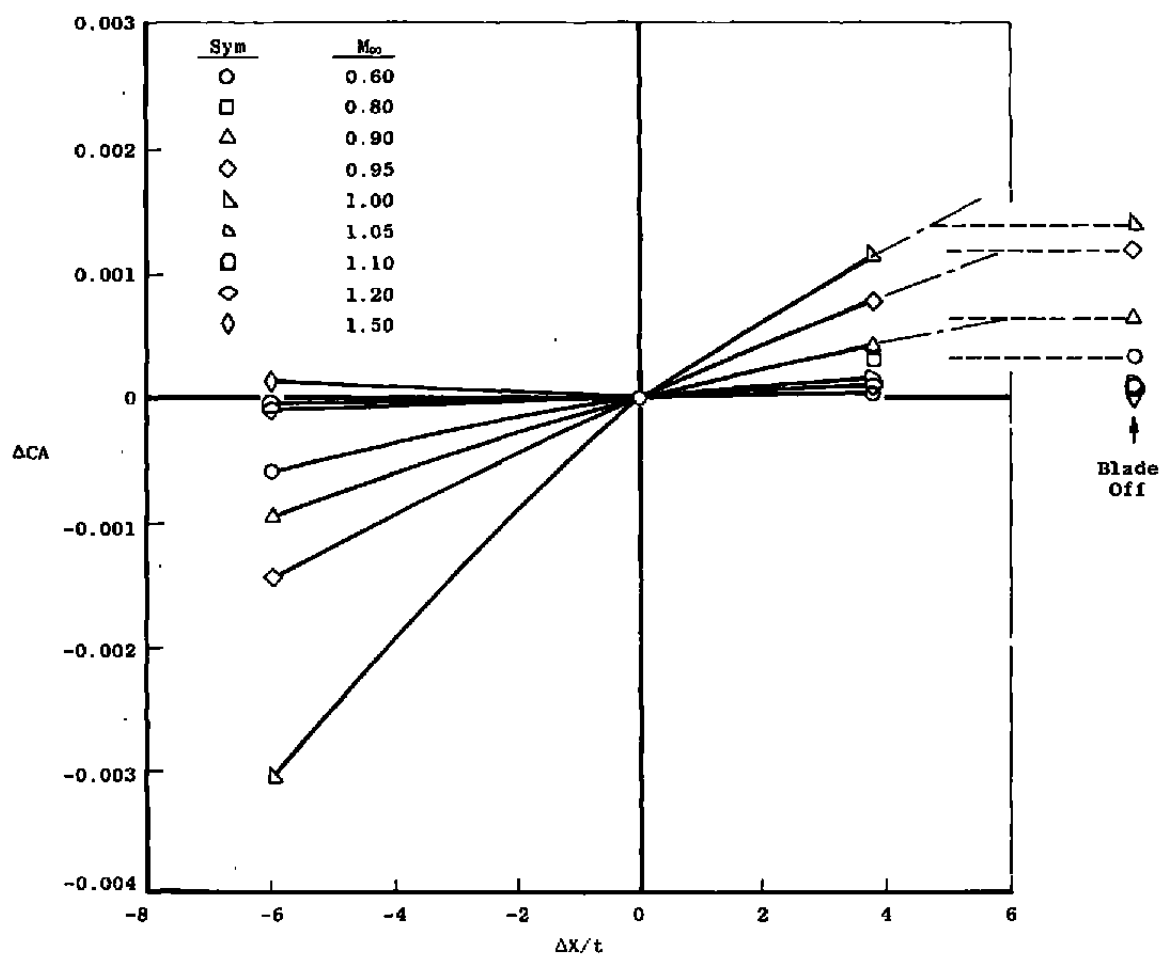


Figure 42. Sensitivity of nozzle-afterbody axial force to aft support blade position, max A/B 6.6 nozzle, NPR = 4.8, $\alpha = 0$.

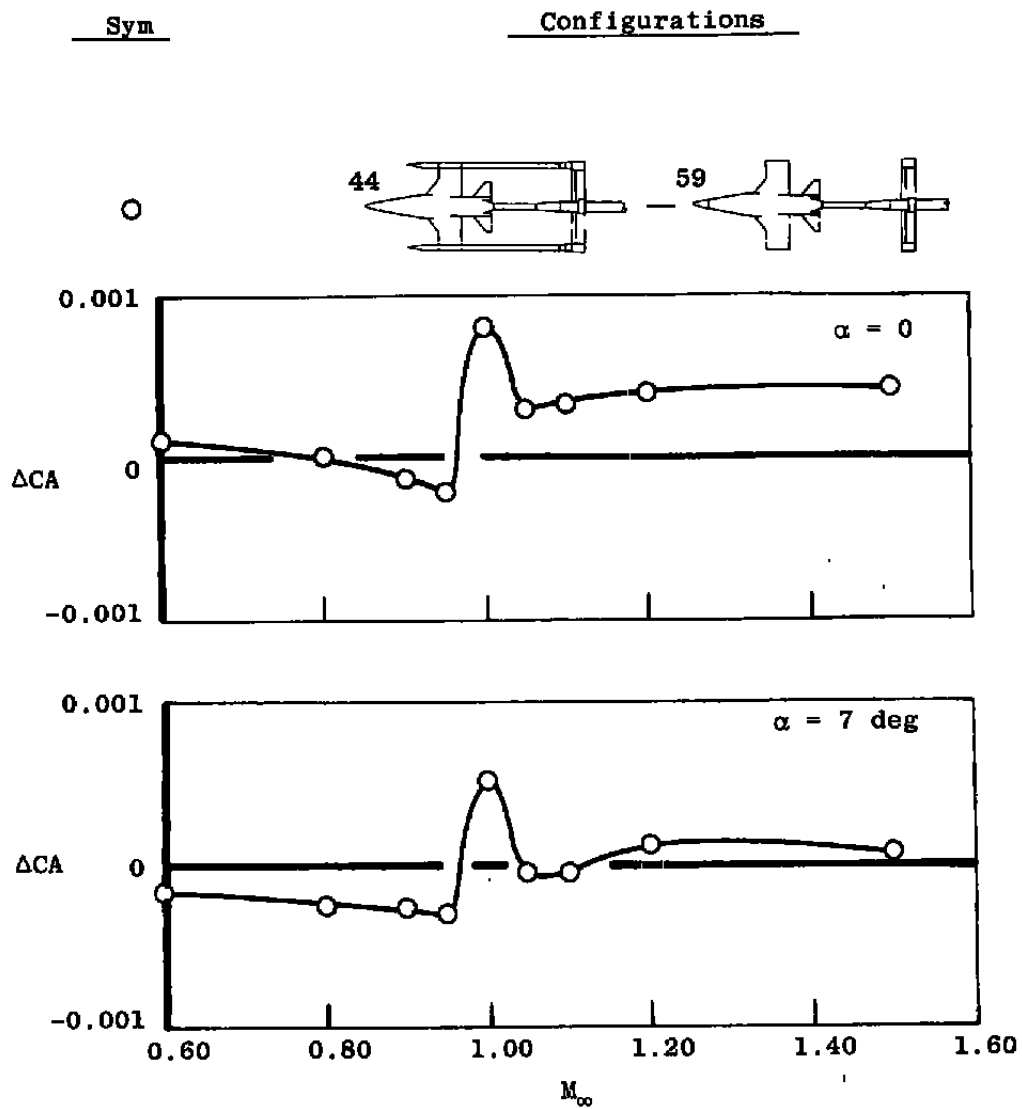


Figure 43. Wingtip boom interference on nozzle-afterbody axial force, large sting support system, max A/B 6.6 nozzle, NPR = 4.8.

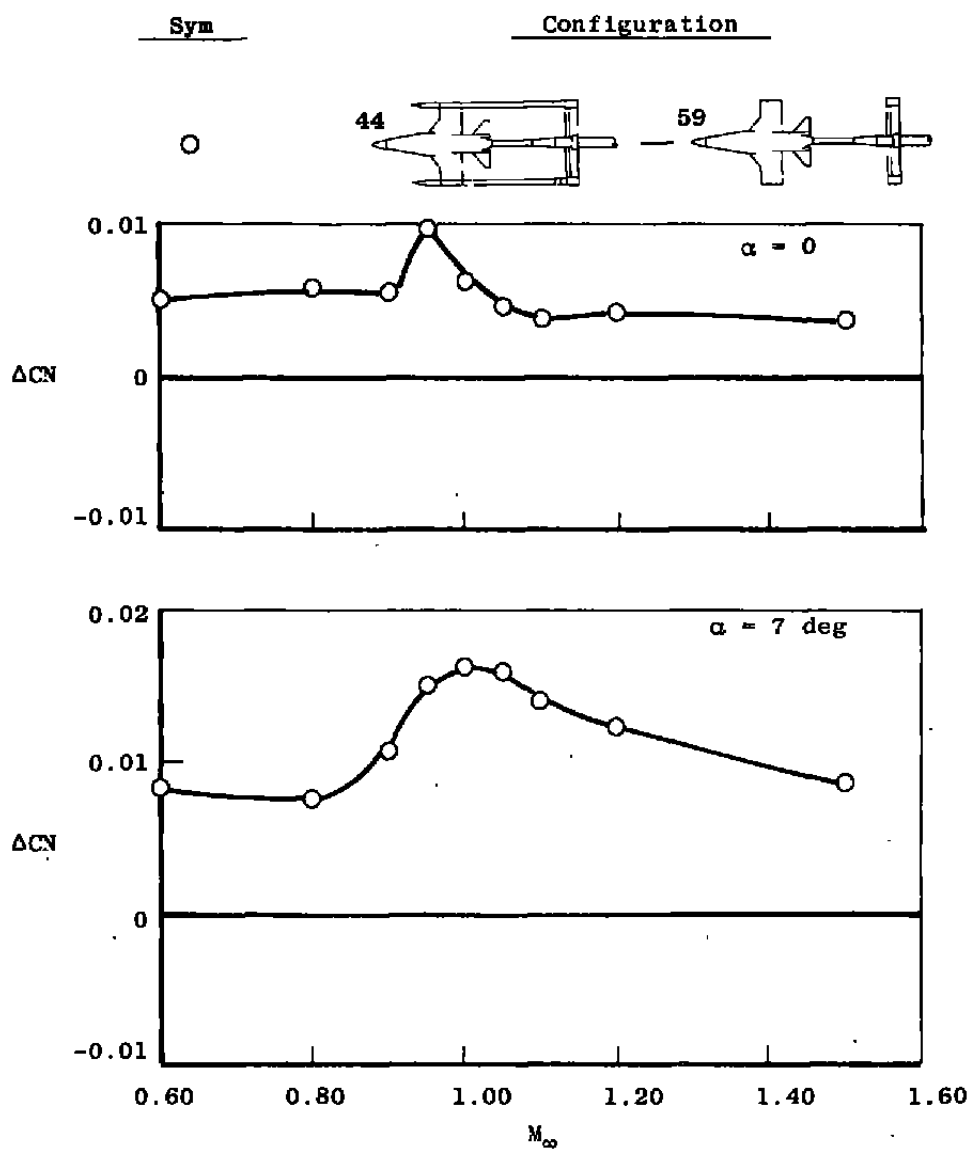


Figure 44. Wingtip boom interference on nozzle-afterbody normal force, large sting support system, max A/B 6.6 nozzle, NPR = 4.8.

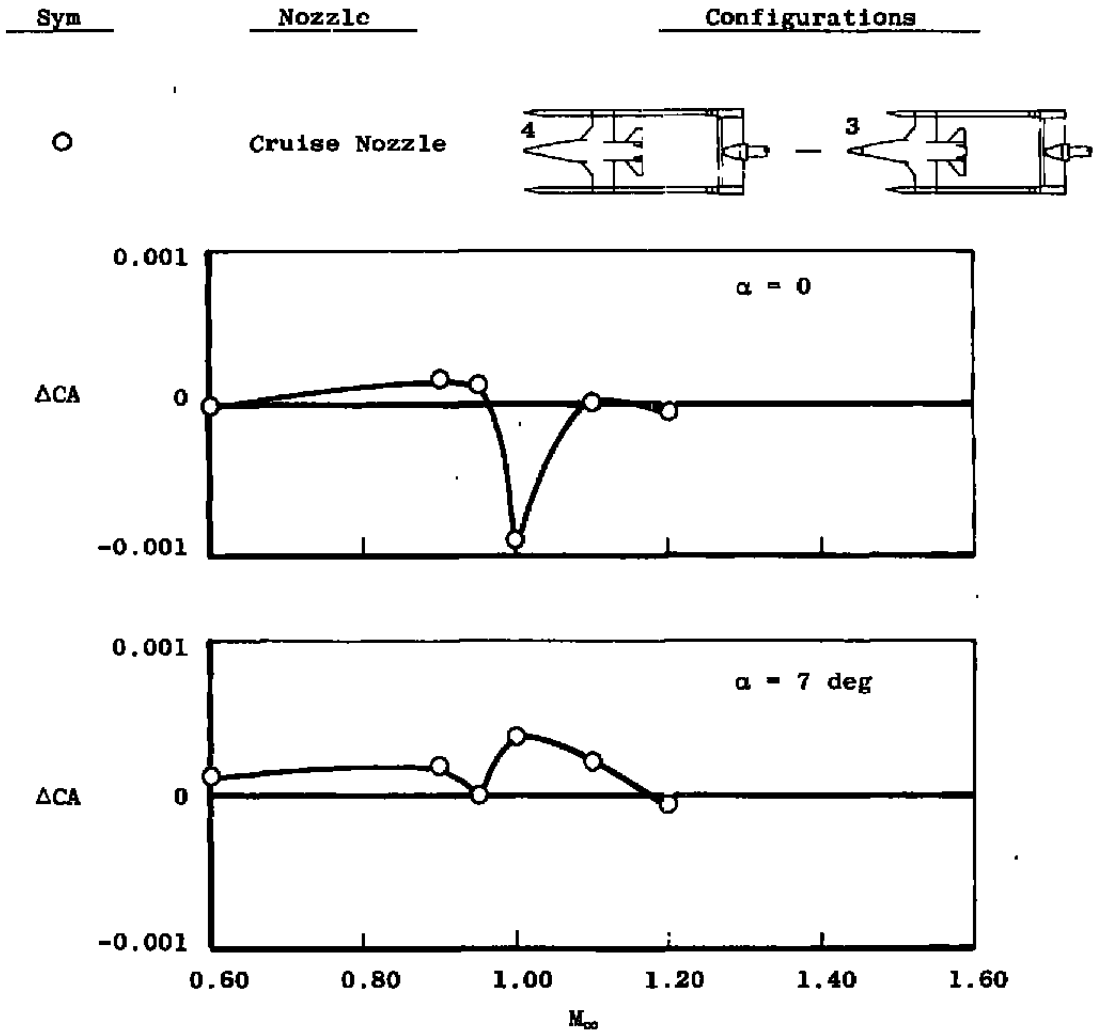


Figure 45. Effect of boom-tip axial location on nozzle-afterbody axial force, wingtip support system, cruise 3.4 nozzle, NPR = 3.3.

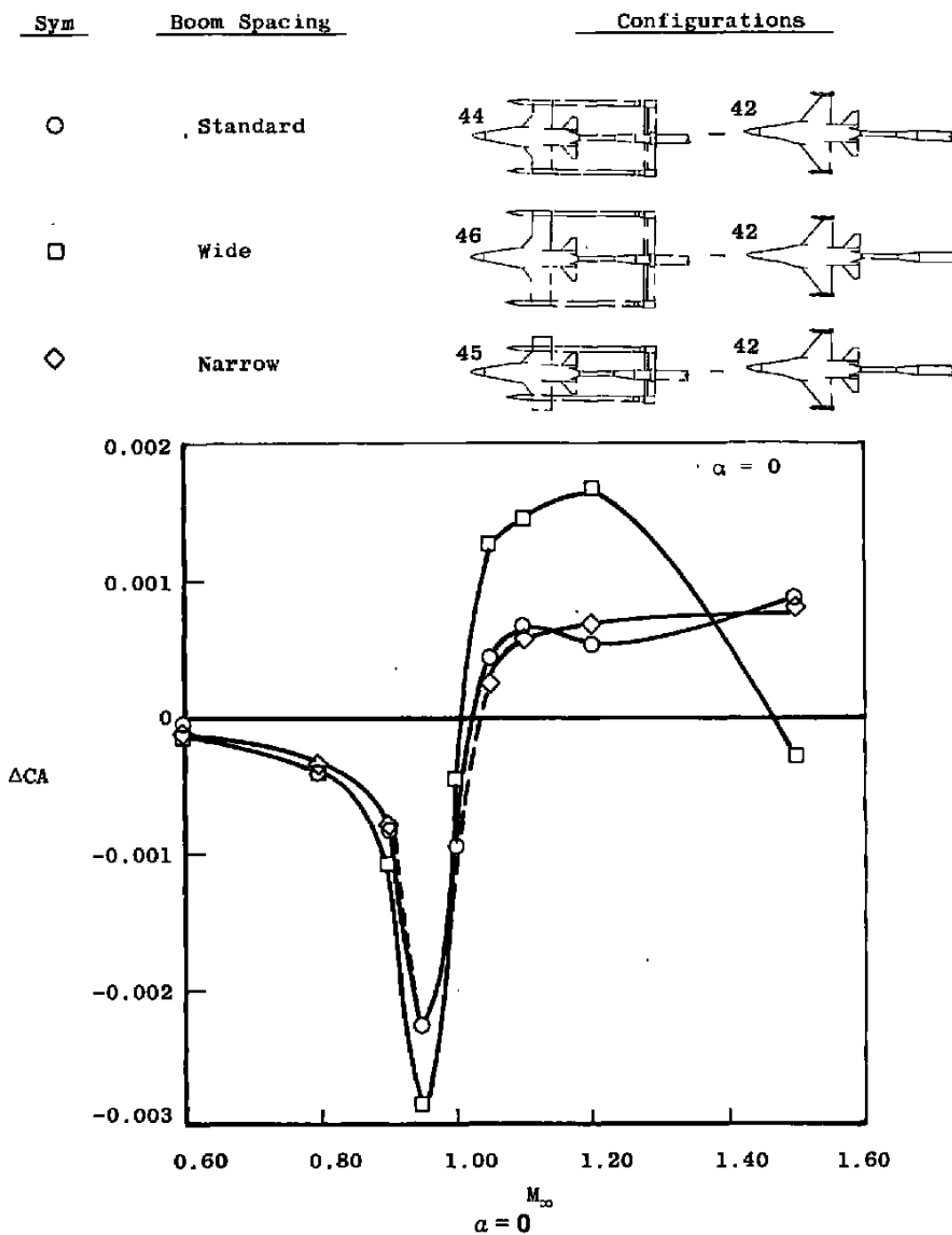
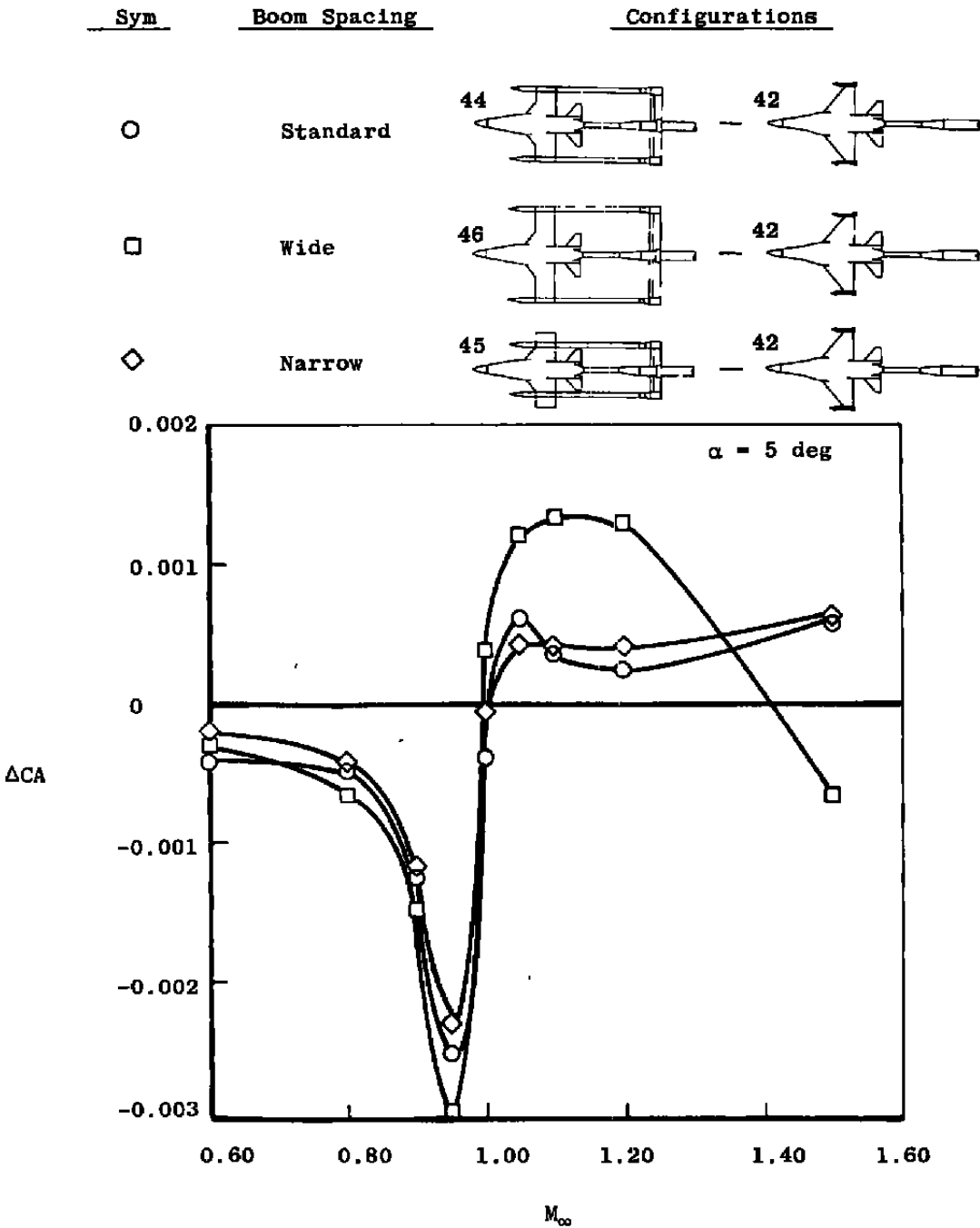


Figure 46. Effect of wingtip boom lateral spacing on nozzle-afterbody axial force, large sting support system, max A/B 6.6 nozzle, NPR 4.8.



b. $\alpha = 5 \text{ deg}$
Figure 46. Concluded.

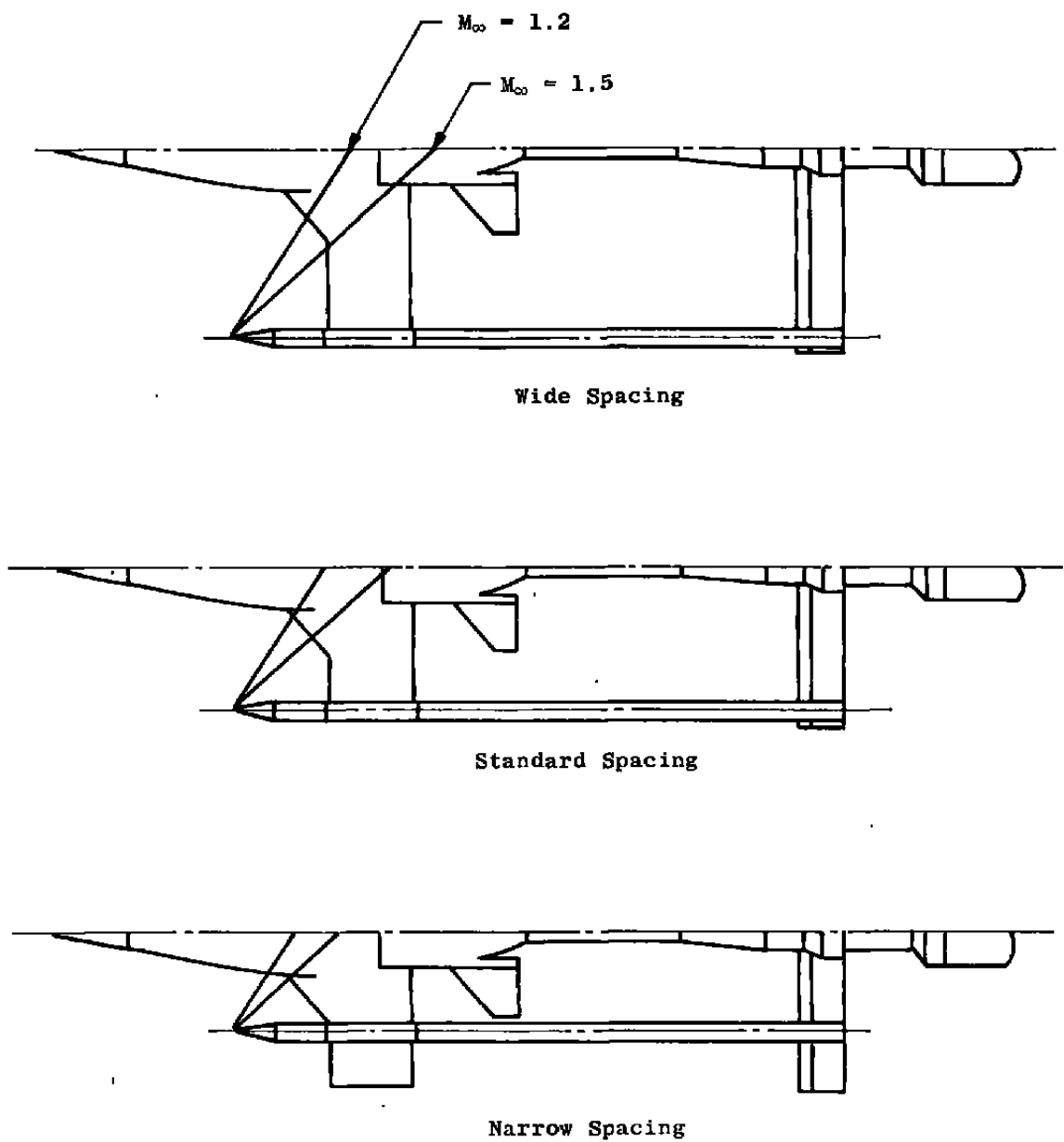


Figure 47. Illustration of boom-tip shock wave interaction with model.

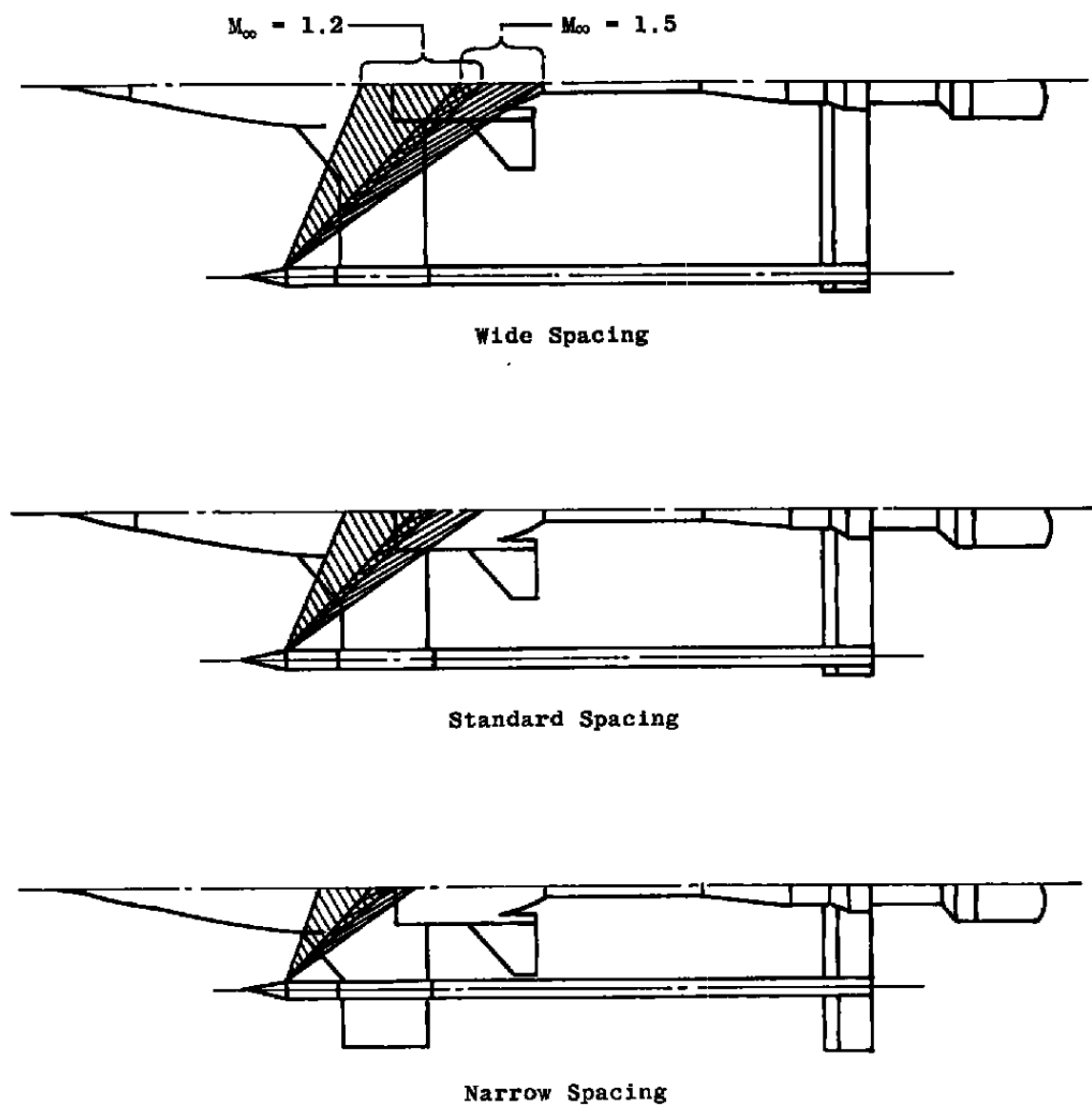


Figure 48. Illustration of boom-tip expansion fan interaction with model.

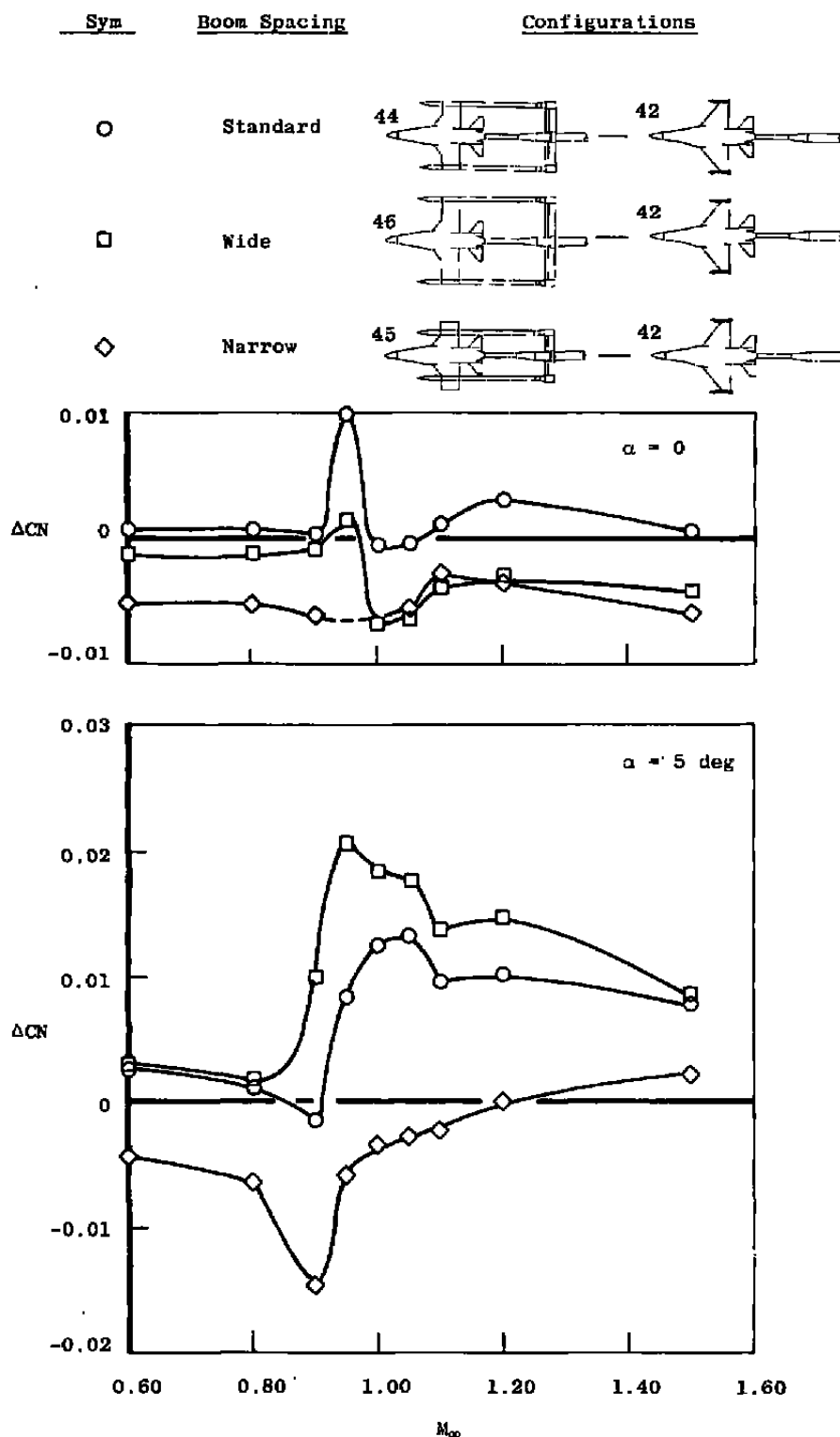


Figure 49. Effect of wingtip boom lateral spacing on nozzle-afterbody normal force, large sting support system, max A/B 6.6 nozzle, NPR = 4.8.

Sym	Nozzle	NPR	Configurations
○	Cruise 3.4	3.3	6 3
□	Max A/B 6.6	4.8	11 14

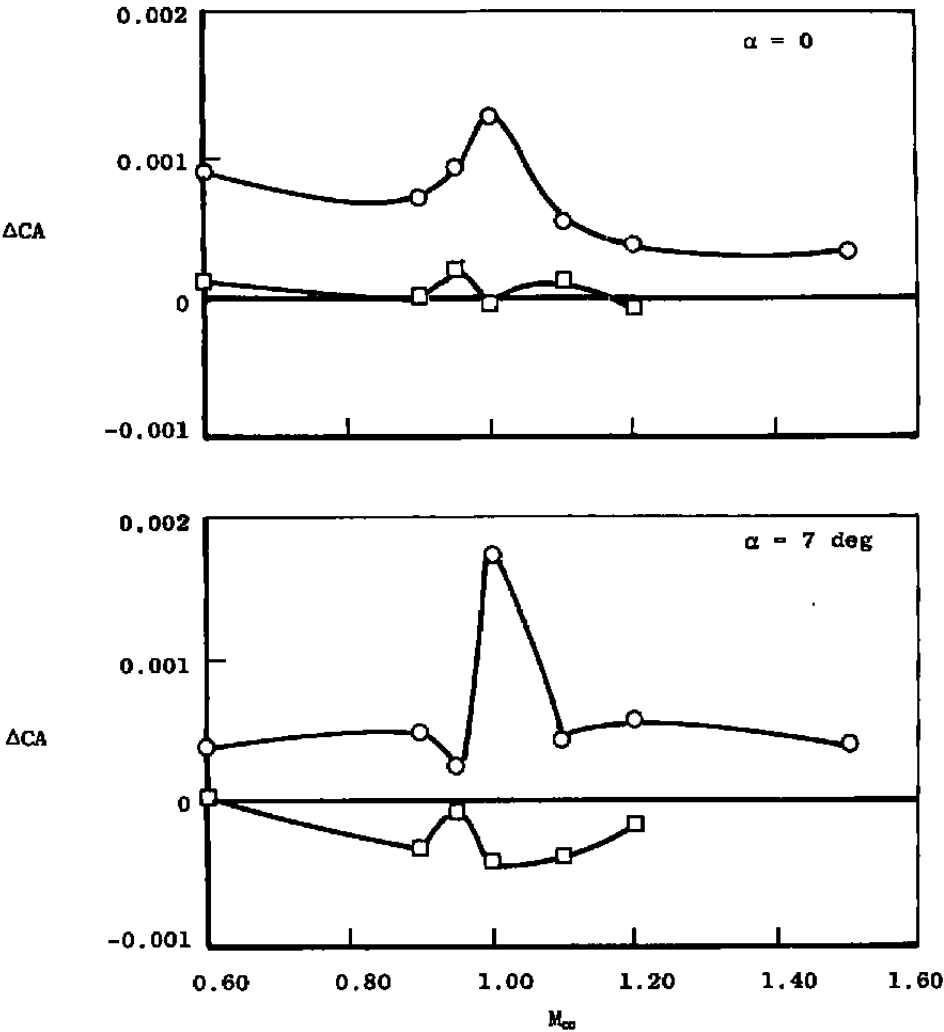


Figure 50. Effect of wingtip boom diameter on nozzle-afterbody axial force, wingtip support system.

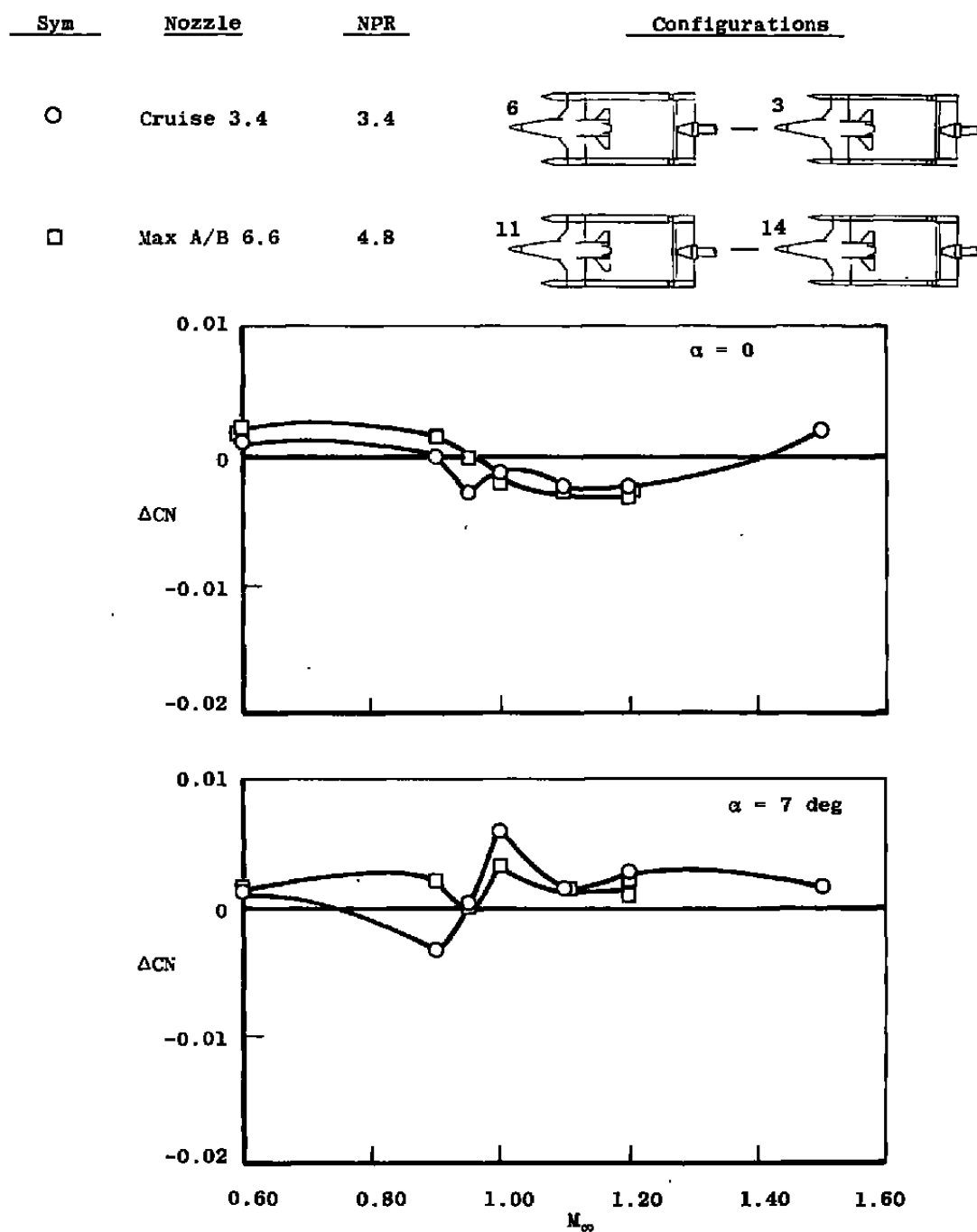


Figure 51. Effect of wingtip boom diameter on nozzle-afterbody normal force, wingtip support system.

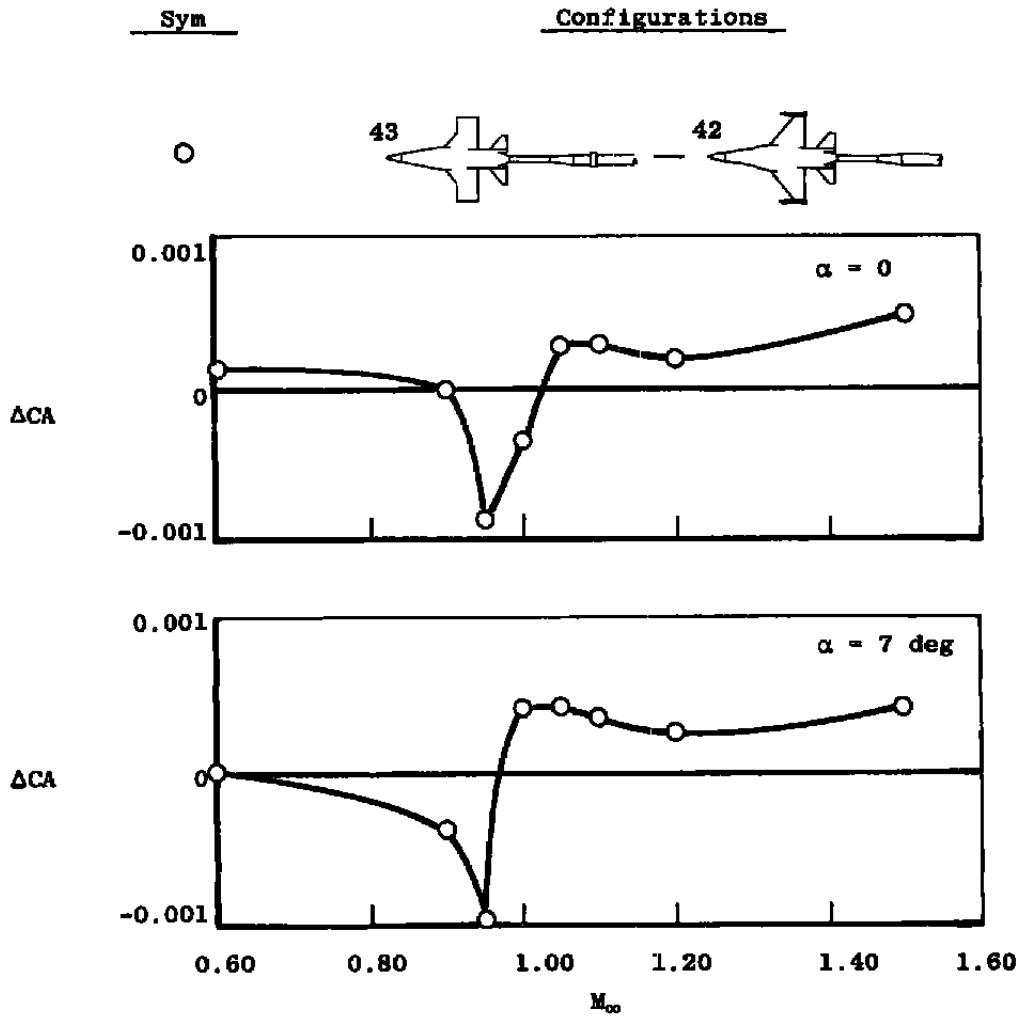


Figure 52. Effect of wing-planform modification on nozzle-afterbody axial force, large sting support system, max A/B 6.6 nozzle, NPR = 4.8.

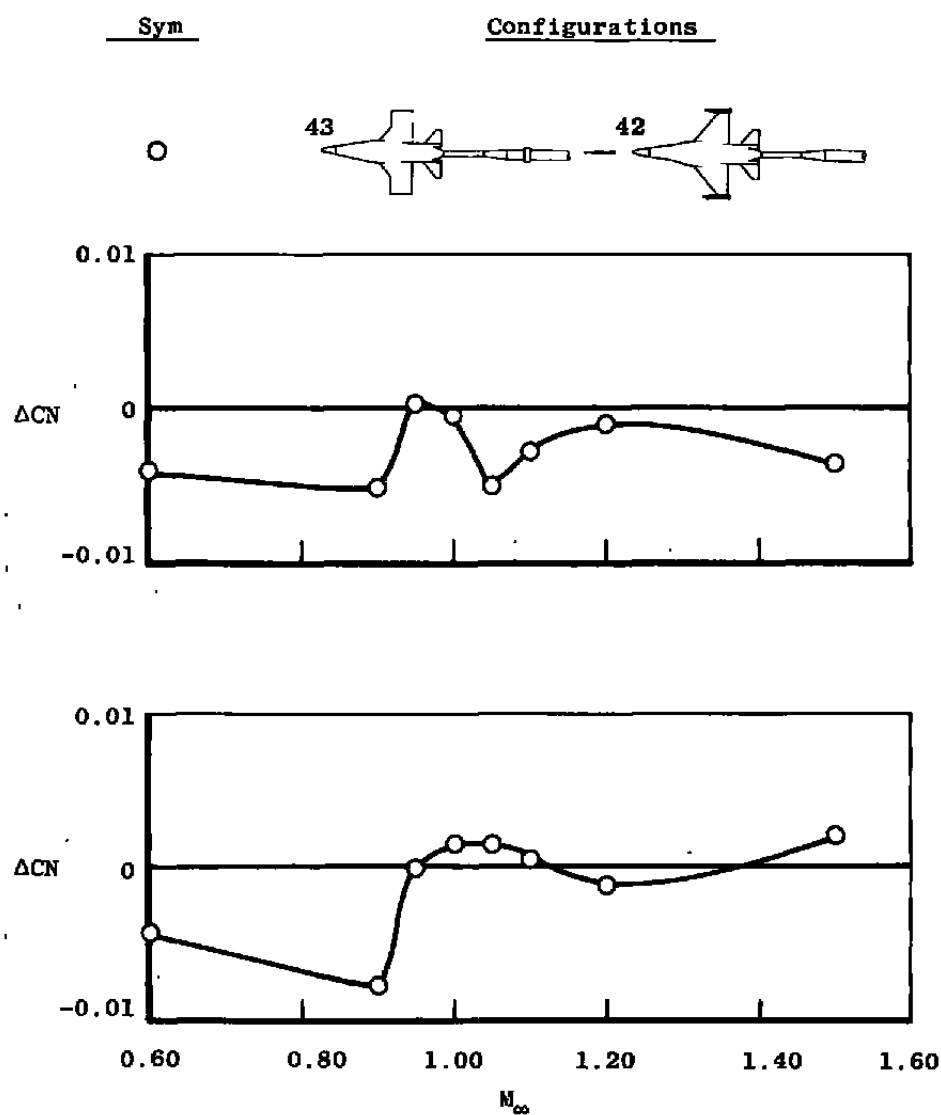


Figure 53. Effect of wing-planform modification on nozzle-afterbody normal force, large sting support system, max A/B 6.6 nozzle, NPR = 4.8.

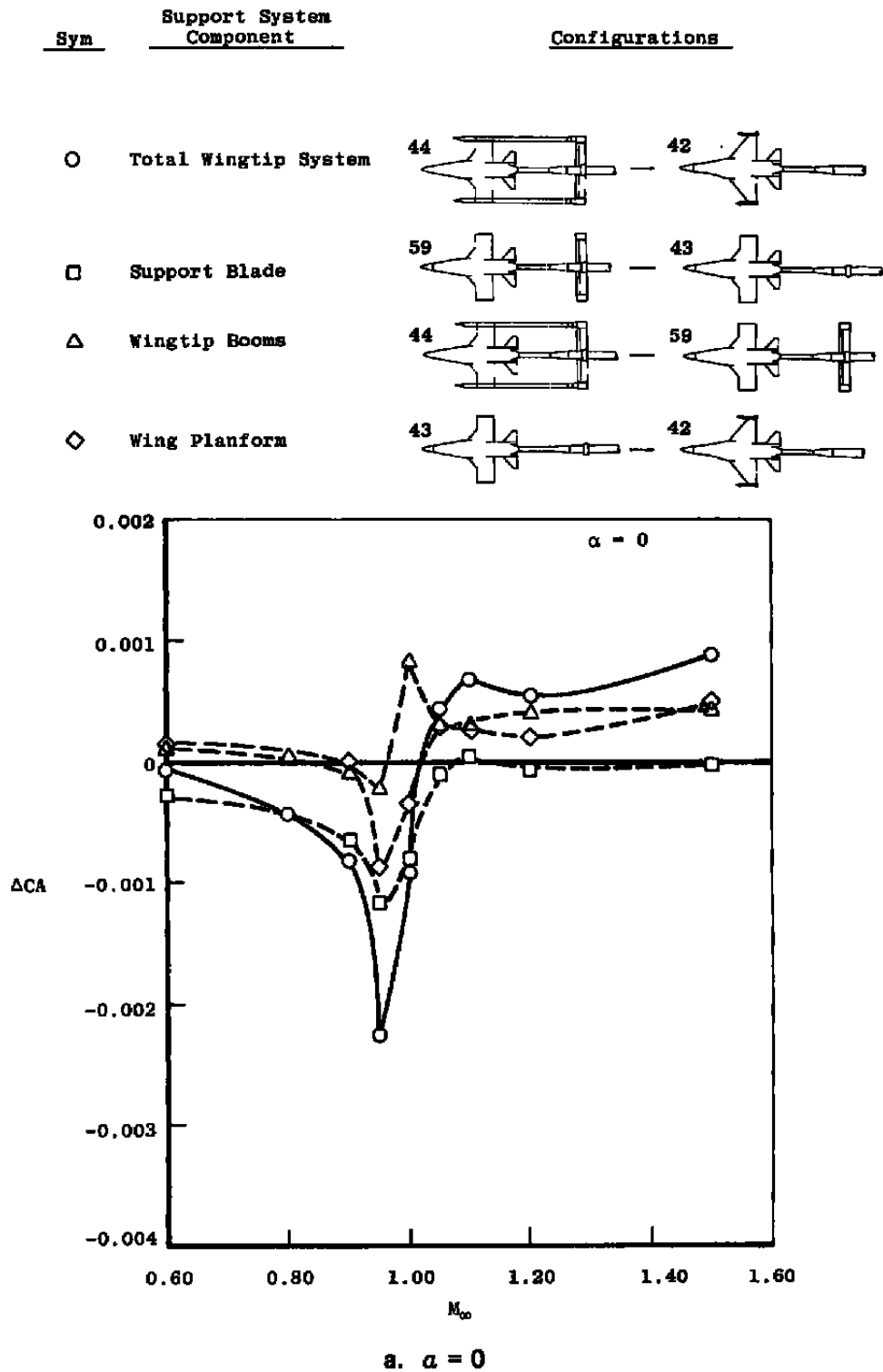
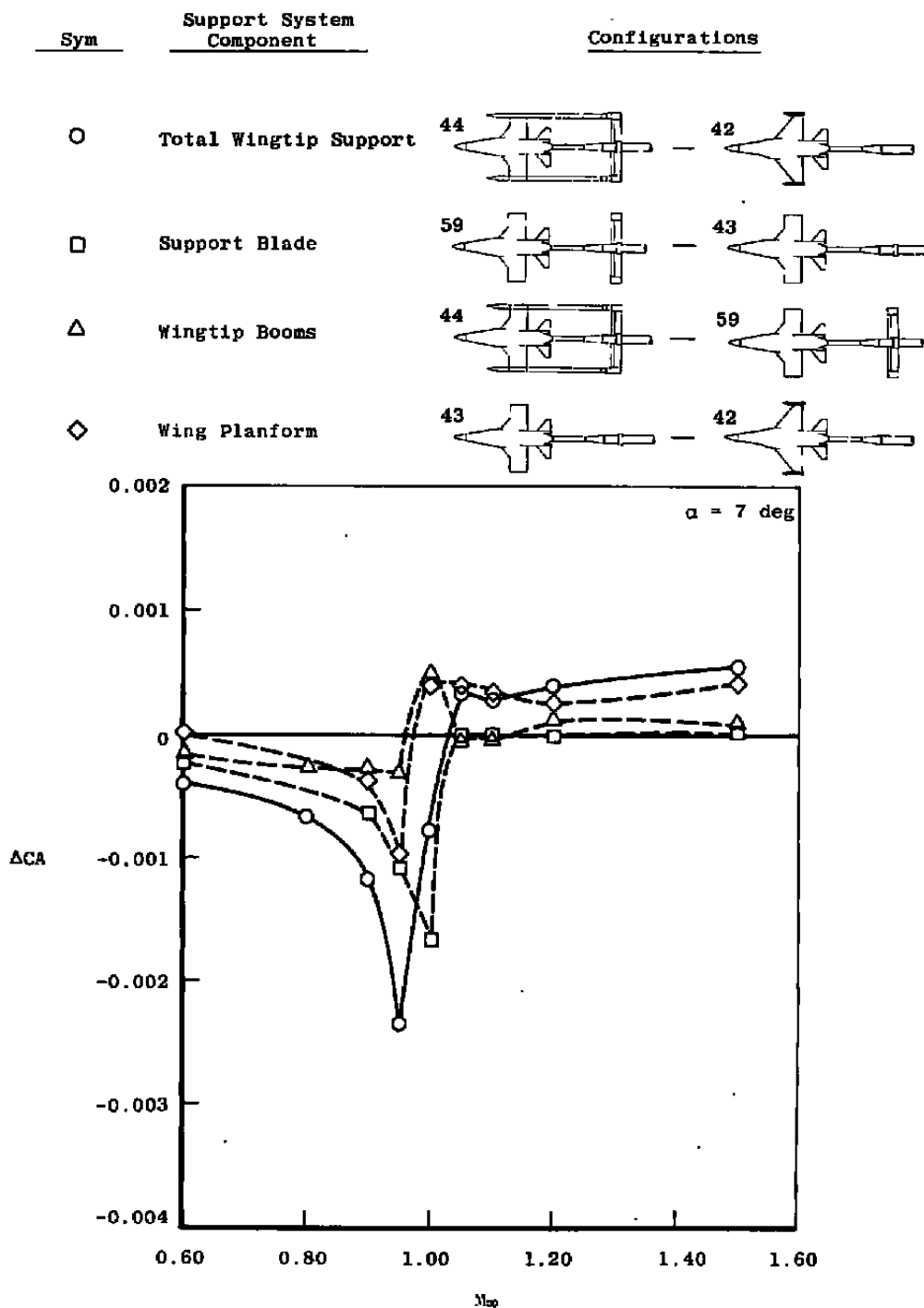


Figure 54. Comparison of total wingtip and various wingtip component interference increments on nozzle-afterbody axial force, large sting support system, max A/B 6.6 nozzle, NPR = 4.8.



b. $\alpha = 7 \text{ deg}$
 Figure 54. Concluded.

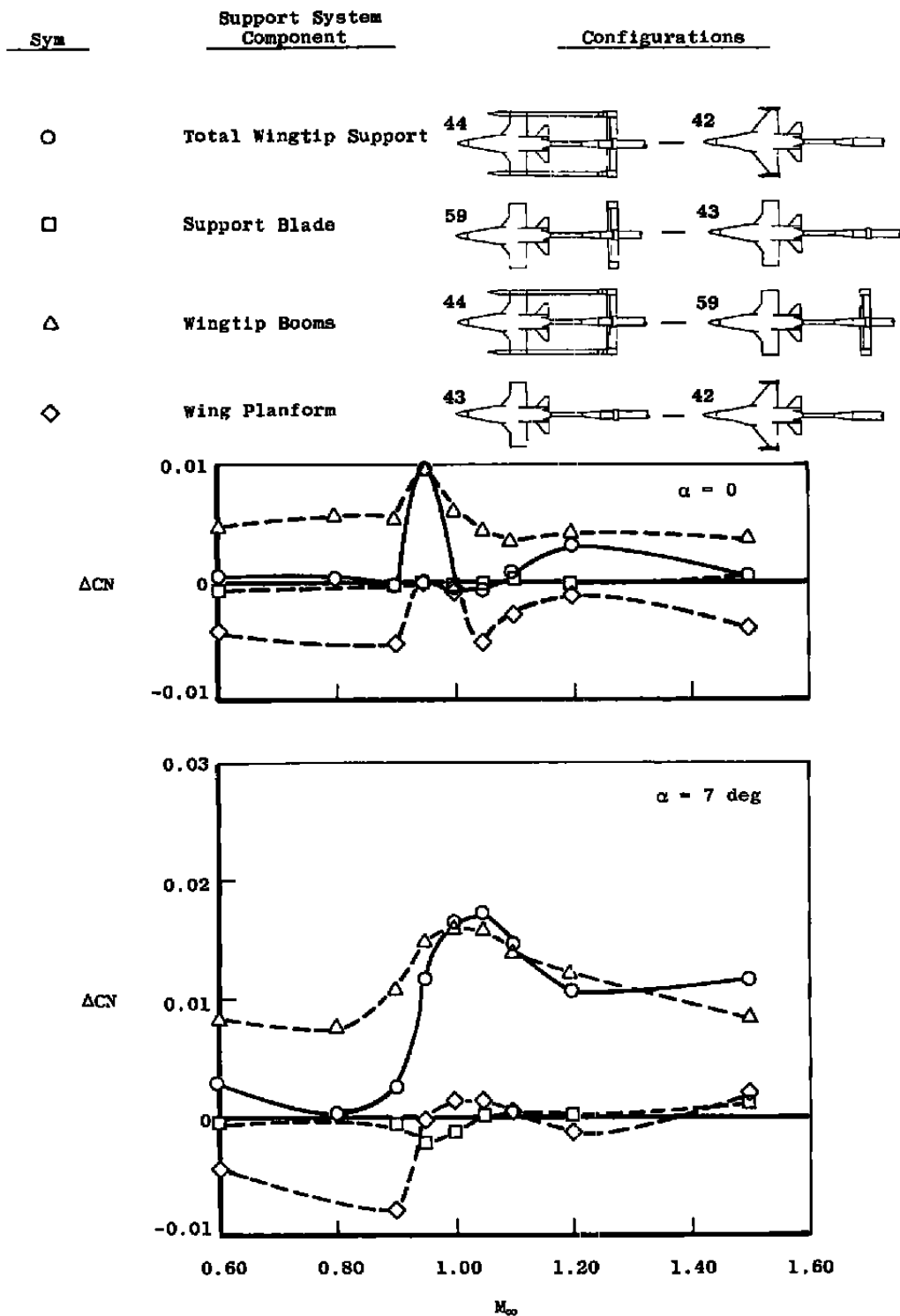


Figure 55. Comparison of total wingtip and various wingtip component interference increments on nozzle-afterbody normal force, large sting support system, max A/B 6.6 nozzle, NPR = 4.8.

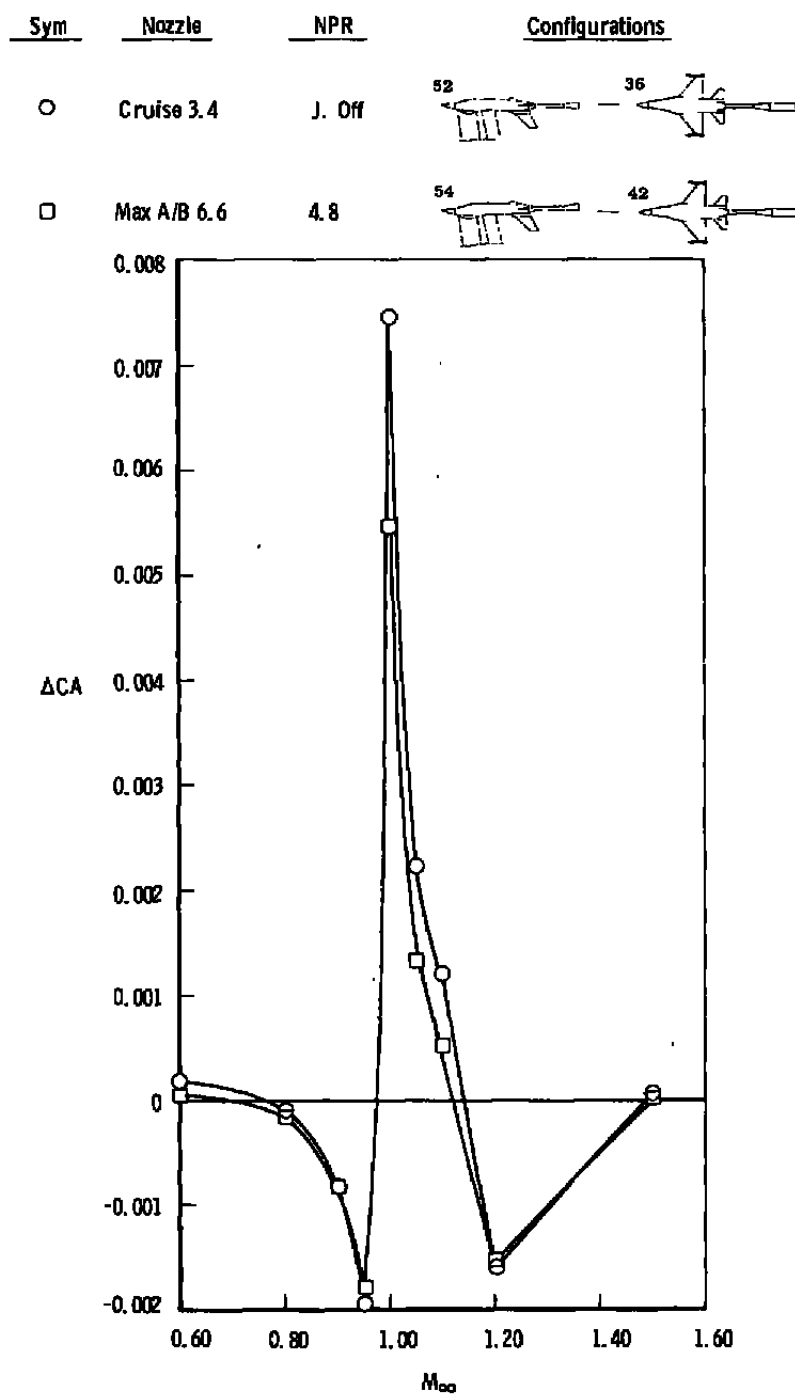
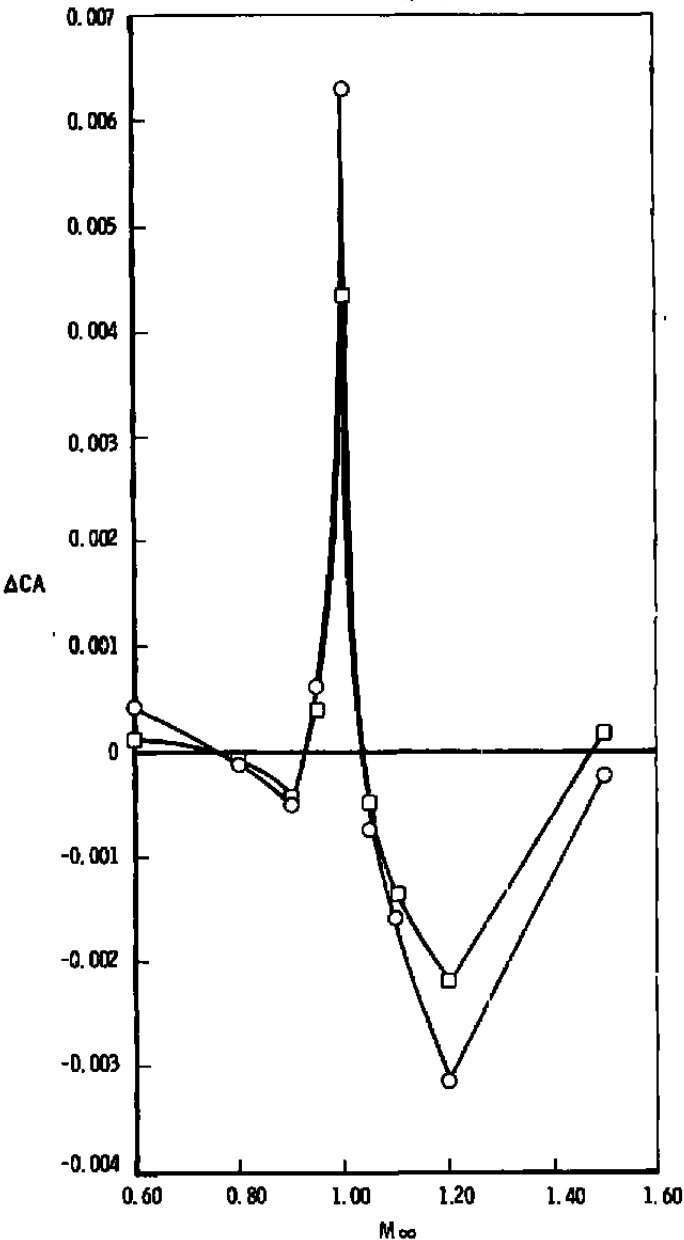


Figure 56. Strut interference on nozzle-afterbody axial force.

Sym	Nozzle	NPR	Configurations
○	Cruise 3.4	J. Off	52 — 38
□	Max A/B 6 6	4.8	54 — 42



b. $\alpha = 7^\circ$
Figure 56. Concluded.

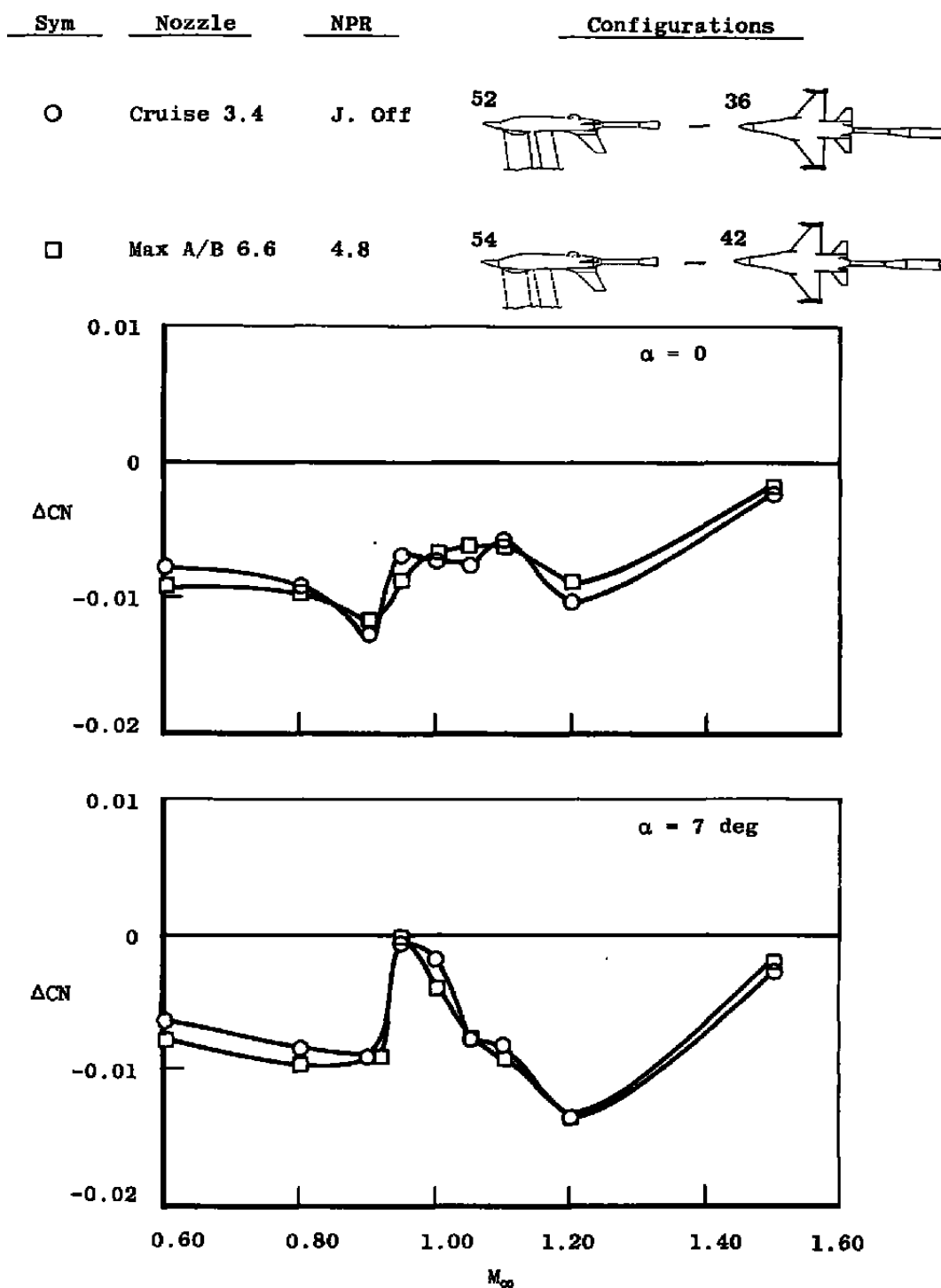
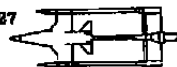
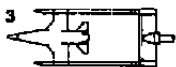
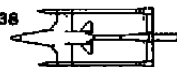


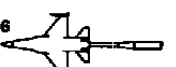


Figure 57. Strut interference on nozzle-afterbody normal force.

Sym	Support System	Configurations	Sting Diam.	NPR
○	Annular Jet Simulation	 — 	2.4	3.3
□	Wingtip	 — 	2.75	J. Off
△	Strut	 — 	2.75	J. Off

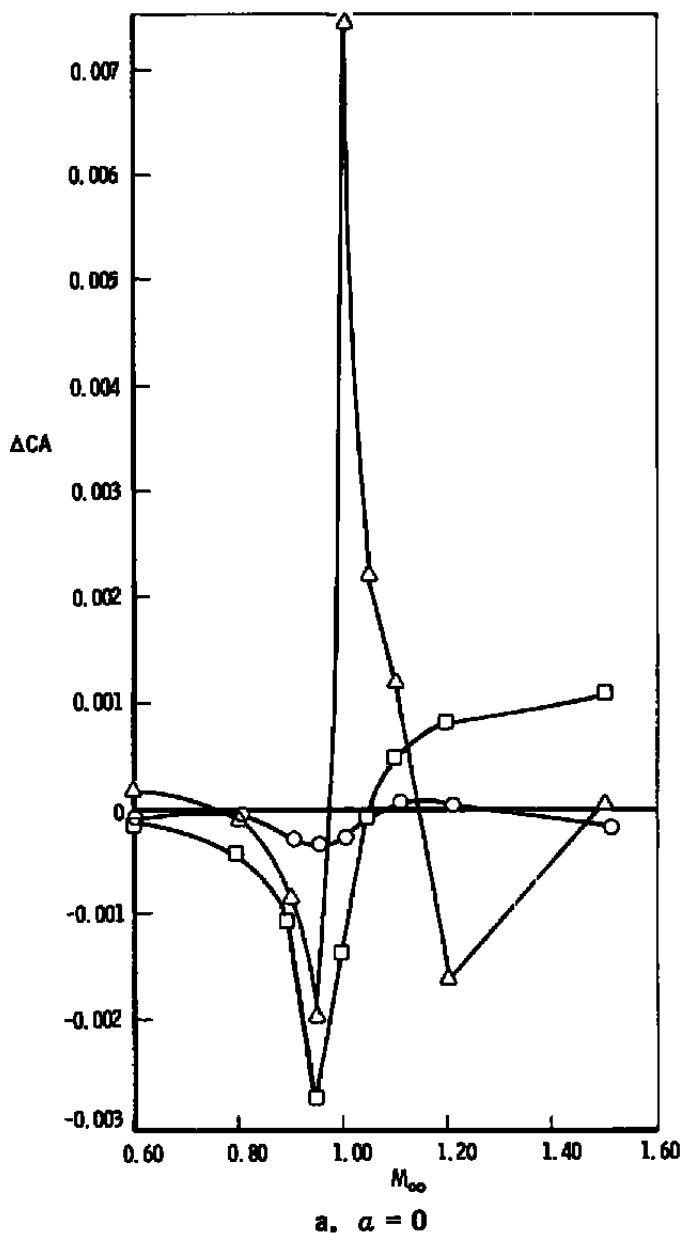
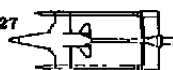
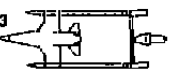
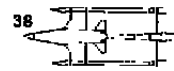
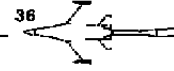

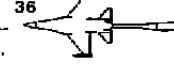


Figure 58. Comparison of interference on nozzle-afterbody axial force from sting, wingtip, and strut support systems, cruise 3.4 nozzle.

Sym	Support System	Configurations	Sting Diam.	NPR
○	Annular Jet Simulation	 — 	2.4	3.3
□	Wingtip	 — 	2.75	J. Off
△	Strut	 — 	2.75	J. Off

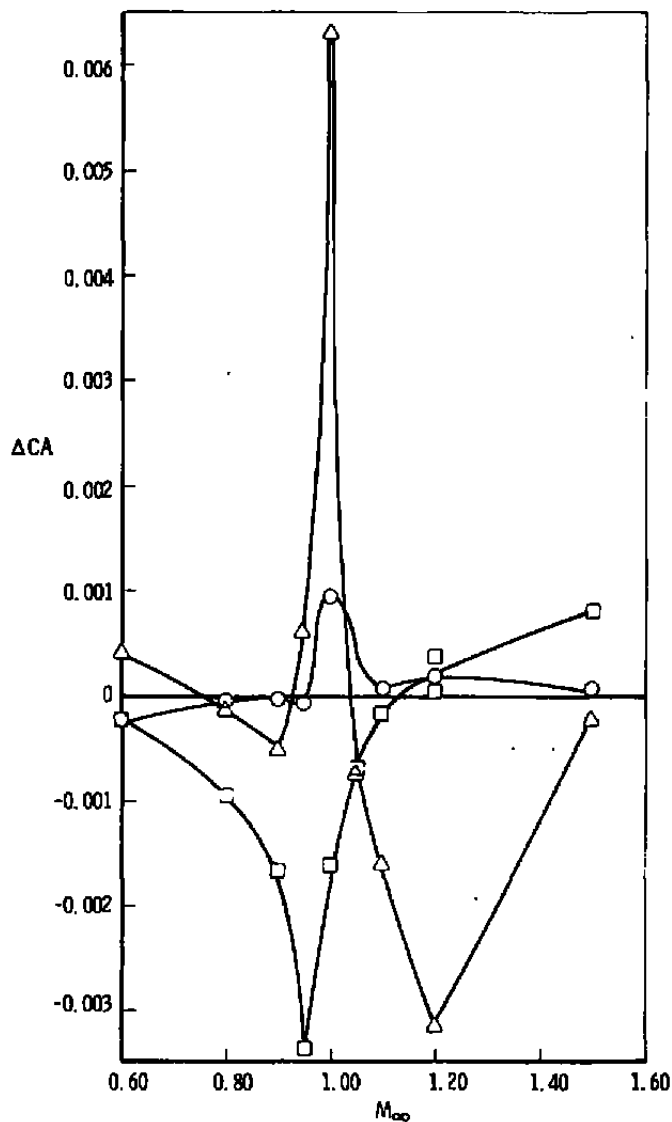
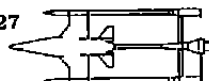
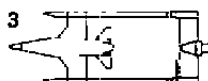
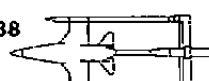
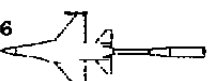
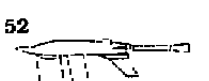
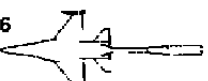
b. $\alpha = 7$ deg

Figure 58. Concluded.

Sym	Support System	Configurations	Sting Diam.	NPR
O	Annular Jet Simulation	27  — 3 	2.4	3.3
□	Wingtip	38  — 36 	2.75	J. Off
Δ	Strut	52  — 36 	2.75	J. Off

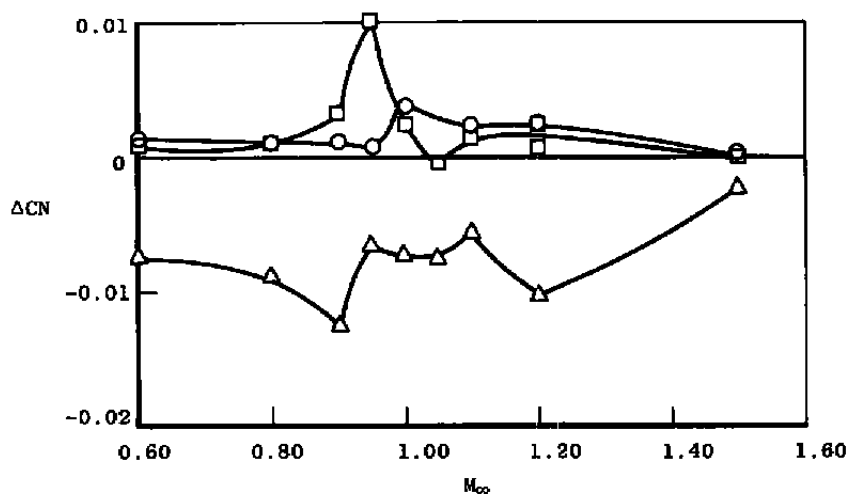
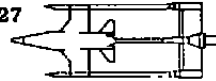
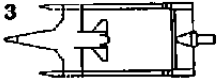
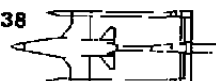
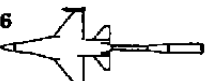

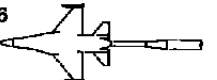
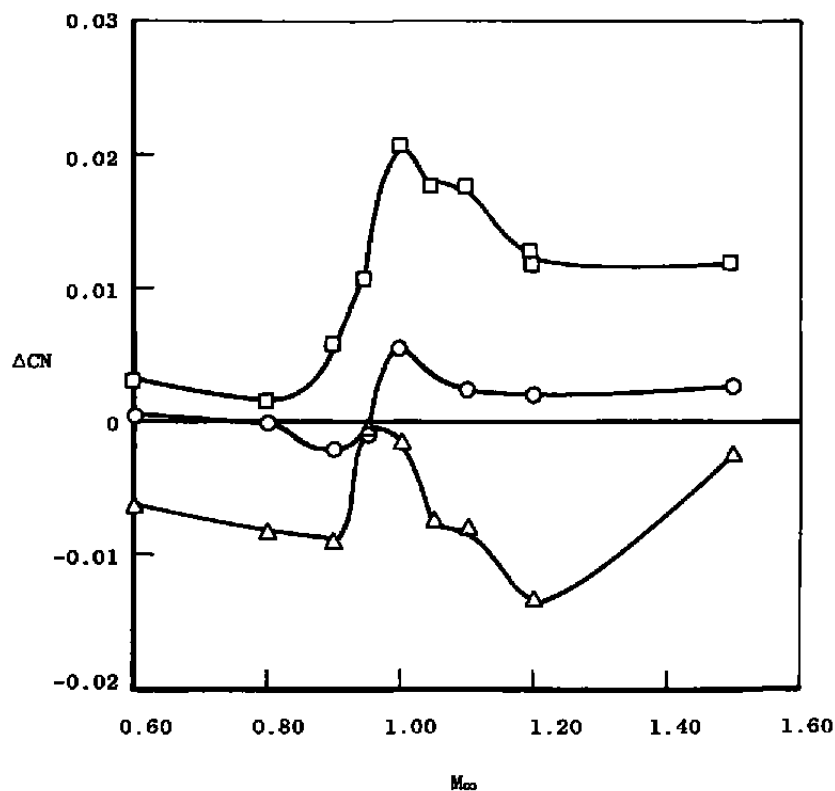
a. $\alpha = 0$

Figure 59. Comparison of interference on nozzle-afterbody normal force from sting, wingtip, and strut support systems, cruise 3.4 nozzle, $\alpha = 0$.

<u>Sym</u>	<u>Support System</u>	<u>Configurations</u>	<u>Sting Diam.</u>	<u>NPR</u>
○	Annular Jet Simulation	27  — 3 	2.4	3.3
□	Wingtip	38  — 36 	2.75	J. Off
△	Strut	52  — 36 	2.75	J. Off



b. $\alpha = 7$ deg
Figure 59. Concluded.

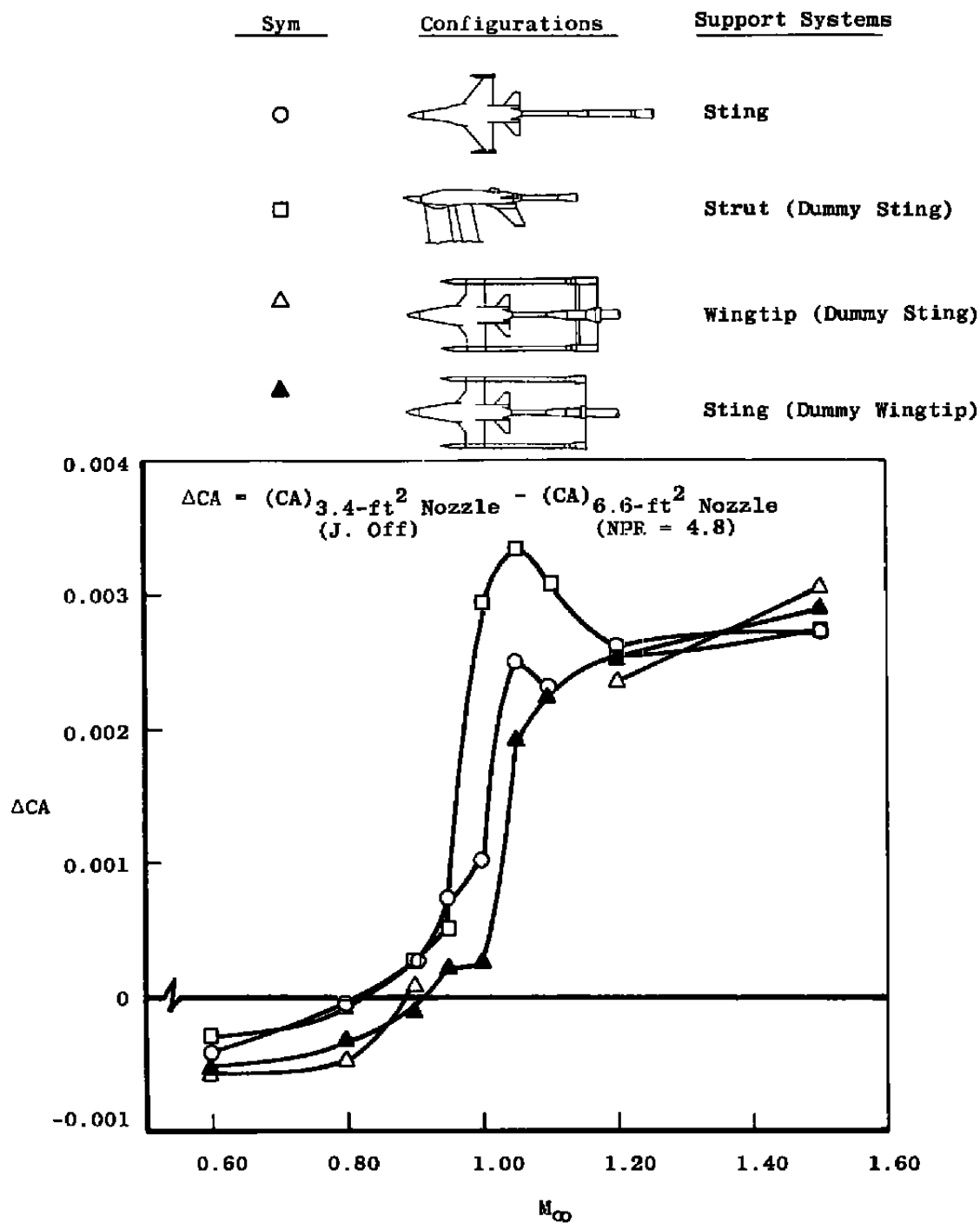


Figure 60. Influence of support interference on nozzle configuration evaluation

Table 1. Configuration List

Configuration Description					
Config No.	Support System	Dummy Support System	Nozzle Geometry	A _e , ft ²	Configuration Variable
1	Wingtip	None	Elliptical	3.4	Boundary-Layer Rake Study
3			Cruise		
4					Standard Boom Installed in Most Forward Position, Boom Tip at Nose of Model
6					1.5-in.-diam Wingtip Boom in Standard Position
7					Wingtip Support Blade in Alternate Position One (Blade Tip at F.S. 88.277)
10			Max A/B	6.6	Wingtip Support Blade in Alternate Position One (Blade Tip at F.S. 88.277)
11					1.5-in.-diam Wingtip Boom in Standard Position
14					
15			Part A/B	5.1	
16			Max A/B	7.75	
17			Circ Arc	3.4	
20		Large String	Cruise	3.4	
21			Max A/B	7.75	
22			Max A/B	6.6	
23			Part A/B	5.1	
25		Small String	Max A/B	6.6	
27			Cruise	3.4	
28		Small String			String Taper in Most Forward Position, 14.25 in. from Nozzle Exit ($X^*/D_B = 2$)
30					
31			Part A/B	5.1	
32			Max A/B	6.6	
33			Max A/B	7.75	
56	Wingtip	Small String	Cruise	3.4	String Taper in Most Forward Position, as Config 28; Fairing for Large Dummy String Used

Table 2. Configuration Identification

Configuration Description					
Config No.	Support System	Dummy Support System	Nozzle Geometry	A _e , ft ²	Configuration Variable
34	Large String	None	Max A/B	7.75	Cylindrical Extension Installed
35			Elliptical	3.4	Separation Study
36			Cruise		Flight Simulation
38		Wingtip			Standard Wingtip System
39				Inboard Boom Position	
40				Outboard Boom Position	
41		None	Part A/B	5.1	Flight Simulation
42		None	Max A/B	6.6	Flight Simulation
43		Wingtip (Modified)			Modified Wing Only (Booms, Pads, & Blade Off)
44		Wingtip			Standard Wingtip System
45					Inboard Boom Position
46				Outboard Boom Position	
47		None		Cyl Ref	7.75
57		None	7.75		Aero Model Tie-in
58		Wingtip	Max A/B	6.6	Support Blade 6.75 in. Aft of Standard Position
59		Wingtip (Modified)			Modified Wing Planform with Standard Blade (Booms & Pads Off)
51	Strut	None			Standard Strut Support
52		Large String	Cruise	3.4	Strut Interference ($X^*/D_B = 3.0$)
54			Max A/B	6.6	Strut Interference
60					Sting Taper Study ($X^*/D_B = 1.0$)
61					Sting Taper Study ($X^*/D_B = 1.5$)

Table 2. Configuration Identification

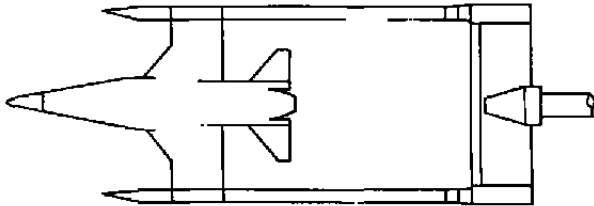
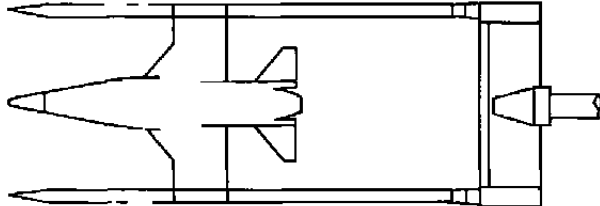
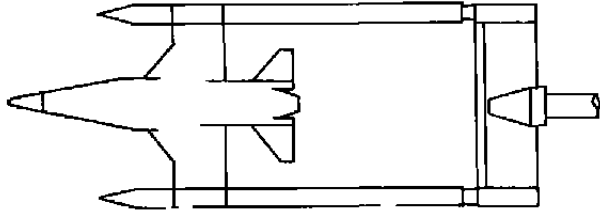
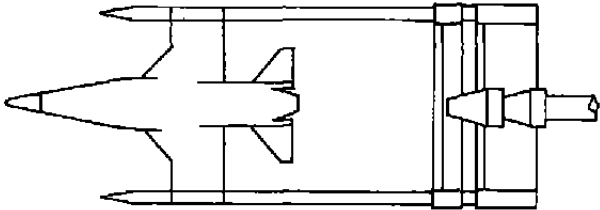
Config	Nozzle	Support System	Dummy Support	Other Config Description	Config	Nozzle	Support System	Dummy Support	Other Config Description
3 15 14 16	Cruise 3.4 Part A/B 5.1 Max A/B 6.6 Max A/B 7.75	Wingtip ↓ ↓	None ↓ ↓		4	Cruise 3.4	Wingtip	None	Booms Extended to Model Nose
									
Config	Nozzle	Support System	Dummy Support	Other Config Description	Config	Nozzle	Support System	Dummy Support	Other Config Description
6 11	Cruise 3.4 Max A/B 6.6	Wingtip ↓	None ↓	Large Diam Booms (1.5 x Std)	7 10	Cruise 3.4 Max A/B 6.6	Wingtip ↓	None ↓	Support Blade Moved Forward to F.S. 88.277
									

Table 2. Continued.

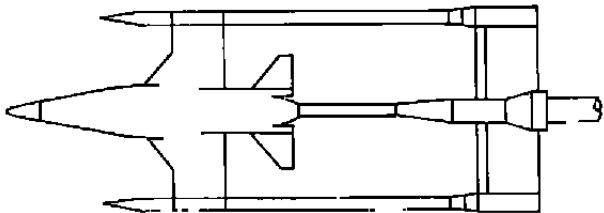
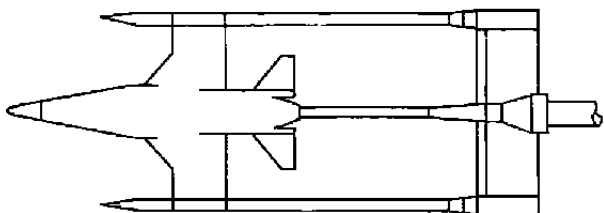
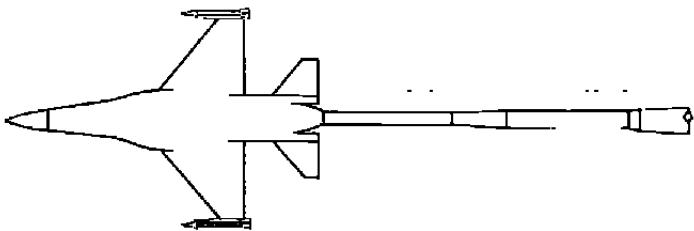
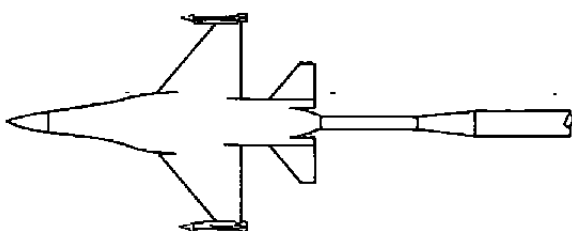
Config	Nozzle	Support System	Dummy Support	Other Config Description	Config	Nozzle	Support System	Dummy Support	Other Config Description
20 21 22 23	Cruise 3.4 Max A/B 7.75 Max A/B 6.6 Part A/B 5.1	Wingtip ↓	Large Sting ↓		25 27	Max A/B 6.6 Cruise 3.4	Wingtip ↓	Small Sting ↓	
									
Config	Nozzle	Support System	Dummy Support	Other Config Description	Config	Nozzle	Support System	Dummy Support	Other Config Description
30 31 32 33	Cruise 3.4 Part A/B 5.1 Max A/B 6.6 Max A/B 7.75	Small Sting ↓	None ↓		36 41 42 47	Cruise 3.4 Part A/B 5.1 Max A/B 6.6 Max A/B 7.75	Large Sting ↓	None ↓	
									

Table 2. Continued.

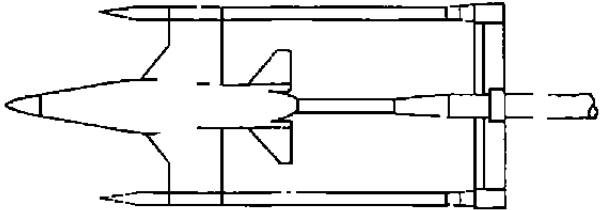
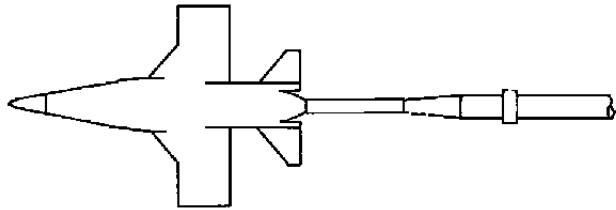
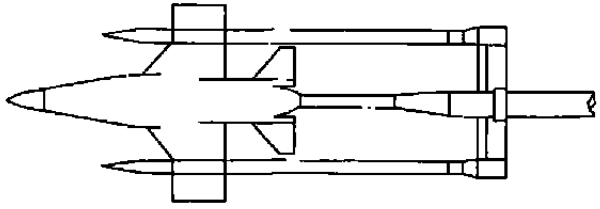
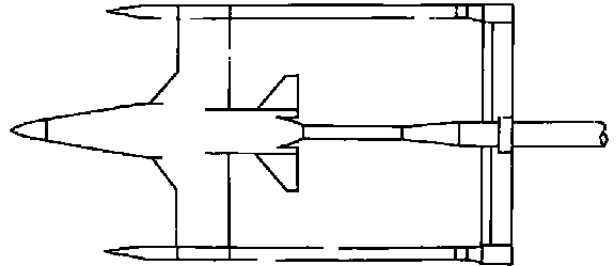
Config	Nozzle	Support System	Dummy Support	Other Config Description	Config	Nozzle	Support System	Dummy Support	Other Config Description
38 44	Cruise 3, 4 Max A/B 6, 6	Large Sting ↓	Wingtip ↓		43	Max A/B 6, 6	Large Sting	Modified Wingtip	Booms, Pads, and Blade Off
									
Config	Nozzle	Support System	Dummy Support	Other Config Description	Config	Nozzle	Support System	Dummy Support	Other Config Description
45	Max A/B 6, 6	Large Sting	Wingtip	Inboard Boom Position	46	Max A/B 6, 6	Large Sting	Wingtip	Outboard Boom Position
									

Table 2. Continued.

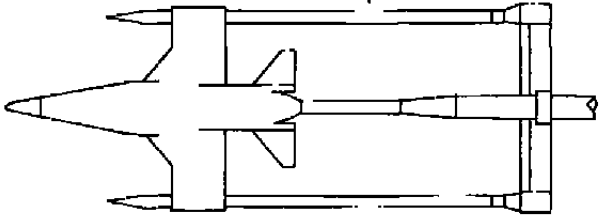
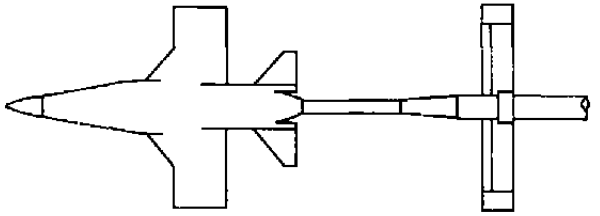
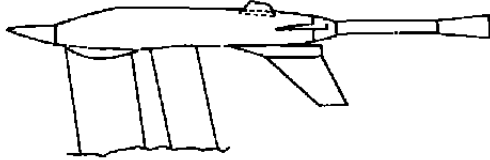
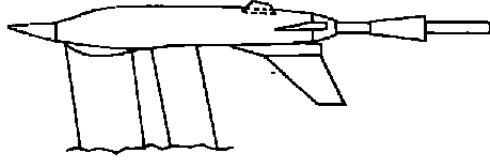
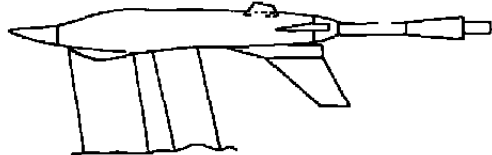
Config	Nozzle	Support System	Dummy Support	Other Config Description	Config	Nozzle	Support System	Dummy Support	Other Config Description
58	Max A/B 6.6	Large Sting	Wingtip	Support Blade Moved Aft to F. S. 105.628	59	Max A/B 6.6	Large Sting	Modified Wingtip	Booms and Pads Off
									
Config	Nozzle	Support System	Dummy Support	Other Config Description	Config	Nozzle	Support System	Dummy Support	Other Config Description
52 54	Cruise 3.4 Max A/B 6.6	Strut ↓	Large Sting ↓	Large Sting Taper, $X/D_B = 3.0$ ↓	60	Max A/B 6.6	Strut	Large Sting	Large Sting Taper, $X/D_B = 1.0$
									

Table 2. Concluded.

Config	Nozzle	Support System	Dummy Support	Other Config Description				
61	Max A/B 6.6	Strut	Large Sting	Large Sting Taper, $X/D_B = 1.5$				
								

NOMENCLATURE

ABXXX	Circumferential location of afterbody pressure orifices, deg
ALPHA	Model angle of attack, deg
A_E	Model nozzle exit area, in. ²
A_e	Full-scale nozzle exit area, ft ²
A_{ref}	Model wing reference area, 3.7037 ft ²
A_T	Nozzle throat area, in. ²
B.L.	Butt line, in.
CA	Axial-force coefficient of the complete nozzle and afterbody region of the model, force/ $q_\infty A_{ref}$
CAAB	Axial-force coefficient of the afterbody region of the model, force/ $q_\infty A_{ref}$
CAN	Axial-force coefficient of the nozzle, force/ $q_\infty A_{ref}$
CN	Normal-force coefficient of the complete nozzle and afterbody region of the model, force/ $q_\infty A_{ref}$
CONF	Configuration
C_p	Pressure coefficient, $(p_x - p_\infty)/q_\infty$
DELHR	Horizontal tail deflection angle, positive leading-edge deflection is up, deg
D_B	Equivalent model diameter, 7.125 in.
D_E	Nozzle exit diameter, in.
D_M	Maximum sting diameter at downstream end of sting taper, in.
D_S	Sting diameter at nozzle exit plane, in.
D_T	Nozzle throat diameter, in.
F.S.	Fuselage station, in.
L	Model length, 62.21 in.

M_{∞}	Free-stream Mach number
NPR	Nozzle total pressure to free-stream static pressure ratio
NPREF	Effective jet nozzle pressure ratio for an annular jet based on maximum jet diameter (see Section 4.2.1.1)
p_x	Local static pressure, psfa
PN•PT	Data identification number
PT	Free-stream total pressure, psfa
p_{∞}	Free-stream static pressure, psfa
q_{∞}	Free-stream dynamic pressure, psf
RN	Free-stream Reynolds number per foot
TS	Tunnel station, in.
t	Aft support blade thickness, 1.778 in.
X	Axial distance from FS 0
X_1	Axial distance from nozzle exit plane to downstream end of sting taper, in.
X'	Axial distance from nozzle exit plane to beginning of sting taper, in.
α	Model angle of attack, deg
ΔCA	Incremental value of nozzle-afterbody axial-force coefficient
ΔCN	Incremental value of nozzle-afterbody normal-force coefficient
ΔX	Incremental movement of aft-support blade from nominal position, in. (downstream is positive movement)

SUBSCRIPTS

c	Conventional full plume
S	Small sting
L	Large sting